INFORMATION TO USERS

This manuscript has been reproduced from the microfilm master. UMI films the text directly from the original or copy submitted. Thus, some thesis and dissertation copies are in typewriter face, while others may be from any type of computer printer.

The quality of this reproduction is dependent upon the quality of the copy submitted. Broken or indistinct print, colored or poor quality illustrations and photographs, print bleedthrough, substandard margins, and improper alignment can adversely affect reproduction.

In the unlikely event that the author did not send UMI a complete manuscript and there are missing pages, these will be noted. Also, if unauthorized copyright material had to be removed, a note will indicate the deletion.

Oversize materials (e.g., maps, drawings, charts) are reproduced by sectioning the original, beginning at the upper left-hand corner and continuing from left to right in equal sections with small overlaps.

ProQuest Information and Learning
300 North Zeeb Road, Ann Arbor, MI 48106-1346 USA
800-521-0600

Fluid Dynamics and Mass Transport in Rotating Channels with Application to Centrifugal Membrane Separation

by

Jon George Pharoah
B.A.Sc., University of Waterloo, 1994
M.A.Sc., University of Victoria, 1997

A Dissertation Submitted in Partial Fulfillment of the
Requirements for the Degree of
DOCTOR OF PHILOSOPHY
in the
Department of Mechanical Engineering.

We accept this dissertation as conforming
to the required standard

Dr. N. Djilali, Co-Supervisor (Dept. of Mechanical Engineering)

Dr. G.W. Vickers, Co-Supervisor (Dept. of Mechanical Engineering)

Dr. S. Dost, Member (Dept. of Mechanical Engineering)

Dr. T.M. Fyles, Outside Member (Dept. of Chemistry)

Dr. K. Nandakumar, External Examiner (University of Alberta)

Supervisors: Dr. Ned Djilali, Dr. Geoff Vickers

Abstract

Centrifugal membrane and density separation (CMS) is a novel technology proposed for treatment of waste water and industrial process streams. This cross flow filtration process combines the energy recovery inherent to centrifugal reverse osmosis (CRO) with the potential alleviation of membrane fouling and concentration polarization due to the favourable effects of centrifugal and Coriolis accelerations.

This dissertation presents a computational study of CMS undertaken to understand the basic hydrodynamics and mass transfer of the processes and to provide insight for the design of CMS devices. Two distinct membrane models were developed, the porous wall model (PWM) and the source term model (STM), and incorporated into Computational Fluid Dynamics (CFD) codes which solve the full Navier-Stokes equations coupled to a scalar transport equation which accounts for dissolved species. These models are used to simulate two and three dimensional laminar flows in both non-rotating and rotating reverse osmosis membrane cartridges and to predict permeate fluxes.

Plate and frame geometries are first examined and it is determined that CMS benefits most from channels with streamwise directions directed radially. It is also shown that the benefits of CMS can be attributed largely to the secondary flows and mixing associated with Coriolis acceleration, and the PWM and the STM are found to perform similarly in the case of reverse osmosis. Next, the STM is used to perform a parametric study of the flow and mass transfer in rectangular and square rotating channels. It is shown that while normal rotation is preferable to spanwise rotation, relatively small deviations from the spanwise orientation are adequate to achieve most of the normal rotation performance, and that differences between the two orientations

are minimal in the case of square channels. Also, the flow characteristics are again shown to correlate well with the the magnitude of the Coriolis acceleration.

Flows in triangular and circular channels are also considered, and are shown to perform similarly to rectangular channels. These channel orientations have application in hollow fiber membrane modules and potentially in spiral wound membrane modules.

Finally, the flow and mass transfer in channels with periodic streamwise obstacles are considered. Such obstacles are related to feed spacers used in spiral wound membrane elements and impact considerably on the flow characteristics and mass transfer performance. Flow obstacles are shown to increase mass transfer performance in all cases, with alternating surface mounted performing best. A preliminary investigation is undertaken into rotating flows with periodic obstacles, and the flow fields are shown to depend strongly on the blockage ratio and on the Rossby number. In most cases, it is found that mass transfer performance does not necessarily correlate with either wall shear stress or the *local* flow field.

Several general conclusions regarding CMS can be drawn from this work. It is preferable to operate a CMS devices at low flow rates, which is contrary to conventional wisdom in membrane separation. Secondly, the mixing induced by channel rotation is both more effective and more efficient than the mixing induced by the feed spacers considered here. Finally, the magnitude of the Coriolis acceleration is the dominant parameter in determining CMS performance. This means that a CMS device can either operate at relatively low rotational speeds with flow in the radial direction, or at higher speeds but lower angles of inclination with respect to the rotational axis.

Examiners:

Dr. N. Djilali, Co-Supervisor (Dept. of Mechanical Engineering)

Dr. G.W. Vickers, Co-Supervisor (Dept. of Mechanical Engineering)

Dr. S. Dost, Member (Dept. of Mechanical Engineering)

Dr. T.M. Fyles, Outside Member (Dept. of Chemistry)

Dr. K. Nandakumar, External Examiner (University of Alberta)

Table of Contents

List of Tables

List of Figures

Nomenclature

A_{out}	Area of membrane associated with one control volume $[m^2]$
A_i	Area of membrane associated with one control volume $[m^2]$
$\bar{c}$	Average concentration across membrane $[kg/m^3]$
c_f	Feed concentration $[kg/m^3]$
c_f	Local friction coefficient [-]
C_f	Circumferentially averaged c_f [-]
C_{fx}	X component of c_f [-]
c_p	Permeate concentration $[kg/m^3]$
c_p	Pressure coefficient [-]
$\mathcal{D}$	Diffusivity $[m^2/s]$
D	Channel dimension $[m]$
D_h	Channel hydraulic diameter $[m]$
Ek	Ekman number, $Ek = \nu/D^2\Omega$
h	Half height of channel [m]
i, j, k	Coordinate directions in computational space
j_v	Solution volume flux $[m/s]$
J_s	solute mass flux $[kg/(m^2 s)]$
$J_{1,2}$	Component mass fluxes $[mol/(m^3 s)]$
l	Vertical dimension of control volume
L_p	Hydraulic permeability [m/(s Pa)]
L_x	Streamwise dimension of channel [m]
L_z	Spanwise dimension of channel [m]
P	Static Pressure [Pa]
P_e	Excess pressure [-]
P_i	Local pressure [Pa]
P_{fe}	Flux element averaged pressure [Pa]
r_p	Permeate release radius [m]

R	Rejection based on concentration [-]
R'	Rejection based on mass fraction [-]
R_i	Accelerations due to rotational frame $[m/s^2]$
Re_w	Reynolds number Based on x, $Re_w = v_w D/\nu$
Re_D	Reynolds number based on D [-]
Re_h	Reynolds number based on channel half height [-]
Ro	Rotation number based on D [-]
S	Circumferential coordinate [-]
Sc	Schmidt number [-]
S_ϕ	Volumetric Source term in ϕ equation
S_ϕ^o	S_ϕ at previous time step
t	Time [s]
T	Temperature $[^oC]$
u, v, w	Velocity components in x,y and z directions [m/s]
U	Bulk velocity $[m/s]$
u_i	Velocity vector $[m/s]$
U_o	Average streamwise velocity at channel inlet [m/s]
v_w	Transpiration velocity $[m/s]$
V	Volume of control volume $[m^3]$
V_{av}	Bulk velocity $[m/s]$
x_j	Position vector $[m]$
x, y, z	Cordinate axes
X_r	Reattachment length $[m]$

Greek Symbols

α	Roll angle [-]
β	Yaw angle [-]
γ	Pitch angle [-]
Γ	Molecular diffusivity $[kg/ms]$
δ_{ij}	Kronecker delta [-]
δ_t	Time step [s]
δ_x	Control volume dimension
δ_y	Control volume dimension
ϵ_{ilm}	Alternating tensor [-]
μ	Molecular viscosity [kg / m s]
ν	Kinematic viscosity $[m^2/s]$
Π	Osmotic Pressure [Pa]
ϕ	Mass fraction [-]
ϕ_{av}	Spanwise averaged mass fraction [-]
ϕ^o	Mass fraction at previous time step [-]
ϕ_o	Mass fraction at channel inlet [-]
ϕ_i	Local mass fraction [-]
ρ	Density $[kg/m^3]$
ρ_{out}	Density of fluid passing through a membrane BC face $[kg/m^3]$
ρ_i	Local density $[kg/m^3]$
ρ_p	Density of permeate$[kg/m^3]$
ρ_f	Density of feed $[kg/m^3]$
σ	Reflection coefficient [-]
ω	Solute permeability (osmotic pressure based) [s/m]
ω'	Solute permeability (concentration based [m/s]
Ω	Rotational speed $[s^{-1}]$

Acronynms

AR	Aspect Ratio
CMS	Centrifugal Membrane Separation
CRO	Centrifugal Reverse Osmosis
PWM	Porous Wall Model
RO	Reverse Osmosis
STM	Source Term Model

Acknowledgements

I would like to sincerely thank Dr. Ned Djilali for his guidance, friendship and support over the past seven years. During this time, I have grown tremendously and I cannot imagine a better graduate experience than that which I have enjoyed under Dr. Djilali. I would also like to thank my co-supervisor, Dr. Geoff Vickers, and the members of my examining committee: Dr. T.M. Fyles, Dr. S. Dost and Dr. K. Nandakumar. I must also thank my fellow graduate students including Anotai Suksangpanomrung, Ian Spearing, Torsten Berning, Juan Carretero and in particular Gonçalo Pedro who put up with an interminable stream of senseless babble as the ideas and understanding were developing. Discussions with Alvin Bergen were also instrumental to the development of this work.

Nine years ago, I was introduced to Computational Fluid Dynamics by a professor at the University of Waterloo. This same professor showed me the way to graduate studies and set me on the path that led to this point and that I will follow through my career. I am forever indebted, Dr. Stubley.

Finally, I must thank my wife Stephanie and my son Luke who make it all worthwhile.

To family, friends and the pursuit of knowledge.

Chapter 1

Introduction to Centrifugal Membrane Separation (CMS)

1.1 Membrane Separation

Membrane separation processes are used in a wide variety of industries and processes including the production of potable water, the de-inking of recycled paper and the de-watering of fruit juice. Membranes are finding increased use in all these industries due to the energy efficiency of membrane processes which do not rely on phase changes. The current worldwide membrane market is estimated at 6.55 billion US$ and is anticipated to grow 8.3 % per year [1]. Membrane separation is a process which makes use of a semi-permeable membrane in order to separate a feed stream into a permeate stream and a concentrate, or retentate stream. While dead end separation, wherein all the feed passes through the membrane, is sometimes used, this work will focus on cross flow filtration, as depicted conceptually in figure 1.1.

The membranes used to perform the separation can be packaged in one of four

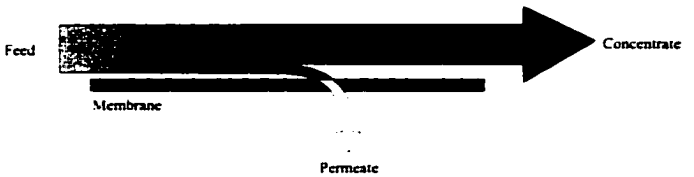

Figure 1.1: Cross flow filtration

common arrangements: plate and frame, spiral wound, hollow fibre and tubular.

In both plate and frame and spiral wound modules the membrane is produced as a flat sheet. In the case of plate and frame modules the membrane sheets are simply attached frames which are stacked together in such a fashion that a feed flow channel is formed between the frames. Plate and frame modules suffer from the fact that the packing density, or the amount of membrane area which can be packed into a given volume, is quite low and the manufacturing costs tend to be high. Spiral wound elements neatly address both these problems. A typical spiral wound element is shown in figure 1.2. First two membrane sheets are placed back to back separated by a permeate spacer and sealed with glue on three sides. Next, the remaining side is connected to a porous permeate tube which runs through the centre of the completed module. Finally, a feed spacer is placed adjacent to each active membrane surface and the membrane sheet is rolled around the permeate tube to create a cylindrical module. The feed spacers create feed channels by insuring that the rolled up membranes do not contact each other while the permeate spacers provide a spiral path for the permeate to reach the central tube.

Both hollow fibre and tubular membranes consist of tubes of membrane material. Hollow fibres are typically small diameter ($<$ 1mm) and the entire tube is cast from the desired polymer while tubular membranes are much larger (diameter $\approx$ 2.5 cm) and are supported on a porous pressure vessel. Hollow fibre membranes are typically packaged in large bundles and the feed flow can either be through the fibres

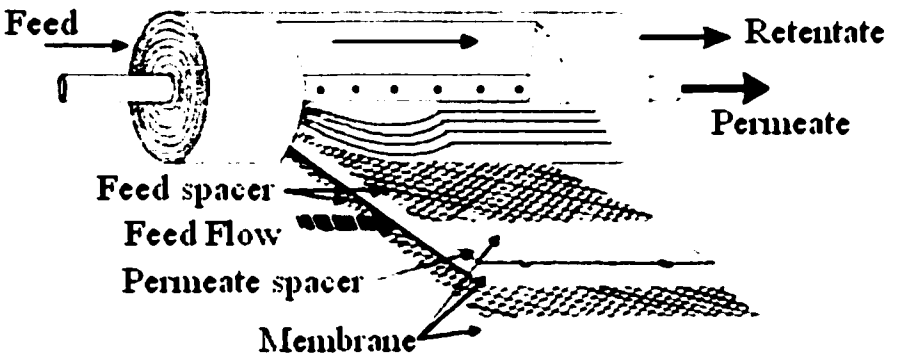

Figure 1.2: Spiral wound membrane element

themselves (lumen-shell), or around the bundles with permeate flowing into the fibres (shell-lumen).

Irrespective of the module chosen, cross flow filtration processes may be classified into four subprocesses depending on the particle cut-off of the membrane: reverse-osmosis, nano-filtration, ultra-filtration and microfiltration 1.3, as shown in figure 1.3.

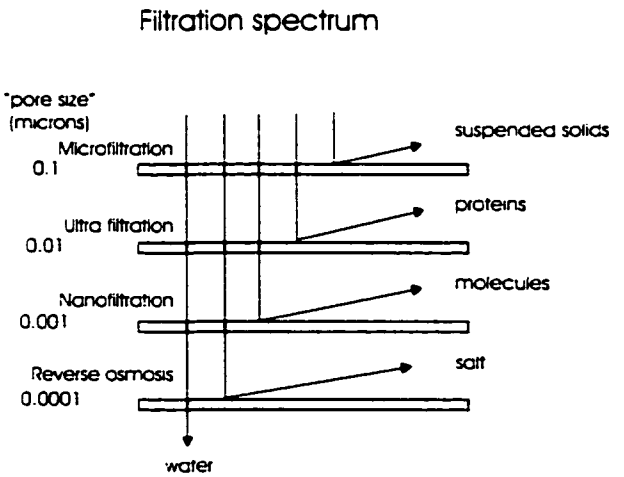

Figure 1.3: Filtration spectrum

Two of the major problems associated with membrane separation processes are membrane fouling and concentration polarization. Fouling occurs when the membrane is physically obstructed, either by a buildup of particulates on the surface or by membrane compaction, whereas concentration polarization refers to the formation of a high concentration boundary layer adjacent to the membrane which results in a local increase in the osmotic pressure and a reduction of the permeate production. Also, in the case of reverse osmosis and specifically with regards to desalination, the process energy requirements can be quite high since the feed stream pressure must be increased significantly beyond the osmotic pressure of the the feed solutions: typical feed pressures in sea water desalination plants are of the order of 5 MPa (735 psi).

While the methodologies developed herein are applicable to the entire spectrum of filtration processes the focus of this dissertation will be reverse osmosis desalination since CMS was originally developed in this optic and the experimental program has also focused on this application.

1.2 History of Centrifugal Membrane Separation

Early CMS work focused on sea water desalination, which is a reverse osmosis process, and accordingly, was referred to as centrifugal reverse osmosis (CRO). This work was originally conceived primarily to conserve energy by taking advantage of a rotating environment to recover the energy contained in the high pressure concentrate stream.

In conventional separation processes such as reverse osmosis, process pressures are achieved using high pressure pumps, and, typically, a turbine is required downstream to recover energy from the high pressure exhaust stream. Significant energy efficiency gains have been demonstrated with CRO, shown schematically in figure 1.4, in which process pressure is developed within a spinning centrifuge. The feed stream in CRO

enters the axis at low pressure and is pressurized as it flows radially outwards to the membrane. After exiting the membrane, the concentrate stream is depressurized as it returns to the axis and exits the rotor. Thus, the feed stream in CRO *enters at low pressure* and the exhaust stream *leaves at low pressure*, allowing inherent energy recovery without the addition of an auxiliary turbine. Reduction in specific energy consumption of more than 35% over non-rotating RO have been reported by Wild *et al.* [2] for a prototype producing 7.5 m^3/day of fresh water. It was also shown that the theoretical energy efficiency of CRO increases with system capacity, and up to 70 % reduction in specific energy consumption was predicted for units producing over 1000 m^3/day.

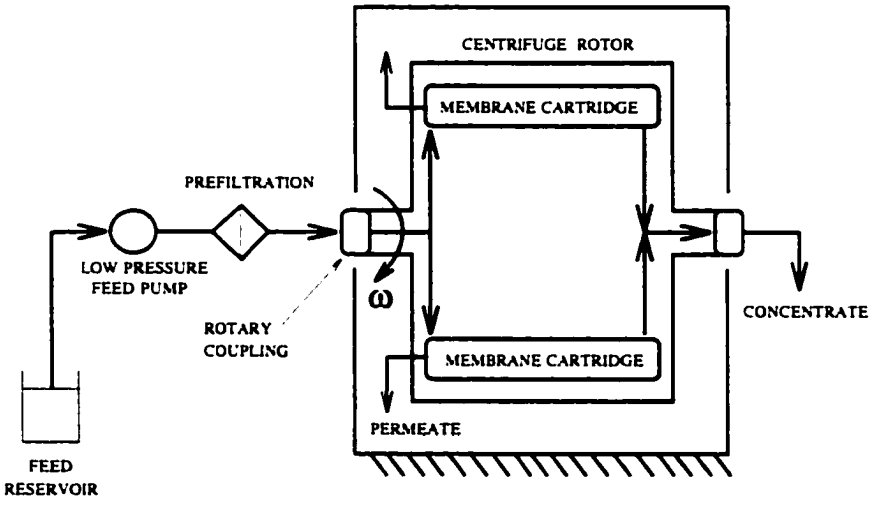

Figure 1.4: Schematic of Centrifugal Reverse Osmosis and Centrifugal Membrane Separation

Two prototypes, shown in figures 1.5 and 1.6, were built upon these ideas, and used conventional spiral wound reverse osmosis elements arranged in a gattling gun configuration around an axis of rotation. This means that while the bulk flow was in an axial direction, the membrane had active faces directed both towards and away from the axis of rotation. It was later proposed that the rotating environment could

additionally effect membrane performance, but since the focus of the original prototypes was to show energy efficiency, there was never any direct comparison of the membrane performance in these devices with those of similar non rotating systems. If additional benefits exist then the concept of rotating membrane separation extends beyond reverse osmosis to the entire filtration spectrum. This concept is a generalization of CRO, and is given the name Centrifugal Membrane Separation (CMS).

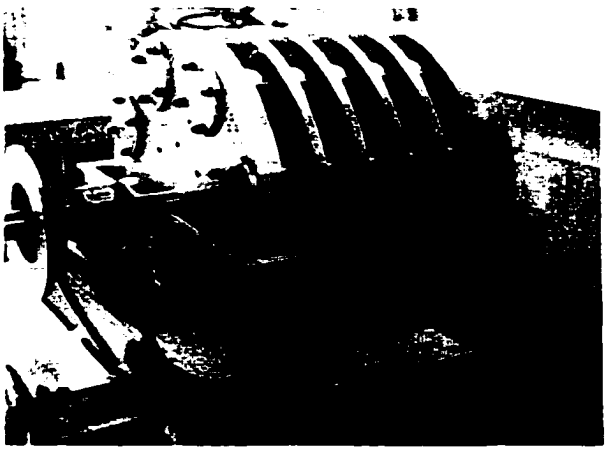

Figure 1.5: The first CRO prototype

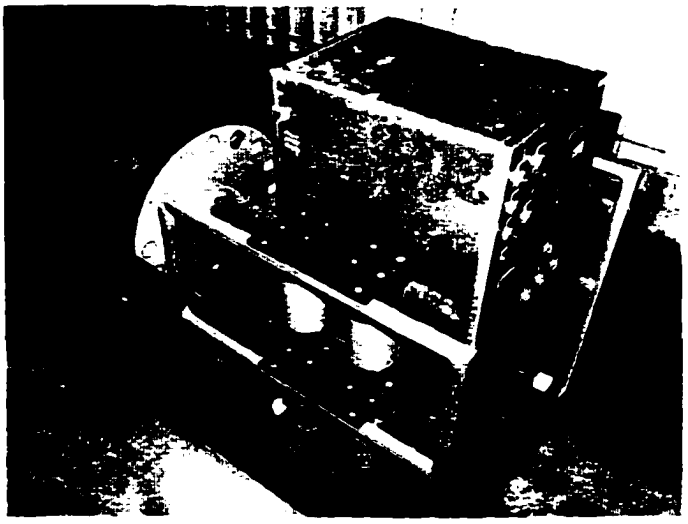

Figure 1.6: The second CRO prototype

In order to isolate the effect of membrane orientation, a CMS test apparatus, shown in figure 1.7, was designed and built which could accommodate custom plate and frame membrane discs.

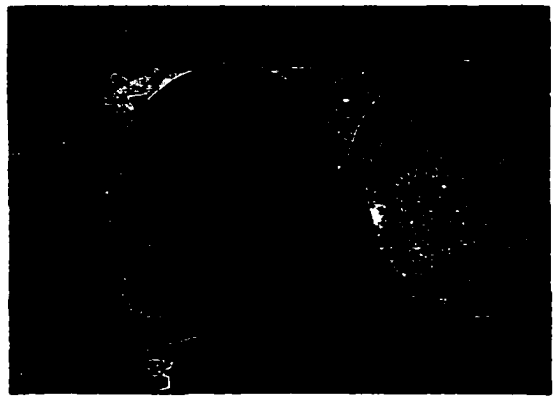

Figure 1.7: CMS experimental apparatus.

Early CMS experiments were carried out using these plate and frame membranes, depicted in figure 1.8. Lexan discs were machined such that when stacked, they formed feed flow channels of length 0.084m with a 0.0571m x 7.62×10^{-4} m ($4.34 \times 10^{-5} m^2$) cross section. Membrane material was then glued onto the face of the discs such that the resulting channels had an active membrane on one face. The membrane stack could be rotated allowing various membrane orientations with respect to the axis of rotation.

Typically, there were nine open channels stacked in the CMS apparatus, four of which had active membrane on one face, and five of which were plain machined lexan channels.

This work, and the associated modelling which will be presented in Chapter 3, clearly showed that the effect of membrane orientation with respect to the axis of rotation was significant and that CMS performance could be enhanced by a judicious choice of membrane orientation.

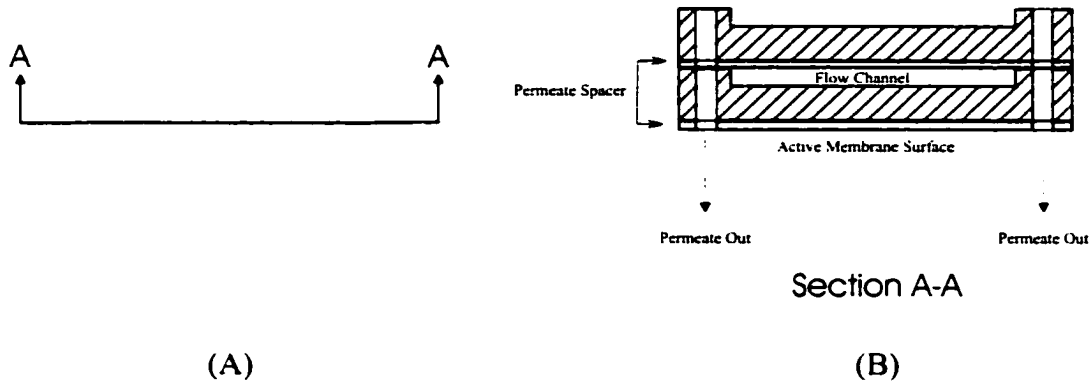

Figure 1.8: Membrane stack

In order to capitalize on this additional benefit and to scale up the experiments, a new CMS head, capable of housing a small radially oriented commercial spiral wound membrane element, was constructed. The primary difference between the plate and frame membranes (figure 1.8) and the spiral wound membranes (figure 1.2) is that the spiral would elements require the use of a feed spacer in order to keep the membranes from contacting. Two representative spacers taken from modules used at UVic are shown in figure 1.9. Clearly, these spacers have a profound effect on the flow in the resulting channels and, it is expected, on membrane performance. This effect must be correctly modelled if membrane performance is to be understood. In either case, though, it is important to quantify the flow regime of a given point in the operating space. A detailed account of the operating range of the various CMS devices is given in Appendix A.

Since the focus of this work is the fluid dynamics and mass transfer in rotating systems, it is instructive to set the stage by reviewing the parameters governing such types of flows.

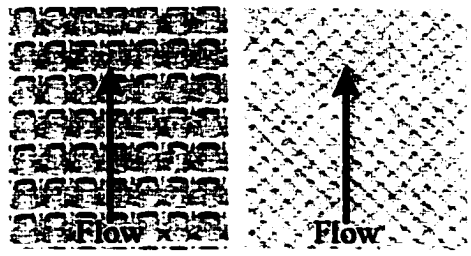

Figure 1.9: Feed spacers removed from modules at UVic. Ladder type spacer on the left and diamond type spacer on the right.

1.3 Fluid Mechanical Parameters

There are five basic non-dimensional parameters which are important in characterizing the flow in a CMS device: the Reynolds number (Re), the wall Reynolds number (Re_w) the Rossby number (Ro), the Ekman number (Ek) and the Schmidt number (Sc).

The Reynolds number is a classical parameter characterizing non-rotating viscous flows, such as flow in conventional membrane separation. This parameter is also relevant to rotating cases and represents the ratio of inertial to viscous forces.

$$Re_D = \frac{\rho U D}{\mu} \tag{1.1}$$

where ρ, U, D and μ represent respectively density, bulk velocity, hydraulic diameter and dynamic viscosity. Since fluid permeates through the membrane, the normal component of velocity at the membrane surface is non-zero. The wall Reynolds is defined as above, with the velocity scale replaced with the normal component of velocity, v_w.

$$Re_w = \frac{\rho v_w D}{\mu} \tag{1.2}$$

The Rossby and Ekman numbers characterize flows in rotating channels such as in CMS. The Rossby number represents the ratio of convective acceleration to Coriolis acceleration,

$$Ro = \frac{U}{\Omega D} \tag{1.3}$$

and the Ekman number represents the ratio of viscous forces to Coriolis forces

$$Ek = \frac{\nu}{\Omega D^2} \tag{1.4}$$

where Ω and ν are the rotational speed and the kinematic viscosity. The Reynolds, Rossby and Ekman number are related by

$$Re = \frac{Ro}{Ek} \tag{1.5}$$

Finally, the Schmidt number relates the viscous diffusion of momentum to the mass diffusion of dissolved species (in this case NaCl).

$$Sc = \frac{\nu}{\mathcal{D}} = \frac{\mu}{\rho \mathcal{D}} \tag{1.6}$$

1.4 Objectives of the Present Study

The primary objective of this work is to examine the flow and mass transfer in geometries of significance to both conventional membrane separation and to CMS. This will necessarily involve the application of membrane models to flows in both rotating and non-rotating channels. The insight gained from this study will both lead to a

better understanding of the transport phenomena involved in membrane separation and will provide guidance in the design of future membrane separation devices.

1.5 Outline of Thesis

Each chapter in this dissertation is written to stand alone as much as possible, and accordingly, an independent literature overview is presented in each chapter. Chapter 2 sets the stage for the dissertation by outlining the basic equations governing the transport phenomena in membrane systems. Also presented and discussed are two different membrane models which can be applied to membrane flows: the porous wall model (PWM) and the source term model (STM). In chapter 3, the PWM is applied to reverse osmosis desalination in geometries representative of the plate and frame CMS device. These results indicate that radially outward flows are favourable and that the STM is adequate for parametric studies of reverse osmosis flows. Chapter 4 presents a parametric study of fluid flow and mass transfer in rectangular channels with flow in the radially outward direction while chapter 5 investigates similar flows in channels of both triangular and circular cross sections. Chapter 6 presents a preliminary investigation of fluid flows in geometries representative of spacer filled channels. Both non-rotating and rotating flows are considered. Finally, in chapter 7, the impact of the results on CMS is considered. Conclusions are drawn, and recommendations made.

Chapter 2

Flow and Membrane Modeling

2.1 Flow Field Equations

The flow in a CMS device is governed by the conservation of mass, the Navier-Stokes equations, and, when a dissolved second phase is present, a scalar transport equation. As shown in appendix A, the Reynolds number of the flow in a reverse osmosis membrane channel is of the order of 10^2 and the flow may therefore be assumed to be laminar. The governing equations in a rotating frame of reference take the following conservation form:

$$\frac{\partial \rho}{\partial t} + \frac{\partial}{\partial x_j}(\rho u_j) = 0 \tag{2.1}$$

$$\begin{aligned}\frac{\partial}{\partial t}(\rho u_i) + \frac{\partial}{\partial x_j}(\rho u_j u_i) + \rho R_i = -\frac{\partial P}{\partial x_i} + \rho g_i \\ + \frac{\partial}{\partial x_j}\left\{\mu\left(\frac{\partial u_i}{\partial x_j} + \frac{\partial u_j}{\partial x_i}\right) - \frac{2}{3}\mu\frac{\partial u_l}{\partial x_l}\delta_{ij}\right\}\end{aligned} \tag{2.2}$$

$$\frac{\partial}{\partial t}(\rho\phi) + \frac{\partial}{\partial x_j}(\rho u_j \phi) = \frac{\partial}{\partial x_j}\left(\Gamma \frac{\partial \phi}{\partial x_j}\right) \tag{2.3}$$

where ϕ is the mass fraction of dissolved species, g_i is the gravity vector and R_i is an acceleration term which can be used to solve the equations in rotating frames of reference,

$$R_i = \epsilon_{ilm}\omega_l \epsilon_{mnk}\omega_n x_k + 2\epsilon_{ilm}\omega_l u_m \tag{2.4}$$

or, alternatively in vector notation, as

$$\overrightarrow{R} = \overrightarrow{\Omega} \times \left(\overrightarrow{\Omega} \times \overrightarrow{r}\right) + 2\ \overrightarrow{\Omega} \times \overrightarrow{U} \tag{2.5}$$

where the first term corresponds to centrifugal acceleration, the second term corresponds to Coriolis acceleration, ω_l ($\overrightarrow{\Omega}$) is the rotation vector, x_k ($\overrightarrow{R}$) is the position vector with respect to the rotational axis and ϵ_{ijk} is the alternating tensor, which takes a value of 1 for cyclic permutations of ijk, -1 for acyclic permutations and 0 otherwise. The centrifugal acceleration is often combined with the pressure through the definition of a reduced pressure,

$$p = P - \overrightarrow{\Omega} \times \left(\overrightarrow{\Omega} \times \overrightarrow{r}\right) \tag{2.6}$$

In the case of variable fluid properties, the fluid density and viscosity is determined based on the local concentration using empirical correlations developed in [3].

The governing equations can also be presented in non-dimensional form.

$$\frac{\partial v}{\partial \tau} + Ro\ v \cdot \nabla v + 2\Omega \times v = -\nabla p + Ek\ \nabla^2 v \tag{2.7}$$

where the fluid is assumed to be incompressible with constant properties and all variables have been non-dimensionalized. The governing equations in this form are the starting point for asymptotic solutions, since it is clear that the Rossby number and the Ekman number indicate the relative importance of the inertial and viscous terms respectively.

In component form, assuming steady fully developed conditions with flow in the x direction($\partial/\partial x = 0$), and an axis of rotation parallel to the y axis the governing equations become

$$\frac{\partial v}{\partial y} + \frac{\partial w}{\partial z} = 0 \tag{2.8}$$

$$Ro\left(v\frac{\partial u}{\partial y} + w\frac{\partial u}{\partial z}\right) + 2w = 1 + Ek\left(\frac{\partial^2 u}{\partial y^2} + \frac{\partial^2 u}{\partial z^2}\right) \tag{2.9}$$

$$Ro\left(v\frac{\partial v}{\partial y} + w\frac{\partial v}{\partial z}\right) = -\frac{\partial p}{\partial y} + Ek\left(\frac{\partial^2 v}{\partial y^2} + \frac{\partial^2 v}{\partial z^2}\right) \tag{2.10}$$

$$Ro\left(v\frac{\partial u}{\partial y} + w\frac{\partial u}{\partial z}\right) - 2u = -\frac{\partial p}{\partial z} + Ek\left(\frac{\partial^2 w}{\partial y^2} + \frac{\partial^2 w}{\partial z^2}\right) \tag{2.11}$$

In addition to the standard boundary conditions (inlet, outlet, no-slip), a selective membrane boundary condition must be specified for the CMS problem.

2.2 Membrane Boundary Condition

The equations governing a perma-selective membrane can be derived using irreversible thermodynamics [4]. Assuming that dynamic reversibility is valid for all cases con-

sidered, and that the membrane is a perfect rejector with respect to convection, then the flux of solution and solvent are respectively given by [3].

$$j_v = L_p(\Delta P - \Delta\Pi) \tag{2.12}$$

$$J_s = \frac{j_v(1-R)}{R}(c_f - c_p) \tag{2.13}$$

where L_p is the membrane permeability, R is the rejection of the membrane, ΔP and $\Delta\Pi$ are the hydrostatic and osmotic pressure differences across the membrane, c_f and c_p are the concentrations of the feed and permeate respectively. In the above equations, the solution flux is presented as a volume flux and the solute flux is presented as a mass flux. Further detail are given in appendix B.

Two different implementations of the above equations are outlined in the following section.

2.3 The Porous Wall Model and the Source Term Model

The Porous Wall Model (PWM), shown on the left hand side of figure 2.1 allows permeate to pass through the membrane, but selectively inhibits the transport of dissolved species. The solute which does not pass through the membrane remains in the feed channel, adjacent to the membrane surface, and the bulk concentration increases. This model correctly accounts for the mass permeating through the membrane, and hence the flow rate in the feed channel decreases along the flow direction and there is a component of velocity normal to the membrane. Since the permeation velocity

is a function of both the local pressure and concentration through equation 2.12 the hydrodynamics and the mass transfer are coupled.

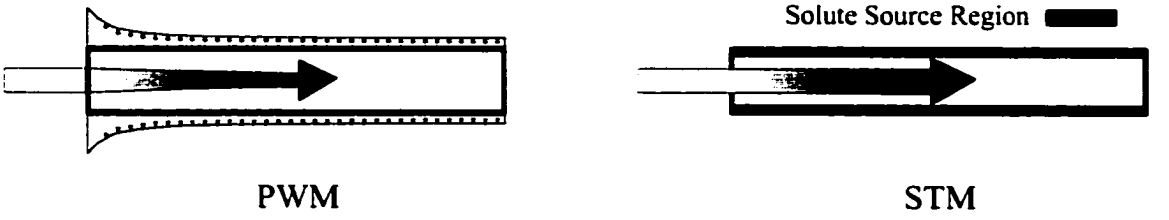

Figure 2.1: The porous wall model (PWM) and the source term model (STM)

Reverse osmosis affords two significant simplifications to the above model: i) The transmembrane pressure is much larger than the pressure drop along the channel, and ii) the permeate flux is vanishingly small such that the effect of permeation velocity and of decreasing flow rate are unimportant in the equations of motion. The permeation is however critically important to the mass transfer equation, as it is solely responsible for the increase in bulk concentration in the feed channel.

The source term model, shown on the right hand side of figure 2.1, takes advantage of this and decouples the hydrodynamics and the mass transfer. The hydrodynamics are solved using a conventional wall boundary condition and can accordingly be solved by any 'standard' CFD code without modification. The mass transfer equation is then solved with the addition of a source term adjacent to the membrane surface to account for the concentrating effect of the membrane. Equation 2.12 can be used with a constant transmembrane pressure to determine the local permeate mass flux, and the amount of solute which must be added locally in the source region is given by

$$\phi_{source} = \phi \rho A_i j_v - J_s \tag{2.14}$$

where A_i is the area of the section of membrane under consideration.

The main benefit of the source term model is that the hydrodynamics and the mass transfer are decoupled. This means that a hydrodynamics solution can be calculated for a given geometry and flow rate and this solution can be used to predict membrane performance over a range of feed concentrations and operating pressures. Since the hydrodynamics solution is orders of magnitude more costly than the mass transfer solution, this greatly reduces the cost of the predictions. Also, a commercial CFD package can be used without modification for the hydrodynamics solution and the mass transfer can be calculated either using the same package or separately.

2.4 Model Limitations

The PWM is applicable over the entire range of membrane processes since the permeation velocity is explicitly accounted for in the formulation. Not only does this ensure the correct mass flow at each section in a module, but it also ensures that the correct module pressure drop is calculated. This pressure drop is especially important when the process pressure is low since it results in a reduced driving force for the separation. An additional benefit of the PWM is that it is possible to vary fluid properties with concentration in order to account for the effect of density stratification.

The STM allows for a great increase in computational efficiency by decoupling the mass transfer solution from the hydrodynamics solution. The compromises for this model are:

- The permeation velocity at the wall is neglected
- The channel pressure drop is usually neglected in determining the trans-membrane pressure

- The solution properties must remain constant with respect to the hydrodynamics solution

For these reasons, the STM is limited to reverse-osmosis separations with transmembrane pressures significantly higher than the channel pressure drop. An additional limitation of the STM is that the membrane area must be sufficiently small to ensure the mass flow through the membrane remains small compared to the feed mass flow. Even when the permeation velocity is everywhere small, if the membrane is large enough it is possible that the concentrate flow rate could decrease enough that the mass transfer would be affected. The validity of the STM is examined in detail in chapter 3.

Both models are capable of modelling the effects of concentration polarization up to the point when gel layers begin to form adjacent to the membrane surface. Once these layers form, a new phase is present in the channel. At the very least, this imposes an additional resistance to flow through the membrane. While the models will indicate that the gel concentration has been surpassed, additional physics and chemistry would have to be included to correctly model the flow beyond this point.

Neither model as presented is suitable for modelling membrane fouling. Fouling is inherently a time dependent process where the permeate flux decreases with time due to pore narrowing, pore blocking or the build-up of a fouling layer adjacent to the membrane surface. Again, the additional physico-chemical processes would have to be accounted for.

2.5 Overview of Numerical Solutions

The PWM was implemented in the commercial code TASCflow 2.6 [5]. TASCflow is a finite volume based finite element code which solves the complete Navier-Stokes

equations on collocated body fitted multi-block meshes. The continuity equation and the momentum equations are solved in a fully coupled manner which makes this code particularly well suited to both rotating flows and to flows with transpiration. Steady state solutions are arrived at by a physical time marching procedure and this means that unsteady solutions are possible provided a small enough time step is used. The implementation of this model required additional source code beyond the standard user modifiable routines.

The STM was implemented in the commercial code cfx 4.2 [6]. Cfx is a finite volume code which also solves the complete Navier-Stokes equations on collocated body fitted multi-block meshes. The hydrodynamics and the continuity equation are not solved in a coupled fashion and while the code has options for unsteady flow, steady flow solutions are arrived at through the use of relaxation techniques. The STM was implemented using only the standard user modifiable Fortran routines provided with the Cfx code.

Chapter 3

The Effect of Membrane Orientation

3.1 Introduction

Two of the major problems associated with membrane separation processes are fouling and concentration polarization. Fouling occurs when the membrane is physically obstructed, either by a buildup of particulates on the surface or by membrane compaction, whereas concentration polarization refers to the formation of a high concentration boundary layer adjacent to the membrane which results in a local increase in the osmotic pressure and a reduction of the permeate flux. To capitalize further on the rotational effects present in CRO, a combined experimental/numerical investigation was undertaken to develop membrane configurations which reduce fouling and concentration polarization due to the secondary flows induced by centrifugal and Coriolis accelerations. This work complements the current experimental work which is aimed at applying the CMS process in reverse osmosis [7] and in ultrafiltration of

protein solutions and colloidal mixtures [8] where the potential benefits are greater still.

In this chapter, the porous wall model is applied to geometries consistent with the CMS plate and frame configuration. The purpose is to develop an understanding of the effect of membrane orientation in a rotating environment. Various membrane orientations with respect to the axis of rotation are investigated. This orientation, which affects both Coriolis and centrifugal accelerations, is defined by assigning a reference configuration, and three successive rotations, (pitch, roll, yaw) about the z,x and y axes respectively. A coordinate system is attached to the membrane, with feed flow in the x direction and the membrane normal in the y direction Figure 3.1 depicts the reference, (0.0.0), position and three sample orientations as viewed from the viewpoint of the membrane, while figure 3.2 depicts sample orientation with respect to a viewpoint attached to the axis of rotation.

The specific objectives of this work are to apply the PWM to investigate the effect of system rotation on the reverse osmosis membrane separation of aqueous NaCl solutions. Of specific interest is an in-depth understanding of the parameters influencing the permeate flux, and the membrane surface concentrations in the experimentally difficult environment of a CMS device. The model will also be used to determine optimal membrane configurations and orientations.

3.1.1 Fluid Mechanical Background

Flows in partly porous stationary and rotating ducts are also found in heat exchangers, solar-energy collectors, porous walled flow reactors, pulp and paper processing, and fuel cell stacks. Laminar flow in a 2-D channel with porous walls was considered by Berman [9] who obtained a first-order perturbation solution often used for

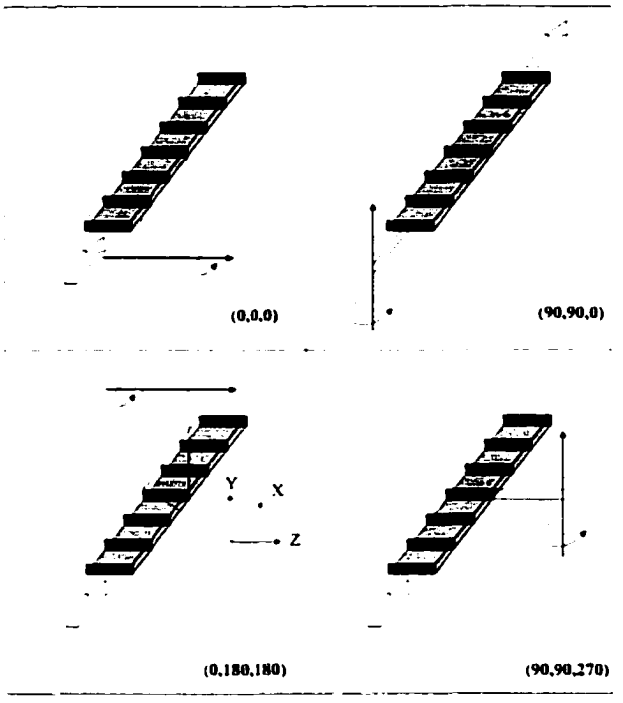

Figure 3.1: Membrane orientation with respect to the axis of rotation from the viewpoint of the membrane. Angles represent successive rotations in (Pitch, Roll, Yaw). The dark shaded sections represent reference planes on which visualizations will be presented. Note: in the physical device the rotation axis is held constant and the membrane orientation is altered.

validation. An experimental study of laminar flow and heat transfer in square ducts with a single porous wall [10] has shown that significant changes occur with respect to pressure drop, Nusselt number and entrance lengths depending on the wall velocity. Numerical modeling of membrane flows to 1994 was reviewed by Bouchard *et. al.* [11], wherein all models used simple analytic solutions, such as that of Berman, for the fluid flow and numerically solved a convection diffusion equation to account for solute transport. The most comprehensive numerical model related to membrane flows is that of Pellerin et al. [12], in which the steady 2-D Navier-Stokes solutions were solved in conjunction with a transport equation for the dissolved phase and Darcy's law to determine the transpiration velocity. Turbulence was modeled

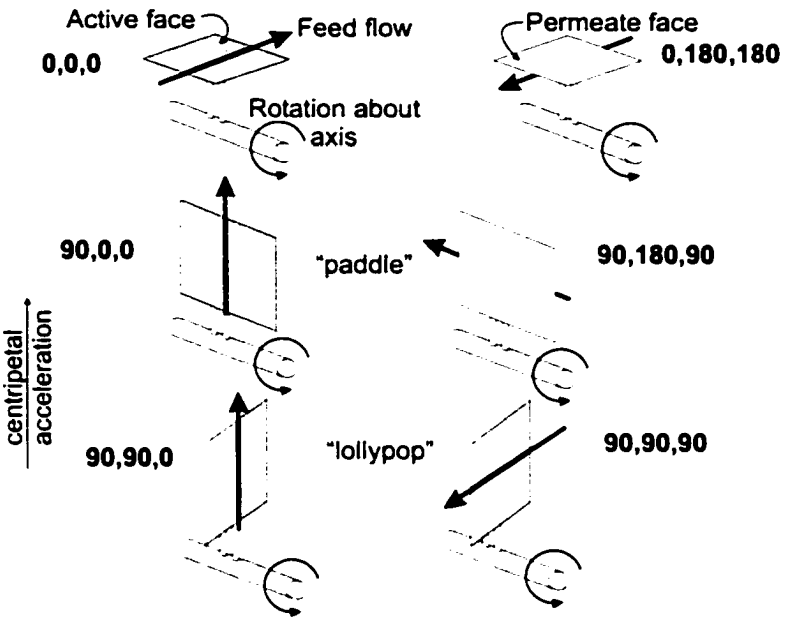

Figure 3.2: Membrane orientation with respect to the axis of rotation from the viewpoint of the rotational axis. Angles represent successive rotations in (Pitch, Roll, Yaw).

using the density-weighted ensemble-averaged equations (Favre averaging) together with the $k - \epsilon$ model. The model did not properly account for low Reynolds number turbulence, but nonetheless highlighted the significant differences arising from turbulence.

The potential benefits of fluid dynamical instabilities in alleviating concentration polarization and fouling have been recognized for some time. Belfort [13] discussed for instance the effect of unsteadiness due to oscillating pressure gradients, "furrowed" flow channels and centrifugal acceleration. In a series of subsequent papers, Belfort and co-workers investigated the effectiveness of Dean vortices in flux enhancement and fouling reduction (see, e.g. Ref. [14]). The reduction in concentration polarization due to centrifugal acceleration was also investigated by Andeen [15] using commercial hollow-fiber membranes. The same system was subsequently used to demonstrate

reduced particulate fouling as well [16]. Pulsatile flow is another method that has been proposed for controlling and minimizing concentration polarization and fouling [17, 18]. In the present study the focus is the combined effect of centrifugal and Coriolis acceleration. To our knowledge this thesis and the companion paper [19] are the first to report on the latter in the context of membrane separation.

A general review of the fluid mechanics of centrifugal separation of mixtures in rotating vessels is given in [20], with an emphasis on the importance of Coriolis forces under various conditions and a discussion of various approaches for modeling monodisperse suspensions and their limitations. Three-dimensional numerical investigations of flow and heat transfer in rotating square ducts, together with reviews of earlier work, are presented in [21] for laminar flow and in [22] for turbulent flow. Investigations of flow in rotating ducts with a porous wall are scarcer, but a recent 3-D numerical study of the mixed convection problem is presented in [23]. A vorticity-velocity formulation was used and the equations were parabolized to allow a marching integration in the axial direction.

In this chapter we present three-dimensional computations, using the full Navier-Stokes equations, of the low Reynolds number laminar flow of a salt-water solution in a long channel with a reverse-osmosis filtration membrane on one side. Both stationary and rotating cases are considered and the relative effects of centrifugal and Coriolis accelerations are investigated.

3.2 Implementation

The present version of the PWM has been implemented into the commercial CFD package TASCflow3d [5]. TASCflow3d is a Navier-Stokes code which solves the Cartesian form of the equations presented in chapter 2 over collocated body fitted grids

using a finite volume based finite element method. Steady solutions are arrived at by stepping through time using first order backwards differencing. While the code provides several options for the discretization of the convective terms, all of the simulations presented here employed a flux limited higher order upwind scheme for these terms. Centrifugal buoyancy is implicitly included, as the dependence of density and viscosity on the local value of the concentration in accounted for.

Figure 3.3 depicts a flux element on the membrane surface which is made up of partial faces from the four nodes bounding the flux element. Properties and variables are constant over a flux element and are determined as numerical averages of the four surrounding nodal values. The solute flux is specified by setting the value of φ_{out} based on the experimentally determined rejection. This value of φ_{out} is then used in calculating all fluxes through the membrane surface. All the other terms are based on the flux element values so that the viscous terms and the fluxes through the other faces are still based on the higher concentration present on the feed side of the membrane.

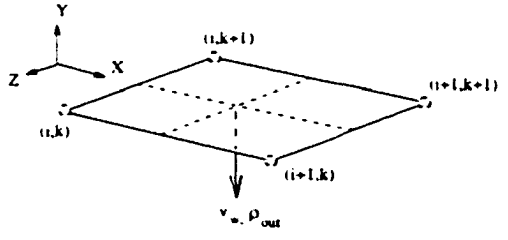

Figure 3.3: Flux element on membrane surface.

The velocity components parallel to the membrane surface are set to zero in accordance with the no slip condition, and the normal component of velocity is set according to Equation (2.12).

3.3 Model Validation: Non-rotating flow

3.3.1 Berman Solution

In a preceding study [3], the present model, designated as the Porous Wall Model (PWM), was initially validated against the Berman solution [9] consisting of symmetrical flow between two parallel membrane plates as in figure 3.4. The channel

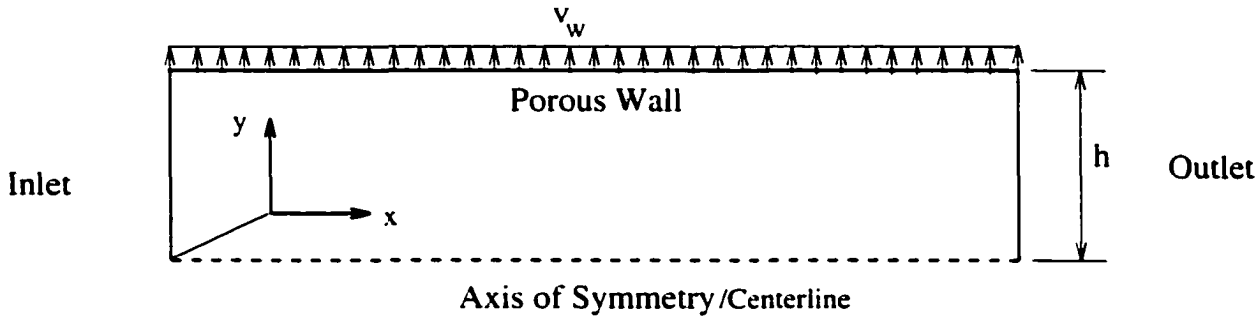

Figure 3.4: Geometry used for initial validation against Berman solution.

dimensions used for these simulations were those of the actual CMS channel, and the feed solution was taken to be 22.000 ppm salt at 26^oC (density $\rho = 1012.12 kg/m^3$ and kinematic viscosity $\nu = 9.0344 \times 10^{-4} kgm/s$). Figures 3.5 and 3.6 present comparisons of the calculated velocity components at various distances along the channel for a channel Reynolds number of $Re_h = 2hU/\nu = 250$, and a wall Reynolds number $Re_h = hv_w/\nu = 0.1$. Two different grid sizes were used, and excellent agreement was obtained on both grids.

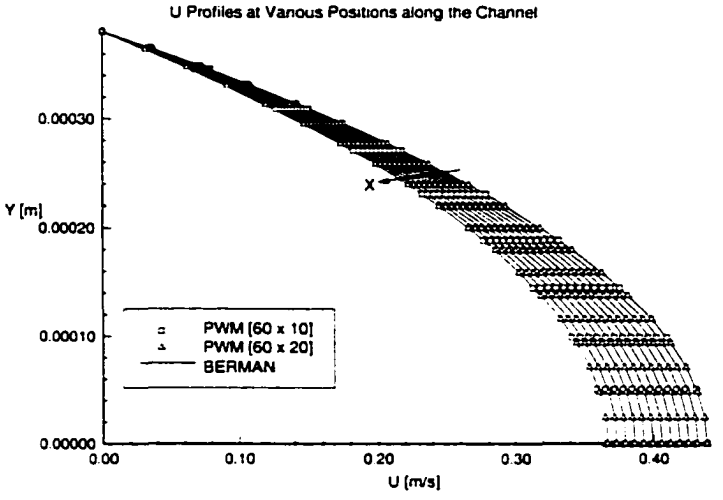

Figure 3.5: Profiles of U normal to the porous wall at various distances along the channel. $Re_h = 250, Re_w = 0.1$

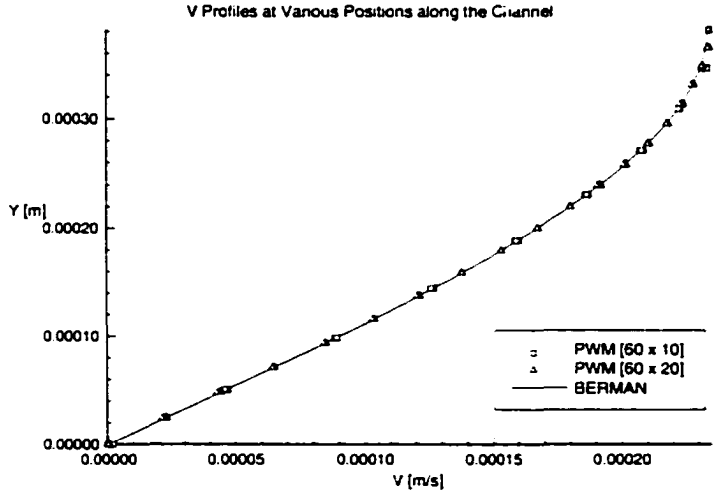

Figure 3.6: Profiles of V normal to the porous wall at various distances along the channel. $Re_h = 250, Re_w = 0.1$

3.3.2 Conventional membrane separation

Next, the model was further validated considering conventional (non-rotating) reverse osmosis desalination. Experimental data was generated in a parallel study using a static test bench, designed to house the custom CMS membrane stacks described above, and employed nine parallel flow channels, four of which had an active membrane on the one side of the channel. A full description of the experimental program is given in [7]. The feed flow rate was 2 L/min, which results in an average channel Reynolds number of $Re_h = 72.5$, where h is the channel half height. Figure 3.7 compares the predicted permeate fluxes with the measurements. The numerical results were obtained using the parameters outlined in the validation column of table 3.2 for three inlet concentrations and, with one exception, assumed the flow was two dimensional. Additional three dimensional predictions which account for side wall effects were obtained for feed concentrations of 35,000 parts per million NaCl using feed rates of 4L/min ($Re_h = 145$) and a process pressure of 500 psi (3.4 MPa).

Two trends are immediately apparent in examining Figure 3.7: the model correctly predicts the trends shown in the concentration polarization experiments, but over-predicts the experimentally determined permeate fluxes. Also, as expected, increasing the feed flow rate increases the permeate flux and accounting for side walls (500 psi case) decreases the permeate flux. The absolute error between the simulations and the experiments is of the order of $4 \times 10^{-4} kg/(m^2 s)$, giving a relative error of 6% at the highest flux. The relative difference between the slopes ranges from less than 1% to 4.8%. These differences are not unreasonable considering the difficulty in controlling experimental parameters such as membrane permeability, feed concentration and applied pressure.

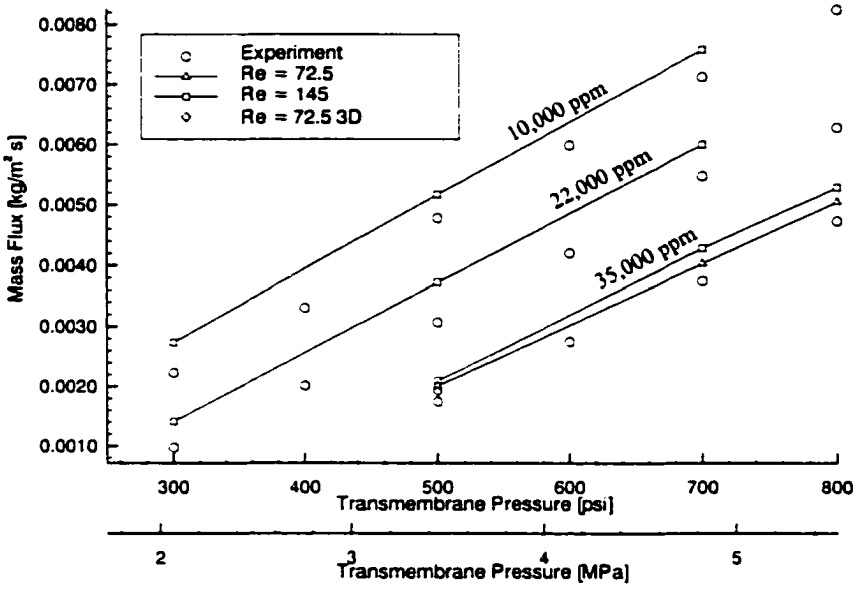

Figure 3.7: Comparison of experimental permeate mass flux data and CFD calculations for conventional membrane separation. Concentrations are in parts per million NaCl

3.4 The Effect of Rotation and Orientation

Rotation can be expected to induce asymmetry and spanwise motion and hence a breakdown of the two-dimensionality. In order to investigate the relative effects of channel orientation, three-dimensional simulations were carried out in a channel of half height h = 0.381 mm, of length 220h, and aspect ratio 8. A constant inlet velocity, corresponding to a Reynolds number of 145, was specified with an NaCl concentration of 22,000 parts per million ($\phi = 0.022$). The membrane boundary condition is applied on the y=-h face between x/h=7.4 and x/h=213 with the remainder of the y=-h surface set as an impermeable wall. A fully developed outlet condition was used on the x=220h face, and while this is not strictly correct with wall permeation, it is anticipated that this will affect the simulation only locally near the exit since membrane fluxes are small compared to the bulk flow. The remaining boundary faces

(y=h, z=+/-8h) are specified as impermeable walls. The axis of rotation is located 1650h (0.6286 m) away from the center of the membrane and the rate of rotation is 50 rad/s. A uniform grid of [120,20,153] was used for all simulations.

The various simulations performed are summarized on table 3.1, which also includes the sense of the Coriolis and centrifugal accelerations. The additional simulation parameters are listed in table 3.2 under the CMS column.

orientation	properties	Coriolis	centrifugal
Static	Variable	0	0
(0,0,0)	Variable	+y	+y
(0,0,90)	Variable	0	+y
(0,180,180)	Variable	+y	-y
(90,90,0)	Variable	-z	+x
(90,90,270)	Variable	-z	-z
(90,90,0)	Constant	-z	0
(90,90,270)	Constant	-z	0

Table 3.1: Simulations performed to investigate the effect of system rotation for various membrane orientations. The direction in which the additional acceleration terms act are given for each case. Centrifugal accelerations are listed as 0 when no density gradients exist.

Properties	Validation	CMS
Temperature $[^oC]$	26	25
Permeability, $L_p \times 10^{12}$ $[m/(sPa)]$	1.83	2.24
Rejection. R [%]	98.5	98.0

Table 3.2: Parameters used for the numerical simulations.

3.4.1 Secondary Flow Patterns and their Effect on Salt Concentration

Figure 3.8 depicts the distribution of salt concentration (in terms of mass fraction) on the membrane surface. All simulations involving additional acceleration terms show a greatly reduced surface concentration and accordingly, a significant increase in permeate production over the conventional process. Each case, however, features a distinct concentration pattern, which can be understood by investigating the flow patterns inside the feed channels. Figure 3.9 shows the secondary, or in-plane, velocity vectors for various sections along the channel for the (0,0,0) case. Initially, there are only wall bound vortices which grow towards the center of the channel as the distance from the inlet is increased. These vortices account for the reduced concentration adjacent to the sidewalls for this case. As these vortices meet, additional vortex pairs are formed, first at the center of the channel, and finally filling the entire channel. Again, the effect of the formation of these additional vortex pairs is clearly evident on the surface concentration distribution.

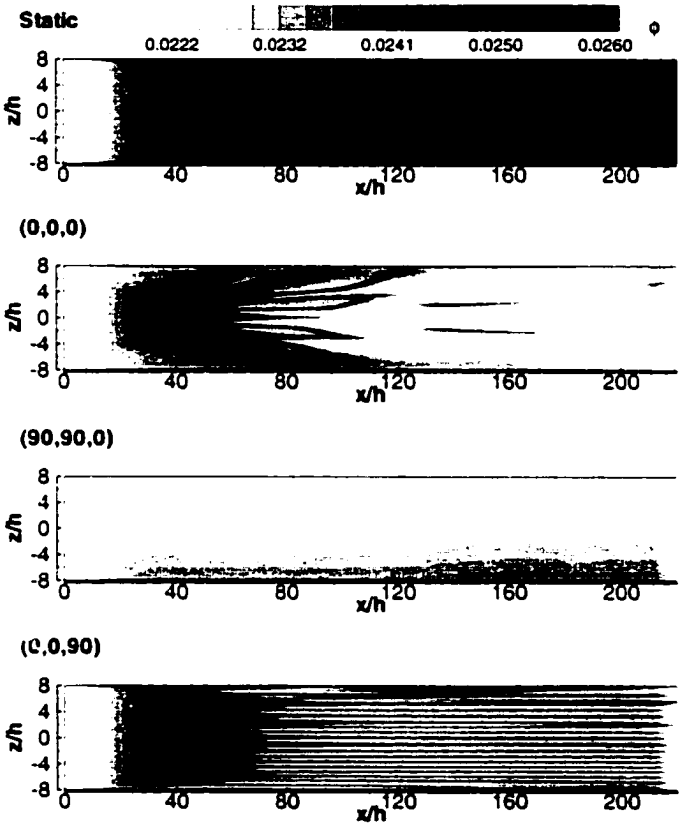

Figure 3.8: Surface salt concentration along the channel for various orientations. Dark shading indicates high concentrations, as per contour legend at top.

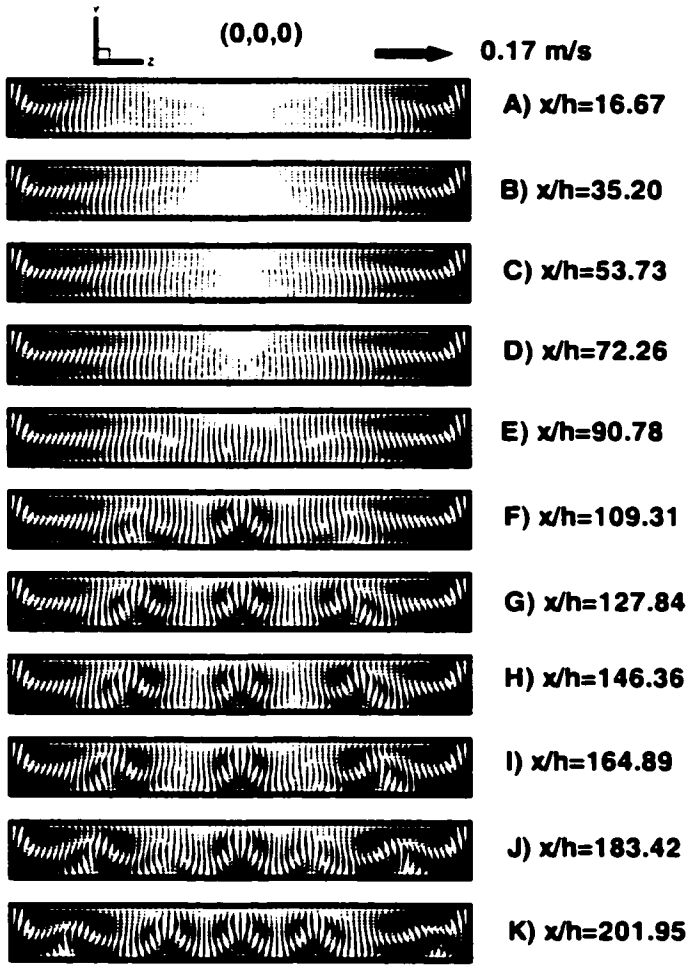

Figure 3.9: Secondary velocity vectors for orientation (0.0.0).

Figures 3.10 and 3.11 show the corresponding in-plane velocity vectors and salt concentration contours at $x/h = 200$ for the four cases presented above. In the static case, there is no secondary motion and a large buildup of concentration occurs. Orientation (0,0,0) features a number of vortices, or roll cells, which form adjacent to the membrane and mix the fluid locally. Orientation (90,90,0) features two elongated cells which cover the entire span causing a complete breakdown in the symmetry of the velocity profile and concentration distribution. Finally, orientation (0,0,90), which has no Coriolis acceleration on the bulk flow, features very weak convection cells ($<$ 10% of the strength of the previous cases) which are considerably smaller and more numerous than the Coriolis induced structures evident in the (0,0,0) case. These cells form first next to the channel sidewalls, and spread inwards to fill the channel.

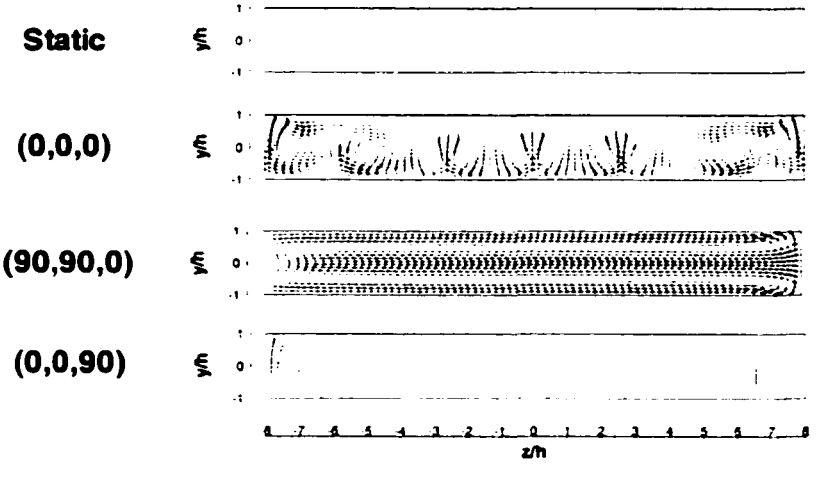

Figure 3.10: In plane velocity vectors at x/h=200 for various simulations. Velocity vectors are magnified 10 times in the (0,0,90) case.

The relative strength of these secondary motions is demonstrated in figure 3.12 which shows relief surfaces of the streamwise velocity at the same position in the channel. The static case is typical of unperturbed laminar flow with a maximum

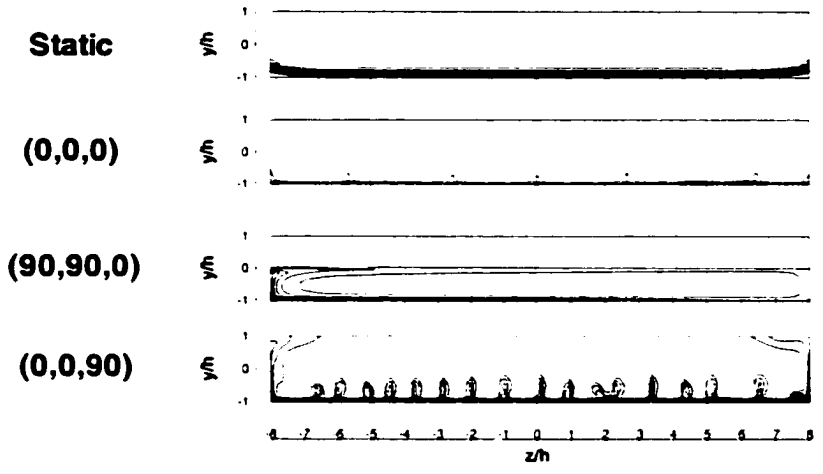

Figure 3.11: In plane salt concentration contours at x/h=200 for various simulations. Fifteen evenly spaced contour lines are plotted between $\phi = 0.0222$ and $\phi = 0.026$.

velocity at the center of the channel, whereas the effects of the secondary motions are readily apparent in the cases (0,0,0) and (90,90,0). In orientation (0,0,0), the entire profile is shifted towards the membrane surface ($y/h = -1$) and the influence of the roll cells is clearly evident. In orientation (90,90,0) the secondary structures carry fluid towards the lagging sidewall (z=8h) and significantly broaden the profile perpendicular to the membrane. This broadening of the profile, which is evident to a lesser degree in the (0,0,0) orientation, will serve to increase the shear stress on the membrane surface. There is no noticeable effect of the secondary motions in the case (0,0,90), which has no Coriolis acceleration on the streamwise velocity component, as might have been anticipated from the weakness of the secondary motions.

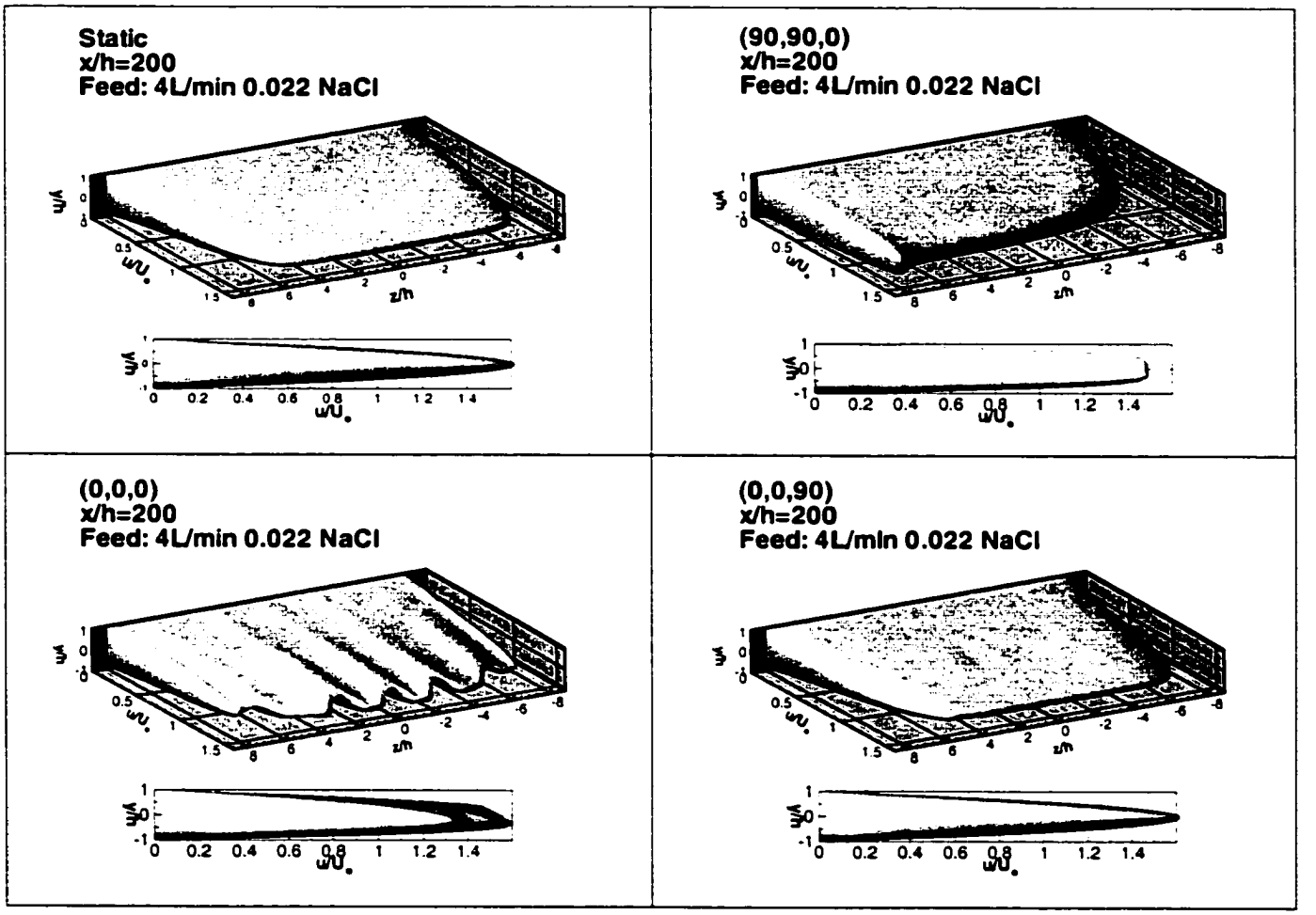

Figure 3.12: Relief plot of streamwise velocity component for conventional (static) membrane separation.

3.4.2 Spanwise Averaged Evolution of Membrane Surface Salt Concentration

In order to assess the overall effect of system rotation on surface concentration, the values presented in Figure 3.8 were averaged in the spanwise direction (z) at each position (x) along the membrane surface. These spanwise averaged salt concentrations are presented in Figure 3.13 and provide a good overview of the effect of rotation. Both orientations using a pitch and a roll of 90° (Coriolis in the spanwise direction) feature a flat concentration distribution which is only marginally higher ($\approx$ 4%) than the feed concentration, offering the potential for both significantly enhanced permeate production and for the use of longer flow channels. The remaining rotating cases are similar in the sense that the surface concentration builds until it reaches a maximum and then rapidly decreases to a seemingly constant level. Simulations (0,0,0) and (0,180,180), which both have Coriolis accelerations directed away from the membrane surface, have the same initial concentration growth rate; but in the former case, where the centrifugal acceleration is aligned with the Coriolis acceleration, the drop off occurs by x/h$\approx$ 60. In the (0,180,180) case, the Coriolis and centrifugal accelerations are opposed, and the concentration drop off does not occur until x/h $\approx$ 125. The static case and (0,0,90), neither of which have Coriolis acceleration on the bulk flow, have the same initial concentration growth rate, with the latter beginning to decrease by x/h $\approx$ 60, but remaining higher than the case with Coriolis accelerations on the bulk flow.

Several of these results are well correlated with the parallel experimental program [7]. In particular, a decrease in performance of the (0,0,90) and the (0,180,180) orientations with respect to the (0,0,0) orientation is found. The overall agreement of the computational model with observations is very satisfactory, particularly when noting that experimental variations due to changes in permeability from membrane

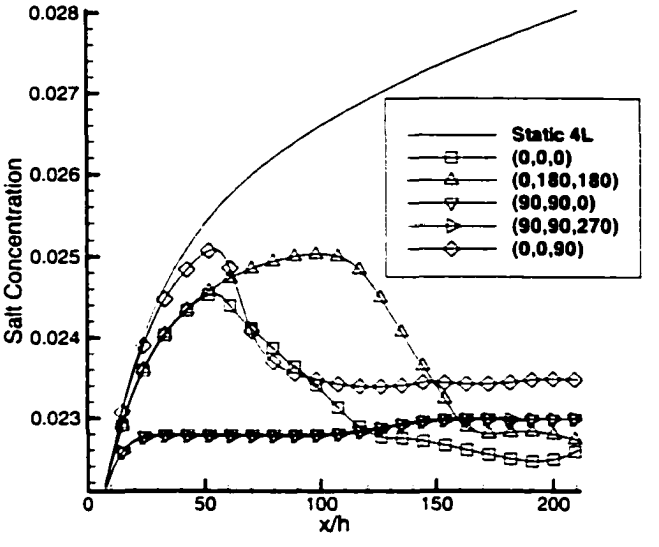

Figure 3.13: Evolution along the channel of the spanwise averaged salt concentrations.

to membrane are not adjusted for in the numerical model.

3.5 Further Analysis of System Rotation

3.5.1 The Effect of Density Variation

Figure 3.14 compares the (90,90,0) and (90,90,270) orientation with and without density variations. In the latter case the centrifugal instabilities are removed by switching off the terms corresponding to variation of density with concentration in the numerical solution. The figure shows that the relative increase in surface concentration when density variation is used to account for centrifugal accelerations is less than 0.5% for both cases. At this level of refinement, a small distinction can be made between the (90,90,0) case and the (90,90,270) case: in the latter the Coriolis and centrifugal

accelerations are aligned and the performance is marginally improved. Another effect of density is revealed by referring back to figure 3.13. The only difference between the (0,0,0) case, and the (0,180,180) case is that the sense of the centrifugal acceleration term has changed with respect to the density gradient created at the membrane surface (the sense of the Coriolis acceleration is the same in both cases). In the case of (0,0,180) the feed solution is stably stratified with respect to centrifugal acceleration, and the development of the roll cells in the interior of the channel is delayed by approximately 60 channel half heights. This shows that while centrifugal instabilities on their own produce weak secondary motions there are clear interactions between the two instabilities. The overall significance of this interaction, however, would diminish greatly with increasing channel length.

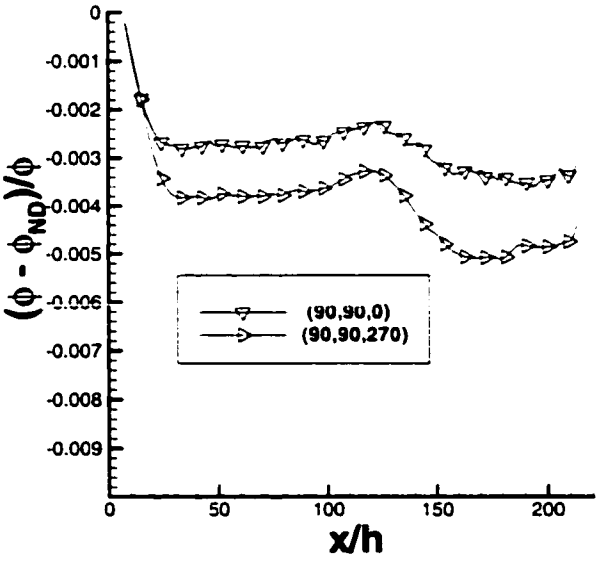

Figure 3.14: Spanwise averaged increase in surface concentration with the addition of centrifugal forces through variable density.

3.5.2 Shear on the Membrane Surface

All membranes considered in this work have a surface normal that is parallel to the y coordinate direction. For this configuration, we can derive two components of the shear on the membrane surface,

$$\tau_{xy} = \mu \left(\frac{\partial u}{\partial y} + \frac{\partial v}{\partial x} \right) \tag{3.1}$$

$$\tau_{zy} = \mu \left(\frac{\partial w}{\partial y} + \frac{\partial v}{\partial z} \right) \tag{3.2}$$

and the magnitude of the shear stress,

$$\tau = \sqrt{\tau_{xy}^2 + \tau_{zy}^2} \tag{3.3}$$

Since, in the present work, the viscosity varies as a function of the local concentration, the above shear stresses are calculated using the local viscosity, and a shear rate is defined using the feed viscosity. Figure 3.15 presents the spanwise distribution of membrane surface concentration and shear rate, $S = \frac{\tau}{\mu_{feed}}$, at x/h=200. Each of the four cases presented are markedly different, with, in general, a maximum in shear rate corresponding to a minimum in concentration. The static case features relatively flat profiles and a high concentration, while all other cases have gradients in the spanwise direction. The (0,0,0) case features a large amplitude, low wavelength, variation, while the (0.0.90) is characterized by a small amplitude short wavelength variation. Clearly, in comparing the static and (0,0,90) cases, the magnitude of the shear rate is not the determining factor in the reduction of membrane surface concentration.

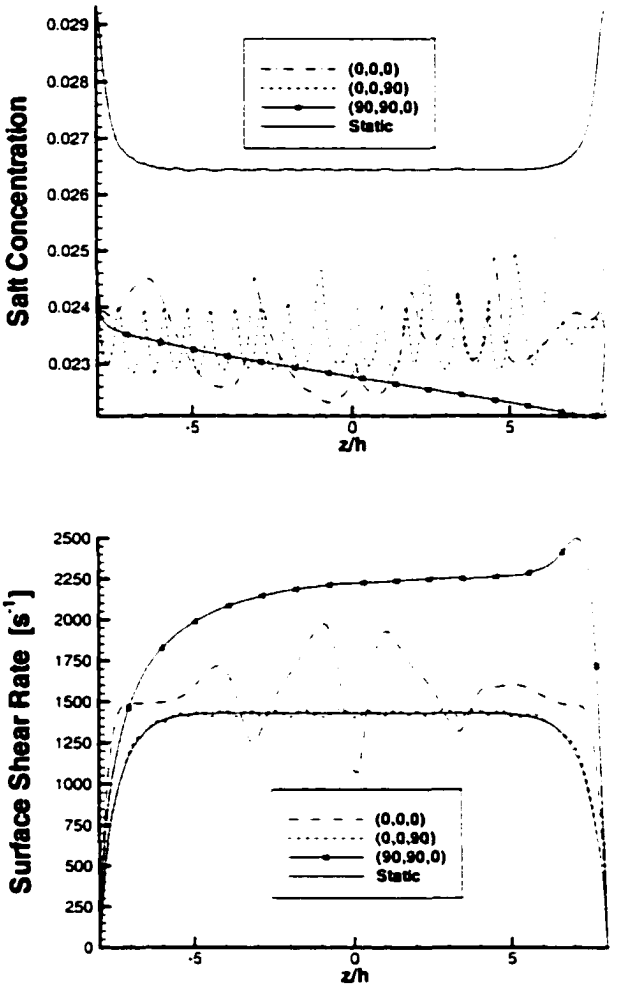

Figure 3.15: Distribution of membrane surface concentration and shear rate across the channel at x/h=200

3.6 Comparison with Source Term Model

In order to assess the validity of the simplified source term model approach, a STM simulation was performed and compared to the corresponding PWM simulation of (90,90,0) which includes the effect of variable density and viscosity. The STM model was implemented in cfx 4.2 by modifying the standard user Fortran routines provided with the code. This simulation used a constant solution density and viscosity, corresponding to a 22,000 ppm NaCl solution and neglected the transpiration velocity at the membrane surface. Figure 3.16 compares velocity profiles near the channel centrelines while figure 3.17 presents comparisons of relief plots of streamwise velocity in the fully developed region. The agreement between the two models is very good, with minor differences evident along the short channel centreline.

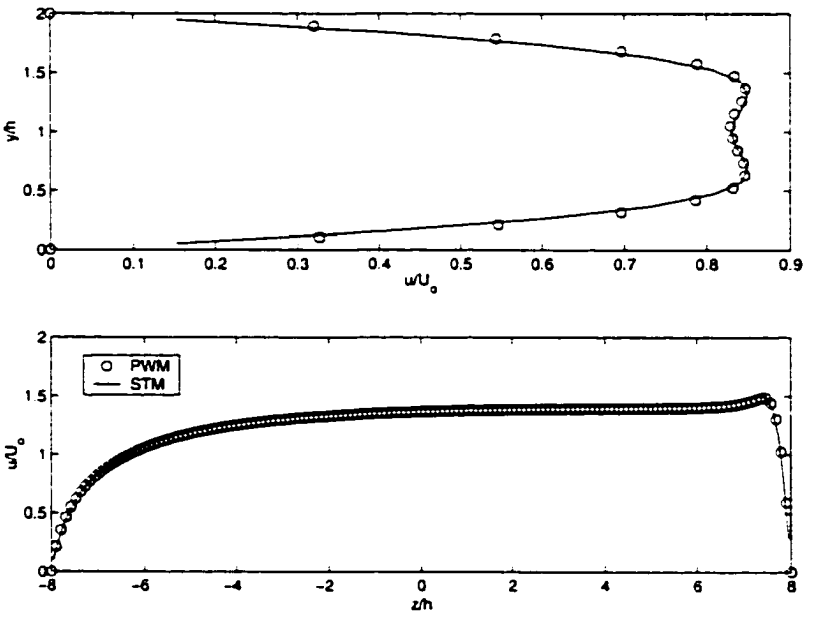

Figure 3.16: Comparison of PWM and STM: streamwise velocity near the channel centrelines.

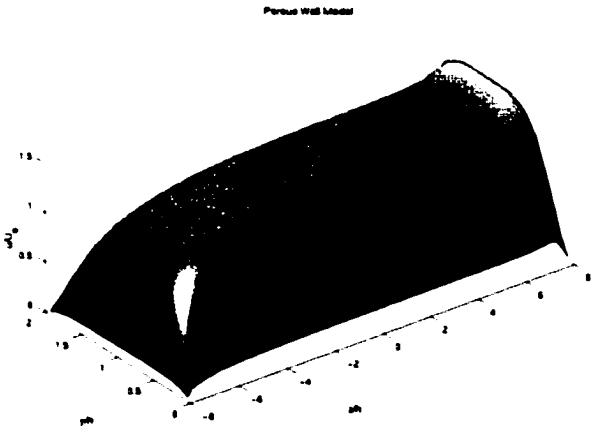

PWM

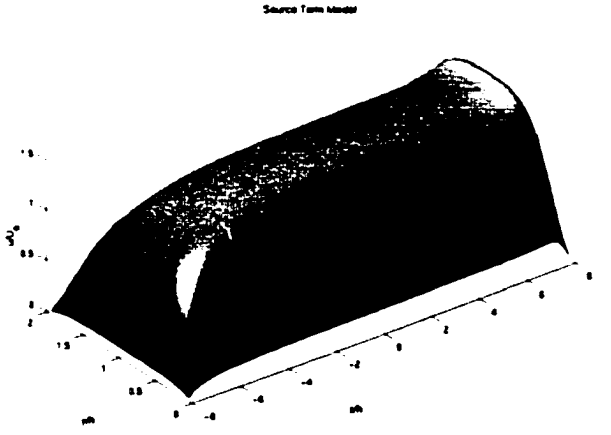

STM

Figure 3.17: Comparison of PWM and STM: relief plots of streamwise velocity in the fully developed region.

The PWM predicted a permeate flux through the membrane of 3.070×10^{-6} kg/s, and the STM is in excellent agreement differing by only 0.5%. Figure 3.18 depicts the spanwise averaged surface concentrations predicted using the two models and uses the same scale as in figure 3.13. The STM predicts a slightly lower concentration, corresponding to the higher permeate flux prediction, with the largest differences occurring where the concentration is increasing. This is perhaps not too surprising considering that the STM is based on volumetric averages adjacent to the membrane while the PWM relies on membrane surface concentrations. Overall though, the differences between the two models are significantly smaller than the differences between the different cases presented in figure 3.13 and the mass flux predictions are in very good agreement.

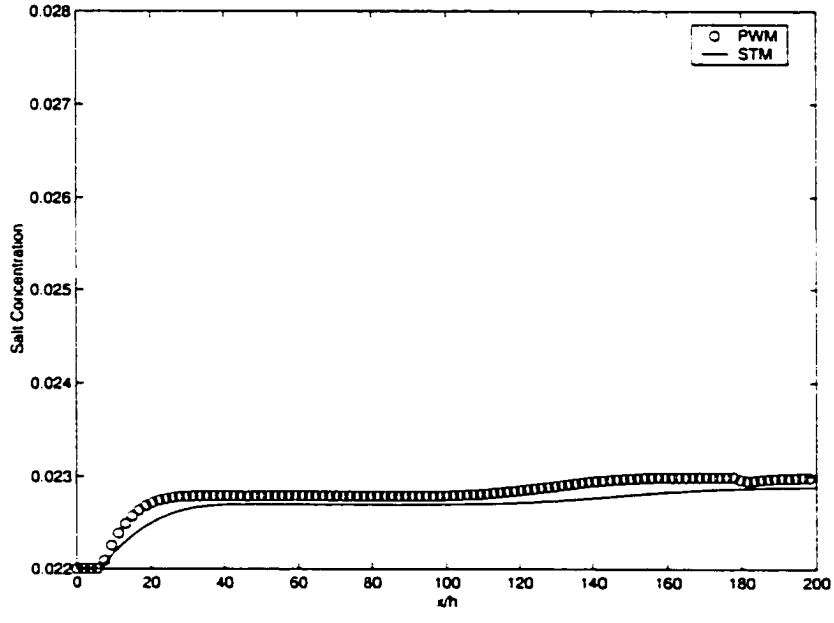

Figure 3.18: Comparison of PWM and STM: spanwise averaged surface salt concentrations.

3.7 Closure

A porous wall model applicable to membrane separation processes has been developed and implemented into the TASCFlow CFD code. The model is able to correctly model the flux vs. pressure behavior in conventional membrane separation. This model has also been used to demonstrate the potential for significantly improved permeate production rates in the case of CMS and to identify three distinct flow regimes depending on channel orientation. This improvement is made possible largely by the Coriolis acceleration, with centrifugal accelerations providing a further modest gain. When considering flows susceptible to concentration polarization, there is no direct correlation between high shear rate and reduced surface concentration - small secondary motions are adequate to significantly reduce flux decline associated with concentration polarization.

The lowest surface concentrations, and hence the highest permeate fluxes are found in channels with radially outward flow, when the Coriolis acceleration is normal to the streamwise velocity. These geometries exhibit lower concentrations along the entire length of the membrane in contrast to the alternative orientations which take longer to develop secondary motions.

All CMS simulations presented above were carried out at a rotational speed of 50 rad/s while the actual CMS experimental apparatus runs at 158 rad/s to develop this pressure. Physically, the simulations correspond to a hybrid combination of a centrifuge and a high pressure pump to develop the process pressure and yet significant benefits are evident even at this rotation rate. Accordingly, it is desirable to perform a systematic parametric study of rotational flows with a view to determining performance over a range of operating speeds. The STM, which is computationally more efficient than the PWM will be used in the next chapter to undertake such a

study.

Chapter 4

Rotating Channel Flows

4.1 Introduction

Generalized rotating channel flows can be found in many engineering applications, from blade and cooling passages in turbomachines to specialized heat exchangers to novel membrane separation processes. The specific interest here stems from work in developing new technology for membrane separation processes which relies on the beneficial effect of Coriolis acceleration to alleviate concentration polarization and fouling [19]. In single phase flow, with small temperature and concentration gradients, it is solely the Coriolis acceleration, present any time there are flows that are not aligned with the rotational axis, which brings about these features. These flows present many interesting features including complex secondary flow patterns which, if properly understood and harnessed, can be of great benefit to design. While many researchers have examined aspects of rotating channel flows the picture is far from complete.

When the Navier-Stokes equations for an incompressible fluid are written in a

rotating frame of reference, as in equation 2.7, the Rossby number multiplies the inertial term while the Ekman number multiplies the viscous term. This makes it plausible to consider asymptotic solutions to these equation as in the early work in rotating flows [24, 25, 26, 27]. In this approach, it is common to assume that the flow is fully developed (translationally invariant), and that a geostrophic core exists in which viscous effects are unimportant and in which the Coriolis term is balanced by the pressure gradient. This implies then that the flow must adjust to the no slip walls through boundary layers in which the viscous terms dominate, and the inertia forces are negligible. These layers are given different names, and have different dimensions depending on their location with respect to the axis of rotation. The layers on the leading and lagging sidewalls are called Stewartson layers, while the remaining two are called Ekman layers. In the case of normal rotation, shown below in figure 4.1 the axis of rotation is aligned with the y-axis, and flow is in the x-direction. In this case, the translationally invariant non-dimensional: Navier-Stokes equations in a rotating frame of reference become

$$\frac{\partial v}{\partial y} + \frac{\partial w}{\partial z} = 0 \tag{4.1}$$

$$Ro\left(v\frac{\partial u}{\partial y} + w\frac{\partial u}{\partial z}\right) + 2w = 1 + Ek\left(\frac{\partial^2 u}{\partial y^2} + \frac{\partial^2 u}{\partial z^2}\right) \tag{4.2}$$

$$Ro\left(v\frac{\partial v}{\partial y} + w\frac{\partial v}{\partial z}\right) = -\frac{\partial p}{\partial y} + Ek\left(\frac{\partial^2 v}{\partial y^2} + \frac{\partial^2 v}{\partial z^2}\right) \tag{4.3}$$

$$Ro\left(v\frac{\partial u}{\partial y} + w\frac{\partial u}{\partial z}\right) - 2u = -\frac{\partial p}{\partial z} + Ek\left(\frac{\partial^2 w}{\partial y^2} + \frac{\partial^2 w}{\partial z^2}\right) \tag{4.4}$$

In the limit of rapid rotation, Ekman layers of order $Ek^{1/2}$ form on the y=0 and

y=D surfaces while Stewartson layers form on the z=± 1.5D sidewalls. The Stewartson layer on the leading sidewall (z=-1.5D) is of order $Ek^{1/4}$ while the Stewartson layer on the lagging sidewall is of order $Ek^{1/4}$. Kheshgi and Scriven [28], who performed finite element solutions of the translationally invariant Navier-Stokes equations, presented the following asymptotic solution for the Ekman layers in the case of rapid rotation

$$u = \frac{1}{2} Ek^{-1/2} [1 - \exp(-y/Ek^{1/2}) \cos(y/Ek^{1/2})] \tag{4.5}$$

$$w = \frac{1}{2} Ek^{-1/2} \exp(-y/Ek^{1/2}) \sin(y/Ek^{1/2})] \tag{4.6}$$

These equations will be used in section 4.3 in support of the unusually fine grid resolution requirements in such flows.

Hart [29] performed experimental work and linear instability analysis on pressure driven flow rotating about an axis perpendicular to the plane of the bulk flow (spanwise rotation) and identified four distinct flow regimes as rotation rates increased from zero; stable parabolic, parabolic modified by secondary motion, axisymmetric rolls and stable Taylor-Proudman. Lezius and Johnston [30] confirmed and extended Hart's work, while Speziale and co-workers [31, 32, 33] performed numerical simulations considering fully developed flow in rectangular channels of finite aspect ratio, including the effect of heat transfer. Kheshgi and Scriven [28] and Nandakumar [34] examined fully developed pressure driven flow in rotating square channels, and found a rich set of flow structures with up to five solutions at certain Rossby numbers. Developing flow in rotating square channels has also been investigated in the laminar regime [21] and in the turbulent regime [22]. Experimental work has also been carried out in laminar square channels [35] and in high aspect ratio turbulent channels [36].

In much of the previous works, the axis of rotation was parallel to the spanwise channel dimension, and increases in aspect ratio were along this axis. Since the Coriolis acceleration is dependent only on the cross product of the fluid velocity and the rotation vector, it is possible to translate the rotational axis with respect to the channel, and to get identical results. Accordingly, radial outward flow (normal rotation) in a rotating channel is equivalent to the previous cases of spanwise rotation with the spanwise and normal directions switched and hence with the inverse of the aspect ratio.

When additional effects are important, such as buoyancy (due to temperature or concentration change), transpiring channel walls [23] or channel curvature [37], this invariance to axis translation no longer exists.

The objective of the present study is to investigate developing flow with mass transfer in rotating rectangular channels with variously oriented axes of rotation. In contrast to several of the previous studies, the flow rate (Reynolds number) will be held constant as the rotational speed is varied. This situation is more relevant to membrane separation, where feed flow rates can strongly impact the separation recovery ratio and hence performance.

4.2 Problem Setup

The geometry of interest, shown in figure 4.1, is a rectangular channel rotating about an axis variously oriented with respect to the axis of rotation. While the figure depicts a channel of aspect ratio 3($L_z = 3D$), channels of aspect ratio 1 are also considered. A channel length of $L_x = 120D$ is used.

Solutions are obtained using the commercial CFD package Cfx 4.2 to solve the constant property Navier-Stokes equations in Cartesian form with the addition of

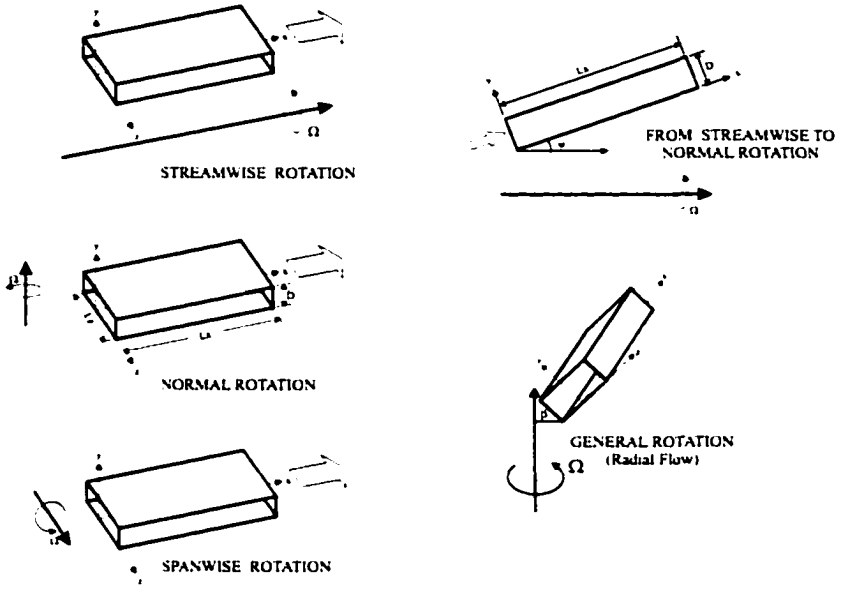

Figure 4.1: Rotating channel geometry. Geometries with radial flow include 'spanwise', 'normal' and 'general' rotation while 'streamwise' and 'streamwise to normal' rotation feature axial flow and flow inclined to the axis of rotation.

acceleration terms to model channel rotation. While the code provides several options for the discretization of the convective terms, all of the simulations presented here employed either a QUICK scheme, or a higher order upwind (HUW) scheme.

All simulations were carried out in the laminar regime, at a Reynolds number ($\mathrm{Re}_D = UD/\nu$) of 100, where U is the uniform velocity specified at the x=0 face. A fully developed condition is specified at the x=120D face, and all remaining faces are solid walls. Rotation was varied from 0 rad/s to 300 rad/s; the corresponding flow parameters are given in table 4.1.

Ω [rad/s]	Ro	1/Ro	Ek
0	∞	0	∞
4.36	20.91	0.0478	0.2091
10	9.12	0.1096	0.0912
25	3.65	0.2740	0.0365
50	1.82	0.5480	0.0182
100	0.91	1.0960	0.0091
125	0.73	1.3700	0.0073
150	0.61	1.6440	0.0061
200	0.46	2.1920	0.0046
250	0.37	2.7401	0.0037
300	0.30	3.2881	0.0030

Table 4.1: Computed Rossby and Ekman numbers. Not all cases were considered for each geometry and orientation.

4.3 Grid Sensitivity Study

In the case of normal rotation, in the limit of rapid rotation, and far from the z = ± 1.5D walls, the flow should approach the solution given by equations 4.5 and 4.6. Figure 4.2 plots the spanwise velocity for various Ek, and clearly shows the Ekman layer is comprised of a wall jet which grow in magnitude and which approach the walls with increasing Ek. These wall jets result in a spanwise component of wall shear stress, which is zero in non-rotating channel flow. Figure 4.3 plots the numerical wall stress relative the analytic wall stress for both Poiseuille flow and for various Ek. In the case of Poiseuille flow, the stress is in the streamwise direction, while in the case of rotation, only the additional spanwise component is considered. Since the Poiseuille solution is quadratic, a second order stress calculation has zero error at all grid sizes. The errors, even with a second order stress calculation, increase significantly with increasing rotation. In the case of Ek=0.0001, a second order calculation on a fine grid ($\delta y/D$ = 0.006) underpredicts the analytic solution by over 20%. This error does not fall below 1% before a very modest Ek=0.01. The first order calculation underpredicts the stress by 6% even in this low Ek.

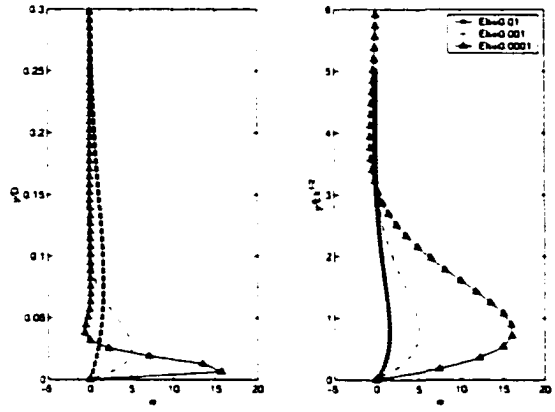

Figure 4.2: Spanwise velocity in the Ekman layer for various Ek.

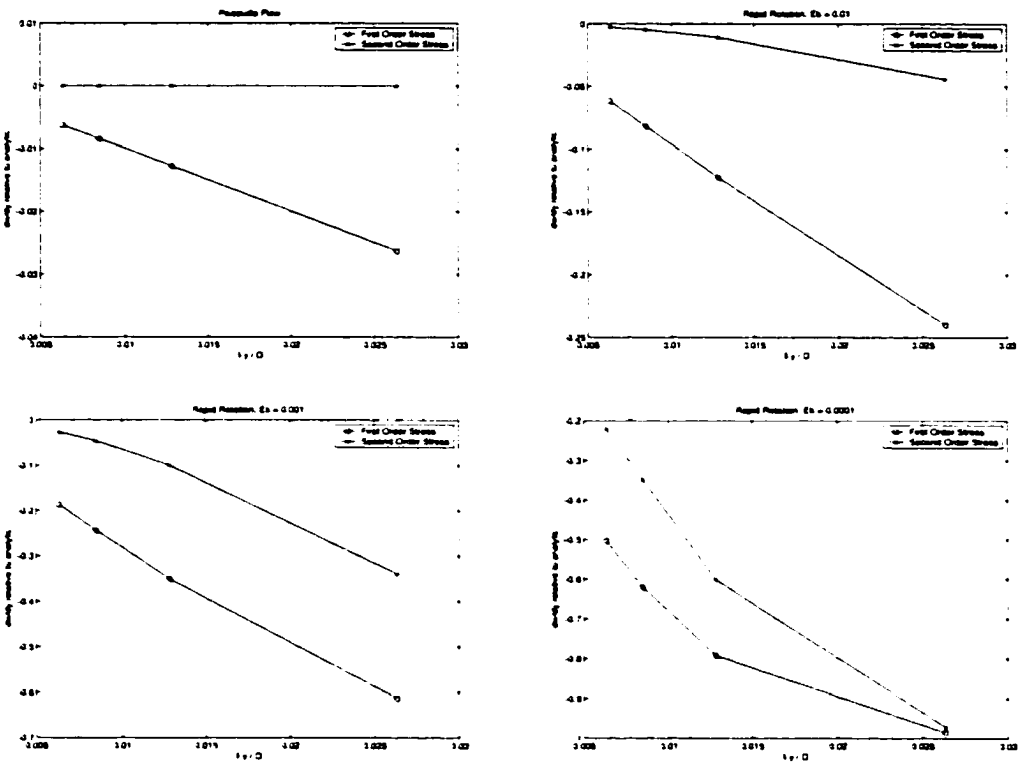

Figure 4.3: Comparison of analytical and numerical wall shear stress for various Ek.

In order to verify these results and the impact of grid resolution, a shorter domain was used, and the flow was solved with four different grids described in table 4.2. The first two grids were uniform in all dimensions, whereas NU5 and NU4 were non-uniform in both y and z with 3 uniform volumes adjacent to both the y=0 face and the y=D face. While second order shear calculations are used in the computational procedure, the following results are obtained from first order calculations from the computed velocity fields.

Figure 4.4 depicts the calculated shear stress on the y=0 face for each grid relative to BASE for a channel rotating with Ek=0.0076 (Ω = 120 rad/s), where h is the half-height of the channel. The streamwise shear component increases by approximately

Grid	Grid Volumes	δy /D
BASE	$[59 \times 39 \times 79]$	0.02564
HALFDY	$[59 \times 78 \times 79]$	0.01282
NU5	$[59 \times 60 \times 80]$	0.00600
NU4	$[59 \times 60 \times 80]$	0.00300

Table 4.2: Grids employed for numerical simulations.

2% over the BASE grid and there is little change between grids NU5 and NU4. The spanwise component changes significantly, increasing by more than 14 % over the base grid and by about 2% between grids NU5 and NU4. The vector sum of the 2 components is shown in part C) of figure 4.4, and shows a 6% increase over the BASE grid and less than 0.5% change between grids NU5 and NU4.

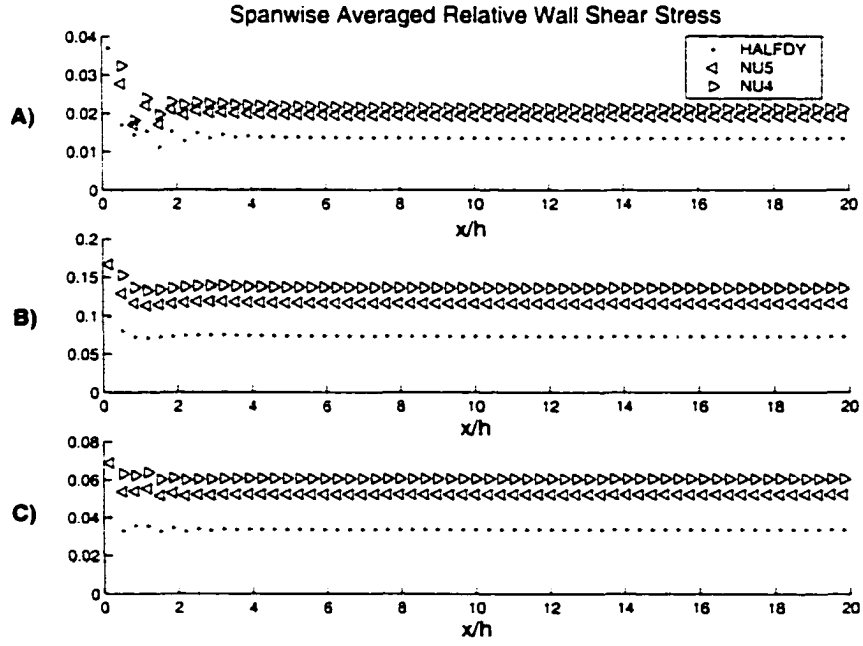

Figure 4.4: Spanwise average shear stress relative to BASE grid for $\Omega = 120s^{-1}$. $(\tau - \tau^{BASE})/\tau^{BASE}$. A) τ_{yx} B) τ_{yz} C) $|\tau|$

Figure 4.5 plots the magnitude of the spanwise average shear at the outlet, non-dimensionalized using the shear on the base grid, as a function of the grid spacing above the y=0 wall. In the rotating case, a linear increase in shear with decreasing grid size is evident, while in the non-rotating cases the curve is clearly approaching an asymptotic value. In terms of dimensional quantities, the shear in the rotating case is almost three times the shear in the non-rotating case. This and the causes of the differing behaviours will be re-visited in the next section.

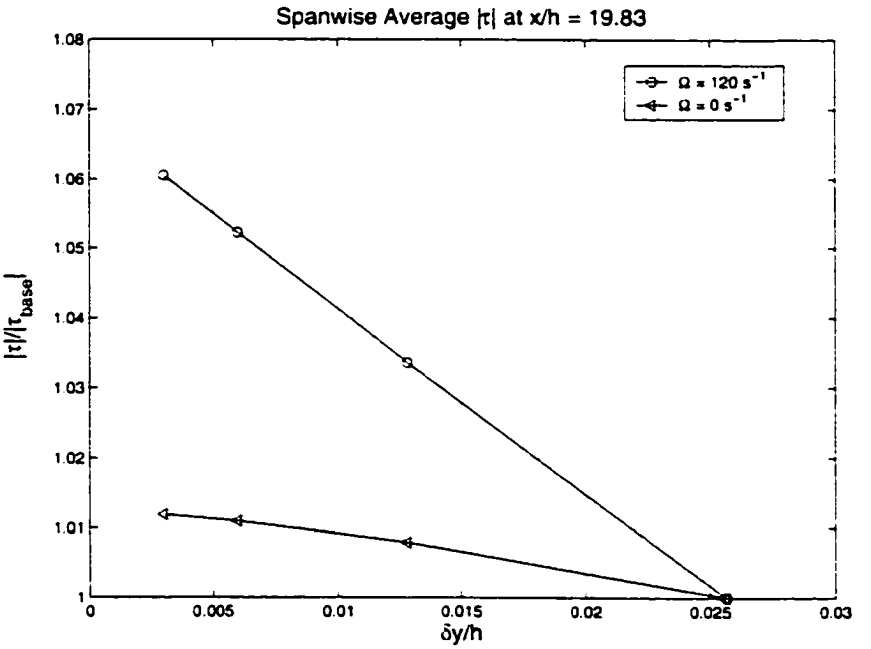

Figure 4.5: Average shear stress as a function of grid spacing normal to the long wall.

Due to the continued dependence of the shear stress on δy, in the case of rotating channel flow, Grid NU4, with the finest near wall spacing, was chosen for the remainder of this study.

4.4 Radial Flow Channels

4.4.1 Normal Rotation

In the case of a channel of aspect ratio 3 undergoing normal rotation with $\Omega > 0$, the leading wall corresponds to z = -1.5D while z = 1.5D is the lagging sidewall. Figure 4.6 presents a relief plot of the streamwise velocity in the fully developed region for various Ro. As Ro decreases (the rotation rate increases) the high speed fluid near the centre of the channel is directed toward the lagging (z = 1.5D) wall causing a maximum far from the channel centre. At Ro = 1.8 two local maxima are beginning to form parallel to and near the y=0 and y=D surfaces, and as Ro decreases further, the profile becomes increasingly symmetric. Figure 4.7 shows the secondary velocity vectors in the case of Ro = 0.3, and clearly illustrates the reason for the formation of local maxima in the velocity profile: a pair of wall jets form and serve to transport fluid back towards the leading sidewall. Figure 4.8 plots contours of streamwise velocity for various Ro in the cases of rectangular and square channels.

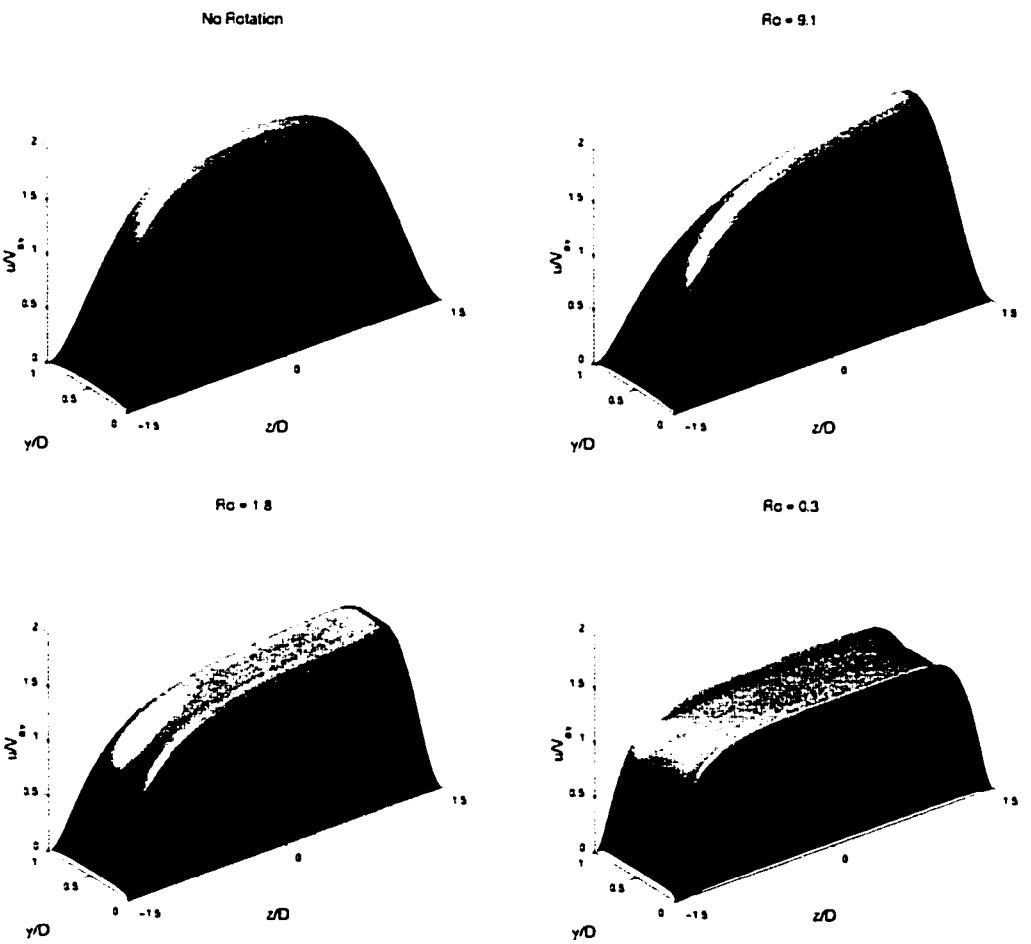

Figure 4.6: Relief plots of streamwise velocity in the fully developed region for various Ro. Normal rotation.

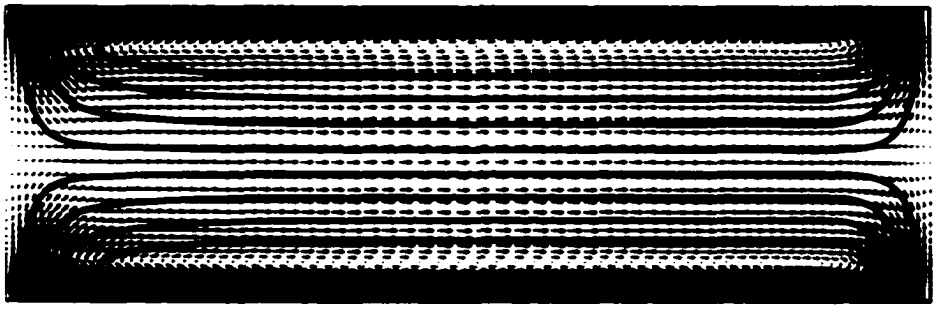

Figure 4.7: Secondary velocity vectors in the fully developed region. Ro = 0.3. Normal Rotation

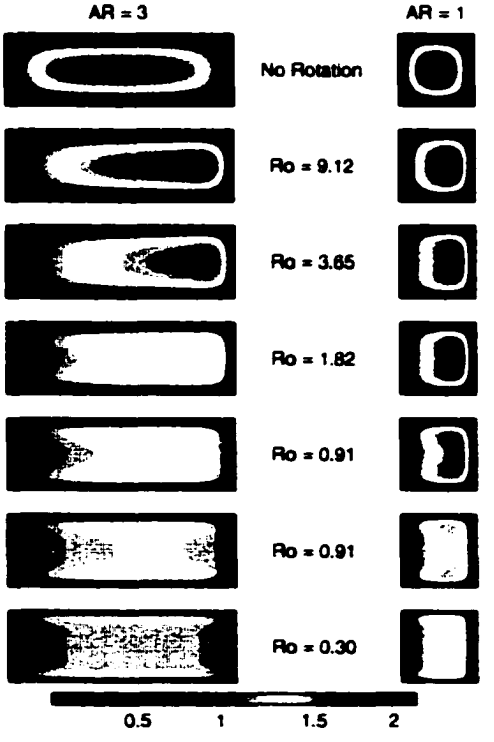

Figure 4.8: Contours of u/V_{av} for various Ro: the effect of aspect ratio.

Figures 4.9 and 4.10 plot the local streamwise velocity in the fully developed region at each of the channel centrelines for various Ro. The profiles parallel to the rotational axis (figure 4.9) are symmetric about the spanwise centerline, and initially feature a gradual flattening near the channel centre, with a correspondingly steeper gradient at the y=0 and y=D surfaces. The curve corresponding to Ro = 1.82 shows the formation of inflexion points and maxima near y/D = 0.3 and y/D = 0.7 and a local minimum at y/D = 0.5. As Ro decreases, the core flow spreads and the maximum velocity decreases. The velocity 'overshoots' are attenuated and their location shifts towards the walls. With further decreases in Ro, the local minimum at the centreline flattens until uniform flow fills almost 60 % of the channel. At this point, the overshoot maxima are located at y/D = 0.12 and y/D = 0.88.

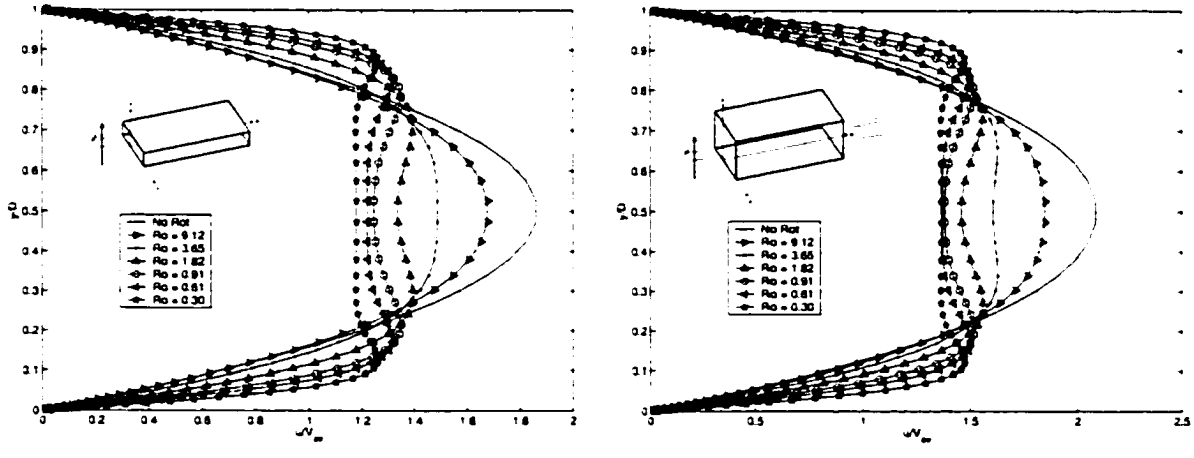

AR = 3 AR =1

Figure 4.9: Streamwise velocity parallel to the axis of rotation at the channel centreline in the case of normal rotation.

In contrast, the corresponding profiles perpendicular to the rotational axis (figure 4.10) are not symmetric as there is a general steepening of the gradient at the lagging sidewall and a flattening of the gradient at the leading sidewall. With a very modest channel rotation (Ro = 9.12) there is a pronounced maximum at z/D = 1.1. As

Ro decreases, an inflexion point develops , this maximum shifts closer to the lagging sidewall and the maximum velocity magnitude decreases. Further decreases in Ro result in increasingly flatter profiles such that at the lowest Ro, uniform flow covers approximately 60 % of the channel.

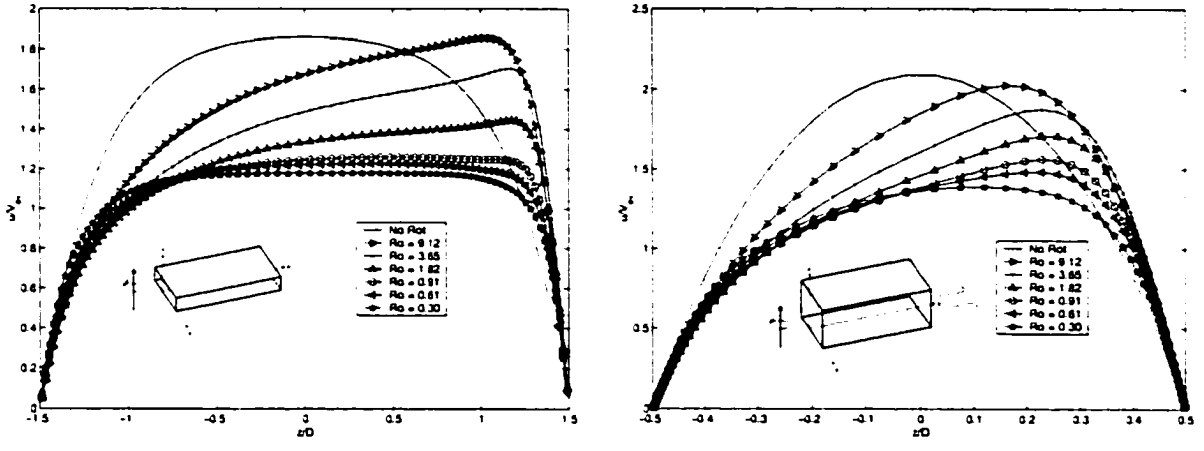

AR = 3 AR = 1

Figure 4.10: Streamwise velocity normal to the axis of rotation at the channel centreline in the case of normal rotation.

Figure 4.11 shows the spanwise velocity component normal to the rotational axis at the channel centreline, and helps interpret the streamwise velocity profiles. As Ro decreases secondary flows develop and transport momentum in the spanwise direction. Again, these profiles are symmetric about the channel centreline. The maximum positive spanwise velocity (w $\approx$ 0.23 V_{av}) occurs at the highest Ro and decreases to $\approx$ 0.09V_{av} as Ro decreases. The maximum negative velocity increases steadily to approximately 0.34 V_{av} as the wall jets approach the y=0 and y=D surfaces. Again, at the lowest Ro, there is a region of uniform velocity covering close to 60 % of the channel.

Figure 4.12 plots the maximum streamwise velocity versus 1/Ro. At very low rotation rates, the maximum velocity is nearly 1.86 V_{av} as in the case of no rotation.

As rotation increases however, the maximum velocity drops sharply and then appears to asymptotically approach a minimum value near 1.25 V_{av}.

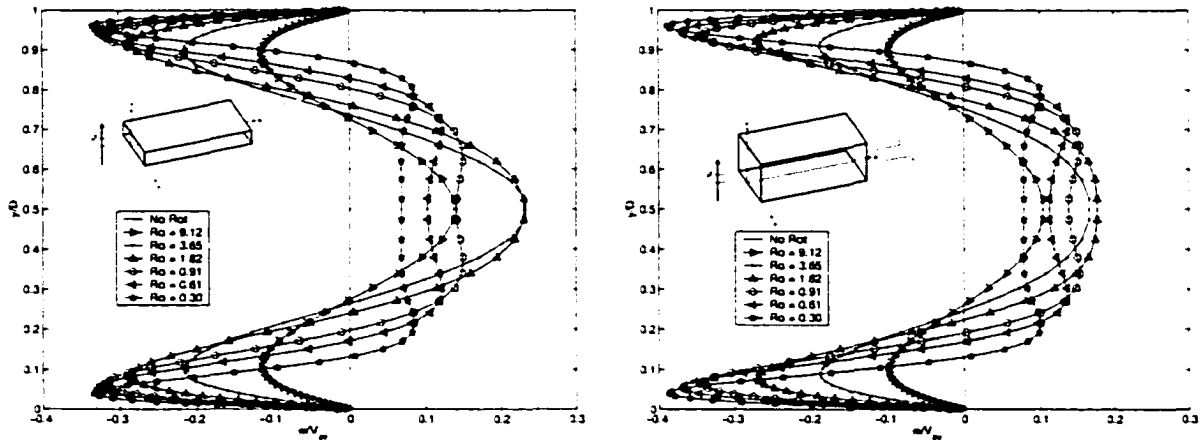

Figure 4.11: Spanwise velocity normal to the axis of rotation at the channel centreline in the case of normal rotation.

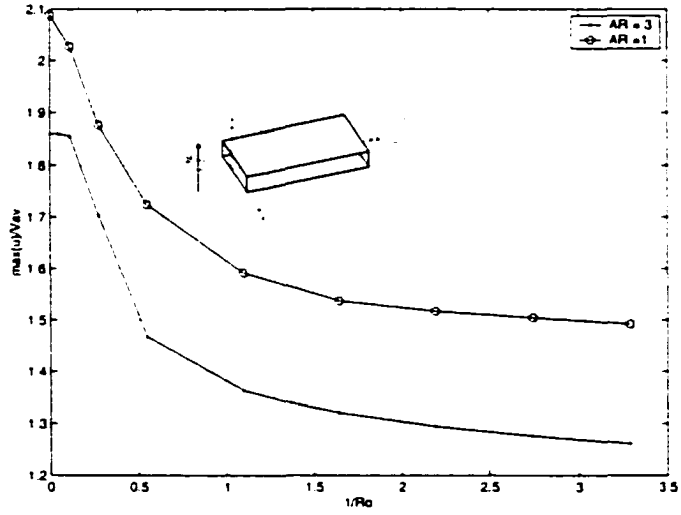

Figure 4.12: Maximum streamwise velocity with increasing rotation in the case of normal rotation.

In fully developed non-rotating channel flow, it is common to express the channel pressure drop in terms of the wall shear stress since a streamwise control volume analysis shows that these two forces are in balance. This is not necessarily the case when the channel is rotating as the Coriolis force is also present. Table 4.3 lists the direction of the Coriolis force due to the velocity components in a channel undergoing rotation. The induced secondary velocity results in a Coriolis force in streamwise direction which has the same profile as the w velocity component.

Velocity Component	Direction of Coriolis Force		
	Normal	Spanwise	General
u	$\hat{k}$	$-\hat{j}$	$-\cos\beta\ \hat{j} + \sin\beta\ \hat{k}$
v	0	$\hat{i}$	$\cos\beta\ \hat{i}$
w	$-\hat{i}$	0	$-\sin\beta\ \hat{i}$

Table 4.3: Directions of the Coriolis force generated by velocity components in a channel undergoing Normal rotation.

Accordingly, it is necessary to define two parameters to characterize fully developed flow in a rotating channel, a non-dimensional pressure drop,

$$c_p = -\frac{\partial p/\partial x}{1/2\rho V_{av}^2} r_h \tag{4.7}$$

and a friction coefficient,

$$c_f = \frac{\tau_{wall}}{1/2\rho V_{av}^2} \tag{4.8}$$

where τ_{wall} is the magnitude of the wall shear stress. In order to perform a streamwise momentum control volume analysis, it is necessary to resolve the streamwise component of this stress, which can be used to define another friction coefficient,

$$c_{fx} = \frac{\tau_{wall_x}}{1/2\rho V_{av}^2} \tag{4.9}$$

The variation of c_f around a cross section in the fully developed region is presented in figure 4.13, where a new local coordinate, s, has been defined around the perimeter of the cross section, and the channel walls have been labelled by their compass points. In all cases, c_f is zero in the channel corners, varies around the perimeter and has identical variations on the NORTH and SOUTH faces. When no rotation is present, the c_f distribution is symmetric on each face and is slightly higher on the NORTH and SOUTH faces than on the WEST and EAST faces. As rotation is introduced, c_f increases on all faces except the WEST (leading) face and the maximum shifts towards the EAST (lagging) face. As Ro decreases, the shear on the NORTH and SOUTH faces increases to approximately 5 times the non-rotating value while the shear on the EAST face nearly doubles.

Figure 4.14 presents the pressure coefficient and various averages of the friction coefficient as a function of 1/Ro in the fully developed region. Area averages of c_f around the perimeter are denoted by C_f and are qualified by compass point when averaged over a single face only. It is evident that the pressure coefficient is very nearly balanced by the streamwise component of the friction coefficient (C_{fx}) which indicates that the Coriolis force generated by the streamwise velocity component is in equilibrium across a cross section as might be anticipated from figure 4.11. At all Ro, the total shear is higher than the channel pressure drop with the greatest differences occurring at the highest rotation rates. Also, the shear averaged over the NORTH and SOUTH faces is consistently and significantly higher than the average around the entire perimeter.

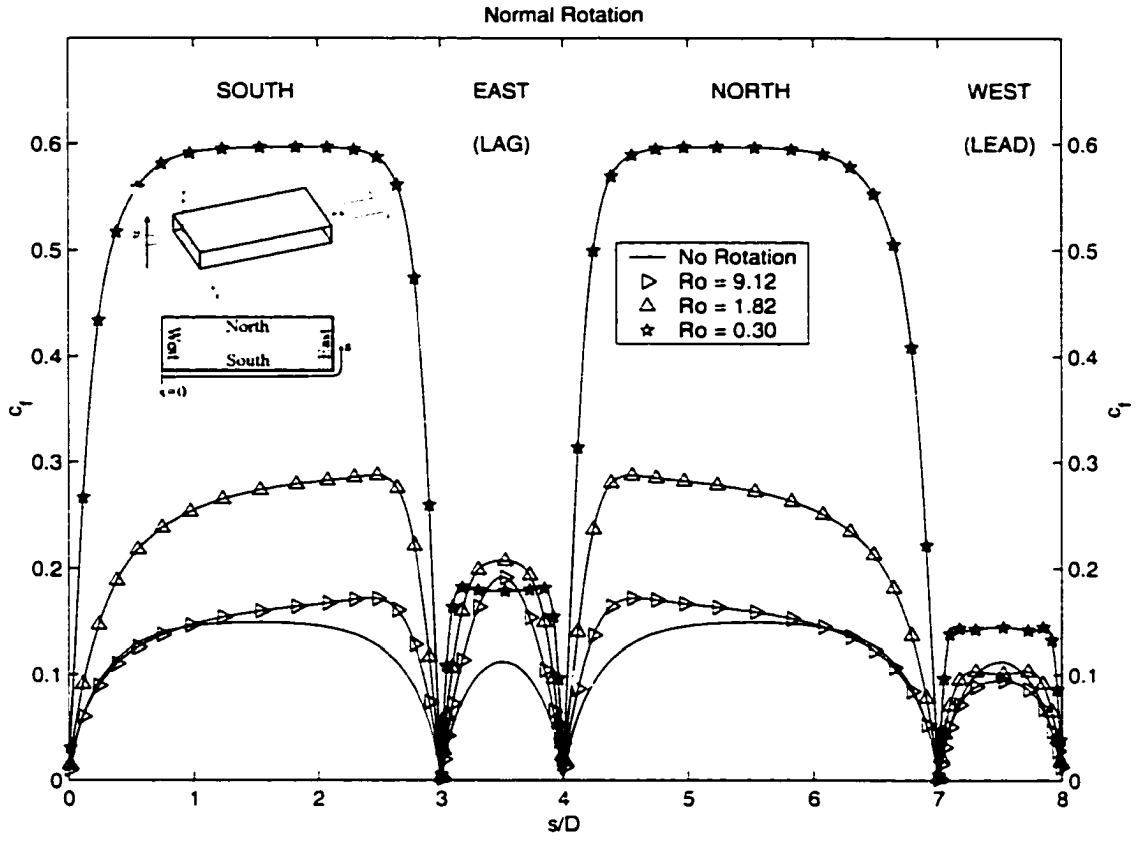

Figure 4.13: Variation of friction coefficient in the fully developed region for various Ro. Normal Rotation.

4.4.2 Spanwise Rotation

In the case of spanwise rotation, the rotational axis is aligned with the z channel dimension as defined in figure 4.1. In this case, the y=D surface is the leading wall while the y=0 surface is the lagging wall. The long dimension of the aspect ratio 3 channel is now aligned with the rotational axis such that this case is akin to normal rotation in a channel of inverse aspect ratio,

$$AR_{\text{spanwise}} = 1/AR_{\text{normal}} \tag{4.10}$$

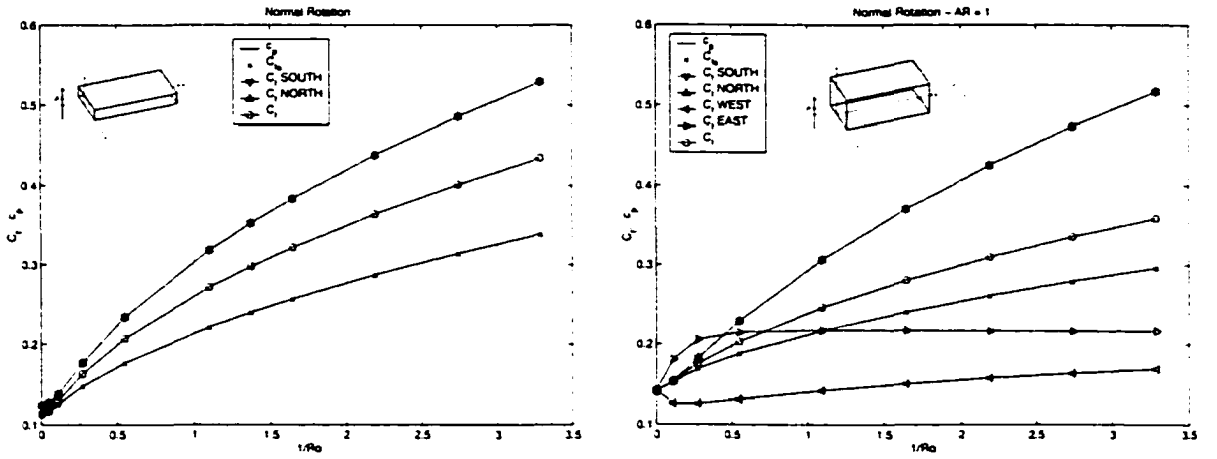

AR = 3 AR = 1

Figure 4.14: Pressure and friction coefficients in the case of normal rotation.

which means that the results presented above for the square channel represent spanwise rotation if the z and y coordinate directions are switched (and the direction of the y-axis switched so as to maintain a right handed system). Accordingly, this section presents results for a channel of aspect ratio 3 only.

Figure 4.15 presents relief plots of the streamwise velocity in the fully developed region for Ro corresponding to those presented in figure 4.6. As will be shown, the fluid is again directed toward the lagging sidewall (y = 0), and again, at Ro = 1.8 there is the formation of two local maxima, which are now near the z = -1.5D and z = 1.5D surfaces. As Ro decreases, these maxima become increasingly pronounced. Figure 4.16 presents secondary velocity vectors and streamlines in the case of Ro = 0.3. Wall jets have again formed, and serve to transport fluid back towards the leading wall. While the secondary flow pattern appears quite different from that developed under normal rotation, it is qualitatively similar but constrained by a much shorter flow path normal to the axis of rotation.

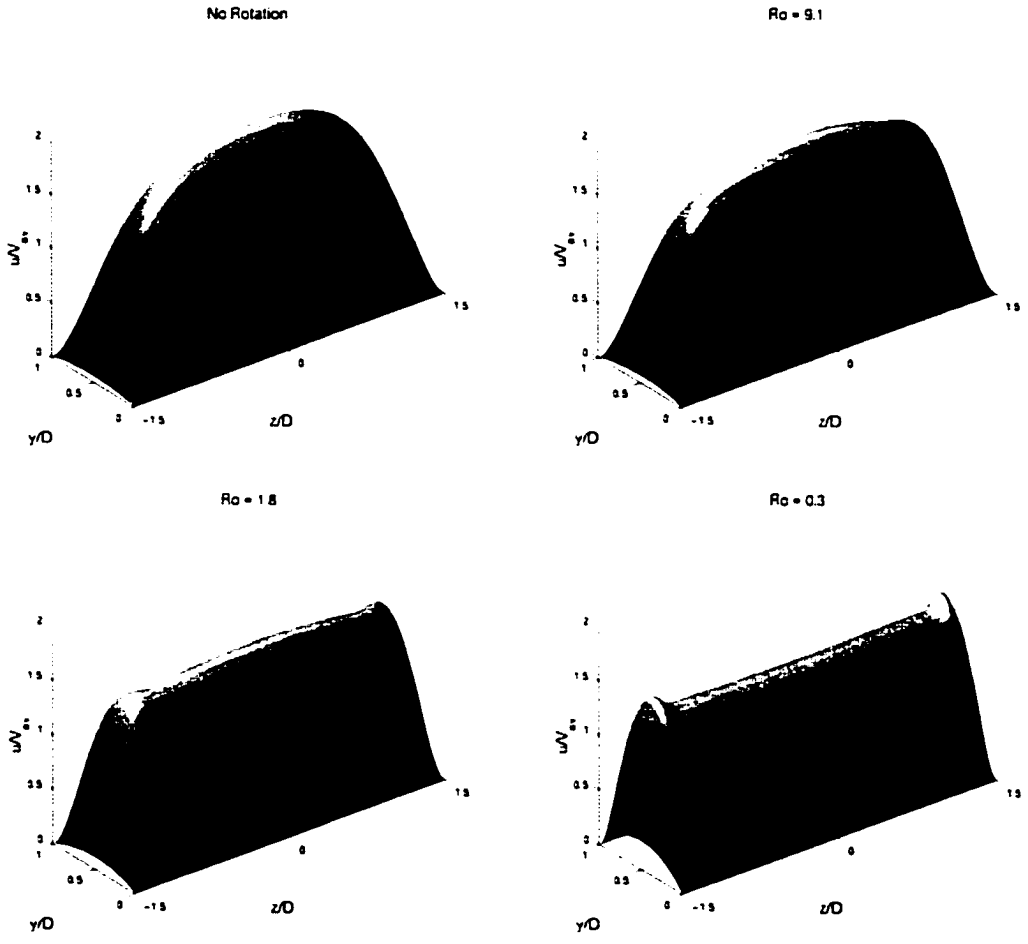

Figure 4.15: Relief plots of streamwise velocity in the fully developed region for various Ro. Spanwise rotation.

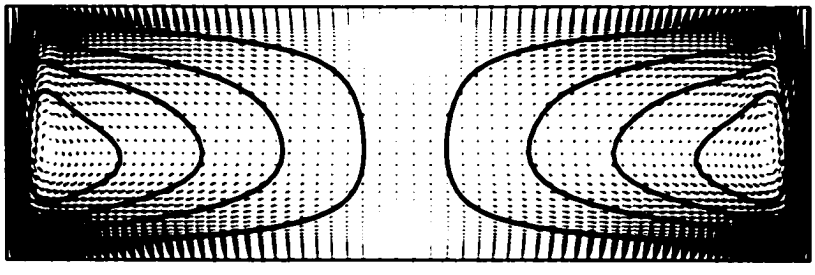

Figure 4.16: Secondary velocity vectors in the fully developed region. Ro = 0.3. Spanwise Rotation

Figures 4.17 and 4.18 plot local streamwise velocity in the fully developed region at each of the channel centrelines for the same Ro presented above. Again, the profiles parallel to the rotational axis (figure 4.18) are symmetric while the profiles perpendicular to rotational axis (figure 4.17) are not. Figure 4.18 is qualitatively similar to figure 4.9. An inflexion point is first evident in the case of Ro = 1.82, but the maxima occur even closer to the wall in this case. At the highest rotation rate, uniform flow covers over 80% of the channel core.

The profiles normal to the rotational axis (figure 4.17 are similar to the those present in normal rotation (figure 4.10) in the sense that there is a steepening of the gradient at the lagging sidewall and a flattening of the gradient at the leading sidewall and the maximum velocity decreases with decreasing Ro. They are also markedly different, though, in the sense that there are no inflexion points and no regions of uniform flow, even at the lowest Ro. The Stewartson layers forming on the leading and lagging sidewalls are larger than the channel dimension, such that they merge, leaving no inviscid region between them.

Figure 4.19 plots the normal velocity parallel to the centreline which is parallel to the axis of rotation and captures the wall jets adjacent to the $z = \pm 1.5D$ sidewalls which are significantly closer to the wall, and more pronounced than in the case of normal rotation. The maximum velocity attained in the jet at the highest rotation is $\approx 0.44V_{av}$ while the maximum velocity in the core is $\approx -0.4V_{av}$. Again in this view, uniform flow covers almost 80 % of the channel at the highest rotation rate.

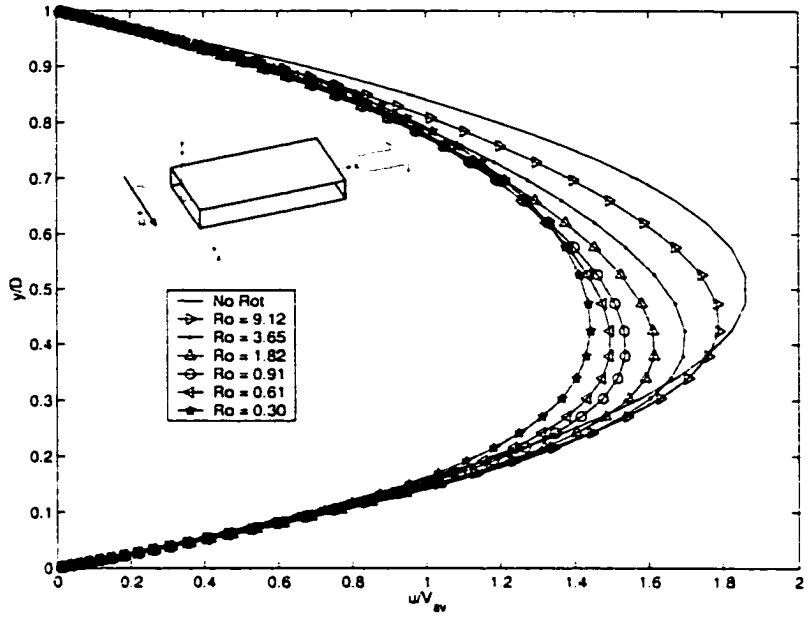

Figure 4.17: Streamwise velocity normal to the axis of rotation at the channel centreline in the case of spanwise rotation.

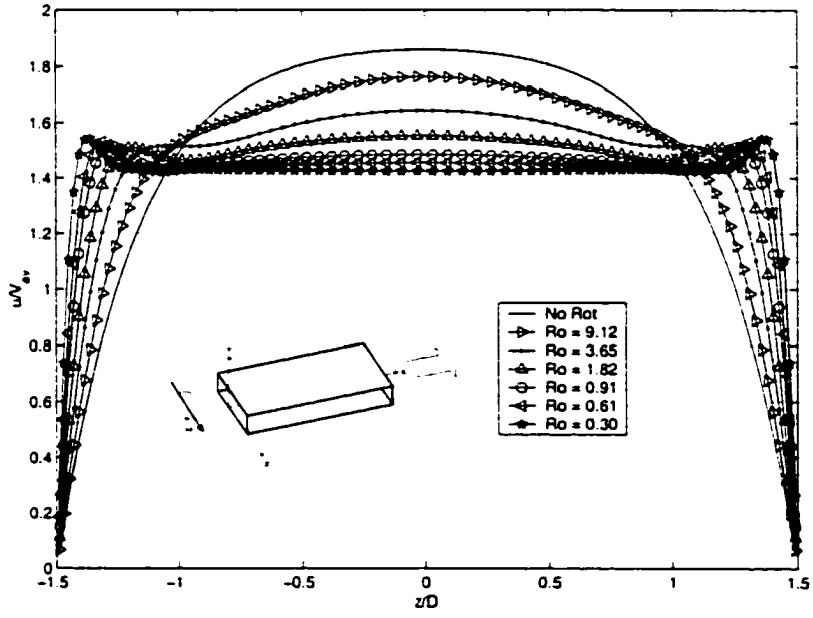

Figure 4.18: Streamwise velocity parallel to the axis of rotation at the channel centreline in the case of spanwise rotation.

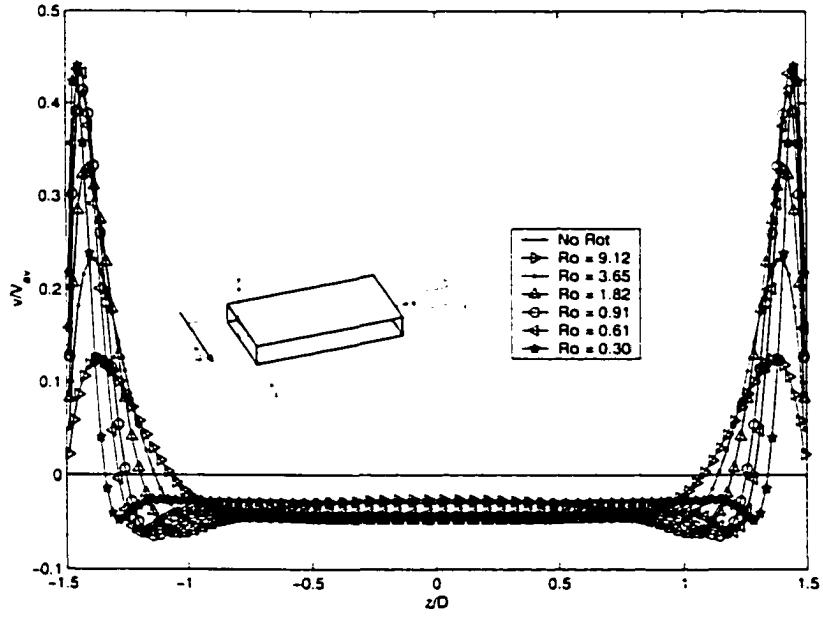

Figure 4.19: Normal velocity parallel to the axis of rotation at the channel centreline in the case of spanwise rotation.

Figure 4.20 plots the maximum streamwise velocity versus 1/Ro. In contrast to the case of normal rotation, the maximum velocity decreases significantly with even slight channel rotation. The curve passes through a minimum at Ro = 0.61 (1/Ro = 1.64) when the maximum has shifted to the sidewall, and then increases slightly to $\approx 1.55V_{av}$ as the maximum moves to the sidewalls.

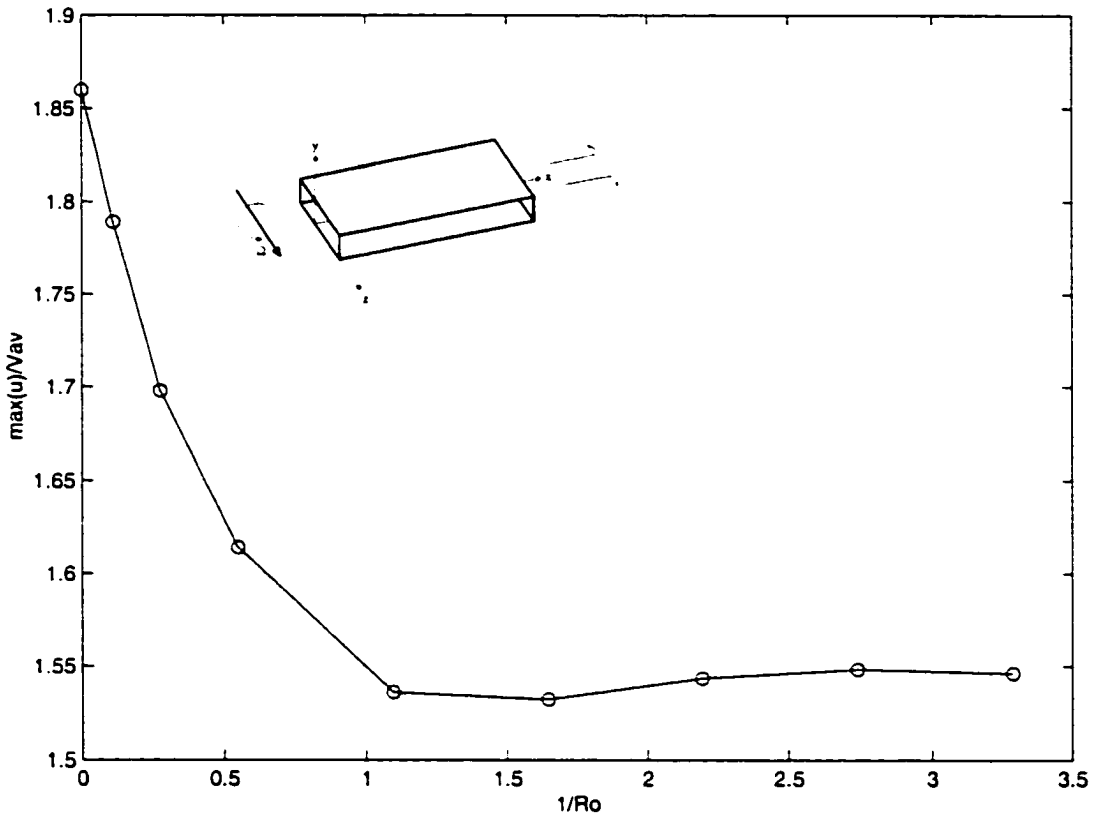

Figure 4.20: Maximum streamwise velocity with increasing rotation. Spanwise rotation.

The variation of c_f around a cross section in the fully developed region is presented in figure 4.21. With the change in the orientation of the rotational axis, it is now the EAST and WEST faces which exhibit identical shear distributions, which in the case of rotation are significantly higher than the shear on the NORTH and SOUTH

faces. The shear distributions on the lagging and leading faces are similar to the case of normal rotation, with the leading faces exhibiting a decreased shear in most cases while the shear on the lagging face increases. Both the leading and lagging surfaces develop two maximums adjacent to the sidewalls and corresponding to the location of the wall jets. The maxima on the lagging and leading sidewall are approximately 1.65 and 1.4 respectively, while the maximum on the sidewalls is ≈ 0.68.

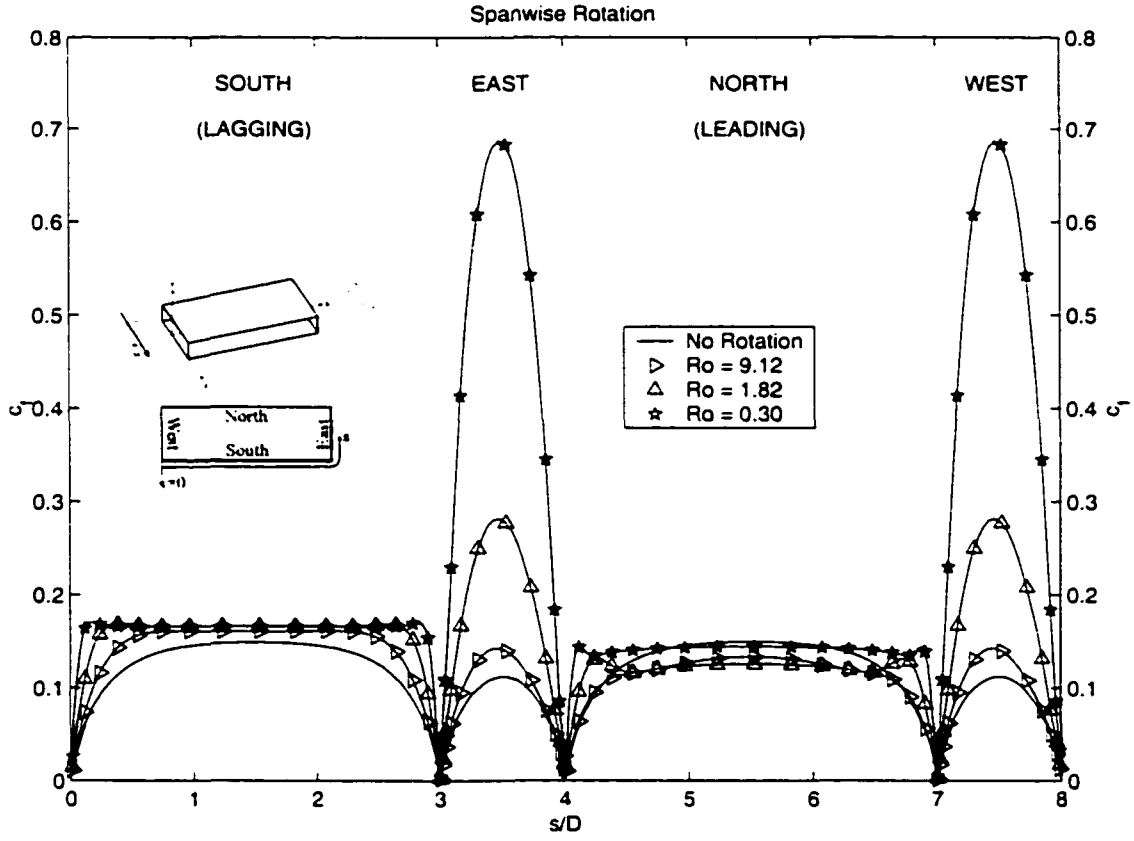

Figure 4.21: Variation of friction coefficient in the fully developed region for various Ro. Spanwise rotation.

Figure 4.22 presents the pressure coefficient and various averages of the friction coefficient with increasing rotation in the case of spanwise rotation. Again, the x component of the shear is very nearly balanced by the pressure drop, but there are

noticeable differences at the highest rotation rates. While the total shear is everywhere greater than the than the pressure drop, the average shear on the lagging face (NORTH) is less than the pressure drop for all rotation rates, and the shear on the lagging (SOUTH) face is initially higher and then crosses the c_p curve near Ro = 0.91 (1/Ro = 1.1).

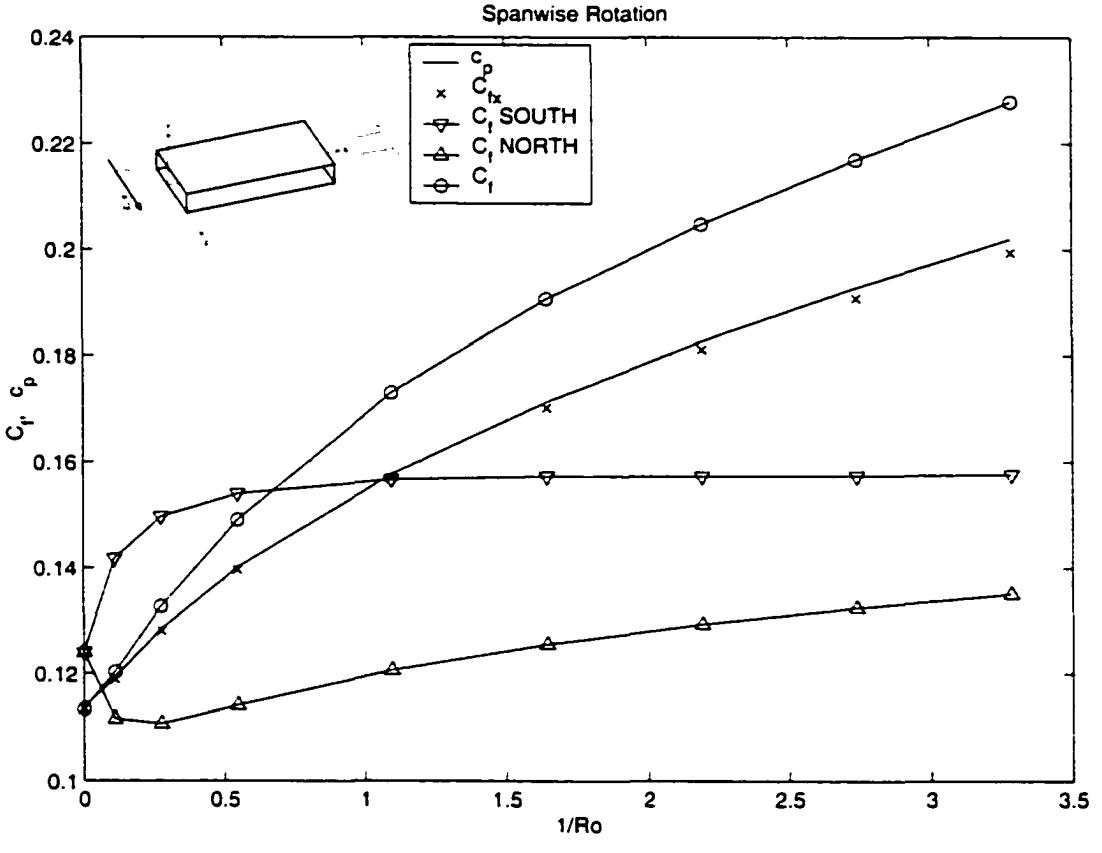

Figure 4.22: Pressure and friction coefficients in the fully developed region in the case of spanwise rotation.

4.4.3 From Streamwise to Normal Rotation

Having investigated both normal and spanwise rotation, this section will explore the transition between the two modes. Figure 4.23 depicts a channel with flow in the radial direction, inclined at an angle β, such that $\beta = 0^o$ corresponds to spanwise rotation and $\beta = 90^o$ corresponds to normal rotation. The channel rotation rate was held constant at $\Omega = 250$ rad/s (Ro = 0.37) and simulations were carried out for $\beta = \{0, 1, 5, 10, 20, 30, 40, 45, 50, 60, 70, 80, 90\}$.

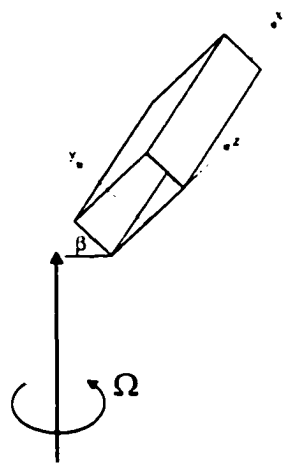

Figure 4.23: General channel rotation with radial flow.

Figure 4.24 depicts relief plots of streamwise velocity in the fully developed region for selected cases while figure 4.25 plots contours of streamwise velocity and secondary streamlines. For small departures from the spanwise and normal rotation cases, the streamwise velocity contours retain essentially the same features, with a slight asymmetry corresponding to a decrease of one velocity maximum and an increase in the other. A radical skewing of the contour takes place at intermediate β as illustrated in figure 4.25 in the case of $\beta = 45^o$. The streamlines clearly depict the character of the induced secondary flows, which in all cases consists of two counter-rotating structures. Each profile features two local maxima. In the limiting cases of spanwise and normal

rotation , the velocity profiles and the secondary flow structures are symmetric about the channel centreline perpendicular to the axis of rotation and hence these maxima are equal. The location of these maxima correspond to the centre of the wall jets which are induced on the channel sidewalls, and as β is increased, these structures and their associated maxima track the rotation vector such that the structure which began adjacent to the z = -1.5D wall extends along the y = 0 wall and the structure which began adjacent to the z = 1.5D wall extends long the y = D wall.

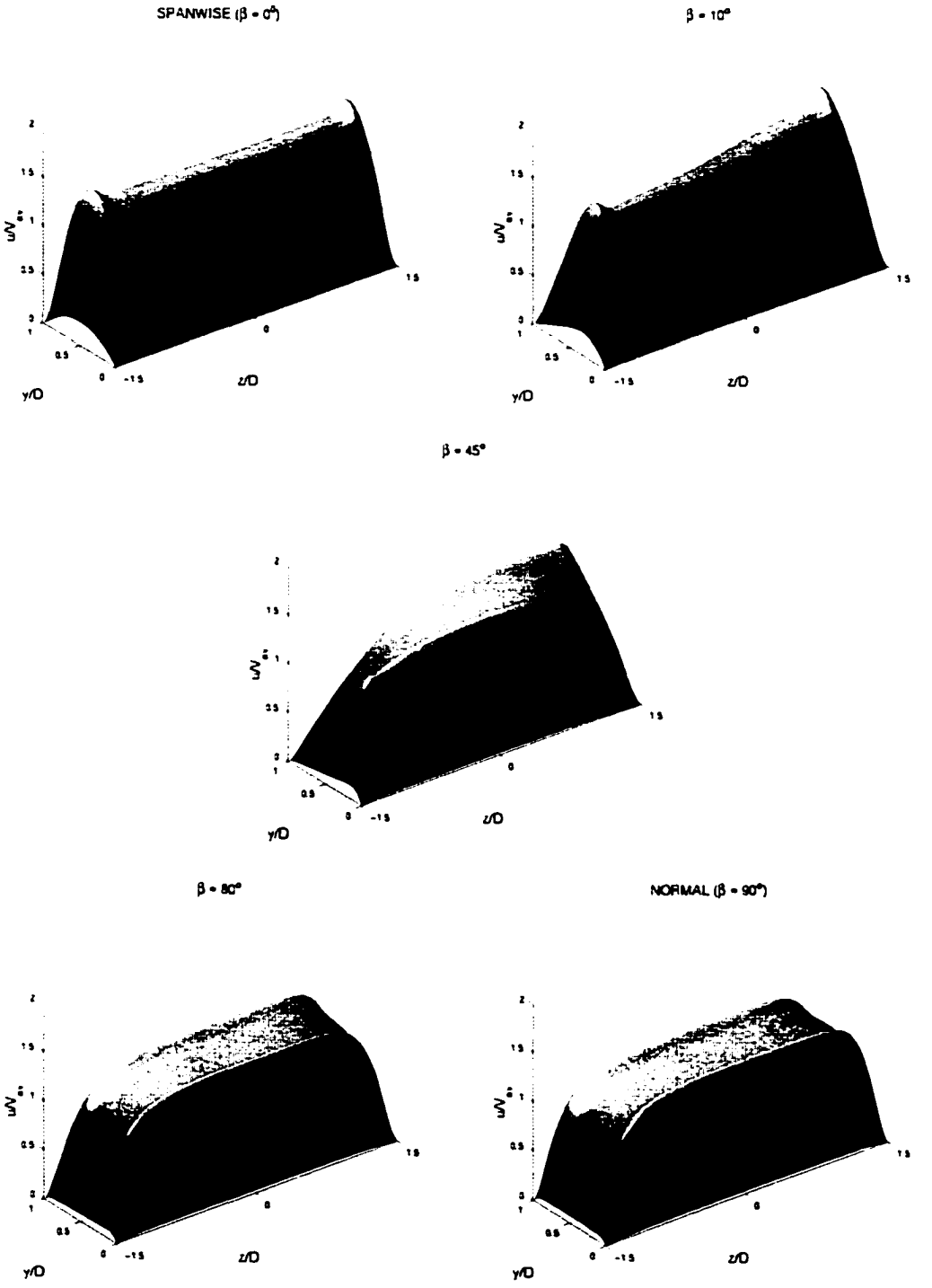

Figure 4.24: Relief plots of streamwise velocity in the fully developed region as rotation is varied between spanwise and normal rotation ($0^o < \beta < 90^o$). Ro = 0.37.

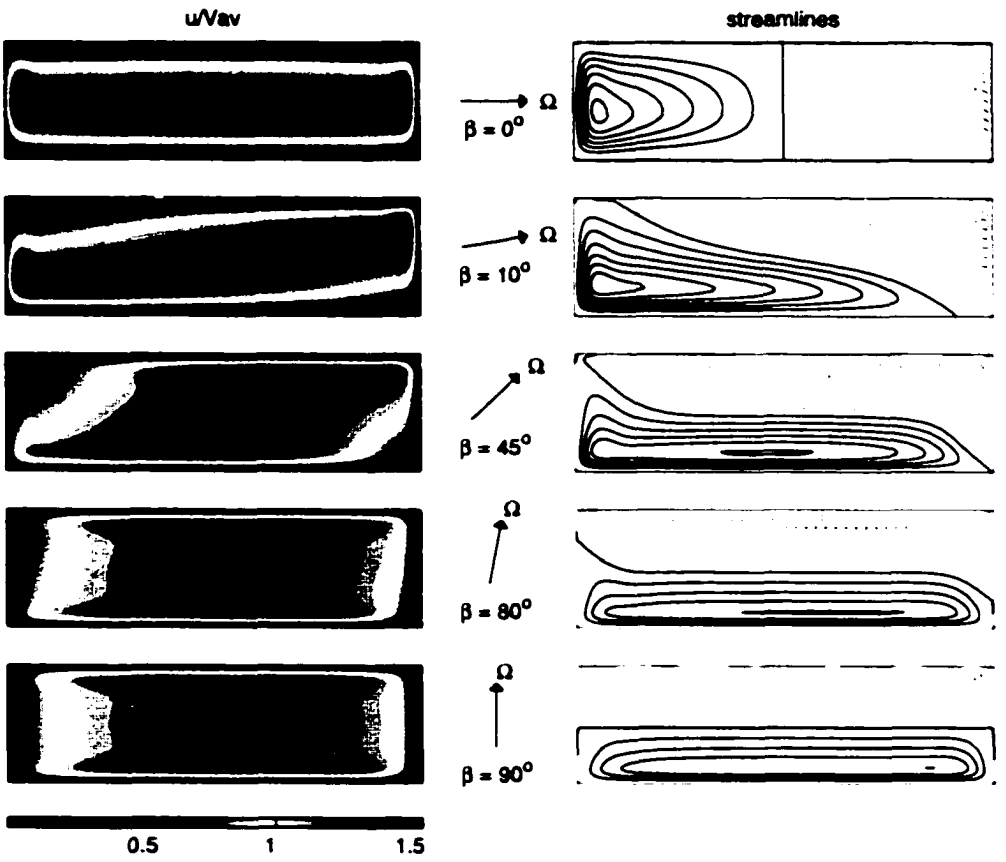

Figure 4.25: Contours of streamwise velocity and secondary streamlines in the fully developed region as rotation is varied between spanwise and normal rotation ($0^o < \beta < 90^o$). Ro = 0.37. AR = 3

Figure 4.26 presents the same plot in the case of a channel of aspect ratio 1. This figure is very similar to figure 4.25 with the exception that the two extreme cases are simply a 90^o rotation of each other since the geometric constraints are now the same in the streamwise and normal directions. As in all cases presented, the secondary velocity pattern consists of two high speed wall jets which are deflected by the each other and by the channel walls such that they circulate through the central region of the cross section. In the case of the square channels the available area in the core of

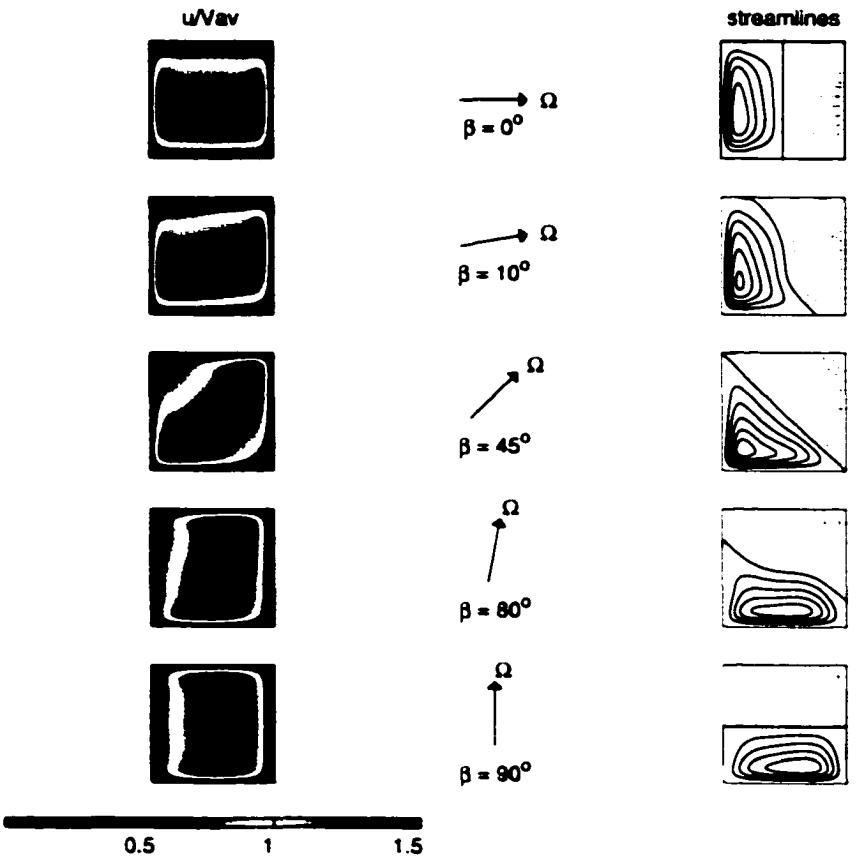

Figure 4.26: Contours of streamwise velocity and secondary streamlines in the fully developed region as rotation is varied between spanwise and normal rotation ($0^o < \beta < 90^o$). Ro = 0.37. AR = 1.

the channel is smaller such that the jet flow does not decelerate as much as in the AR = 3 case.

Figure 4.27 plots the pressure variation in the fully developed region for channels of aspect ratio 3. In each case, there is a large central region, corresponding to a region of uniform velocity, in which the pressure contours are orthogonal to the axis of rotation. In these central regions, the pressure decreases in the lagging direction in order to balance the Coriolis force, indicating that a relatively large geostrophic core exists in each case. The pressure contours then curve as they pass thorough the wall

jets, to intersect the walls at 90°.

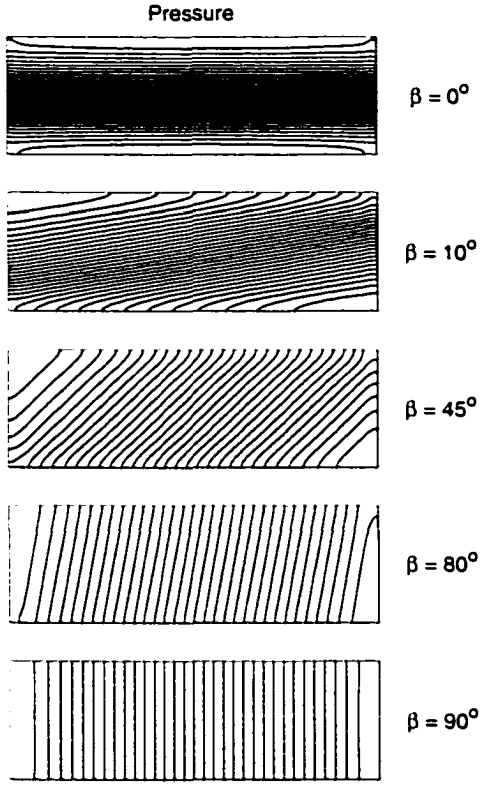

Figure 4.27: Contours of pressure in the fully developed region as rotation is varied between spanwise and normal rotation ($0^o < \beta < 90^o$). Ro = 0.37

The variation of friction coefficient around a cross section in the fully developed region is presented in figure 4.28 for ($0^o < \beta < 90^o$). When rotation is spanwise, or nearly spanwise, the shear on the NORTH and SOUTH faces is low compared the the EAST and WEST faces while normal rotation causes high shear on the NORTH and SOUTH faces, and relatively low shear on the EAST and WEST faces. Significant variations in shear are present in the intermediate cases with high shear regions corresponding to the location of the wall jets and with interruptions in the corners.

Figure 4.29 presents the pressure coefficient and averaged friction coefficients for both square and aspect ratio 3 channels. Not surprisingly, the characteristics of these

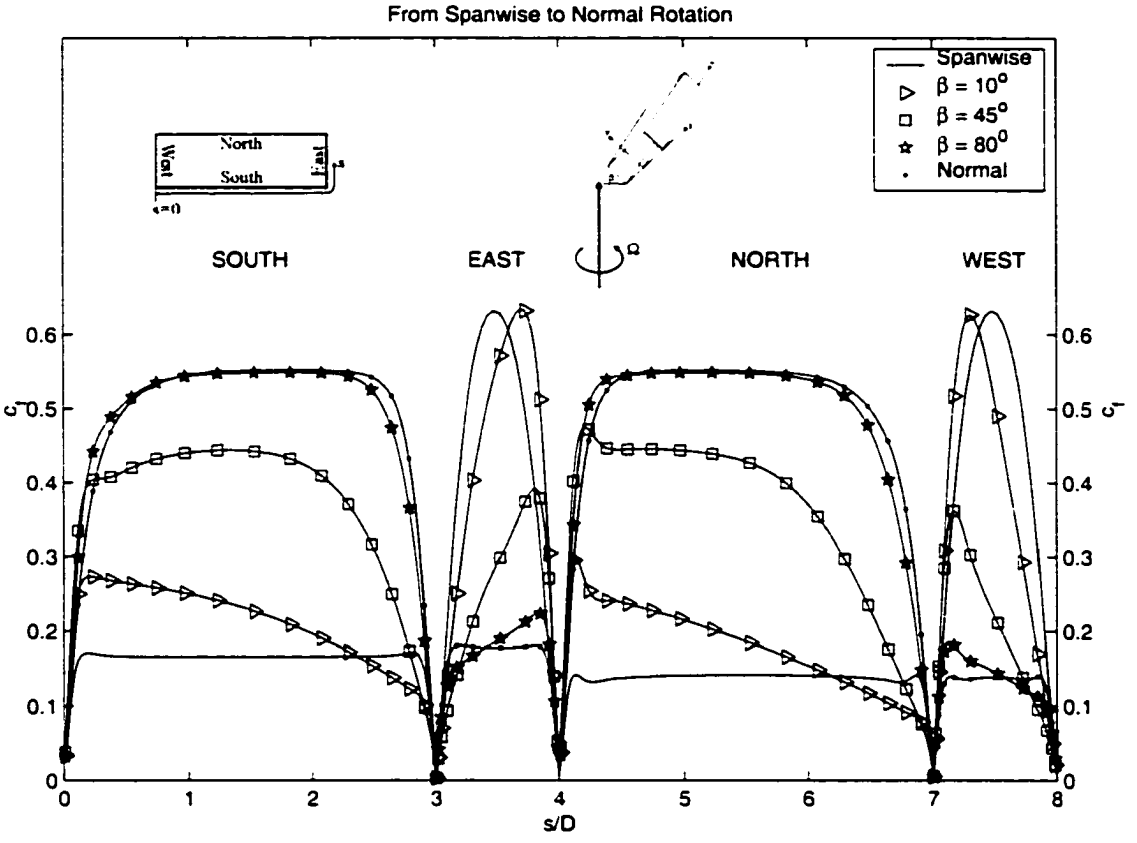

Figure 4.28: Variation of friction coefficient in the fully developed region. Ro = 0.37. Rotation is varied from spanwise to normal.

curves are quite different in the two cases. In the case of aspect ratio 3 channels, both the circumferentially averaged friction coefficient (C_f) and c_p increase monotonically with β reaching a maximum in the case of normal rotation. The curves are however concave down such that the maximum value is very nearly attained by $\beta = 70°$. In contrast, the square channels exhibit a maximum in both these curves when $\beta = 45°$. With respect to these curves, which represent averages over the entire cross section, the solution is the same at $\beta = 0°$ and $\beta = 90°$ further supporting the fact that these two solution are simply 90° rotations of each other. In both cases, C_f is everywhere greater than c_p but in the case of aspect ratio 3 channels, the difference increases

monotonically with β while it is a maximum at $\beta = 45^o$ in the square channels. Also, the friction coefficient on the SOUTH face is consistently higher than that on the NORTH face and this difference diminishes with increasing β, vanishing at $\beta = 90^o$ when the solution becomes symmetric about an EAST-WEST axis. The friction coefficient on both the NORTH and SOUTH faces is lower than c_p at low β. In the rectangular channels, the c_f on the SOUTH face exceeds c_p curve at $\beta \approx 11^o$ and the c_f on the NORTH face surpassing c_p at $\beta \approx 18^o$. These phenomena is delayed in the case of square channels with c_f (SOUTH) crossing c_p at $\beta \approx 25^o$ and with c_f (NORTH) crossing c_p at $\beta \approx 38^o$.

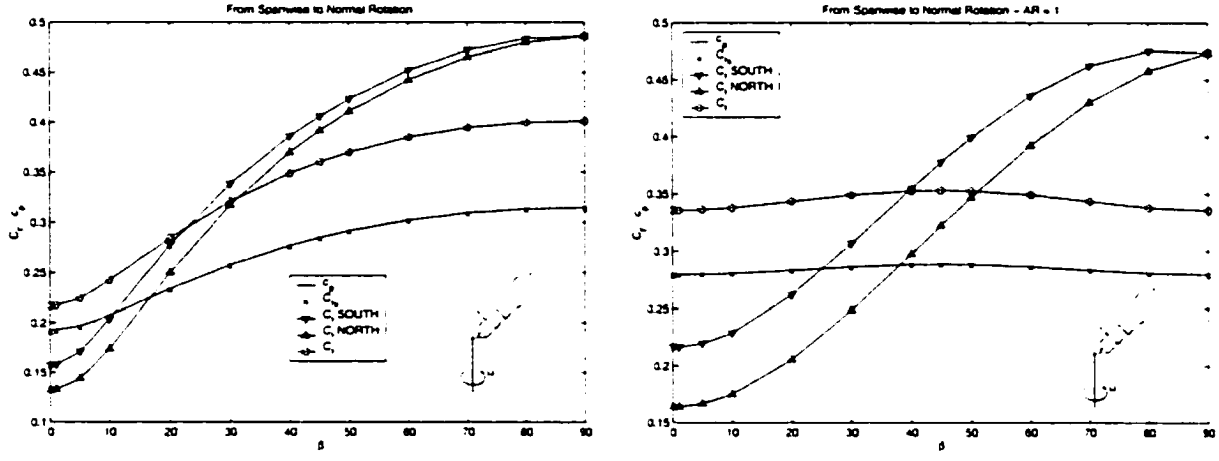

AR = 3 AR = 1

Figure 4.29: Pressure and friction coefficients as rotation is varied from streamwise to normal. Ro = 0.37

4.5 From Axial Flow to Radial Flow

Figure 4.30 depicts a rotating channel with the streamwise coordinate direction making an angle ψ with respect to the axis of rotation.

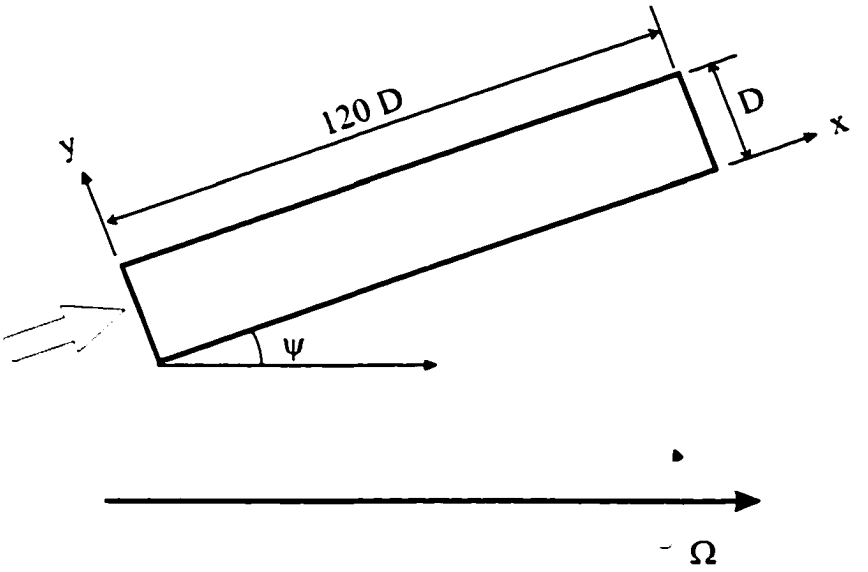

Figure 4.30: Streamwise channel rotation.

The Coriolis acceleration, which is responsible for the above secondary flows,

$$A_{Cor} = 2\Omega \times V = 2|\Omega||V| \sin \psi \tag{4.11}$$

is zero when ψ is zero, and a maximum when $\psi = 90^o$ (normal rotation). Since the Coriolis acceleration achieves 70 % of its maximal value when $\beta = 45^o$ it may be expected that the bulk of the benefits associated with the Coriolis acceleration will be realized at angles much less than $\psi = 90^o$. Since it is the $|V| \sin \psi$ term which contributes to the Coriolis acceleration, appropriate definitions of the Rossby and Ekman numbers are

$$Ro_\psi = \frac{Ro}{\sin\psi} = \frac{V_{av}}{\Omega D \sin\psi} \tag{4.12}$$

$$Ek_\psi = \frac{Ek}{\sin\psi} = \frac{\nu}{\Omega D^2 \sin\psi} \tag{4.13}$$

Simulations were carried out using the same grid as before, a rotational speed of $\Omega = 250$ rad/s and $(0 \leq \psi \leq 90^o)$. Table 4.4 summarizes the simulations carried out in this section.

ψ [^{o}]	Ro_ψ	$1/Ro_\psi$	Ek_ψ
1	20.91	0.0478	0.2091
5	4.19	0.2388	0.0419
10	2.10	0.4758	0.0210
20	1.07	0.9372	0.0107
30	0.73	1.3700	0.0073
45	0.52	1.9375	0.0052
60	0.42	1.3730	0.0042
90	0.37	2.7401	0.0037

Table 4.4: Calculated Rossby and Ekman numbers in the case of 'Streamwise to Normal' channel rotation.

Figure 4.31 depicts streamwise velocities and secondary streamlines for each of the simulations. When $\psi = 0^o$ there are no perceivable changes from the non-rotating case. Very slight increases in ψ, however, generate significant secondary velocities which radically alter the streamwise velocity profile. The trend evident in the velocity profiles is similar to the case of normal rotation, even at remarkably low angles: at low ψ the velocity maximum is shifted to the lagging (z = 1.5D) wall. As ψ is further increased, two local maxima adjacent to the y=0 and y=D sidewalls and the profiles become increasingly flatter with uniform flow covering an increasing area of

the channel. The basic secondary flow structure is established with $\psi = 1°$ with the magnitude of the secondary velocity increasing with increasing ψ and with the maxima approaching the y=0 and y=D walls.

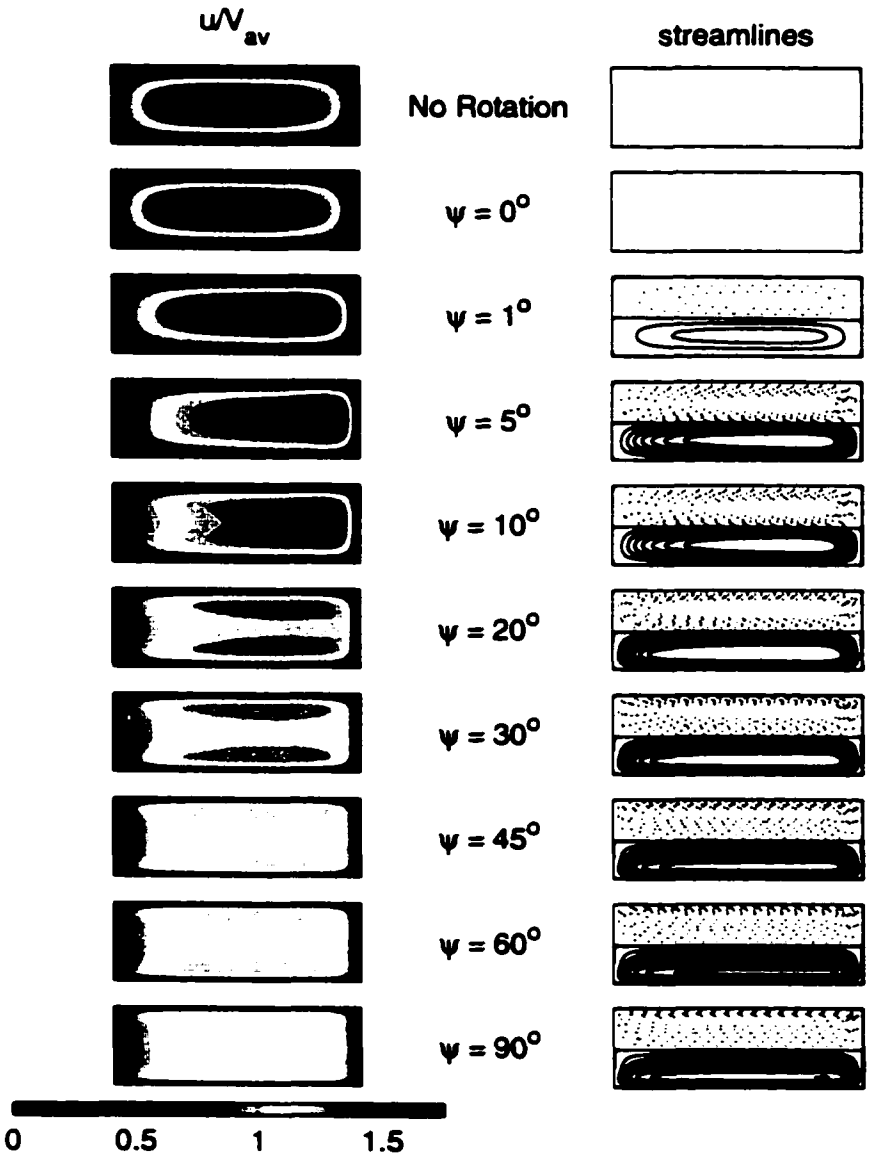

Figure 4.31: Contours of streamwise velocity and secondary streamlines for $0^0 < \psi < 90^o$.

Figure 4.32 plots the variation of friction coefficient around the perimeter in the fully developed region. This plot is very similar to the case of normal rotation with increasing ψ corresponding to increasing Ω. It is clear that increasing β at constant Ω has a very similar effect to increasing Ω in the case of normal rotation ($\beta = 90°$). In order to test this correspondence, two simulations ($\beta = 1°, 30°$) were carried out such that Ro_ψ matched Ro in the case of normal channel rotation presented above. Figure 4.33 compares the circumferential variation of friction coefficient for these two cases, and the agreement is perfect. Figure 4.34 plots the streamwise development of the spanwise average friction coefficient (C_f) for these two cases and shows that there is a slight difference in the flow development between normal rotation and angled channels. This difference however spans an increasingly small portion of the channel with decreasing Ro: at $\mathrm{Ro} = \mathrm{Ro}_\psi = 20.9$ the solutions differ only over the first 17 % of the channel and at $\mathrm{Ro} = \mathrm{Ro}_\psi = 0.73$ the solutions differ only over the first 2.5 % of the channel.

Figure 4.35 presents the averaged friction coefficients and pressure coefficients in the fully developed region as a function of ψ. This figure is qualitatively the same as the corresponding figure in the case of normal rotation (figure 4.14) and based on the above discussion these two curves would be identical were this one plotted versus Ro_ψ instead of ψ.

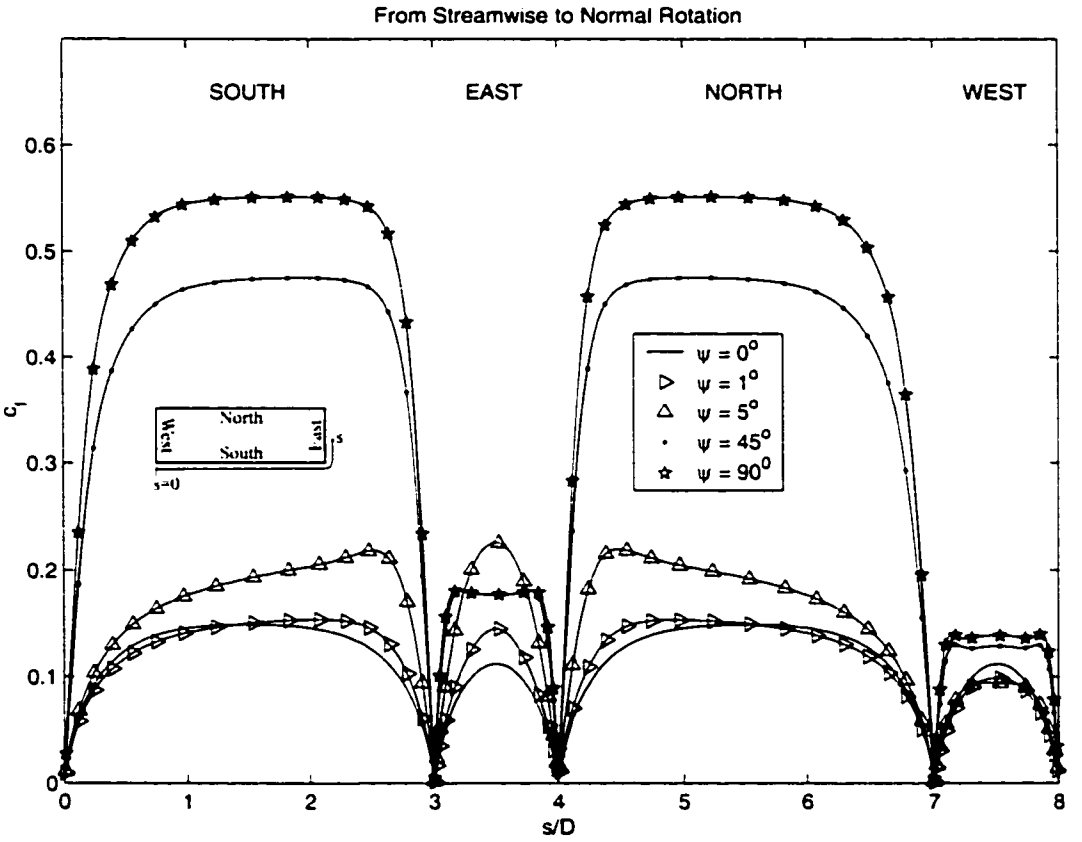

Figure 4.32: Variation of friction coefficient in the fully developed region for various ψ

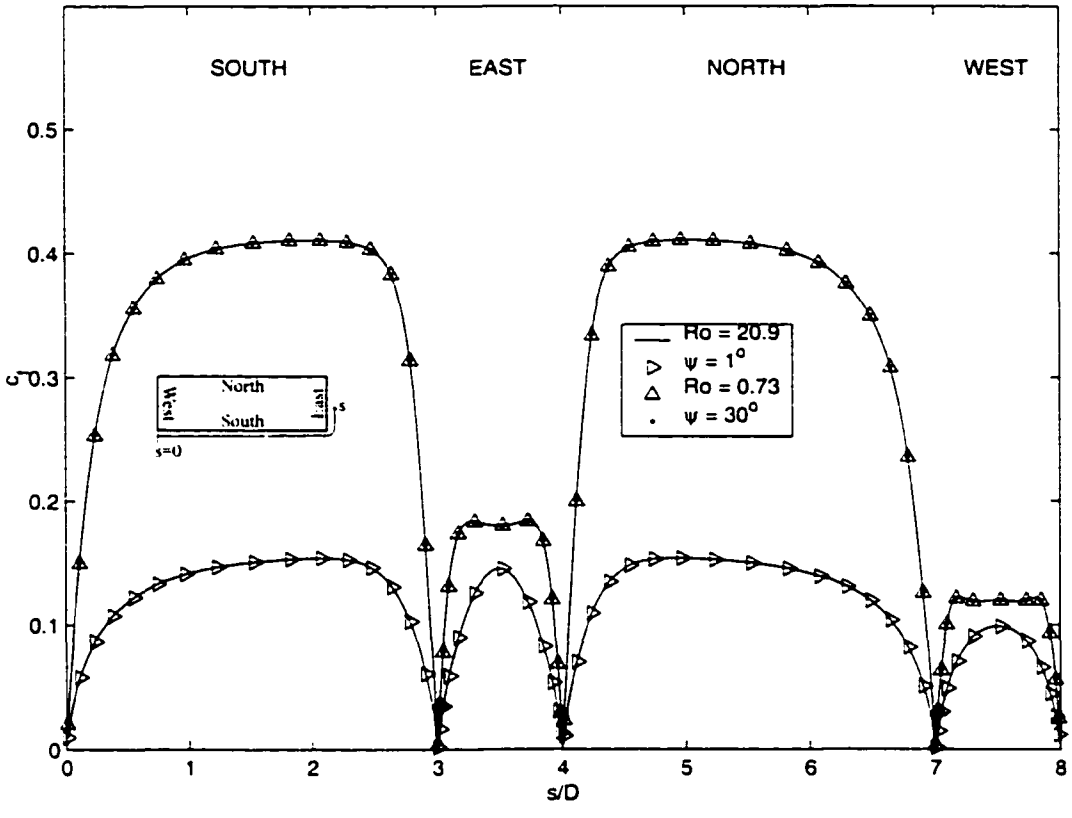

Figure 4.33: Comparison of the friction coefficient with Ro_ψ corresponding to Ro in the case of normal rotation.

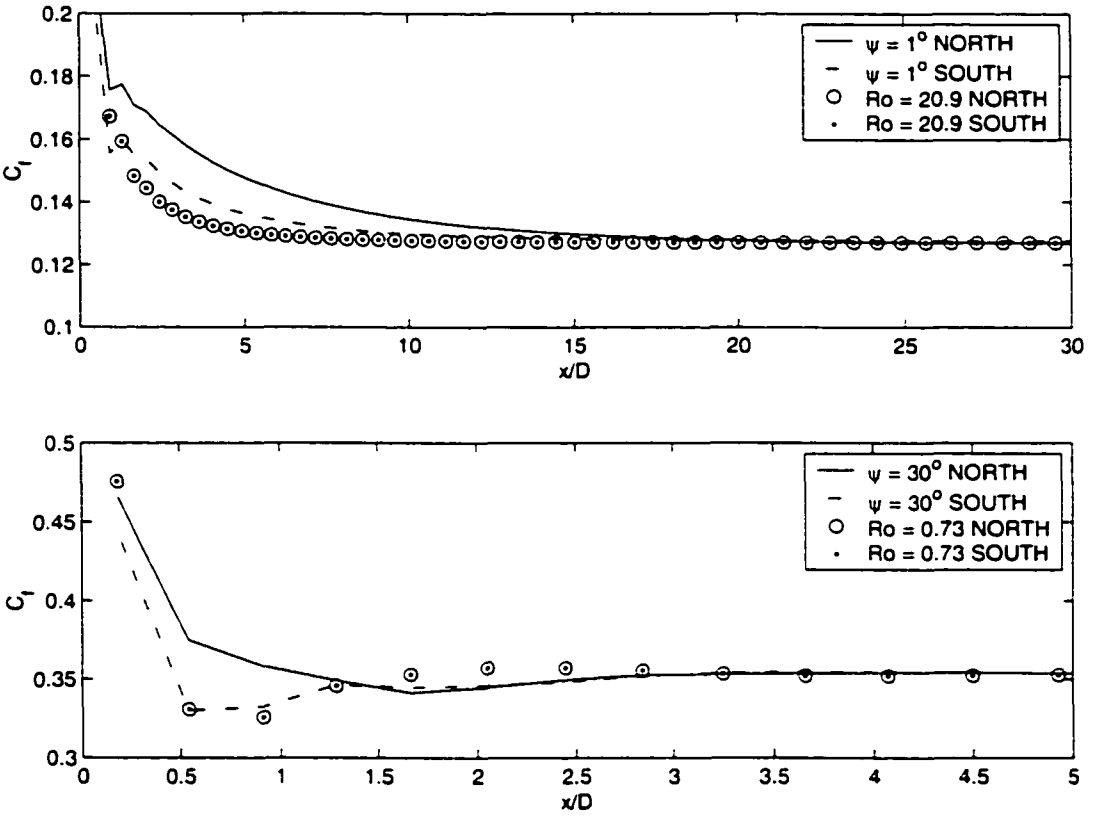

Figure 4.34: Comparison of the streamwise development of friction coefficient with Ro_ψ corresponding to Ro in the case of normal rotation.

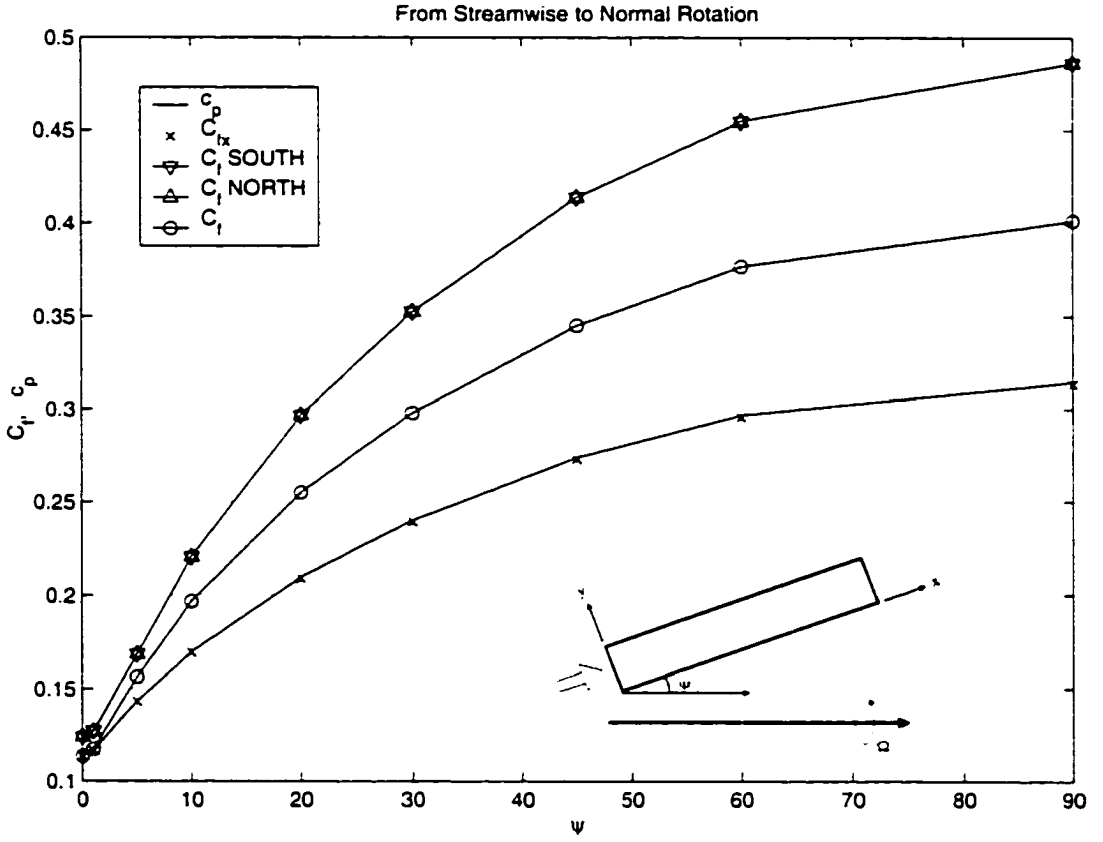

Figure 4.35: Pressure and friction coefficients in the fully developed region in the case of 'streamwise to normal' rotation.

4.6 Mass Transfer

The source term model was used to simulate mass transfer for all cases presented in the previous section. Since the source term model decouples the mass transfer from the hydrodynamics, it was possible to carry out several mass transfer solutions for each case. Membrane was assumed to be on both the y=0 and y=D surfaces, and in most cases, mass transfer simulations were performed for NaCl feed solutions of both 35,000 ppm and 50,000 ppm, at four different transmembrane pressures: 400, 600, 800 and 1000 psi. The membrane permeability, L_p, was set to 1.96×10^{-12} m/(Pa s), and the osmotic back pressure, $\Delta\pi$ was calculated using the membrane surface concentration and the empirical correlation presented in [3], assuming a constant solution temperature of $25°C$.

While the effect of the wall permeation is assumed negligible on the hydrodynamics solution, the transpiration velocity at each point on the membrane can be calculated, and used to indicate membrane performance. Figure 4.36 presents Re_w calculated using the average transpiration velocity over both membrane surfaces in the cases of spanwise, normal and 'streamwise to normal' channel rotation. The first thing to note is that in all cases, Re_w is more than five orders of magnitude less than the bulk flow Reynolds number ($Re_D = 100$). In these cases the inlet flow area is three orders of magnitude smaller than the membrane area so that the mass flow through the membrane is at least two orders of magnitude smaller than the inlet mass flow.

At the lowest transmembrane pressure and feed concentration, polarization is not a limiting factor and there is very little change as rotation is increased. As either concentration or transmembrane pressure is increased, however, concentration polarization becomes significant, and there is a significant increase in Re_w, i.e. permeate flux, as rotation is increased, with normal rotation outperforming spanwise rotation

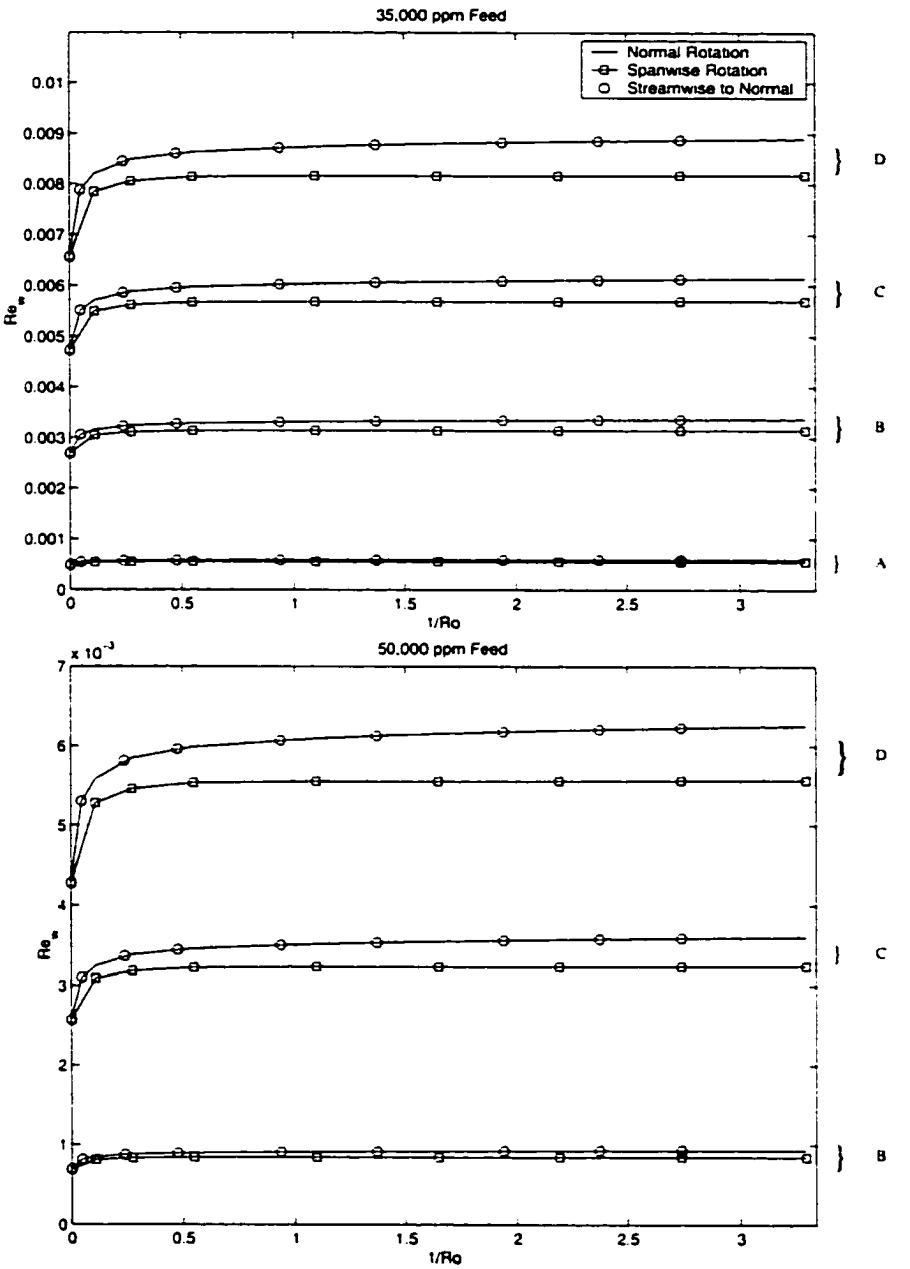

Figure 4.36: Average wall Reynolds number (Re_w), as a function of rotation, determined with the source term model in the cases of: normal rotation, spanwise. rotation and 'streamwise to normal' ($0^o < w < 90^o$) rotation. A: $P_{TM} = 400$ psi. B: $P_{TM} = 600$ psi, C: $P_{TM} = 600$ psi, D: $P_{TM} = 1000$ psi

in all cases. In the case of 'streamwise to normal' rotation, where Ro_ψ is used in place of Ro, the mass transfer rates are identical to the the case of normal rotation, as was the case for the flow field.

Figure 4.37 depicts contours of NaCl concentration at various planes along the channel, in the absence of channel rotation, for a feed concentration of 35,000 ppm and P_{TM} = 1000 psi. Active membrane surfaces are located on the top (NORTH) and bottom (SOUTH) of each frame. The figure shows the development of concentration boundary layers which are thicker in the corners, and which grow with distance from the inlet.

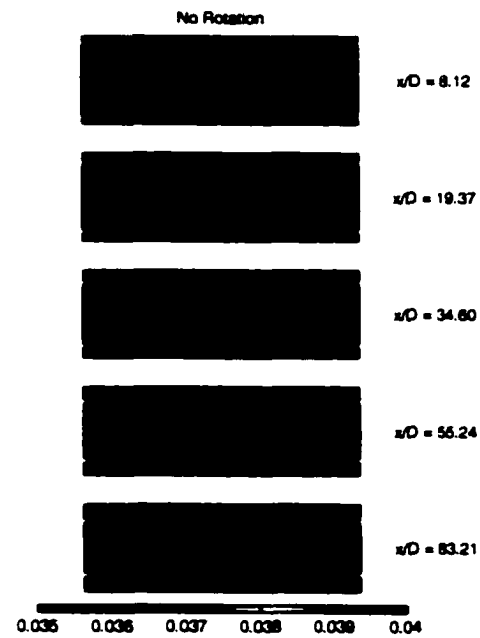

Figure 4.37: Developing contours of NaCl concentration in the absence of channel rotation. P_{TM} = 1000 psi. Active membrane surfaces are located on the top (NORTH) and bottom (SOUTH) of each frame.

Figures 4.38 and 4.39 present NaCl contours on the same planes using the same contour levels but in the cases of normal and spanwise rotation at Ro = 0.37 for aspect ratios of 3 and 1 respectively. Spanwise and normal rotation are very similar

in that the highest concentration occurs at the centre of the leading channel wall with high NaCl concentration fluid convected from this region along the channel centreline perpendicular to the axis of rotation until it meets the opposite wall. This occurs in both orientations at $x \approx 55D$ for the higher aspect ratio channels, and at $x \approx 20D$ for square channel. In the case of normal rotation the leading wall is not a membrane surface so that this maximum will not directly affect membrane performance.

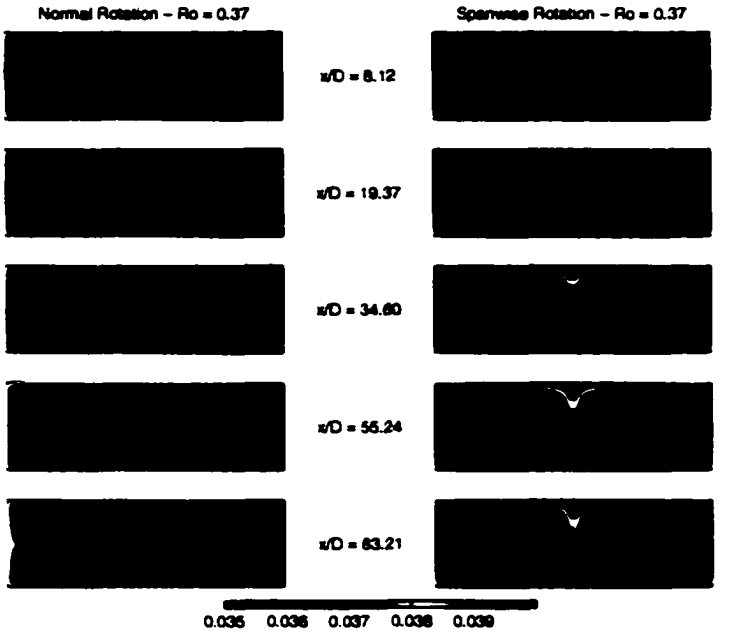

Figure 4.38: Developing contours of NaCl concentration in the cases of normal and spanwise channel rotation. P_{TM} = 1000 psi.

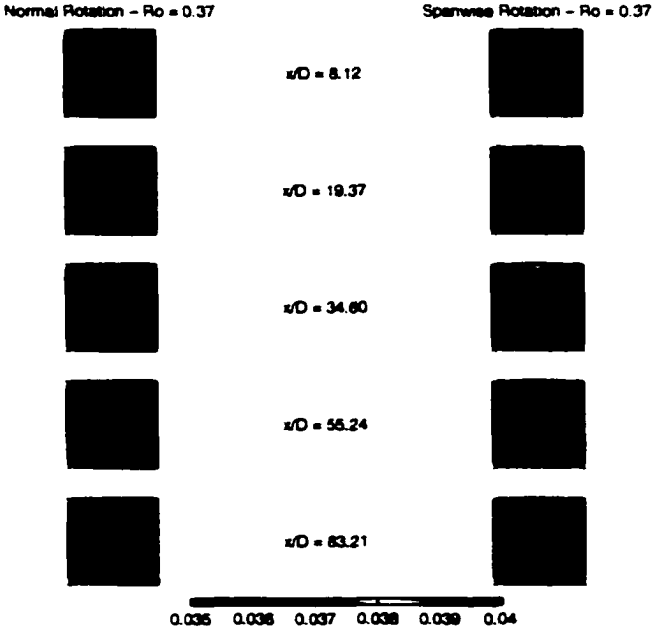

Figure 4.39: Developing contours of NaCl concentration in the cases of normal and spanwise channel rotation. AR=1. P_{TM} = 1000 psi.

Figure 4.40 plots the surface NaCl contours over the entire NORTH and SOUTH membrane faces for the rectangular channels in the cases of no rotation, normal rotation, spanwise rotation and $\beta = 5^o$. In the absence of channel rotation the surface concentration builds steadily and rapidly, is symmetric about z/D = 0 and is identical on the NORTH and SOUTH faces. For this case the concentration is highest at the channel corners at a given streamwise location. Under normal rotation the concentration distributions are also identical on the NORTH and SOUTH faces. Overall, this case exhibits the lowest concentrations. The concentration is lowest near the lagging sidewall and builds to a maximum at the leading sidewall. In the case

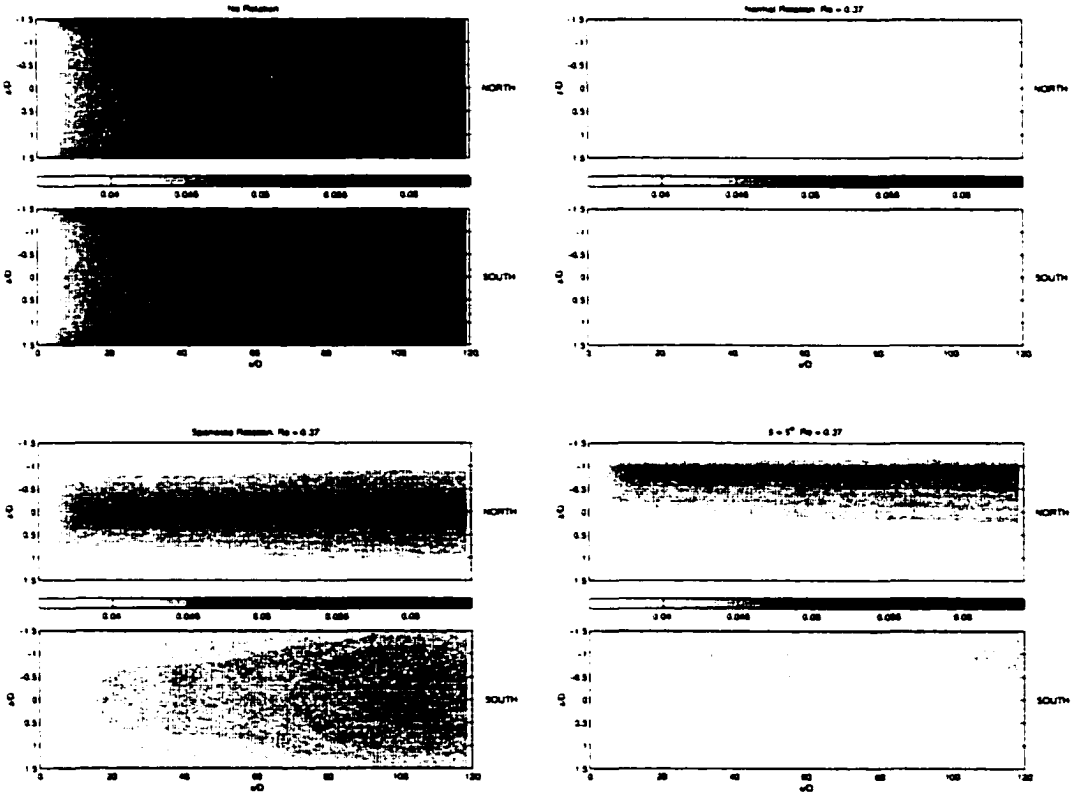

Figure 4.40: Surface NaCl concentration on the NORTH and SOUTH faces for various cases.

of spanwise rotation, the contours are again symmetric about z/D = 0 but differ on the NORTH and SOUTH faces. The maximum concentration in this case is on the NORTH face along z/D = 0 and it drops considerably to a minimum at the sidewalls. The concentration on the SOUTH face shows less variation, but increases along z/D = 0 are evident as the secondary motions carry salt from the NORTH face to the SOUTH face. Slight changes in orientation from spanwise result in significant changes in the concentration distributions. When $\beta = 5^o$ the maximum on the NORTH face shifts to z = -1D and is not as pronounced. The concentration on the SOUTH face is generally lower and is already beginning to resemble the distribution present under normal rotation.

Figure 4.41 presents spanwise averages of the surface salt concentration over the entire membrane area (both the NORTH and SOUTH faces) in the cases of no rotation, spanwise rotation and normal rotation. Irrespective of orientations the square channels outperform the rectangular channels. The largest difference occurs in the case of spanwise rotation and the smallest difference is when the channels are not rotating. Also, irrespective of aspect ratio the channels undergoing normal rotation outperform those undergoing spanwise rotation. In all rotating cases, the concentration first increases at a rate similar to the non-rotating case, flattens and then increases slightly as NaCl is convected along the channel centreline perpendicular to the axis of rotation. As noted above, this occurs at $x \approx 20D$ in the square channels and at $x \approx 55D$ in the case of rectangular channels.

Figure 4.42 depicts the spanwise averaged surface concentrations over the NORTH and SOUTH faces in the cases of normal and spanwise rotation for various Ro at feed concentrations of 35,000 and 50,000 ppm. It is clear in all cases that as rotation increases the average surface concentration decreases. Mild rotations (Ro = 20.91) result in a dramatic decrease in surface concentration which is similar in both orien-

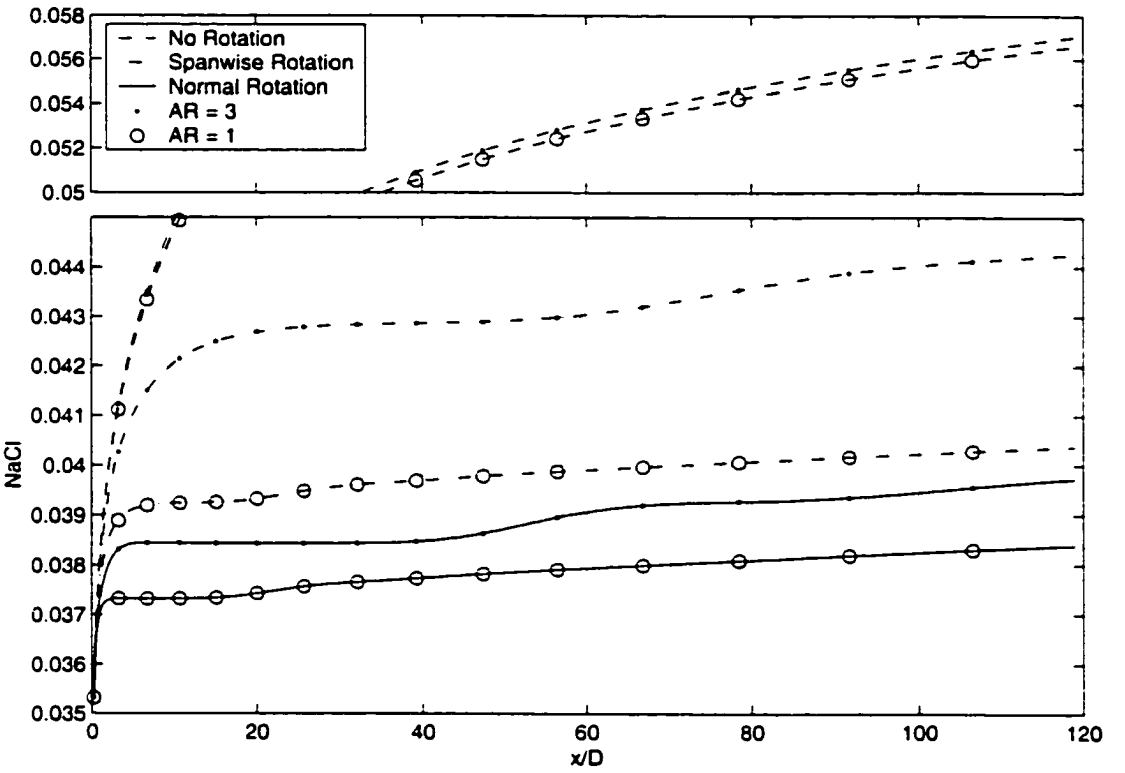

Figure 4.41: Spanwise averaged surface concentration over the NORTH and SOUTH faces: the effects of orientation and aspect ratio. P_{TM} = 1000 psi. Ro = 0.37

tations. Further increases in rotation (decreases in Ro) result in further decreases in concentration, but to a significantly larger degree in the case of normal rotation. It is expected, and will be shown below, that in the case of variations in β the surface concentrations will be bounded by these curves.

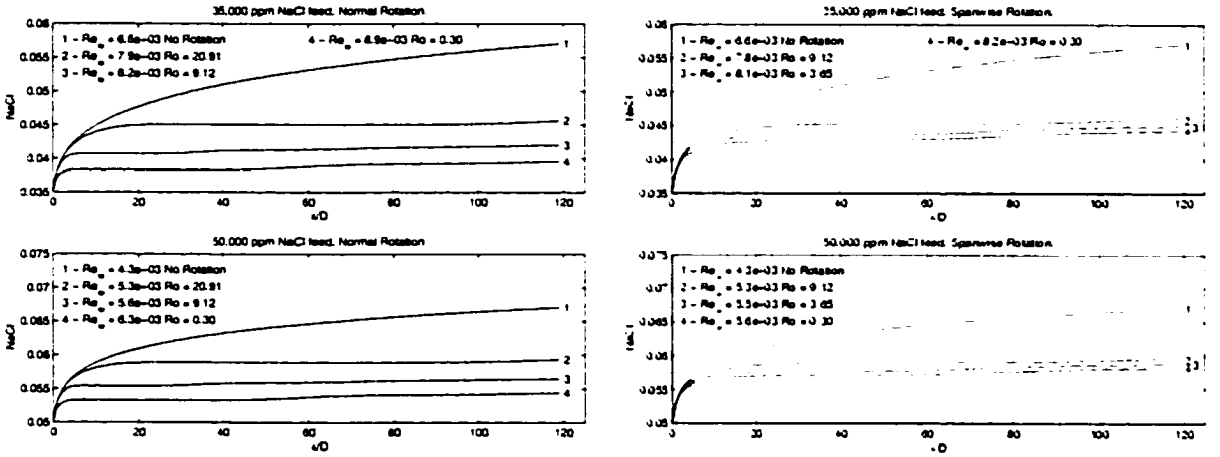

Figure 4.42: Spanwise averaged surface concentration over the NORTH and SOUTH faces. P_{TM} = 1000 psi.

Figure 4.43 shows the developing contours of NaCl as rotation is varied from almost spanwise to almost normal. The concentration on the NORTH surface is significantly altered with variations in β. As the concentration maximum moves from z/D = 0 towards the z/D = -1.5 corner. At $\beta = 80^o$ this maximum occurs on the WEST face (z/D = -1.5D) and impacts only a very small percentage of the membrane area.

The wall Reynolds number, Re_w is directly proportional to the average flux through all membrane surfaces and can therefor be used to determine the flux improvement for each case relative to the non-rotating case.

$$\text{Flux Increase} = \frac{Re_w - (Re_w)_{\text{no rotation}}}{(Re_w)_{\text{no rotation}}} \times 100\% \tag{4.14}$$

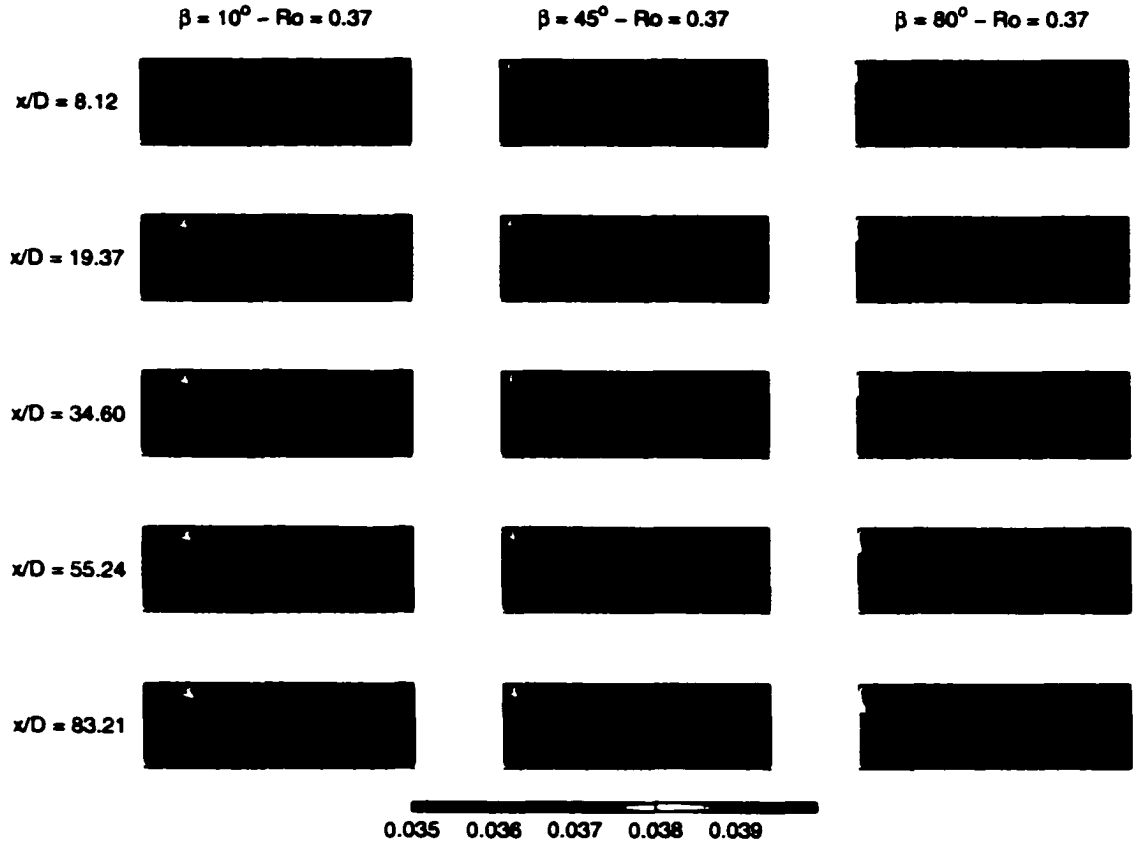

Figure 4.43: Developing contours of NaCl concentration for cases in between normal and spanwise rotation. P_{TM} = 1000 psi.

where (Re_w)$_{\text{no rotation}}$ is evaluated at the same feed concentration as Re_w. In addition, the trans-membrane pressure, P_{TM} can be non-dimensionalized using the excess pressure, P_e

$$P_e = \frac{P_{TM} - \Pi}{\Pi} \tag{4.15}$$

where the osmotic pressure, Π is evaluated at the feed concentration.

Figures 4.44 and 4.45 show the flux improvement in rectangular channels with increasing rotation (1/Ro) for feed concentrations of 35,000 and 50,000 ppm NaCl at various P_e. In all cases the flux improvement rises rapidly with decreasing Ro and

asymptotically approaches a maximal value. In the case of spanwise rotation, the maximal improvement is practically attained by 1/Ro = 0.55 while in the case of normal rotation there are additional but increasingly minor improvements over the entire curve. Flux improvement increases with increasing P_e and with increasing feed concentration and is consistently higher in the case of normal rotation. The maximum improvement under normal rotation is 46.4 % while the maximum improvement under spanwise rotation is 30.25 %.

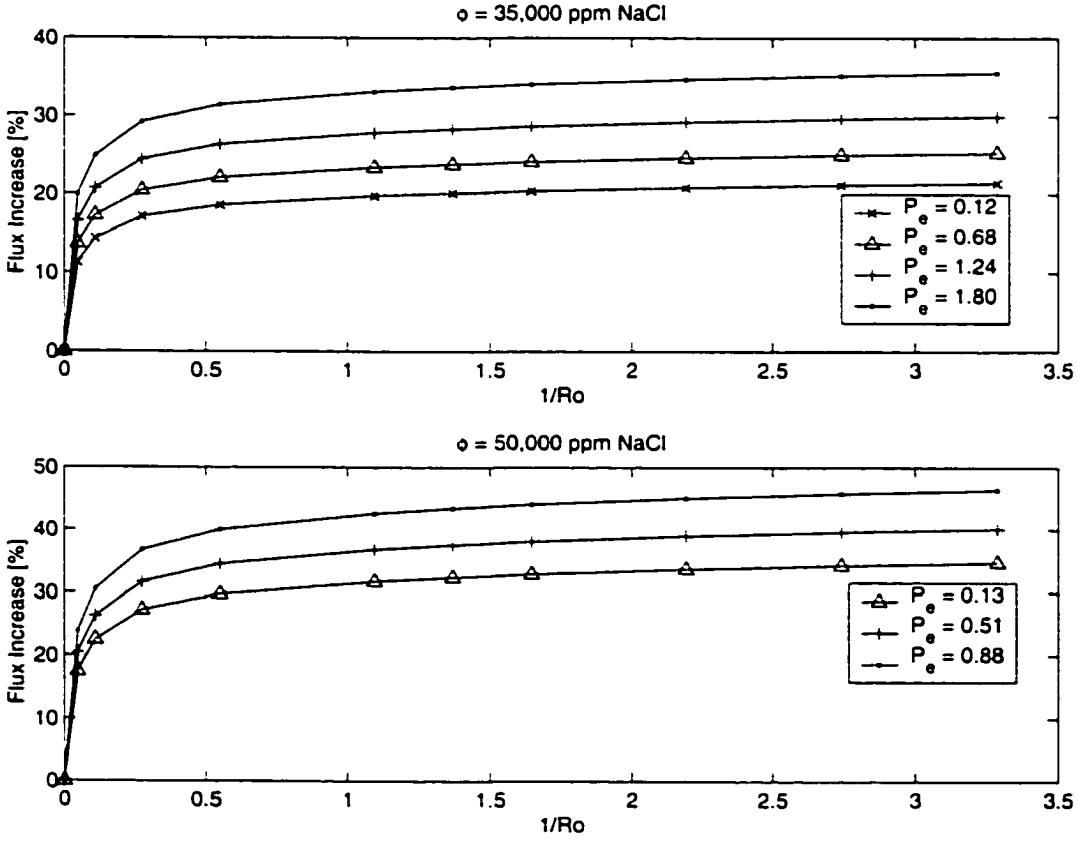

Figure 4.44: Total flux improvement over the non-rotating case for various Ro. Normal Rotation. Aspect Ratio = 3.

Figure 4.46 shows the flux improvement as rotation is varied from streamwise to spanwise for the same feed concentrations at Ro = 0.37 and P_e = 1.80. The maxi-

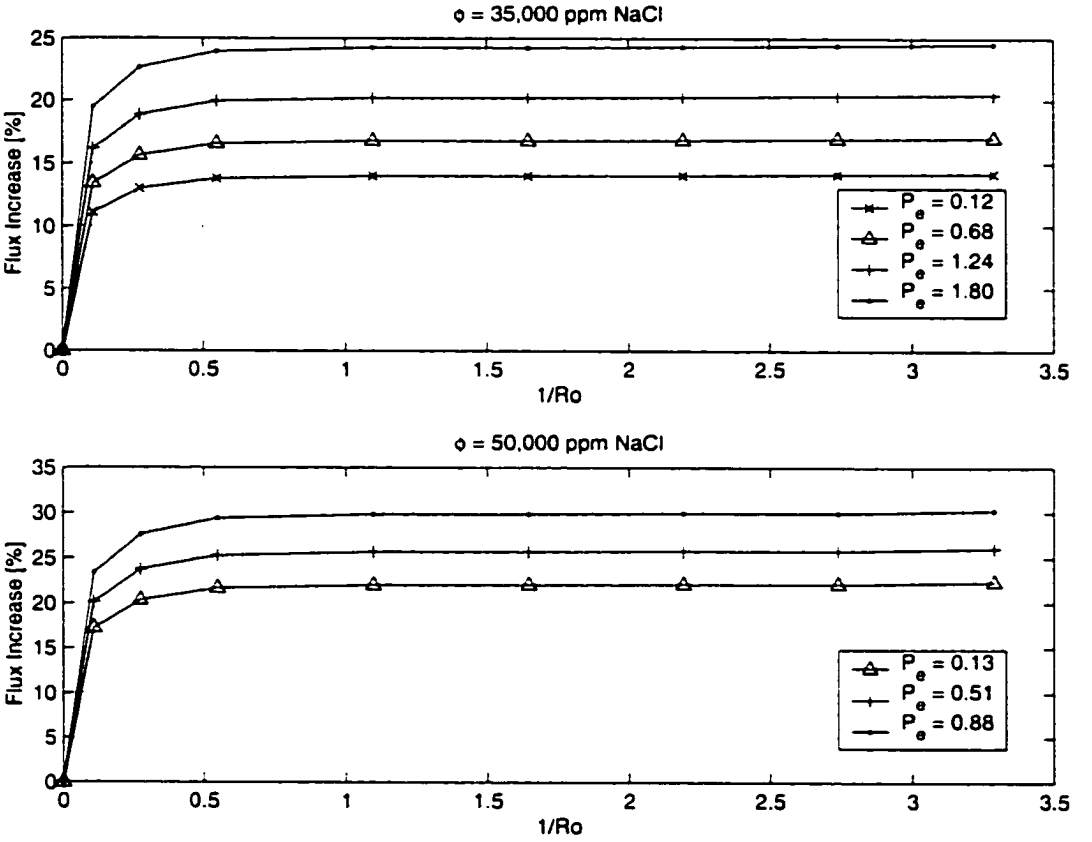

Figure 4.45: Flux improvement over the non-rotating case for various Ro. Spanwise Rotation. Aspect Ratio = 3.

mum improvement is $\approx$ 48% and occurs at the highest feed concentration undergoing normal rotation. At both feed concentrations, the square channels significantly outperform the rectangular channels at low β. This difference decreases such that for $\beta < 25^o$ the difference is a nearly constant 1 % for a 35,000 ppm feed and 2.5 % for a 50,000 ppm feed.

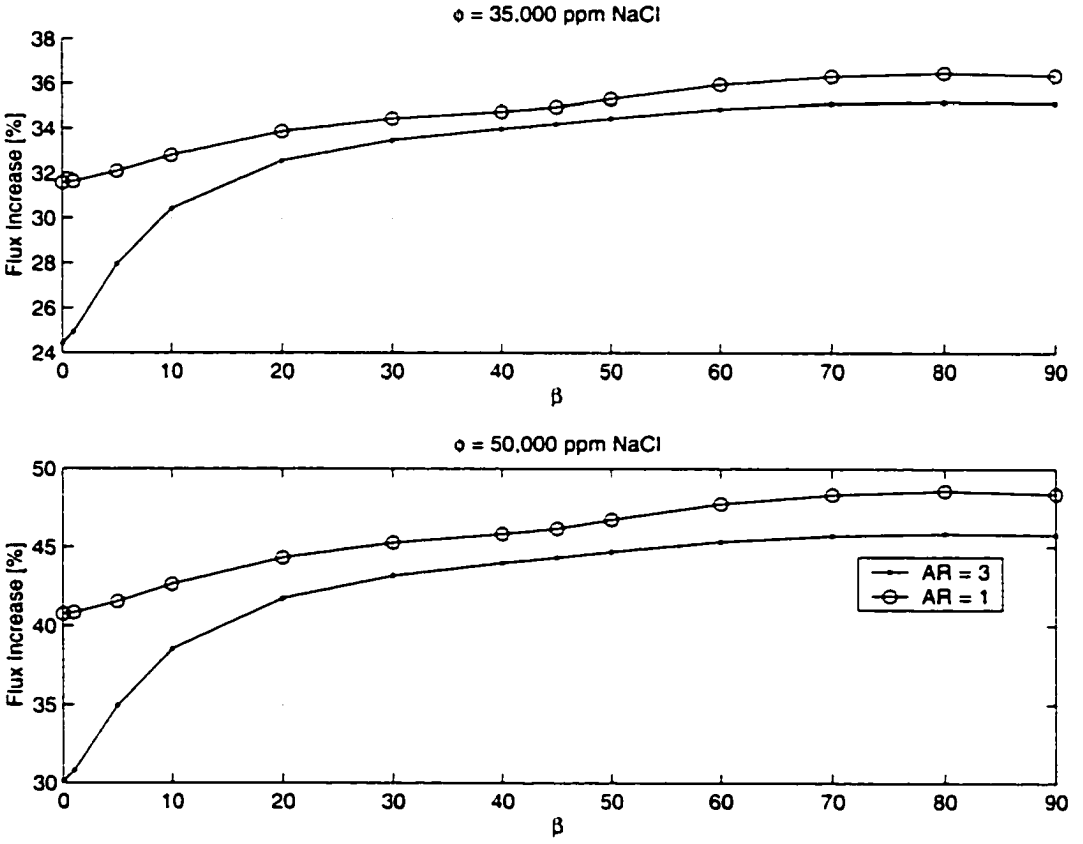

Figure 4.46: Flux improvement over the non-rotating case for Ro = 0.37 as rotation is varied from spanwise to normal. P_e = 1.80

4.7 Closure

This chapter has provided insight into the flow and mass transfer in rotating rectangular and square channels. The STM was used to model reverse osmosis desalination processes in these channels. In particular, the effects of channel orientation, rotation rate, feed concentration and excess pressure are investigated. It is found that all rotating cases having non-zero Coriolis acceleration feature secondary flows which develop at relatively low rotation rates (Coriolis magnitude) and which strengthen with increasing rotation. These secondary flow patterns have a significant impact on the shear and on the mass transfer processes in the channels. The amount of permeate passing through a reverse osmosis membrane is strongly dependent on the surface concentration, and the secondary motions result in significant additional mixing with correspondingly lower surface concentrations.

It is again shown that the membrane performance does not generally correlate with shear. This is perhaps most evident in the case of spanwise rotation where high shear occurs on the walls which do not have membrane on them. The shear on the membrane faces increases only slightly and yet performance increases up to 30 % have been shown. This issue will be revisited in Chapter 7.

By comparing cases of normal rotation to corresponding inclined (from streamwise to normal rotation) channel cases, it is shown that when the geometry is the same the magnitude of the Coriolis acceleration correlates identically with the fully developed solution. Slight variations are evident though in the developing region. It is also shown that varying the geometry with respect to the axis of rotation, either by changing the aspect ratio or by changing the rotation mode, has a significant impact on the secondary flows. With respect to desalination performance, we conclude that

- Normal rotation is preferable to spanwise rotation.

- Deviations from spanwise rotation as small as 20° are adequate to achieve most of normal rotation performance.
- Square channels are preferable to rectangular channels, especially in the case of spanwise rotation.
- Relative performance improves with both increasing feed concentration and with increasing trans-membrane pressure.

Chapter 5

Rotating Non-Rectangular Channels

5.1 Motivation

Channels with differing cross sectional shapes are common in membrane separation. Both hollow fiber and tubular membranes involve circular channels, and spiral wound modules have varying channel sections depending on the geometry of the feed spacer. For instance, a recent experimental study reported by Schwinge *et. al* [38] focused on a corrugated spacer with bends. This particular spacer was made up of a doubly corrugated sheet which formed triangular zig-zag channels when placed on a membrane surface. It is entirely conceivable that a singly corrugated spacer, resulting in straight triangular flow paths could be used to manufacture a spiral wound membrane element. This configuration would have all the packaging benefits of a conventional spiral wound element, but would also provide open triangular channels.

This Chapter presents an investigation of the flow and mass transfer in triangu-

lar and circular channels undergoing normal rotation with a view to assessing their performance in CMS applications.

5.2 Relevant Previous Studies

Non-rotating circular and triangular channels have been previously investigated both in terms of hydrodynamics and in terms of heat transfer. A good compilation of the results in given in [39]. Dutta [40, 41] experimentally investigated the turbulent flow and heat transfer in rotating right triangular channels. Lei [42] computationally studied the developed laminar flow in rotating circular channels, and presented a review of similar studies to that date. Several researchers have also investigated turbulent flow in rotating pipes but none of the previous works are directly applicable to this study, since the flow in a CMS device is laminar and the effect of developing flow on the mass transfer performance is of interest.

5.3 Triangular Channels

This section investigates simultaneously developing flow and mass transfer in the equilateral triangle channel shown in figure 5.1. The simulated channels have a sidelength D=1.0 mm and are 50D long.

A three block grid, shown in figure 5.2 was used to model the hydrodynamics and mass transfer in these channels. Each block extends from a corner to the midpoint of two sides and to the centroid of the distribution, along the symmetry planes of the triangle. The blocks were [50x31x31] and used non-uniform grids with $0.364 < \delta x/D < 2.18$,$0.0038 < \delta y/D < 0.029$, $0.0033 < \delta z/D < 0.033$.

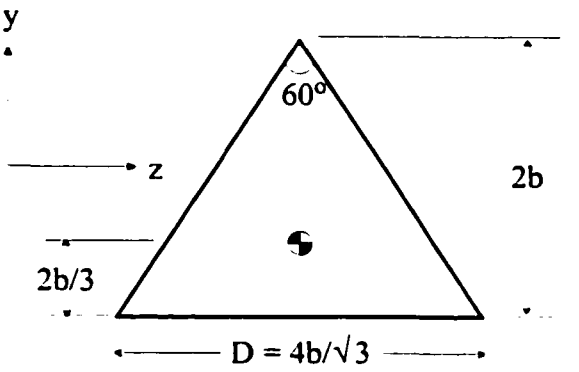

Figure 5.1: Cross section of equilateral triangle duct. Coordinate system is as shown, with the origin at the centroid.

5.3.1 Hydrodynamics

Simulations were carried out at $Re_{D_h} = 100$, where the hydraulic diameter $D_h = D/\sqrt{3}$, for the range of parameters shown in table 5.1. In all cases, rotation is about the y-axis.

Ω [rad/s]	Ro	1/Ro	Ek
0	∞	0	∞
10	27.37	0.0365	0.2737
50	5.47	0.1827	0.0547
100	2.74	0.3653	0.0274
150	1.82	0.5480	0.0182
200	1.37	0.7307	0.0137
250	1.09	0.9134	0.0109
300	0.91	1.0960	0.0091
350	0.78	1.2787	0.0078
400	0.68	1.4614	0.0068

Table 5.1: Rotational cases simulated and the corresponding Rossby and Ekman numbers.

Figure 5.3 compares the streamwise velocity in a channel with no rotation with

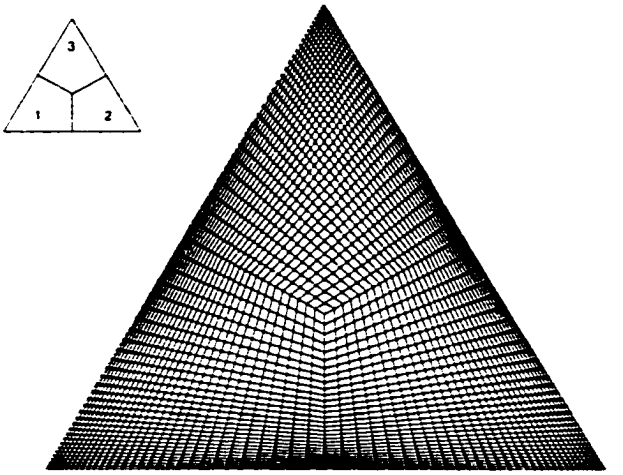

Figure 5.2: Grid used to simulate flow in equilateral triangular channels.

the analytic solution for fully developed flow given by [39].

$$u = \frac{U}{V_{av}} = \frac{15}{8}\left[\left(\frac{y}{b}\right)^3 - 3\left(\frac{y}{b}\right)\left(\frac{z}{b}\right)^2 - 2\left(\frac{y}{b}\right)^2 - 2\left(\frac{z}{b}\right)^2 + \frac{32}{27}\right] \tag{5.1}$$

The maximum difference occurs near the wall, but is everywhere less than 1%, suggesting that the flow is adequately resolved with this grid.

Relief plots of the fully developed streamwise velocity are shown in figure 5.4 for four different cases. When there is no channel rotation ($Ro = \infty$) there is a pronounced maximum occurring at the channel centroid. When rotation is introduced the maximum becomes less pronounced and shifts towards the lagging corner ($Ro =$ 5.47) and, as rotation is increased, a concave region appears on the leading side of the profile ($Ro = 2.74$). Further increases in rotation result in a further flattening of the profile and the growth of the concave region to the extent that two local maxima develop ($Ro = 0.68$): one near the top corner and one adjacent to the y=0 plane slightly closer to the lagging corner. The maximum streamwise velocity is plotted against 1/Ro in figure 5.5. The different flow regimes are also evident in figures

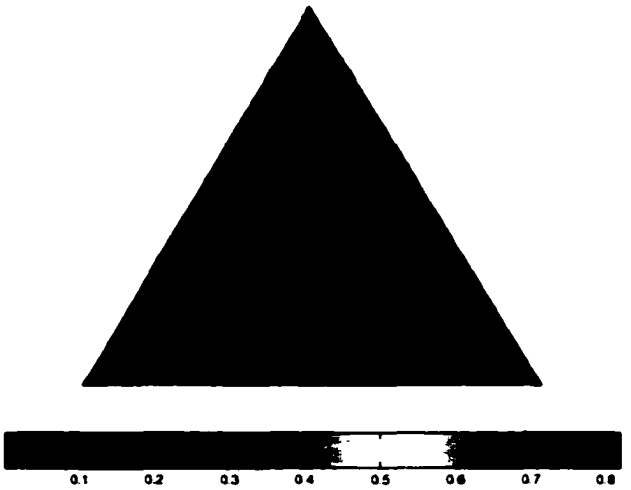

Figure 5.3: Percentage difference between analytic solution and simulation results (no rotation).

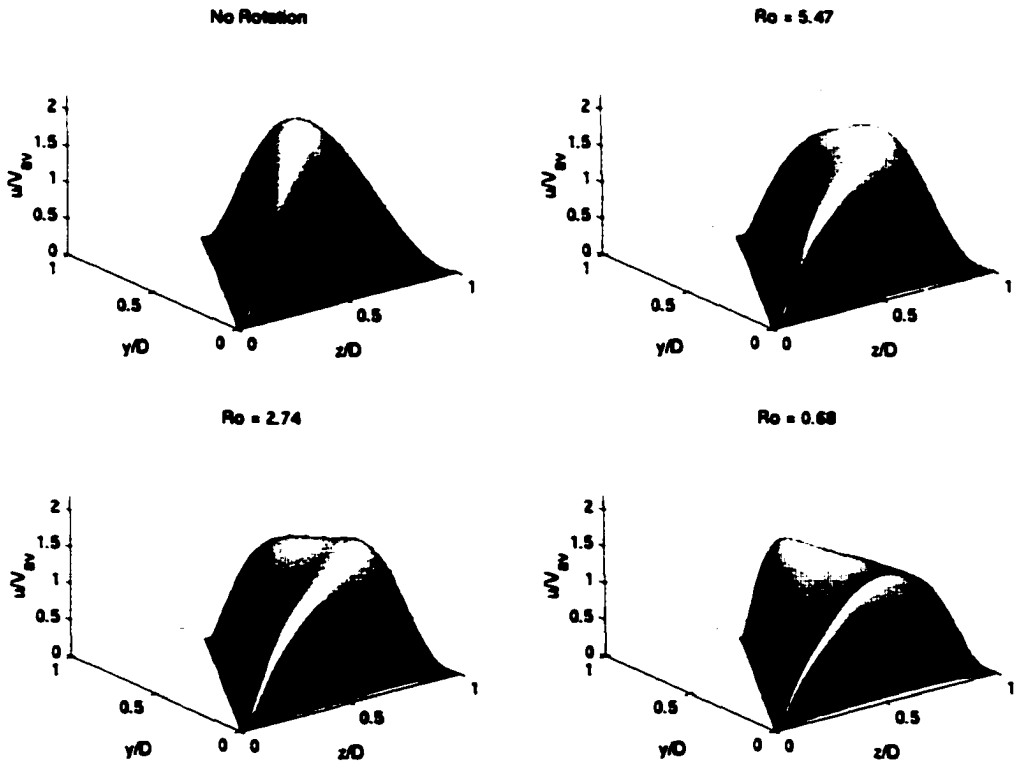

Figure 5.4: Relief plot of streamwise velocity for various rotational speeds.

5.6 and 5.7 which show contours of both streamwise and secondary velocity for all cases. The flattening of the streamwise profiles is clear and results in a nearly inviscid core such that flow is almost geostrophic (Coriolis balanced by pressure). Secondary velocities develop as soon as rotation is introduced and strengthen as rotation is increased.

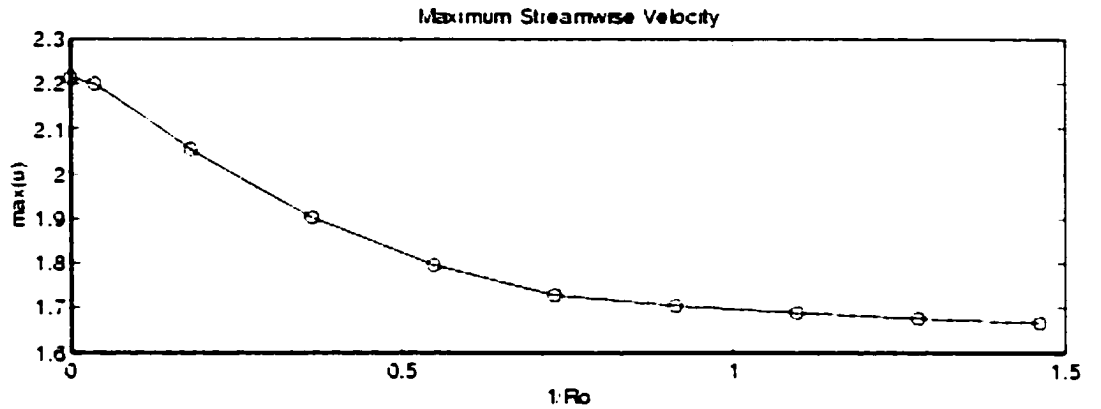

Figure 5.5: Maximum streamwise velocity as a function of 1/Ro.

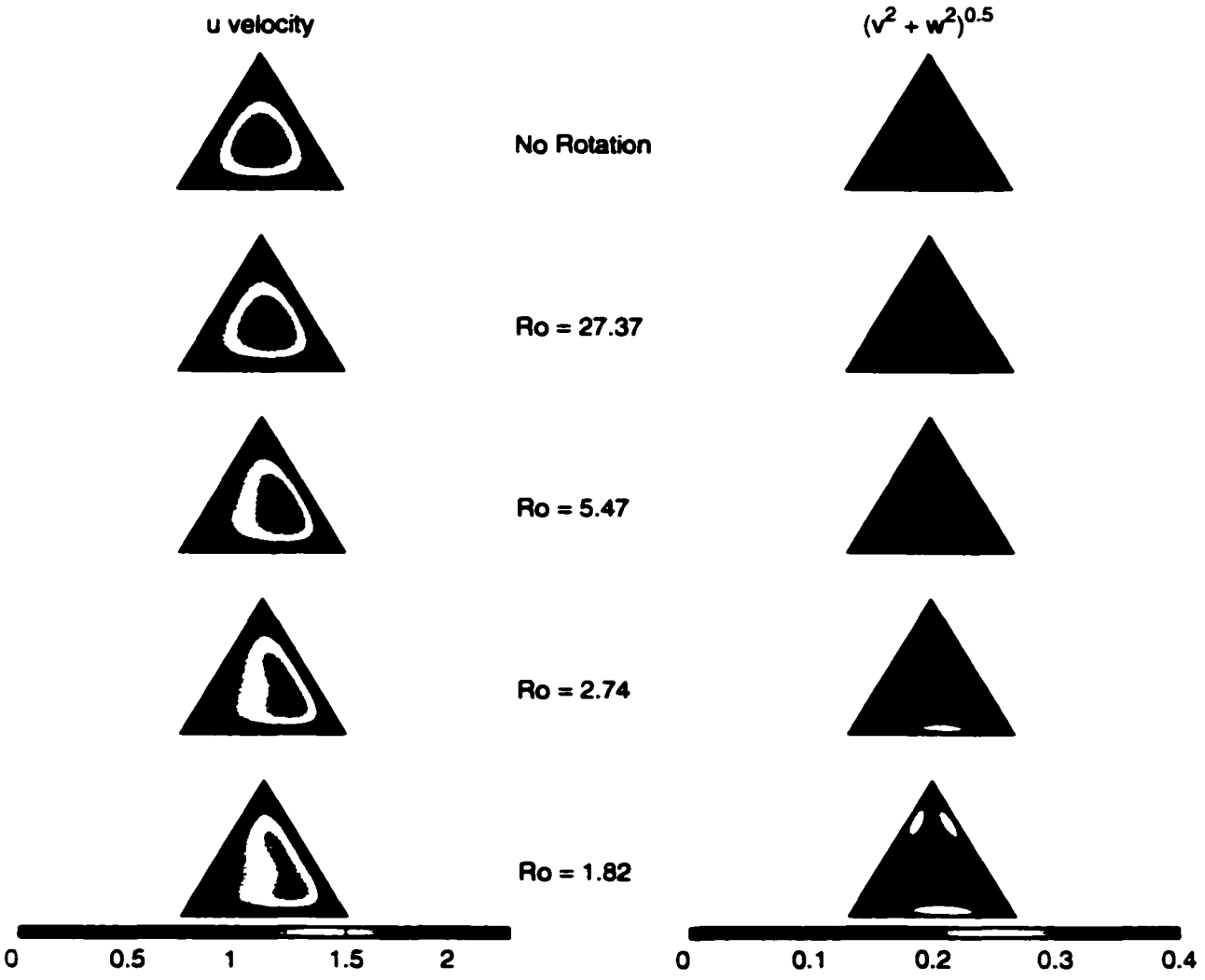

Figure 5.6: Contours of streamwise and secondary velocity for $1.82 < Ro < \infty$.

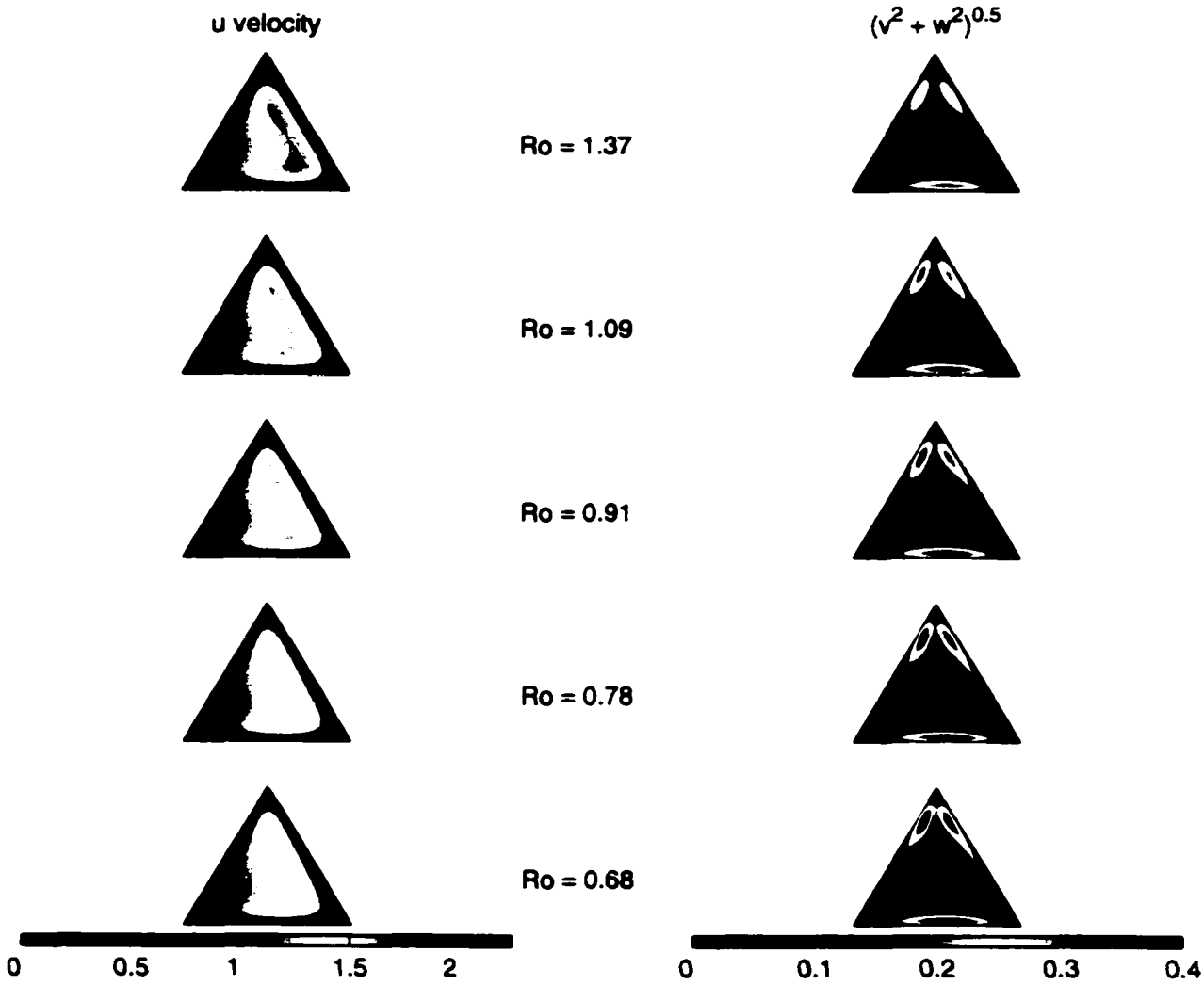

Figure 5.7: Contours of streamwise and secondary velocity for $0.68 < Ro < 1.37$.

Figure 5.8 presents typical secondary velocity vectors in the fully developed region. The secondary flow in the core (near the centroid) is directed from the leading channel corner, through the centroid and towards the lagging corner where it returns towards the leading wall in two jets: one passing through the top corner, and one parallel to the y=0 surface. The spanwise velocity in this second jet is shown in figure 5.9 for various rotating cases. This plot is remarkably similar to that in a rectangular channel. As rotation increases, the jet becomes stronger and approaches the y=0 wall, with a maximum value of over 36% of the bulk velocity.

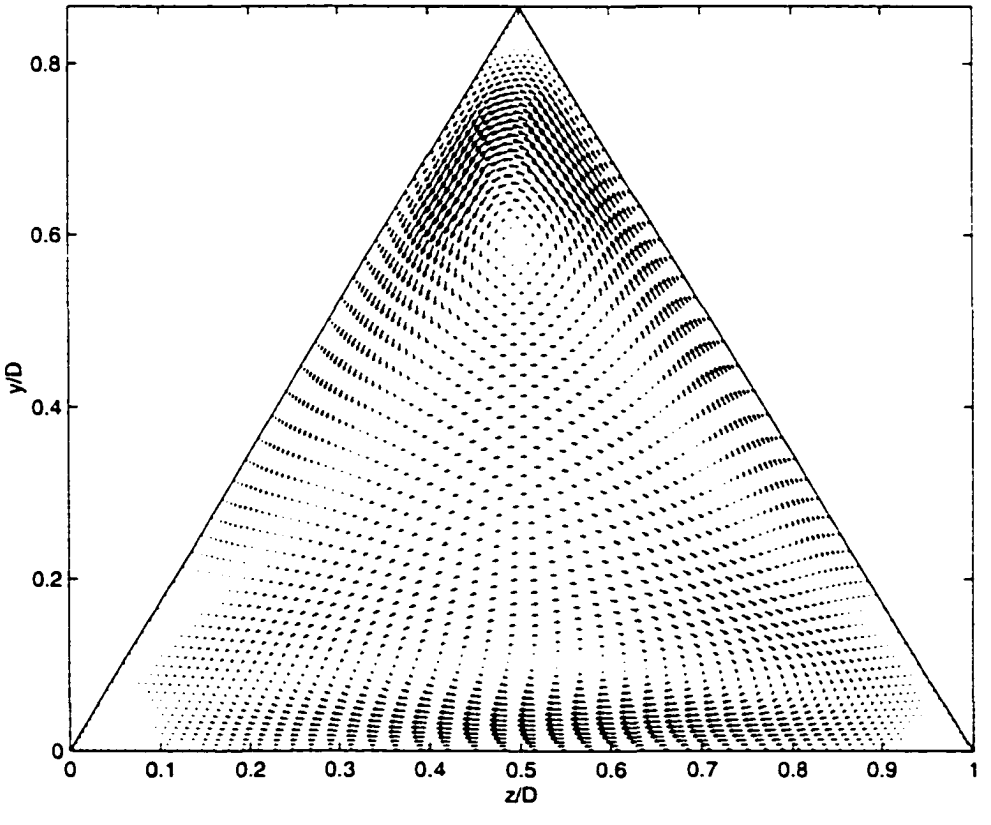

Figure 5.8: Typical fully developed secondary velocity vectors.

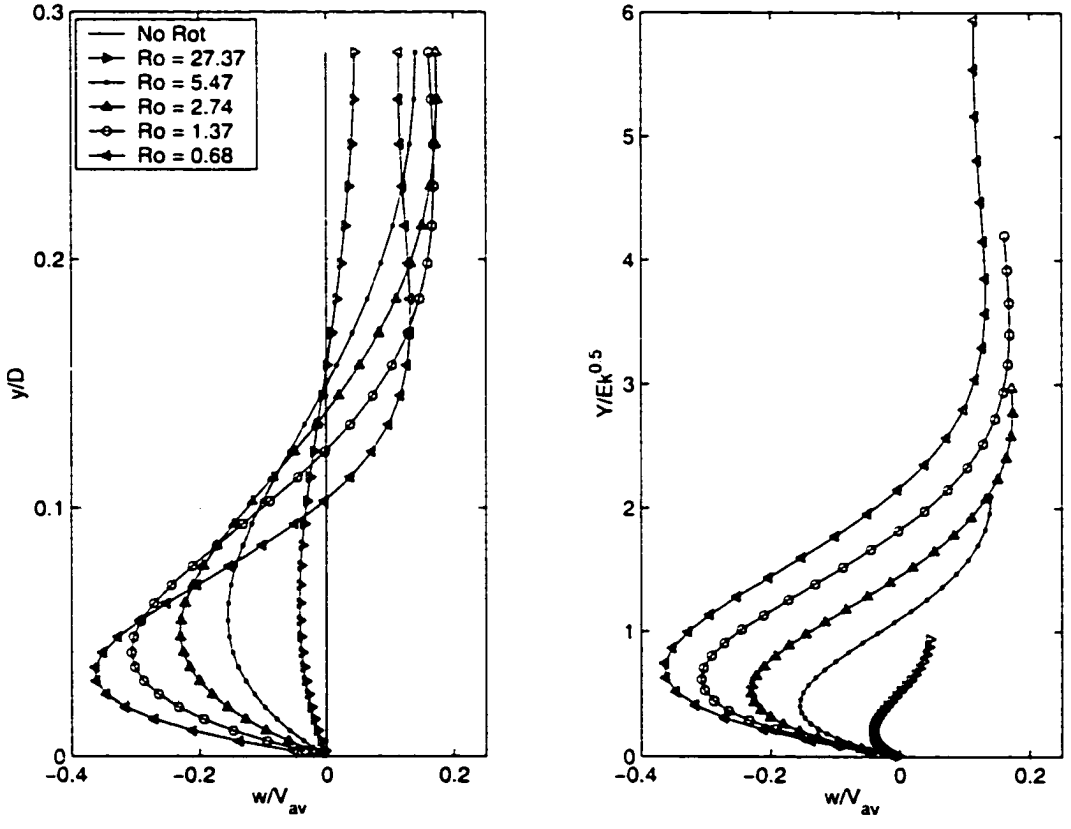

Figure 5.9: Spanwise velocity at z/D = 0.5 for various rotation rates.

It is typical in pipe flow analysis to define a friction factor, or shear stress coefficient which, in the case of non rotating fully developed flow, is directly related to the channel pressure drop. When rotation is present, the shear stress and the pressure drop are no longer equivalent owing to the presence of Coriolis forces. It is therefore more suitable to define a pressure coefficient, as in equation 5.2, using the pressure gradient from the fully developed region, and using the hydraulic radius, r_h, as a length scale.

$$c_p = -\frac{\partial p/\partial x}{1/2\rho \bar{V}_{av}^2} r_h \tag{5.2}$$

In the absence of rotation, this is equivalent to the friction factor but in the case of rotation, it represents the actual pressure drop which is the quantity of interest in most applications. The pressure coefficient, shown in 5.10, increases monotonically with rotation. The non-rotating value of 0.13 is within 0.1 % of the analytic value.

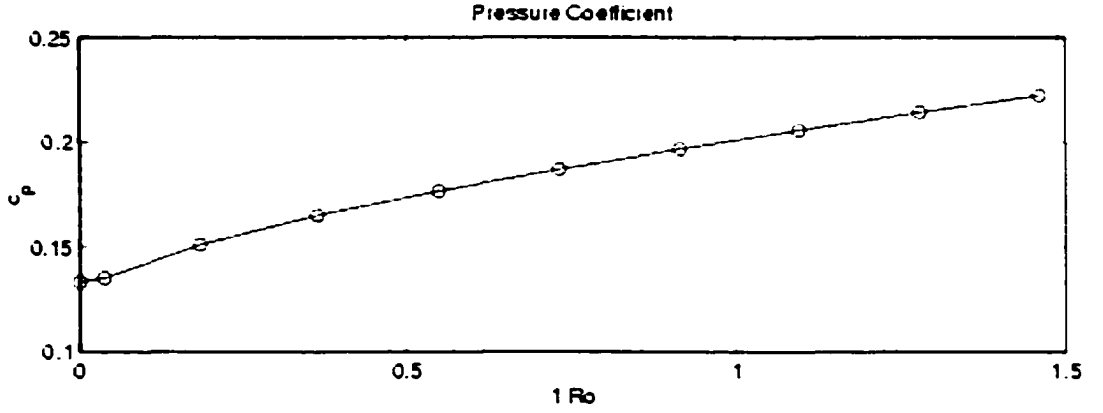

Figure 5.10: Pressure coefficient versus 1/Ro in the case of triangular channels. $Re_{D_h} = 100$.

The cross-stream pressure gradients that build up with rotation and drive the secondary flow and wall jets are illustrated in figure 5.11. As in the case of rectangular channels, this pressure gradient is perpendicular to the axis of rotation, with the

pressure contours curving through the wall jets to intersect normal to the channel walls, consistent with the formation of the wall jets shown earlier.

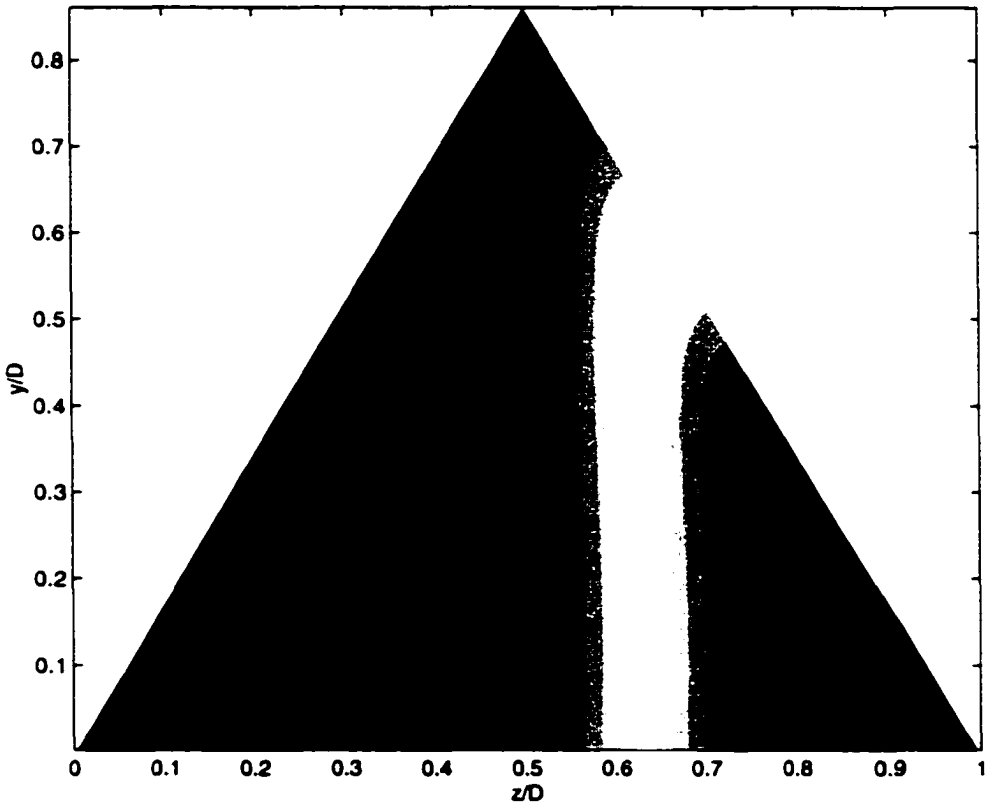

Figure 5.11: Typical pressure contours in the fully developed regime. Lower pressures are found at the leading side while higher pressures are found at the lagging side

5.3.2 Mass Transfer

Mass transfer calculations were carried out using the source term model for NaCl feed concentrations of 35,000 ppm and 50,000 ppm and for pressures ranging from 400 psi to 1000 psi. Figure 5.12 depicts the Re_w values computed using the source term model for each simulation ($3.1 \times 10^{-4} < Re_w < 5.3 \times 10^{-3}$). Membrane is located on the y=0 surface only. It is interesting to note that when the operating pressures are converted to excess pressures the Re_w values are higher in the case of the 50,000 ppm feed solutions.

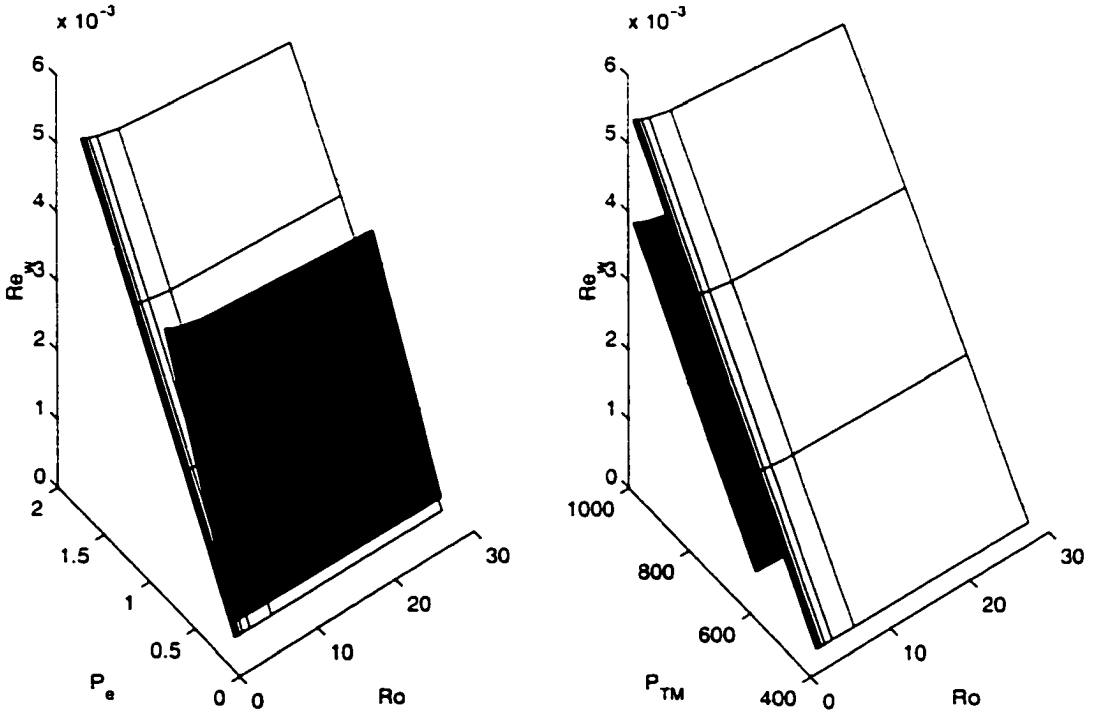

Figure 5.12: Re_w as a function of Ro and applied pressure. The dark surface corresponds to a feed solution of 50,000 ppm while the light surface corresponds to a feed solution of 35,000 ppm.

Figure 5.13 shows the spanwise averaged surface concentrations for cases spanning the complete range of calculations. The non-rotating cases, shown in the left hand column, illustrate the growth of typical concentration boundary layers, while in cases of maximum rotation concentrations remain relatively constant. In all cases involving rotation the maximum concentration attained is significantly less than the corresponding non-rotating case. It is clear, however, that there is minimal concentration polarization at the lower transmembrane pressures, and hence lesser benefits from rotation. Figure 5.14 presents the distribution of surface concentrations for the non-rotating cases. These distributions are symmetric about z/D = 0.5 with high concentrations in the corners affecting larger portions of the membrane with increasing Re_w (P_{TM}) .

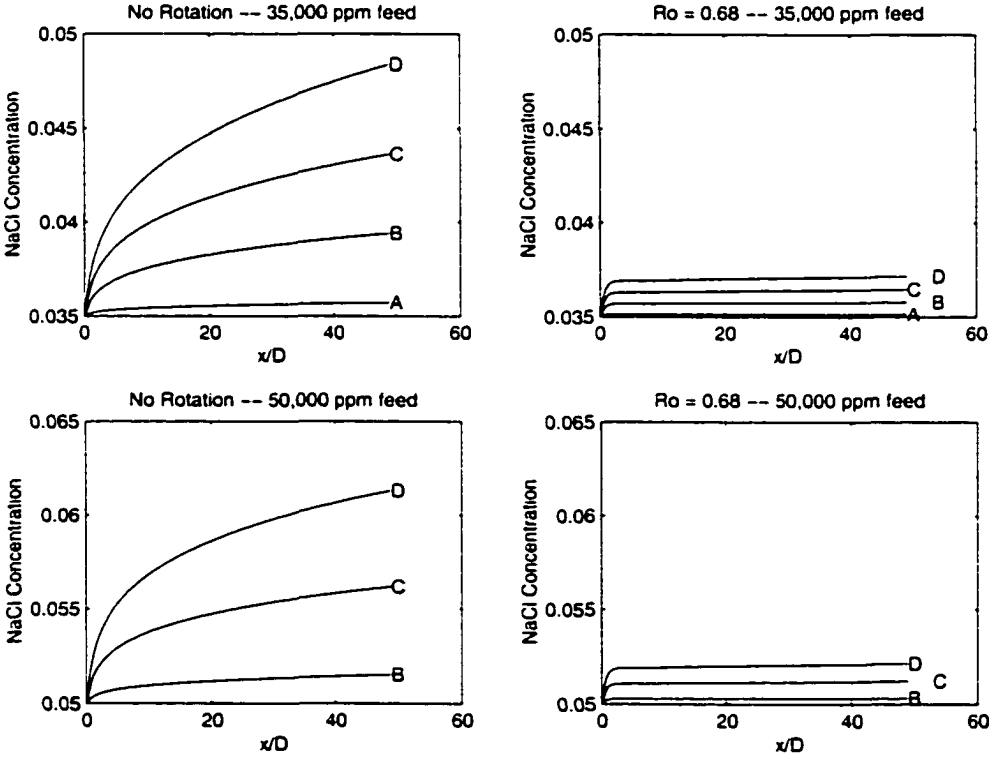

Figure 5.13: Spanwise averaged NaCl concentrations along the channel. A - P_{TM} = 400 psi, B - P_{TM} = 600 psi,C - P_{TM} = 800 psi,D - P_{TM} = 1000 psi

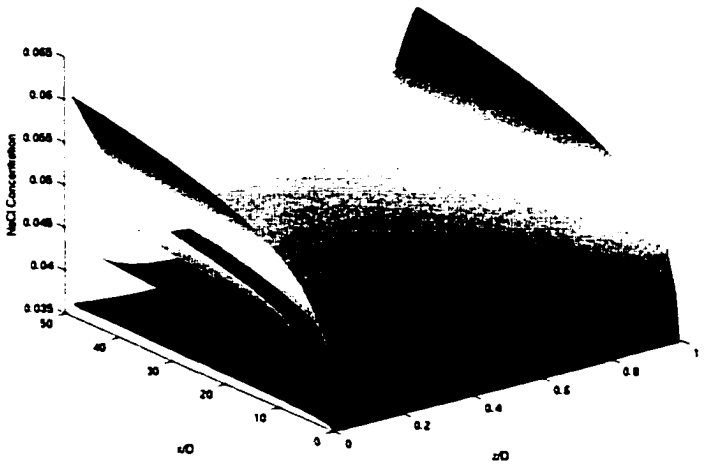

Figure 5.14: Surface NaCl concentrations with no channel rotation for P_{TM} = 400 psi (lowest surface), 600 psi, 800 psi and 1000 psi (highest surface).

Figure 5.15 presents the spanwise averaged surface concentrations obtained at the highest trans-membrane pressures at various Ro while figure 5.16 presents the spanwise surface concentration distributions at x/D = 40.8. Modest increases in rotation significantly decrease the surface concentrations, with the solutions appearing to asymptotically approach a limiting concentration even though Re_w is increasing with rotation. The spanwise distribution is symmetric when there is no channel rotation and relatively higher near the leading sidewall (z/D = 0) when there is rotation. Also, the higher concentrations in the corners both decreases and influences a lesser portion of the membrane with increasing rotation.

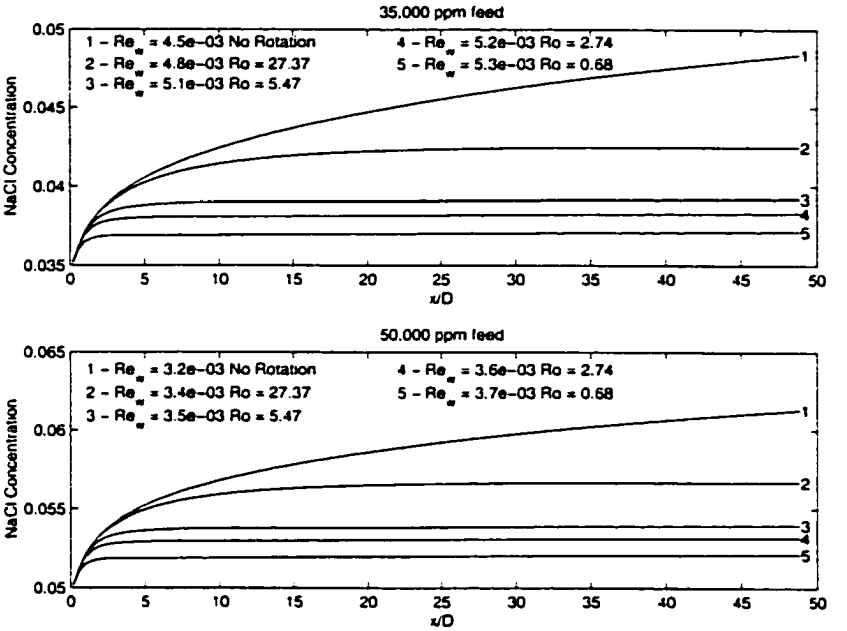

Figure 5.15: Spanwise averaged NaCl surface concentrations along the channel for various Ro. $P_{TM} = 1000psi$

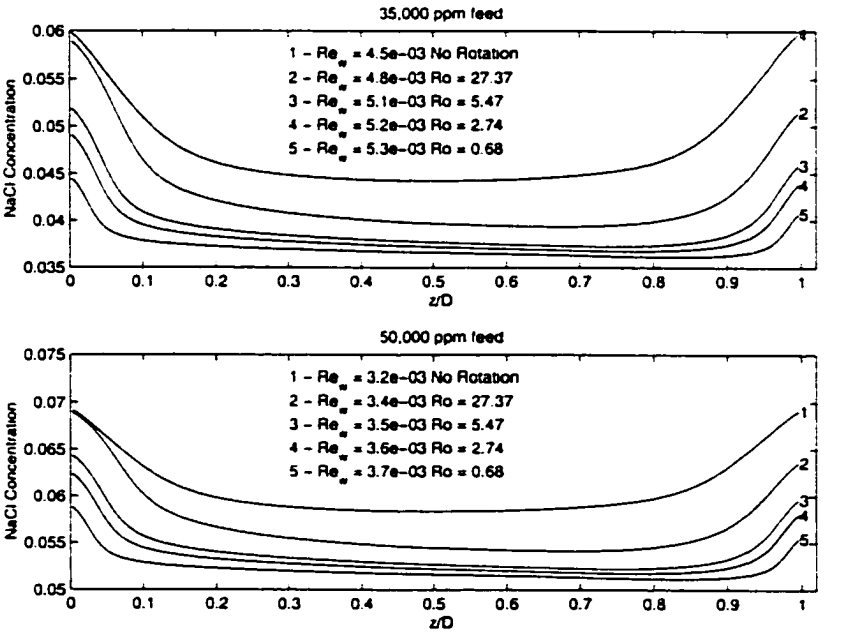

Figure 5.16: Spanwise distribution of surface NaCl concentration at x/D = 40.8. $P_{TM} = 1000psi$

Figure 5.17 presents the profiles of NaCl normal to the membrane surface at the same streamwise location and at z/D = 0.5. Inset in the figure is an expanded view of the profiles near the channel centroid. As rotation is increased, the concentration boundary layers gets increasingly smaller and the secondary flow patterns convect correspondingly more NaCl towards the centre of the channel. This results in increased mixing as evidenced by the increasingly small portions of the curve at the feed concentration of 35.000 ppm.

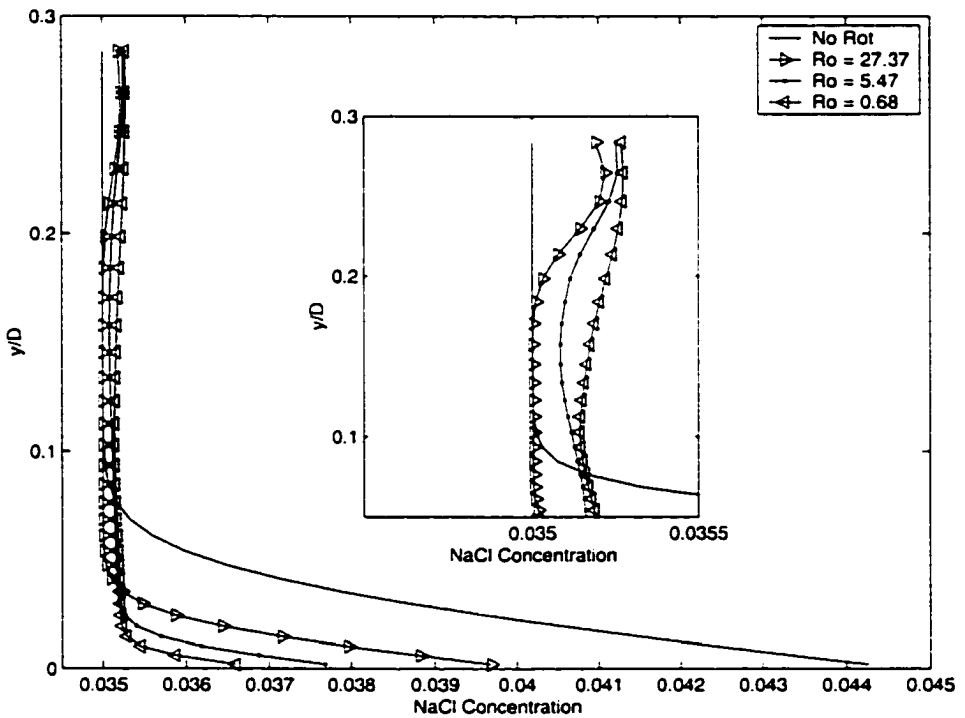

Figure 5.17: NaCl concentration normal to the membrane surface at x/D = 40.8 and z/D = 0.5

The flux improvement, defined by

$$\text{Flux Increase} = \frac{Re_w - (Re_w)_{\text{no rotation}}}{(Re_w)_{\text{no rotation}}} \times 100\% \tag{5.3}$$

is plotted as a function of 1/Ro in figure 5.18. The shape of the curves is very similar to the case of rectangular channels, with flux increasing with increasing rate of rotation, concentration and trans-membrane pressure. The magnitude of the flux increase is significantly lower than the case of rectangular channels, and this is largely due to the fact that a streamwise length of 120D was used for the rectangular channels, while a streamwise length of only 50D was used for the triangular channels. This issue will be revisited in chapter 7.

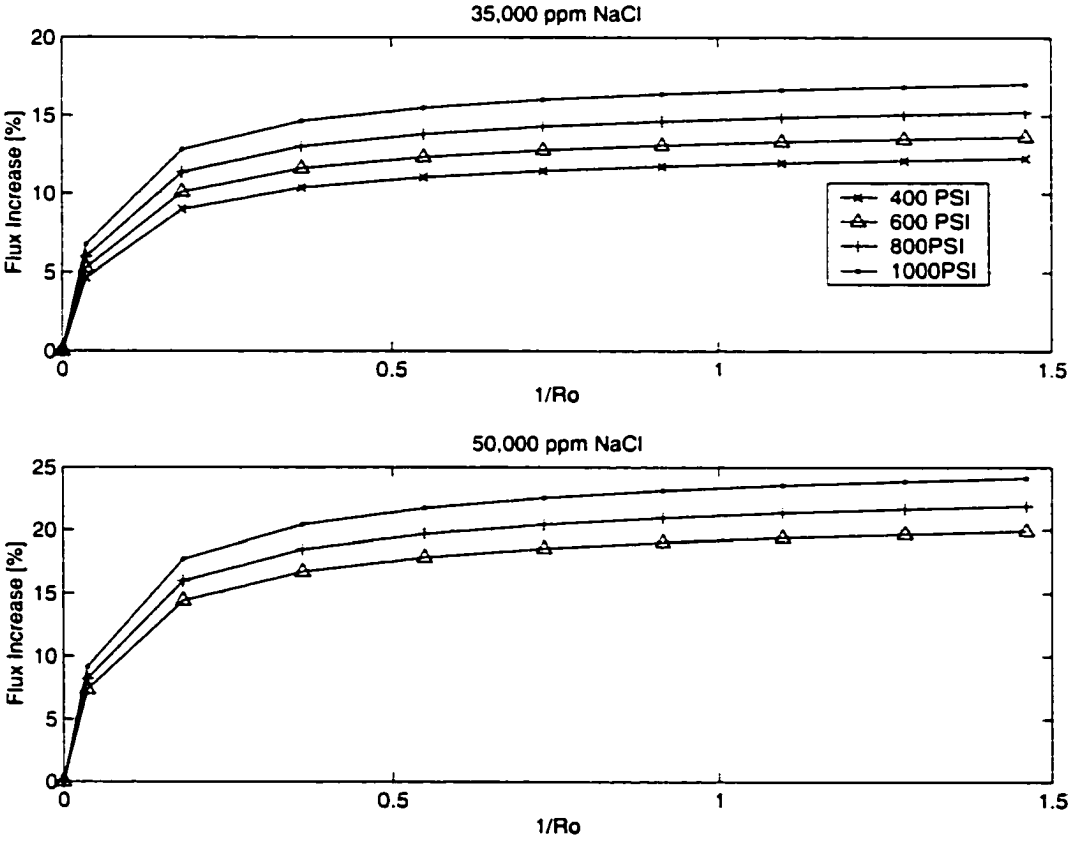

Figure 5.18: Flux improvement over the non-rotating case as rotation is is increased

5.4 Circular Channels

Simulations were carried out with cfx 4.2, using the 5 block grid shown in figure 5.19. Each grid block is [25x25] in cross section and extruded uniformly in the streamwise direction (S), using 159 planes to a length of 15D. Elliptic smoothing was used to maximize the orthogonality of the grid volumes, and the last two circumferential grid lines were fixed at r = (R - dr) and r = (R - 2 dr), where dr/D = 3e-3, as in Chapter 4. The Reynolds number, Re_D was fixed at 100, and rotation was varied from 0 rad/s - 300 rad/s corresponding to Ro = ∞, 3.65, 1.82, 0.46, 0.30 with the axis of rotation aligned with the y-axis. Higher order upwind differencing was used in all simulations.

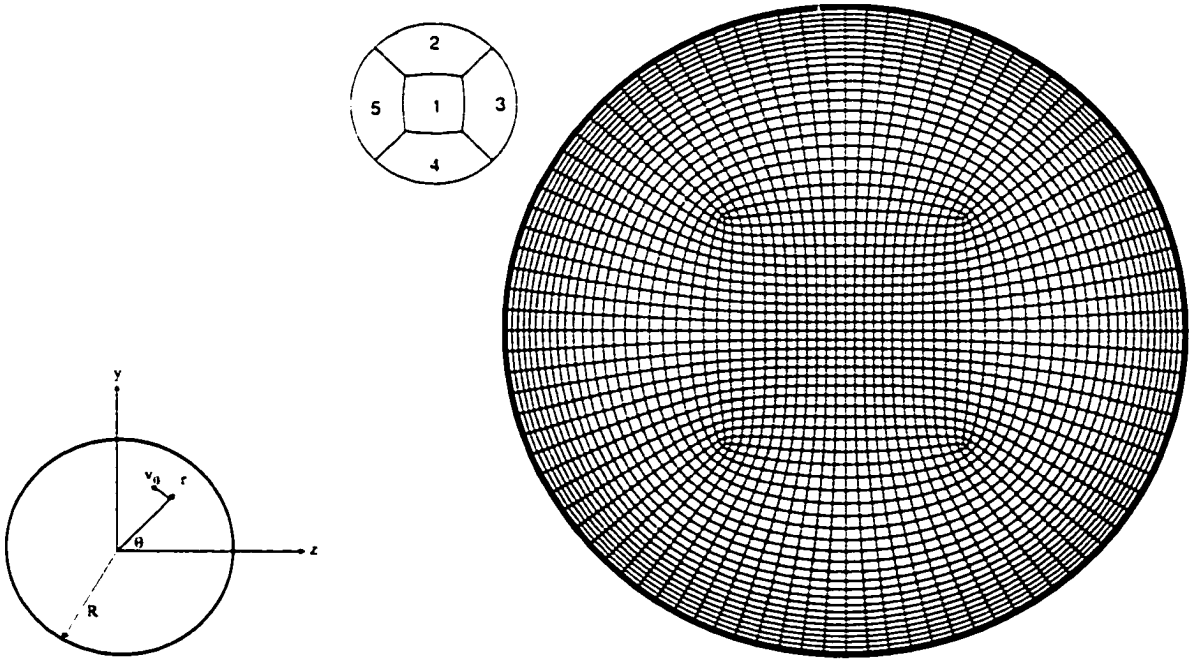

Figure 5.19: Five block grid used to simulate rotating flow in circular pipes

5.4.1 Hydrodynamics

Figure 5.20 depicts relief plots of streamwise velocity in the fully developed region as Ro is decreased. As with both the triangular and the rectangular channels, the flow passes through four different regimes. In the absence of rotation, the profile is axisymmetric with a maximum at the channel centre. As rotation is introduced, this maximum shifts towards the lagging side of the channel (increasing z) and then forms an inverted C shaped ridge spanning ($-\pi/2 < \theta < \pi/2$). At the lowest Ro, the central core of the profile has flattened considerably, resulting in two local maxima around $\theta = \pm\pi/2$.

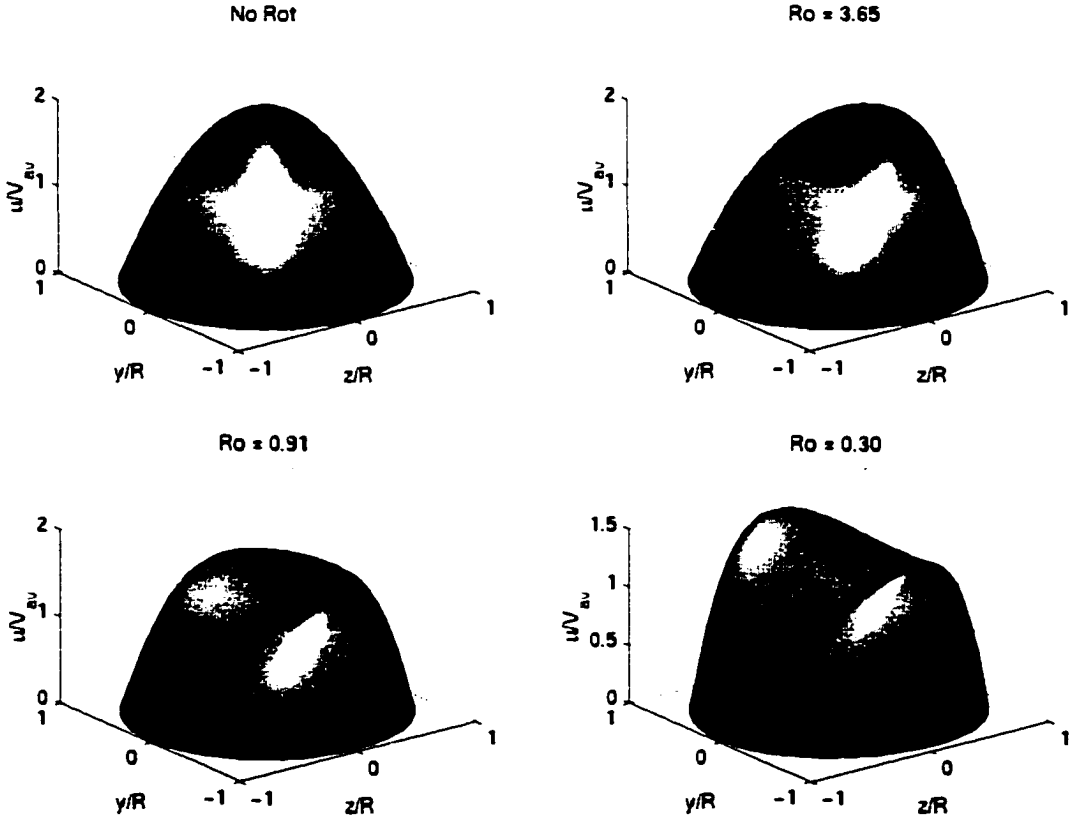

Figure 5.20: Relief plots of spanwise velocity in the fully developed region.

Figure 5.21 plots the streamwise and azimuthal velocity profiles parallel to the axis of rotation, while figure 5.22 plots the streamwise velocity along the centreline perpendicular to the rotational axis. In all cases, the profiles are almost identical to the case of the square channel channel presented in Chapter 4. Again, the Coriolis acceleration acts on the high velocity driving fluid against the direction of rotation. This fluid impinges on the lagging surface and returns to the leading side of the channel in increasingly narrow but strong walls jets. At the highest rotation rate, the maximum magnitude of the azimuthal velocity is almost 40% of the bulk velocity. These secondary velocity patterns are shown in the next section along with the contours of NaCl concentration.

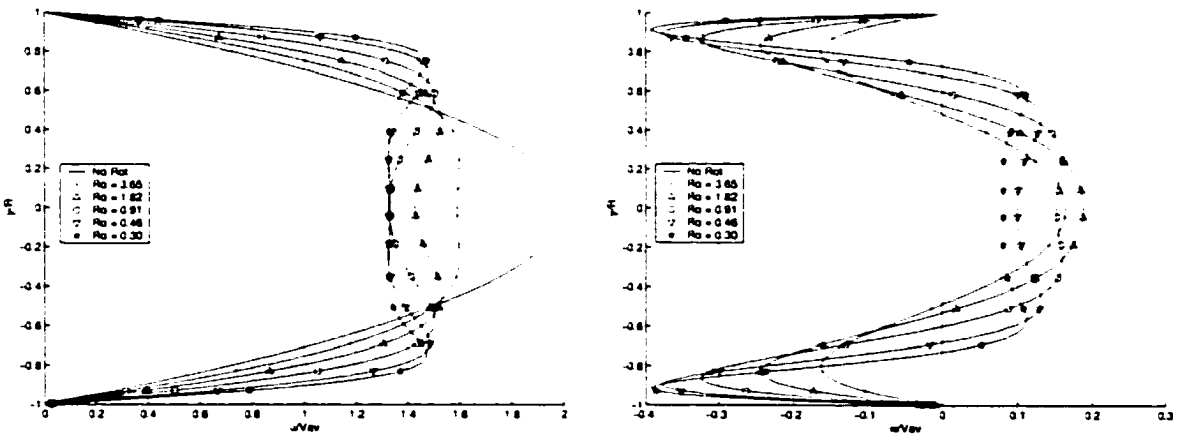

Streamwise Velocity Lateral ('spanwise') Velocity

Figure 5.21: Profiles of streamwise and azimuthal velocity parallel to the axis of rotation.

Figure 5.23 plots the streamwise and azimuthal components of friction coefficient around the circumference, in the fully developed region. In the absence of rotation, the streamwise friction coefficient is constant, and agrees with the analytic solution ($c_f = 0.16$). There is no azimuthal component of wall shear. As rotation is intro-

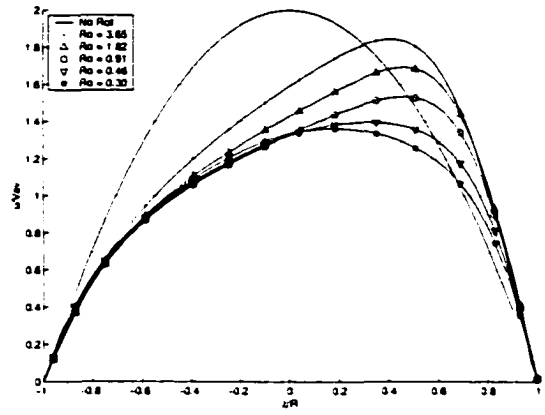

Figure 5.22: Streamwise velocity profile along the axis perpendicular to the axis of rotation.

duced, the streamwise friction coefficient decreases over the range ($-45^o < \theta < 45^o$), and increases elsewhere. The azimuthal friction coefficient increases over the range ($0^o < \theta < 180^o$) and decreases elsewhere. Further increases in rotation rate result in the streamwise friction coefficient exhibiting an absolute minimum at $\theta = 0$, a local minimum at $\theta = 180^o$ and two equal maxima at $\theta = 90^o$ and $\theta = 270^o$. The azimuthal distribution remains similar in shape, but increases in magnitude. In comparison, figure 5.24 presents similar plots in the case of a square channel where the circumferential component is -135^o out of phase with the azimuthal component in the circular case due to the different origin used in the two cases. The profiles in the two cases are very similar both in trend and in magnitude, with the exception that c_f is constrained to zero in the channel corners and the regions of lower shear are constrained to the leading and lagging walls (WEST and EAST) walls between these zeros. Figure 5.25 plots the spanwise averaged friction coefficients as a function of 1/Ro. Again, the result is very similar to the case of the square channel. The average friction coefficients in the circular channels are slightly lower in the case of the square channel however, since the low stress regions are constrained by the zeros at each corner.

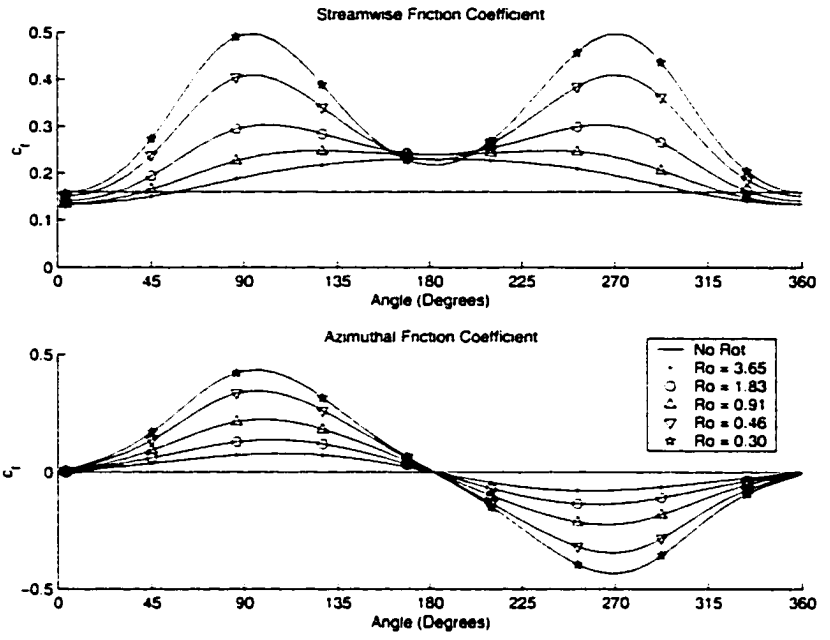

Figure 5.23: Streamwise and azimuthal component of friction coefficient in circular channels.

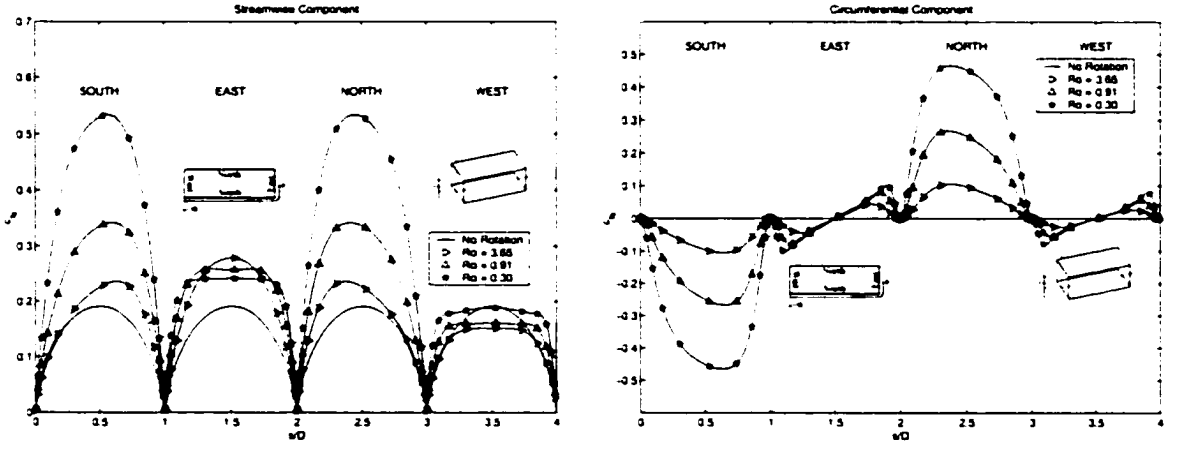

Figure 5.24: Streamwise and circumferential component of friction coefficient in square channels.

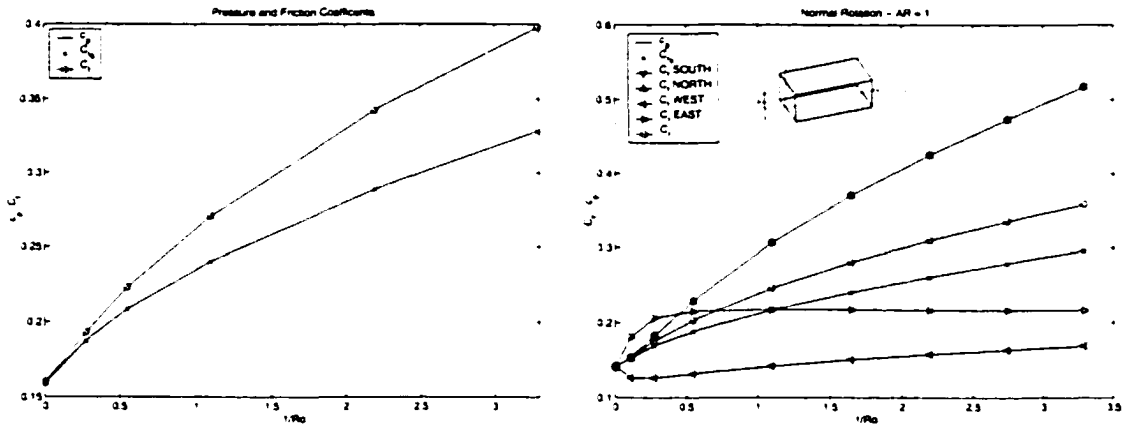

Circular Channel Square Channel

Figure 5.25: Circumferentially averaged friction coefficients in circular and square channels.

5.4.2 Mass Transfer

The STM was used to model membrane separation in the circular channels, using a feed concentration of 35,000 ppm NaCl and a transmembrane pressure of 1000 psi. Figure 5.26 plots NaCl concentrations superimposed on the secondary velocities generated in the channels. In the absence of rotation, there are no secondary velocities, the solutions are axisymmetric and the wall concentrations are much higher than in the other cases. As rotation is introduced, secondary velocities are generated and serve to transport NaCl from $\theta = 0^o$ to $\theta = 180^o$ along the channel walls and back towards $\theta = 0^o$ along through the centre of the channel. This results in a maximal concentration at $\theta = 180^o$. In the cases of Ro = 3.65 and Ro = 1.82, the cross channel velocity along the z-centreline is increasing, and accordingly, higher NaCl concentrations in the centre of the channel are limited to a small band. At Ro = 0.91, the secondary velocity in the core has begun decreasing and there is correspondingly more diffusion in the central region resulting in a larger band of higher concentration fluid. At the same time, the magnitude of the wall jets adjacent to the wall increases monotonically, resulting in continually lower NaCl surface concentrations. Both of these effects combine to result in maximal mixing at the highest rotation rate. This is clearly shown in figure 5.27, which presents relief plots of NaCl concentration at the corresponding streamwise location.

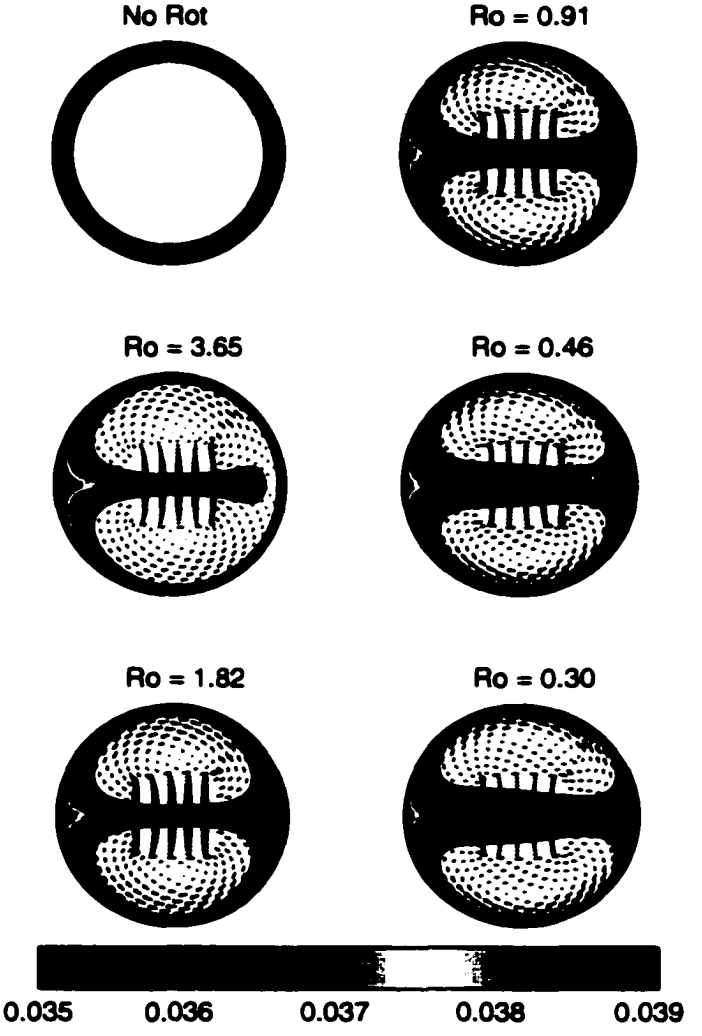

Figure 5.26: NaCl contours and secondary velocities at near the channel outlet.

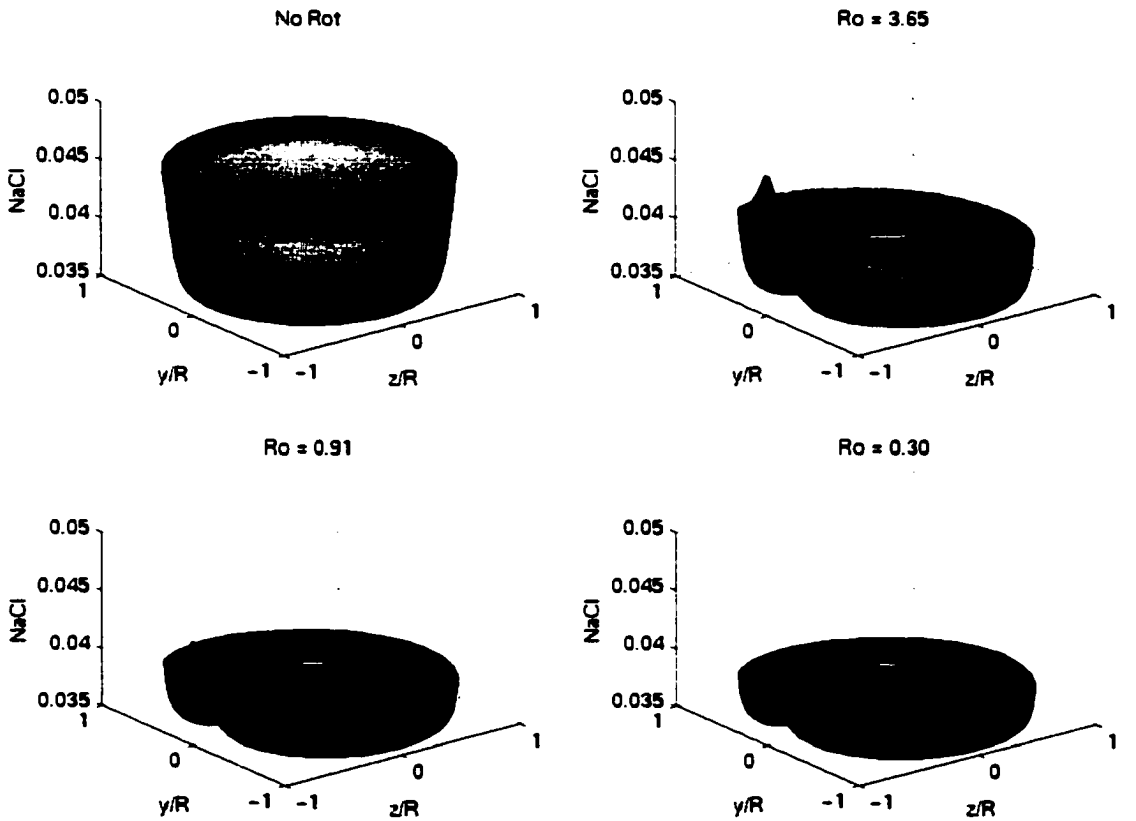

Figure 5.27: Relief plot of NaCl concentration with increasing channel rotation.

Figure 5.28 plots both the circumferentially averaged NaCl concentration along the streamwise direction, and the circumferential variation of NaCl at the same streamwise location as presented above. As in the case of both square and triangular channels, the average surface concentration decreases monotonically, but with diminishing returns, with channel rotation. The circumferential distribution exhibits a maximum at $\theta = 180°$, and at lower rotation rates this maximum is larger than in the case of no rotation. As the rotation rate is increased the maximum decreases to well below the concentration in the non-rotating case. Figure 5.29 plots the NaCl concentration along each channel centreline in the cases of no channel rotation and Ro = 0.3. The lower wall concentrations, and the smaller enhanced mixing in the case of rotation are evident on this plot.

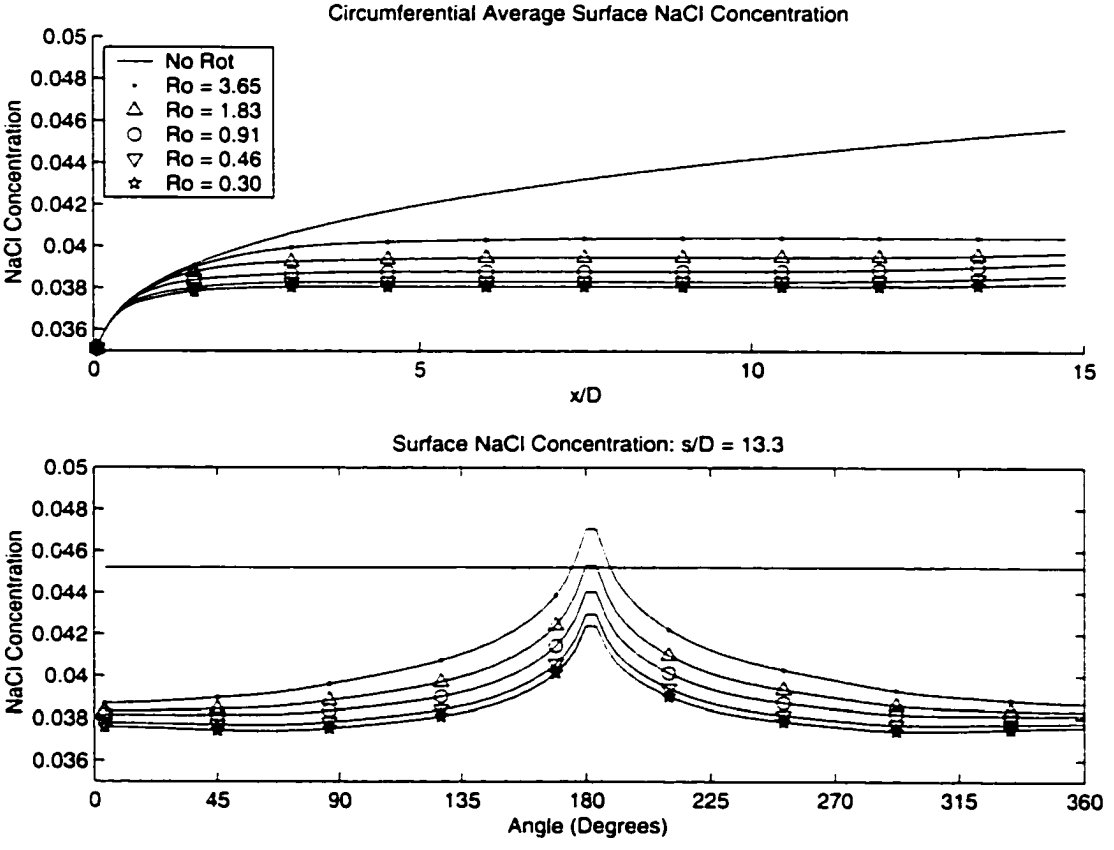

Figure 5.28: Five block grid used to simulate rotating flow in circular pipes

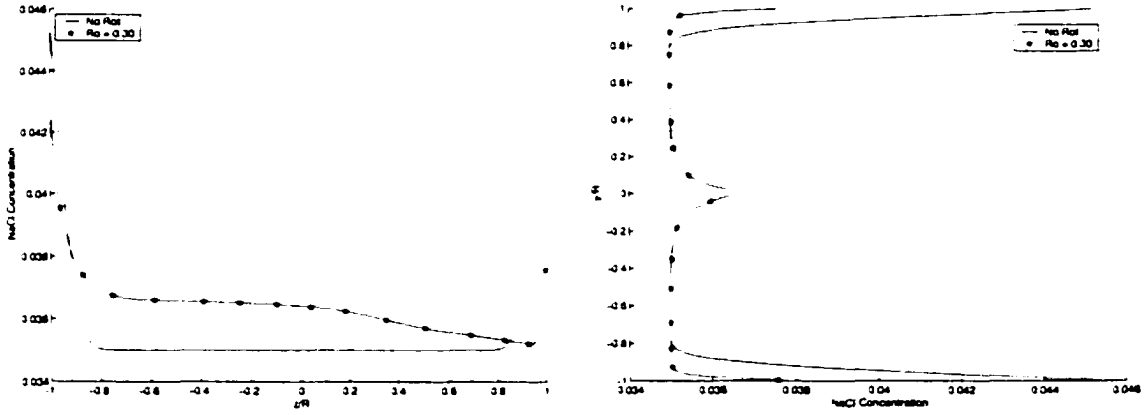

Perpendicular Parallel

Figure 5.29: Profiles of NaCl concentration along centrelines both perpendicular and parallel to the axis of rotation.

5.5 Closure

Simulations of rotating flow and mass transfer have been presented at $Re_D = 100$ in the cases of circular and triangular channels. The overall structure of the secondary flow patterns and their effect on mass transfer are shown to be very similar to the cases of rectangular channels presented in Chapter 4, except that they are slightly modified by the differing geometric constraints. In all cases, channel rotation results in significantly lower surface concentrations and enhanced mixing.

Chapter 6

Laminar Flow and Mass Transfer Over Periodic Arrays of Obstacles

6.1 Introduction

Periodic obstacle flows occur in many engineering applications including wind engineering, heat exchanger design, electronic packaging and internal cooling of gas turbine blades. In membrane separation processes, periodic obstacle flows arise due to the feed spacers which are used to manufacture membrane modules and which come in a variety of configurations.

These obstacles generate strong pressure gradients and separated flow regions both upstream and downstream as illustrated in figure 6.1 which depicts flow over a single obstacle. Depending on the flow parameters and geometry, there is a potential for up to four different separation zones, as shown in the figure: 1) upstream separation due to the adverse pressure gradient caused by the obstacle, 2) obstacle separation due to the sharp upstream corner, 3) primary 'separation bubble' due to the sharp

downstream corner and to the adverse pressure gradient of the expanding flow and 4) secondary 'separation bubble' due the adverse pressure gradient of the expanding flow.

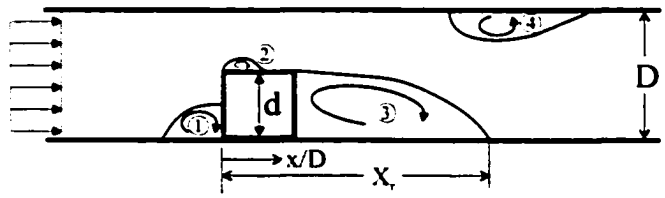

Figure 6.1: Coordinate system and flow over a single obstacle.

The flow in arrays of periodic obstacles is additionally complicated due to flow interactions between obstacles. Figure 6.2 depicts three examples of periodic obstacle flows examined herein: surface mounted obstacles, channel centred obstacles and alternating surface mounted (staggered) obstacles. The characteristics of both the wake created downstream of the obstacles as well as the disturbance created by upstream obstacles impact considerably on the performance of the system. The characteristics of the flow depend strongly on Reynolds number, channel blockage ratio, obstacle spacing, obstacle geometry and system rotation.

In addition to providing structural support, one of the roles of feed spacers is to enhance mass transfer by maximizing solute transfer away from surfaces of active membrane and accordingly minimize membrane surface concentrations. Periodic obstacles can be quite effective to this end since mass transfer is enhanced in the recovery region downstream of an obstacle as well as in regions where the flow is accelerated. In order to find an optimum configuration, the flow field must be determined for a range of geometries and flow conditions.

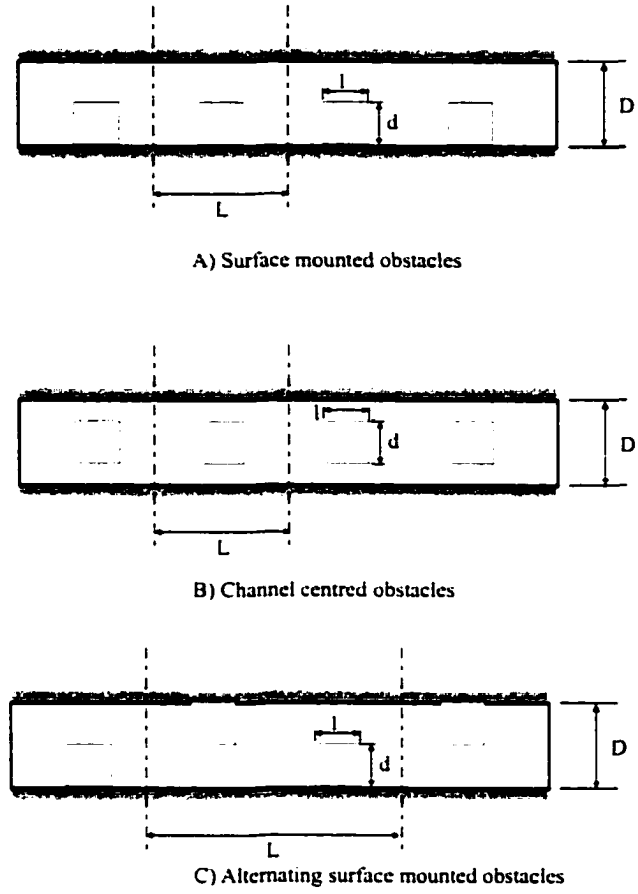

Figure 6.2: Periodic obstacle geometries

Turbulent obstacle flows in various periodic geometries have been investigated both experimentally, e.g. [43, 44, 45] and numerically, e.g. [46, 47].

Patankar [48] studied streamwise periodic laminar flows with heat transfer over arrays of thin plates. Amon *et. al.* [49] performed a numerical and experimental study in communicating channels made up of channel centred rectangular obstacles. Zhang *et. al.* [50],[51], [52] numerically studied unsteady flows in inline and staggered arrays of finite plates. Both Zhang and Amon found significant effects due to unsteadiness while Zhang highlighted the importance of three dimensional effects with unsteadiness.

Several studies have dealt directly with the flow in spacer filled channels including early experimental work by Belfort [53], who measured drag and presented some flow visualization results of enlarged spacers found in electrodialysis devices. Winograd [54] examined mass transfer in similar systems, and developed a simple model, based on laminar flow in unobstructed channels, to correlate the mass transfer performance. Several additional experimental papers have addressed the pressure drop in spacer filled channels including [55, 56, 57]. More recently, DaCosta *et. al.* [58, 59] measured the drag coefficients of various spacer materials found in ultrafiltration membranes. They also developed a simplified model which correlated their experimental data with simplified one dimensional hydrodynamic theories. Their model included terms for the viscous drag (assuming boundary layer flow over isolated cylinders) and form drag (correlated to experimental data) of the spacers, the friction in the channels (assuming laminar flow in unobstructed channels) and momentum losses due to changes in flow direction. Mass transfer was modelled by adding an additional constant to correlations of mass transfer results based on laminar flow in unobstructed channels. Using several experimentally determined constants, their model was able to correlate their data, but their simplifications abstracted significantly from the actual physics in spacer filled channels. A recent paper by Karode and Kumar [60] used CFD to model the hydrodynamics of the same spacer filled channels measured by DaCosta *et. al.*. Their results convey the complexity of the resulting flows, however, they rely on shear rate calculations to infer mass transfer characteristics. Cao *et. al.* [61] also recently used CFD to model simplified spacer geometries using domains consisting of both isolated cylindrical obstacles and pairs of cylindrical obstacles. There are some concerns with the boundary conditions used in these simulations and these researchers also rely on calculations of shear rates to anticipate mass transfer performance.

The goal of the present chapter is to examine laminar flow and associated mass

transfer in periodic arrays of obstacles. Both the hydrodynamics and mass transfer of such flows will be examined in this chapter.

6.2 Computational Procedure

The computational procedure of Chapters 4 and 5 in conjunction with the STM was used with a modification to account for periodicity. Following [48], streamwise periodicity can be accommodated by decomposing the pressure into a linear and a periodic component.

$$p(x, y) = -\beta x + P(x, y) \tag{6.1}$$

where x is the streamwise direction, β is a constant pressure gradient, and P(x,y) is periodic such that P(0,y) = P(nL,y). This concept was implemented in cfx by adding a constant source term to the streamwise momentum equation and by using a periodic boundary condition at x=0 and x=L. Using this method, the channel flow rate, or Re_D, is a result of the calculation and depends upon β. For this reason, a control loop was implemented within the code which adjusted β during the solution procedure to maintain the desired Re_D.

6.3 Grid Study and Validation

Initially, two and three dimensional simulations were carried out over a single obstacle in order to perform a grid study and to validate the code. The geometry chosen for this study corresponds to a numerical and experimental study by Billeness *et. al.* [62]; the domain extends 14.5 obstacle heights upstream and 40 obstacle heights downstream

of a 0.25D square obstacle. Billeness used a staggered grid of [64x45] and a QUICK scheme with a transverse correction for the advective terms. The collocated grids used for this study ranged from [86x61] to [163x61] and used both a QUICK scheme and a higher order upwind (HUW) scheme. While the grid resolution in the normal direction may seem excessive, this is necessary both for high Schmidt number mass transfer computations and for simulations including system rotation [63]. Figure 6.3 compares the x spacing on the various grids.

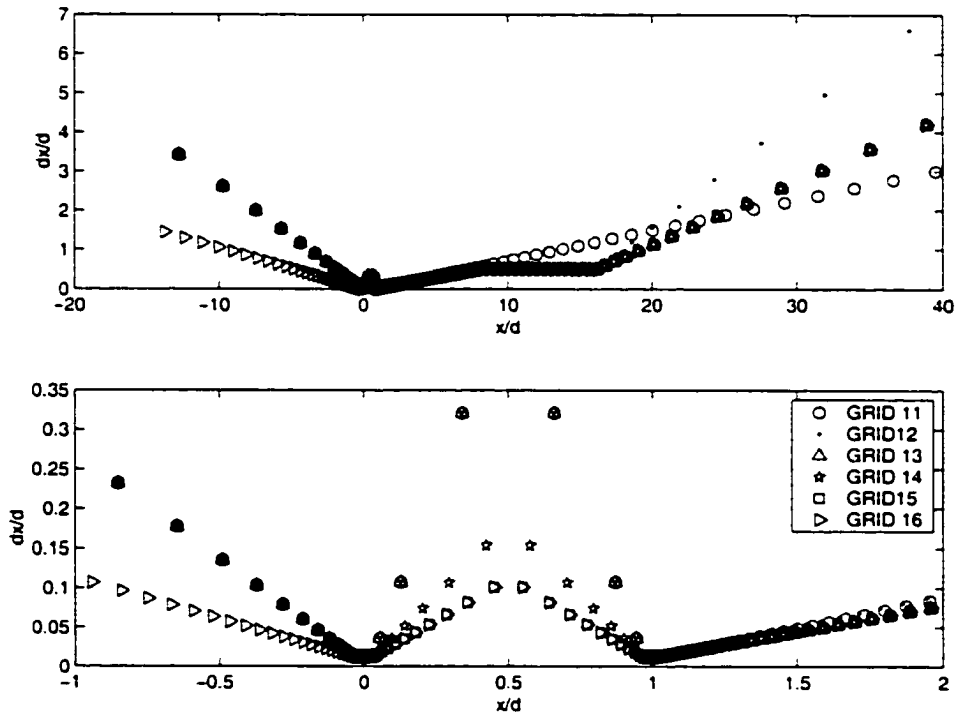

Figure 6.3: Grid spacing

One of the most important parameters characterizing the flow is the reattachment length, X_r, defined in figure 6.1, which corresponds to the length of the recirculating flow region ('separation bubble') that forms downstream of the obstacle. The reattachment length is the distance from the leading edge of the obstacle to the reattachment point, which is refined as the location of vanishing wall shear stress.

Table 6.1 presents the streamwise grid dimensions and computed reattachment lengths, X_r. It is of note that doubling the grid over the obstacle itself increases X_r by 3.4%, while a further doubling of the grid upstream of the obstacle changes X_r by less than 1 %. An additional simulation which doubled the grid spacing at the wall, but kept the number of nodes constant, resulted in a negligible change in X_r. Simulations using a QUICK scheme predicted slightly longer X_r, but did not converge for all cases.

Grid	Total x vols	UPS vols	OBJ vols	X_r/d (HUW/QUICK)
11	111	25	13	14.92/15.13
12	111	25	13	14.98/*
13	124	25	13	14.97/15.11
14	132	25	21	15.41/-
15	138	25	27	15.49/-
16	163	50	27	15.6/-

Table 6.1: Streamwise grids employed for numerical simulations. * = not converged. - = not performed. UPS = upstream. OBJ = object

Figure 6.4 compares the computed velocity profiles with experimental profiles from [62] at $Re_D = 816$. The simulations compare very well with the experiment, with perhaps the largest discrepancy at x/d=14, and these discrepancies are within the range of experimental error reported by Billeness.

In order to check for three dimensional effects, GRID 15 was extruded, using 80 volumes, such that the width of the 3D channel was 40d (note the use of a symmetry condition at z/d=0) corresponding to the water channel used in [62]. Figure 6.5 shows the computed friction coefficient,

$$c_f = \frac{\tau_{wall}}{\frac{1}{2}\rho U^2}, \tag{6.2}$$

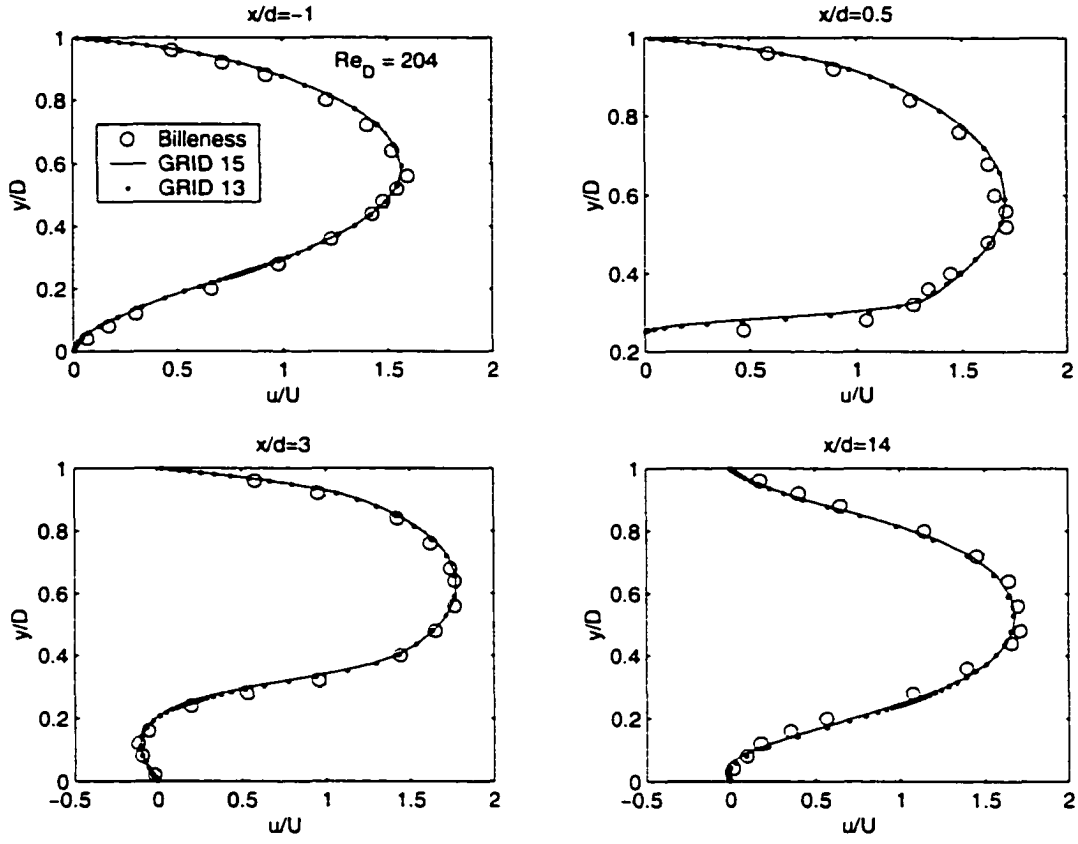

Figure 6.4: Experimental validation: Streamwise velocity profiles.

on the top and bottom walls and the computed reattachment length. A significant portion of the channel is indeed two dimensional and the computed reattachment length in the central region is within 1% of that from the two dimensional simulations.

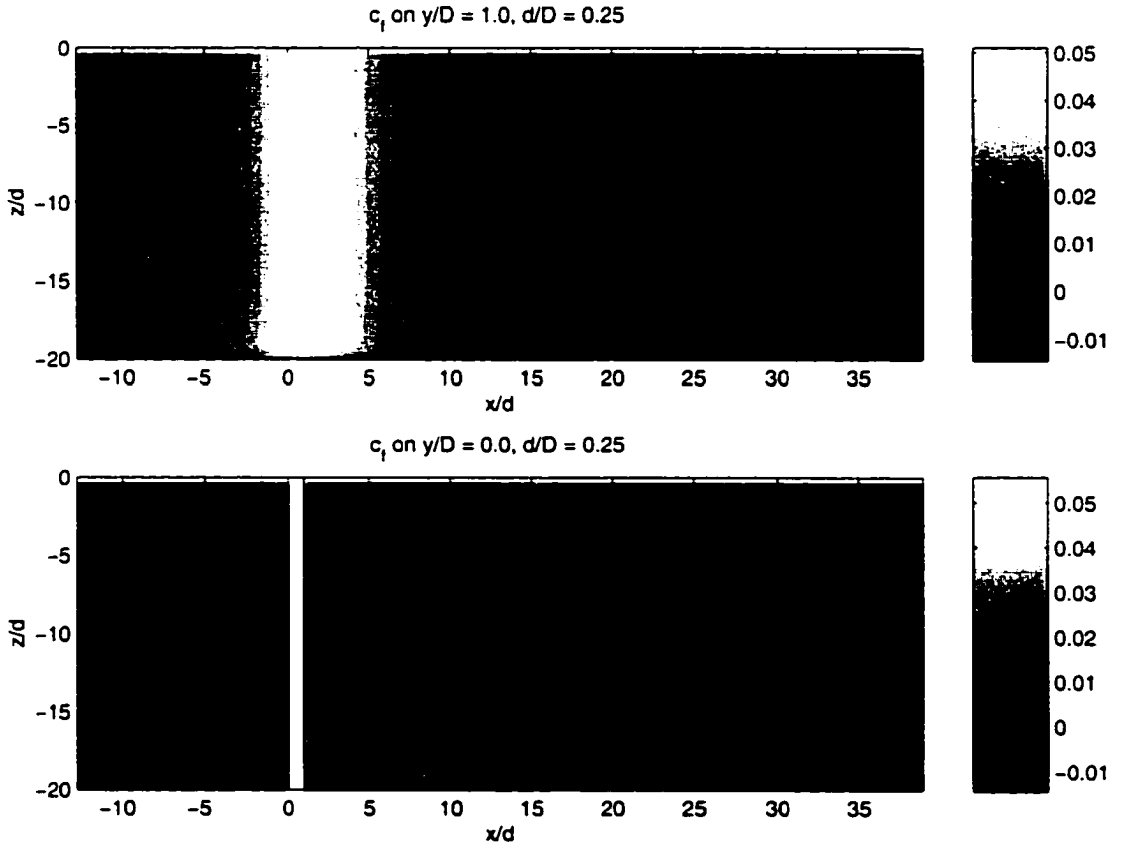

Figure 6.5: c_f on the top (y/D = 1.0) and bottom (y/D = 0) surfaces for $Re_D = 816$. Contour lines of zero shear are overlaid on the bottom surface, clearly showing the reattachment line.

6.4 Periodic Obstacle Flows

The information from the grid study presented above, was used to generate a [119x81] grid for periodic obstacle flows with d/L = 0.05 and d/D = 0.25. The number of nodes normal to the wall was increased from 61 to 81 so as to generate a single symmetric grid amenable to all three obstacle types presented in figure 6.2. Similar grids were also generated for the cases of d/D = 0.50 and d/D = 0.75.

Streamwise periodic solutions were computed for various pressure gradients in the case of surface mounted obstacles. Figure 6.6 presents both the $c_p Re_D$ and the computed reattachment length for various Re_D. c_p is the non-dimensional pressure drop over the channel.

$$c_p = -\frac{\partial p/\partial x}{1/2\rho U^2} r_h = -\frac{3}{1/2\rho U^2} r_h \tag{6.3}$$

The $c_p Re_D$ curve is concave down, indicating that the pressure gradient is increasing at a rate greater than linear with Re_D. The reattachment length increases monotonically until $Re_D = 692$, with an inflexion point between $Re_D = 446$ and $Re_D = 692$. Beyond $Re_D = 692$, the reattachment length is constant. Figure 6.7 presents c_f computed on the top and bottom surfaces for various Re_D. The location of the obstacle is indicated by the shaded rectangle on the y/D = 0 curve. This figure indicates the formation of recirculation zones downstream of the obstacle (regions of negative c_p) which grow with increasing Re_D until the case of $Re_D = 692$, when reattachment no longer occurs on the y/D = 0 surface. These recirculation zones are clearly shown in figure 6.8 which plots streamlines for selected Re_D. In all cases, the maximum c_f occurs on the y/D = 1 surface slightly downstream of the obstacle. This maximum is up to four times greater than the minimum which is located near the middle of the separation bubble on the y/D = 0 surface.

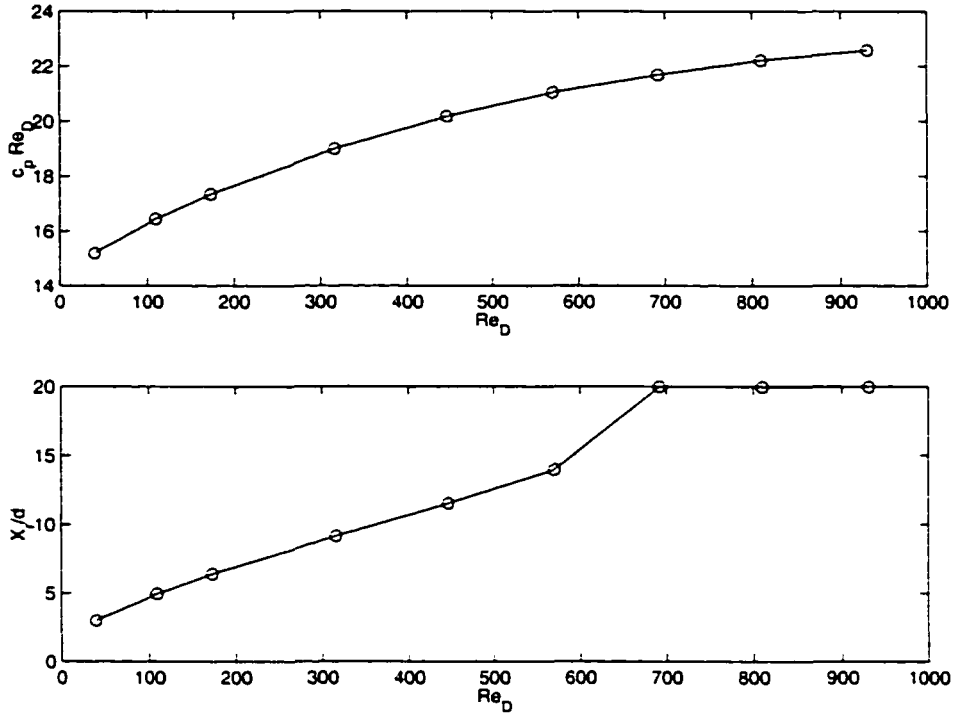

Figure 6.6: Pressure coefficient and reattachment length for various Re_D

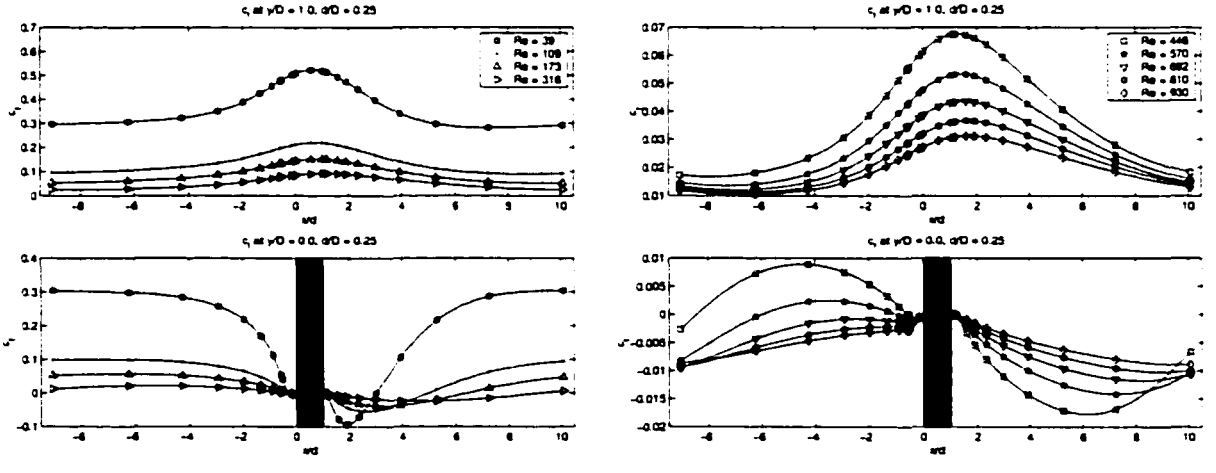

Figure 6.7: Friction coefficient on the top and bottom surfaces for various Re_D. d/D = 0.25

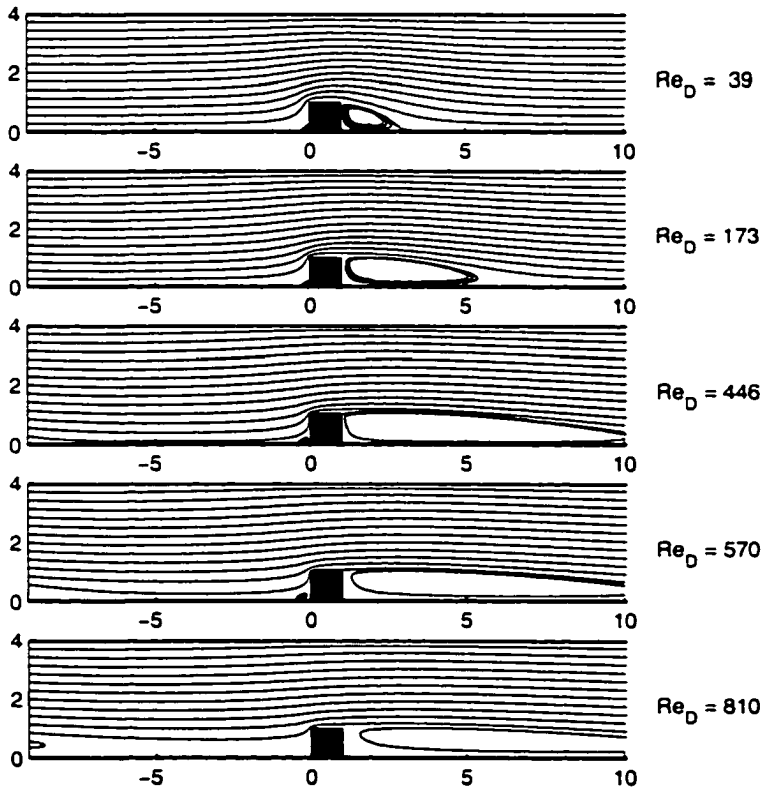

Figure 6.8: Streamlines patterns for secreted Re_D. d/D = 0.25

Figure 6.9 presents the non-dimensional pressure drop for surface mounted obstacles with d/D = 0.25, d/D = 0.50 and d/D = 0.75 and for channel centred obstacles with d/D = 0.25. The pressure drop increases significantly with increasing increasing obstacle size and is higher in the case of channel centred obstacles. Figures 6.10 - 6.13 depict contours of streamwise velocity normalized by the corresponding average velocity, and help to explain the difference between channel centred obstacles and surface mounted obstacles. In either case, the flow is accelerated to roughly the same degree since the channel blockage is the same. This acceleration causes an increase in the friction coefficient (shear rate) which in turn increases the channel pressure drop. In the case of surface mounted obstacles, this higher shear acts on only two surfaces while in the case of channel centred obstacles it acts on four surfaces. Also shown, in black, on these figures is a contour line corresponding to zero velocity. In the cases of surface mounted obstacles, these contour lines intersect the y/D = 0 surface between two obstacles at the point where the flow reattachment occurs. As discussed above, in the case of d/D = 0.25 reattachment occurs on the y/D = 0 surface for $Re_D < 692$. In the case of d/D = 0.50 reattachment ceases to occur between $Re_D = 123$ and $Re_D = 209$, while in the case of d/D = 0.75 reattachment occurs only at the lowest Reynolds number presented ($Re_D = 29$).

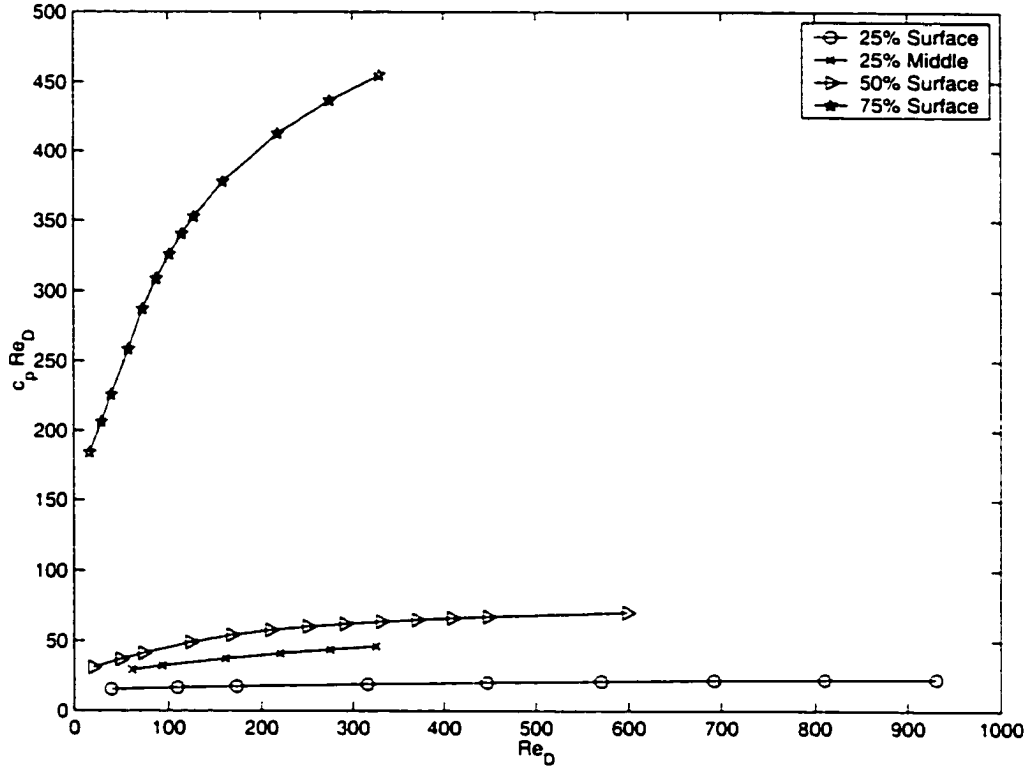

Figure 6.9: $c_p Re_D$ versus Re_D for various geometries.

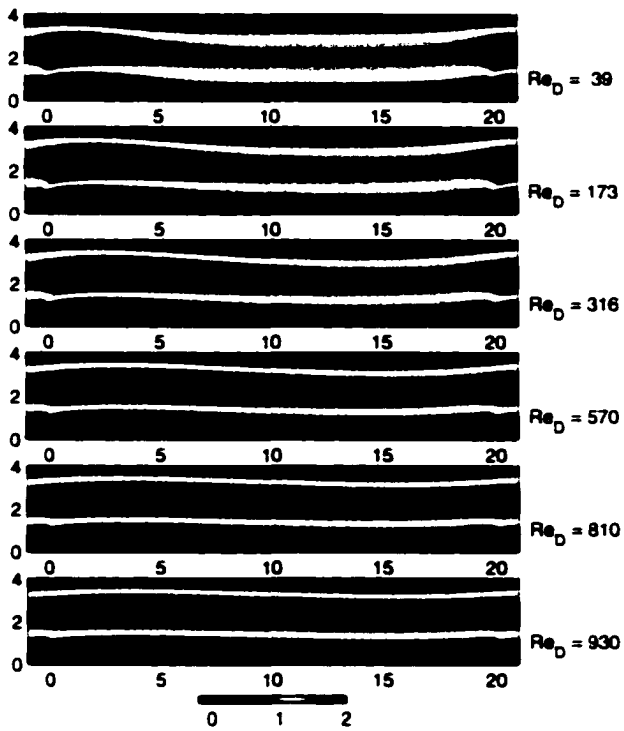

Figure 6.10: Contours of streamwise velocity in the case of d/D = 0.25 surface mounted obstacles.

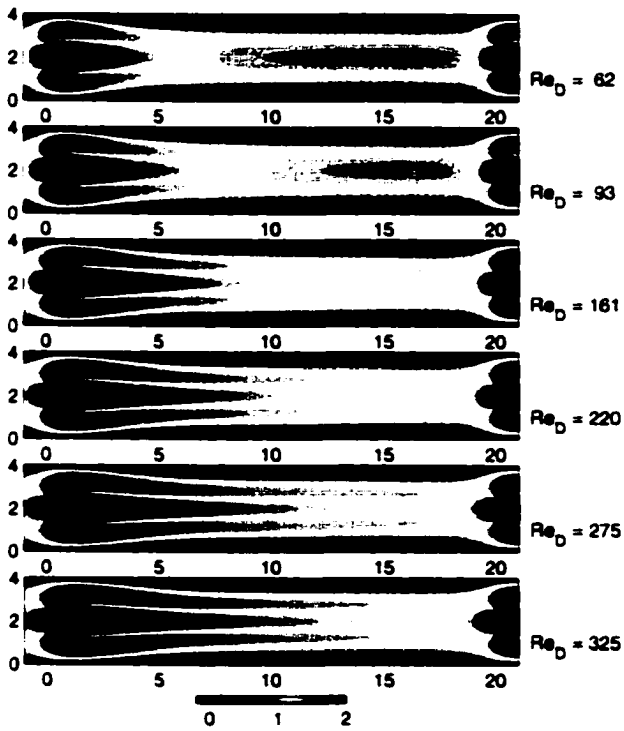

Figure 6.11: Contours of streamwise velocity in the case of d/D = 0.25 channel centred obstacles.

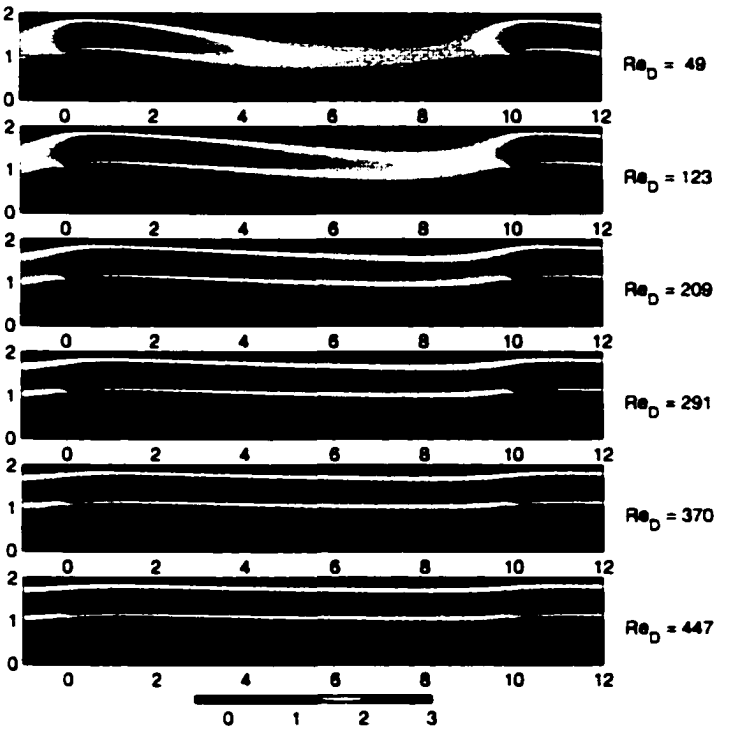

Figure 6.12: Contours of streamwise velocity in the case of d/D = 0.50 surface mounted obstacles.

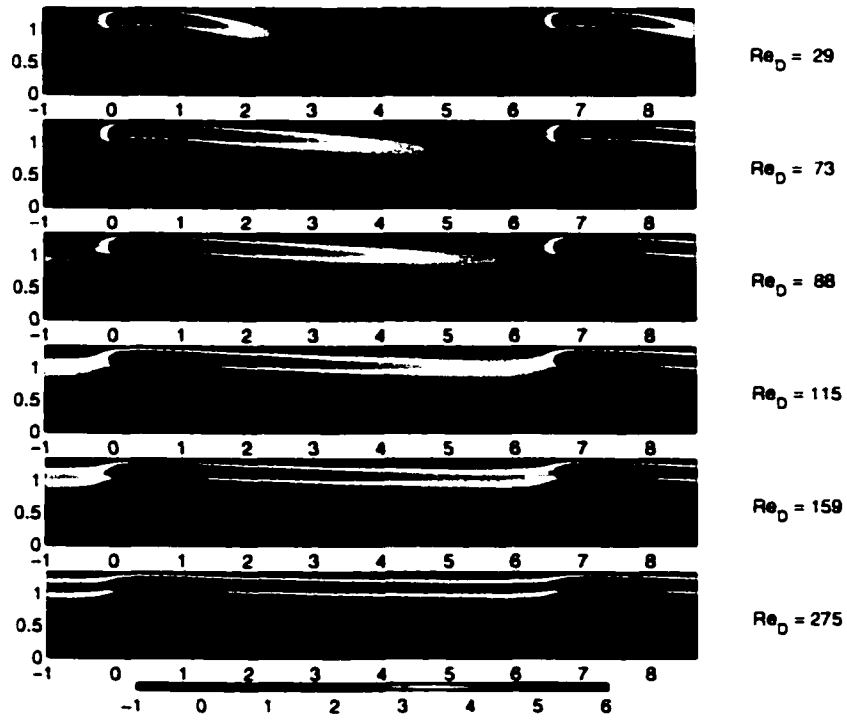

Figure 6.13: Contours of streamwise velocity in the case of d/D = 0.75 surface mounted obstacles.

6.5 Multiple Obstacle Flows

In order to check the validity of the periodic solutions, simulations were performed over a domain consisting of 10 obstacles and in a domain consisting of just one obstacle. Figure 6.14 presents streamlines over an array of surface mounted obstacles having d/D =0.25 and clearly shows small upstream recirculations, larger downstream recirculations, and the absence of reattachment on the bottom surface.

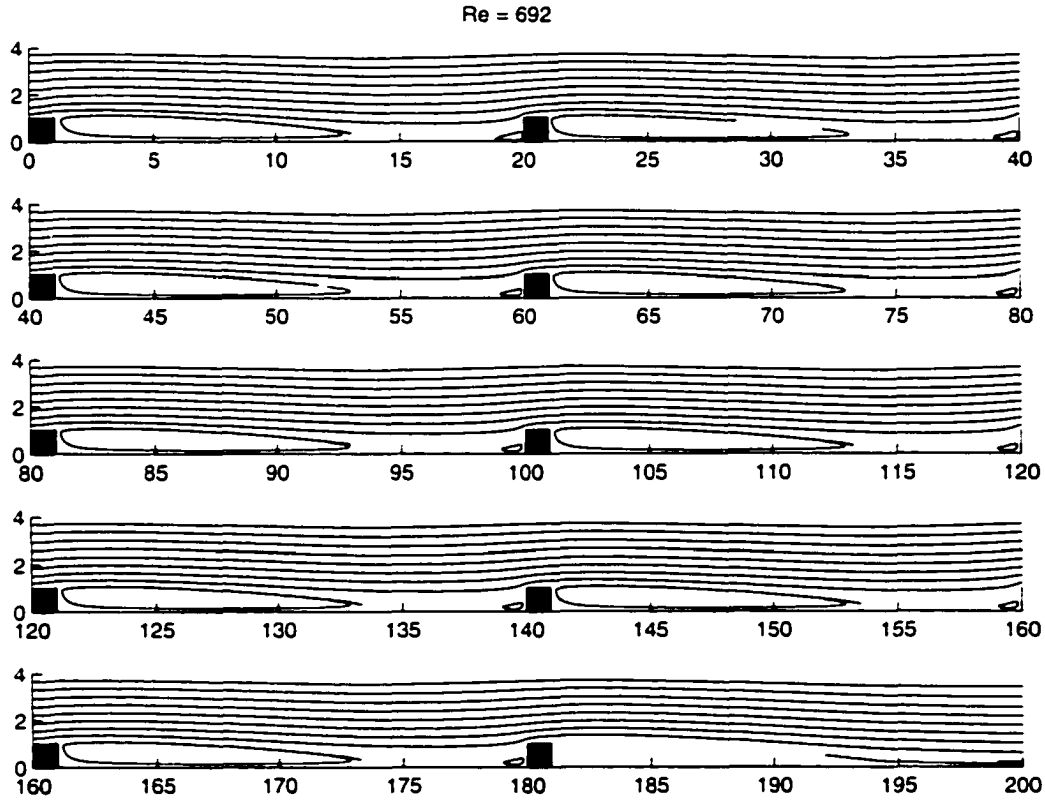

Figure 6.14: Streamlines over an array of 10 surface mounted obstacles. d/D = 0.25. $Re_D = 692$.

Figure 6.15 compares c_f on the bottom surface for both a single obstacle and a periodic array of obstacles at $Re_D = 100$, and $Re_D = 692$. In the case of $Re_D = 100$, there is very little difference, while at $Re_D = 692$ the differences become quite

pronounced. The small recirculation upstream of the obstacle is enlarged to the point where it merges with the downstream recirculation from the previous obstacle. This results in negative c_f values over the entire y/D = 0 surface and explains the apparent jump in X_r presented in figure 6.6; x/d = 20 (Re_D = 692) corresponds to the period of the domain, not the reattachment point.

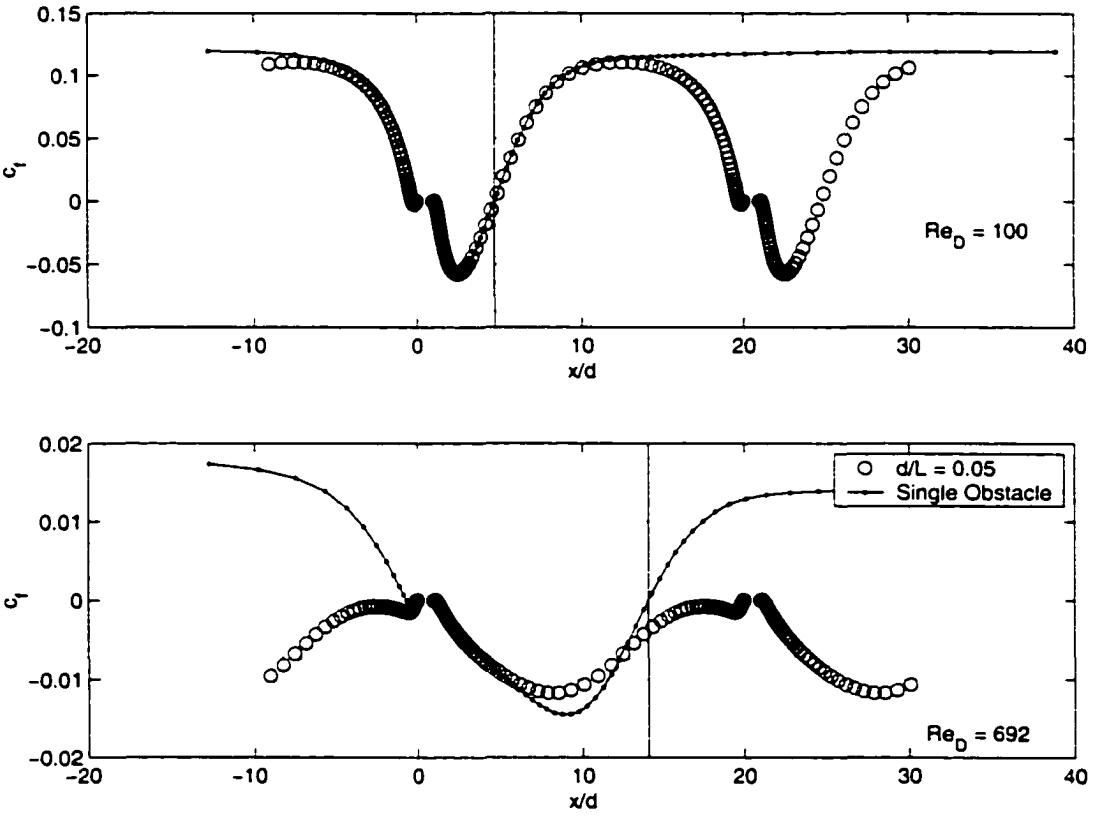

Figure 6.15: Comparison of single obstacle solution with a periodic obstacle solution for Re_D = 100 and Re_D = 692. The vertical lines represent reattachment in the single obstacle case.

Figure 6.16 compares the near-centreline velocity predicted with the periodic solution to several obstacles computed in the array for Re_D = 692. While fairly small, there are noticeable differences between the solutions which approach the periodic solution asymptotically. The differences between the periodic and multiple object

solutions become extremely small by the seventh obstacle. Similar computations at $Re_D = 100$ show that the periodic solution is developed at the first obstacle.

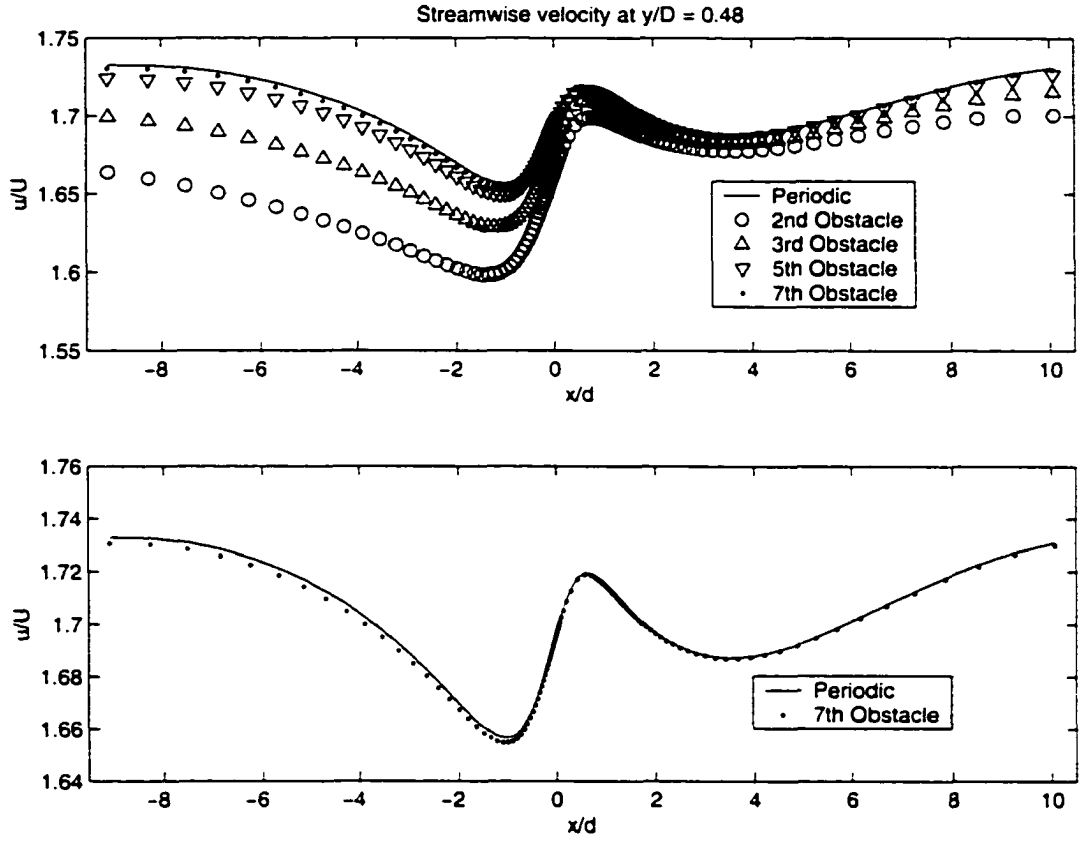

Figure 6.16: Comparison of periodic solution with multiple obstacle solution. $Re_D = 692$

Figure 6.17 and 6.18 present the computed c_f on the bottom and top surfaces at $Re_D = 100$ in the cases of no obstacles, surface mounted obstacles, channel centred obstacles and alternating surface mounted obstacles. Figure 6.17 presents all ten obstacles while an expanded view of only two obstacles, which is the minimum necessary in the case of alternating surface mounted obstacles, are shown in figure 6.18. The flow at this Reynolds number appears again to achieve a periodic solution by the first obstacle. The channel centred obstacles generate symmetric solutions

about the channel centerline with positive c_f everywhere, indicating there is no flow separation on the y/D = 0 and y/D = 1.0 surfaces. Both cases of surface mounted obstacles exhibit recirculation zones downstream of the obstacles and in the case of alternating surface mounted obstacles which are identical in both cases. In this case, the staggered obstacle solution over the second obstacle is identical to the bottom mounted solution with the y/D = 0 surface exchanged for the y/D = 1 surface. This is to be expected, since at $Re_D = 100$ the periodicity has very little effect on the solution; this is not the case for increasing Re_D.

Figures 6.19 and 6.20 present corresponding c_f values in the case of $Re_D = 692$. The case of channel centred obstacles is not shown. When all the obstacles are on the same surface, there is no reattachment between the obstacles. With a staggered obstacle arrangement however, the flow does reattach between obstacles and the peak c_f values on the y/d = 1.0 surface are visibly higher than in the case of surface mounted obstacles.

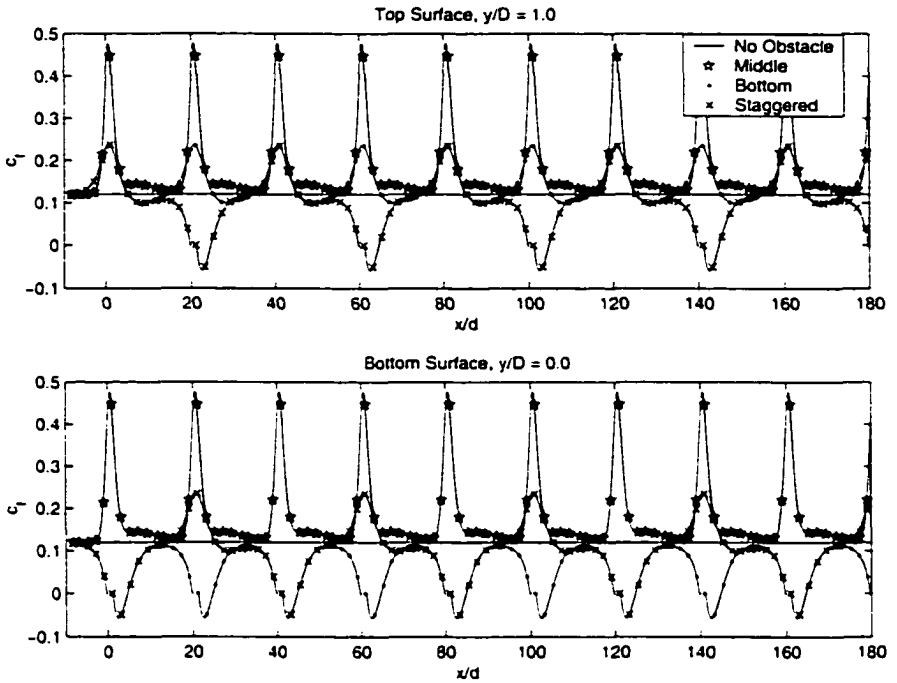

Figure 6.17: Friction coefficient vs x/d for various obstacle arrangements. Re_D = 100. Obstacles are located at x/d =[0.20.40.60.80.100.120.140.160.180]

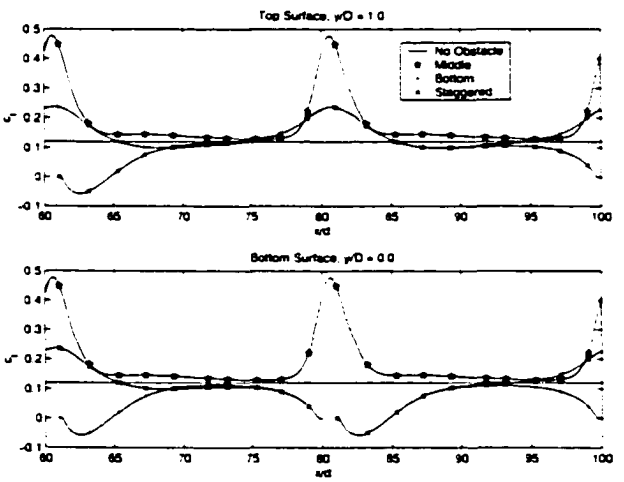

Figure 6.18: Friction coefficient vs x/d for two successive obstacles in the 10 obstacle array. Re_D = 100. Obstacles are located at x/d = [60,80,100]

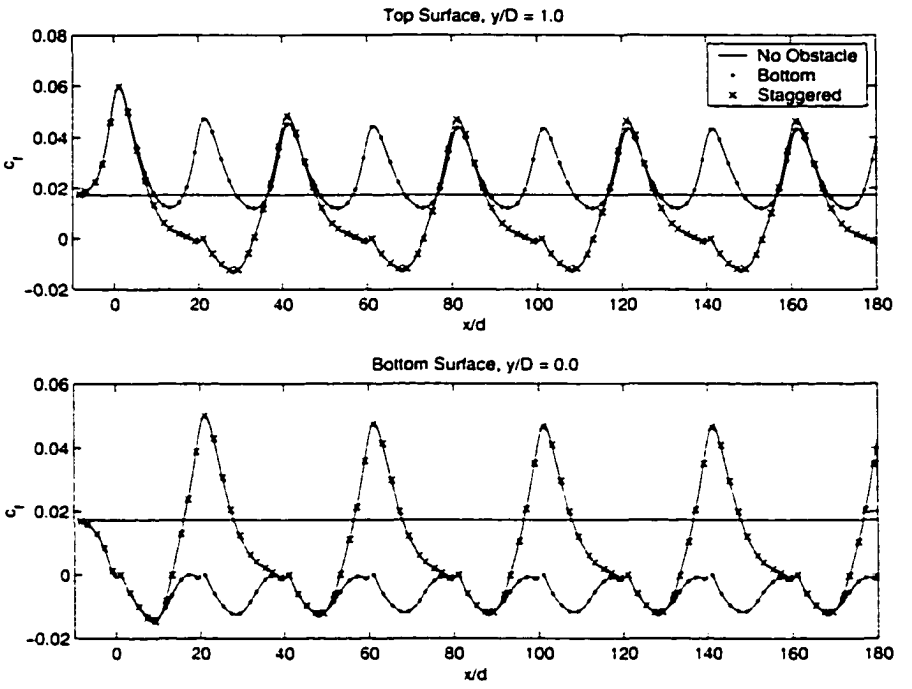

Figure 6.19: Friction coefficient vs x/d for various obstacle arrangements. Re_D = 692. Obstacles are located at x/d =[0,20,40,60,80,100,120,140,160,180]

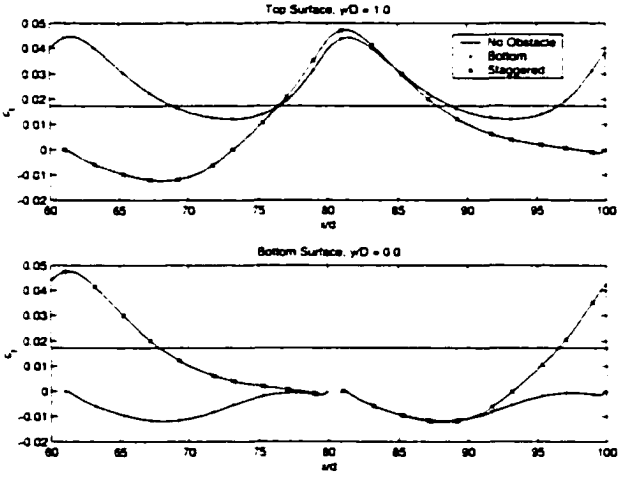

Figure 6.20: Friction coefficient vs x/d for two successive obstacles in the 10 obstacle array. Re_D = 692. Obstacles are located at x/d = [60,80,100]

6.6 Mass Transfer in Multiple Obstacle Flows

The STM model was used to model NaCl concentrations in the above arrays. The applied pressure was 1000 psi and the the feed solution was 35,000 ppm NaCl. The computed Re_w based on the volume flux and the unobstructed membrane area, are given in table 6.2 in the case of $Re_D = 100$, and in Table 6.3 in the case of $Re_D = 692$. All simulations having obstacles exhibit a higher fresh water flux even though using the unobstructed membrane area biases the case of no obstacles. At both Re_D, alternating surface mounted obstacles (staggered arrangement) are the best performing. Computed c_p values are also shown in the case of $Re_D = 100$. This value is related to the drag force on the obstacle and the average shear in the channels and represents the additional cost of pumping the fluid through the obstacle filled channels. It is very interesting to note that while c_p in the channel centred case is almost twice the value for the surface mounted obstacles the surface mounted obstacles significantly outperform the channel centred obstacles.

Geometry	Re_w	Re_w/Re_w(no obstacles)	c_p
No Obstacles	0.00739	1.00	0.12
Channel Centred	0.00808	1.09	0.033
Surface Mounted	0.00832	1.13	0.018
Staggered	0.00845	1.14	0.018

Table 6.2: Re_w, flux improvement and c_p predicted with the STM for various multi-obstacle solutions. $Re_D = 100$

Figure 6.21 presents the surface concentration on the y/D = 0 and y/D = 1.0 surfaces over all 10 obstacles for $Re_D = 100$ and figure 6.22 depicts a close up of the surface concentration over two successive obstacles. In the case of no obstacles, the surface concentration grows monotonically with distance along the channel and is symmetric about the y/D = 0.5. The NaCl distributions are greatly modified by the

Geometry	Re_w	Re_w/Re_w(no obstacles)
No Obstacles	0.00847	1.15
Surface Mounted	0.00898	1.22
Staggered	0.00911	1.23

Table 6.3: Re_w and flux improvement predicted with the STM for various multi-obstacle solutions. $Re_D = 692$. Flux improvement is referenced to the no obstacle solution at $Re_D = 100$.

presence of obstacles. In the case of surface mounted obstacles there is generally a spike in concentration just upstream of an obstacle and a larger decrease just downstream of an obstacle. While the average surface concentrations are lower in the case of obstacle flow, the spikes locally achieve levels in excess of the no obstacle case. The spikes correspond to stagnation points in the corners formed between the obstacles and the membrane surface while the decrease downstream of the obstacles is due to convective transport in the recirculation zone. This recirculation serves to transport NaCl from the surface towards the centre of the channel and hence to significantly mix the flow. In the case of channel centred obstacles, the concentration builds at a rate greater than that of the no obstacle solution and then decreases sharply as an obstacle is passed. The staggered obstacles perform better than the surface mounted obstacles since the concentration decreases due to the convective motion induced by the obstacles is greater than the decrease due to flow acceleration alone. In the case of surface mounted obstacles, the y/D = 0 surface benefits from the additional convective transport, while the y/D = 1 surface benefits from accelerated flow around the obstacle. In the case of the staggered arrangement, both surfaces experience significant decreases in concentration downstream of the obstacles. This results in a significantly lower surface concentrations on the y/D = 1 surface in the case of staggered obstacles. It is clear from the figures that the NaCl concentration on the

y/D = 0 surface closely tracks the case of surface mounted obstacles downstream of the obstacles when the obstacles coincide (x/d = 80). Figures 6.23 and 6.24 present that same plots in the case of $Re_D = 692$. This feature is no longer evident, reflecting the significant change in the characteristics of the 'separation bubbles' due to the interactions between successive obstacles.

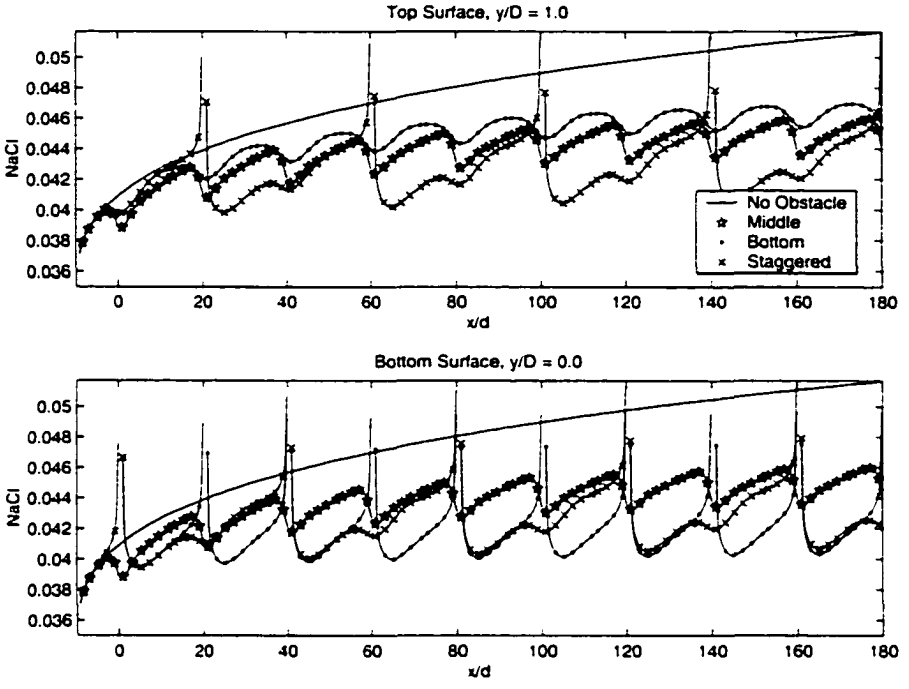

Figure 6.21: Surface NaCl concentration vs x/d for various obstacle arrangements. Re_D = 100. Feed concentration = 35,000 ppm. Obstacles are located at x/d =[0,20,40,60,80,100,120,140,160,180]

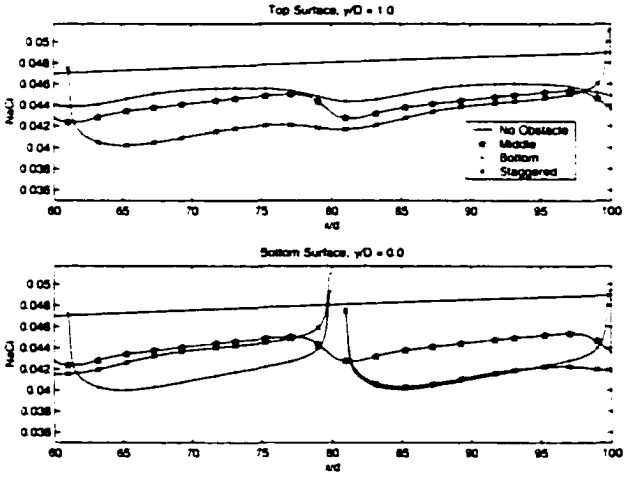

Figure 6.22: Surface NaCl concentration vs x/d for two successive obstacles in the 10 obstacle array. Re_D = 100. Feed concentration = 35,000 ppm. Obstacles are located at x/d = [60,80,100]

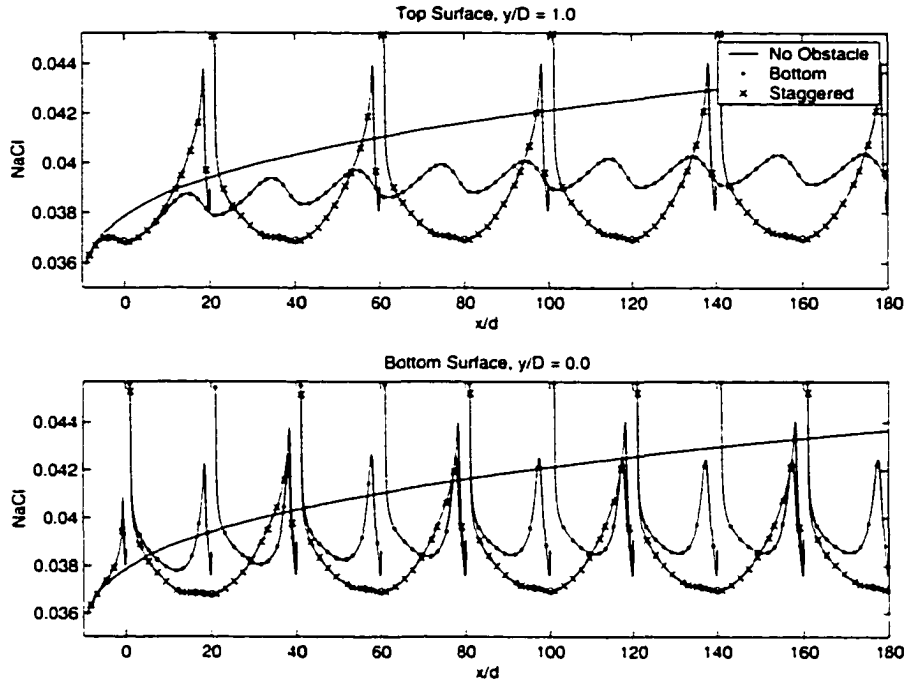

Figure 6.23: Surface NaCl concentration vs x/d for various obstacle arrangements. Re_D = 692. Feed concentration = 35,000 ppm. Obstacles are located at x/d =[0,20,40,60,80,100,120,140,160,180]

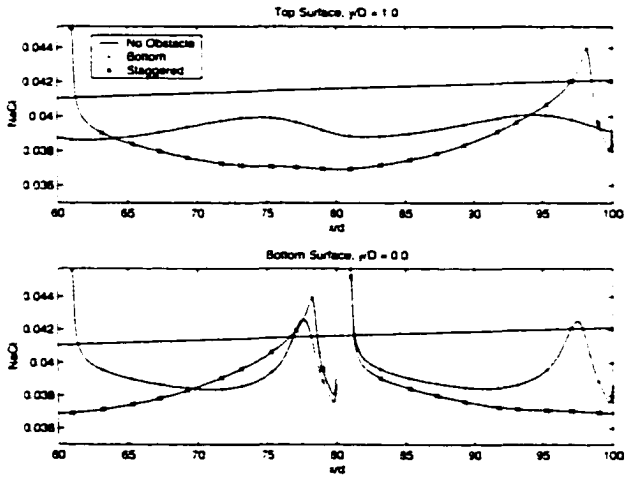

Figure 6.24: Surface NaCl concentration vs x/d for two successive obstacles in the 10 obstacle array. Re_D = 692. Feed concentration = 35,000 ppm. Obstacles are located at x/d = [60,80,100]

6.7 Effect of Rotation

Rotating three-dimensional simulations were carried out in channels of aspect ratio 3 in periodic domains having surface mounted obstacles with d/D = 0.25,0.50,0.75 and L/D = 5.0 at various Re_D. Rotation is about an axis aligned with the short channel dimension, corresponding to the case of 'Normal' rotation presented in Chapter 4. Table 6.4 presents the Rossby and Ekman numbers developed for each rotational speed when $Re_D = 100$. As Ro decreases, the pressure gradient needed to sustain a given Re_D increases, or for the same pressure gradient, Re_D decreases. This is shown in figure 6.25 which presents the computed Re_D vs 1/Ro for a constant pressure gradient in the cases of d/D = 0.25,0.50 and c_f vs. 1/Ro at $Re_D = 100$ for d/D = 0.75. Since the pressure gradient needed to generate a fixed Re_D is not known a priori, a control loop was implemented in the code which adjusted β during the solution to maintain Re_D constant.

Ω [rad/s]	Ro	1/Ro	Ek
0	∞	0	∞
50	1.82	0.5480	0.0182
100	0.91	1.0960	0.0091
150	0.61	1.6440	0.0061
200	0.46	2.1920	0.0046
250	0.37	2.7401	0.0037
300	0.30	3.2881	0.0030
350	0.26	3.8361	0.0026
400	0.23	4.3841	0.0023

Table 6.4: Computed Rossby and Ekman numbers assuming $Re_D = 100$.

In three-dimensions, the wall shear stress has 2 components resulting respectively from the streamwise and spanwise velocity profiles. Accordingly, we can define three different friction coefficients.

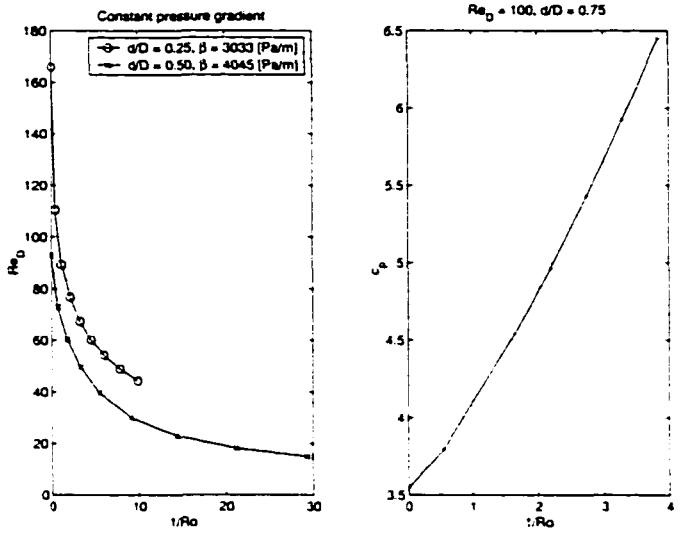

Figure 6.25: The effect of system rotation on Re_D and c_p.

$$c_{fx} = \frac{\tau_{yx}}{0.5\rho U^2} \tag{6.4}$$

$$c_{fz} = \frac{\tau_{yz}}{0.5\rho U^2} \tag{6.5}$$

$$c_f = \sqrt{c_{fx}^2 + c_{fz}^2} \tag{6.6}$$

Figure 6.26 presents the various friction coefficients on the y/D=0 and y/D surfaces in the case of d/D = 0.25 in the absence of channel rotation. While figure 6.27 presents the same data when the channel is a rotating with Ro = 0.33. Overlaid on the figures are contour lines representing respective c_f values of zero. These contour lines correspond roughly to where the flow reattaches. In the case of no channel rotation, the solutions are symmetric about z/D = 0 and there is very little spanwise shear. There is a small upstream recirculation zone ahead of the obstacle and

a larger recirculation zone downstream of the obstacle. When channel rotation is introduced however, the solution changes considerably. The upstream recirculation zone grows slightly while the downstream recirculation shrinks significantly and there is no longer any symmetry in the solution. c_{fz} is negative over most of the surface and has a magnitude similar to c_{fx}. The shrinkage and asymmetry of the 'separation bubble' is illustrated in figure 6.28 which shows contour lines of zero c_{fx} downstream of the obstacle as a function of Ro. Appendix C presents c_f plots on the y/D = 0 and y/D = 1 surfaces over the range of Ro simulated as well as in the cases of d/D = 0.50 and d/D = 0.75. Both as the blockage ratio, d/D, and as Ro is increased, the flows become increasingly complex. In the case of d/D = 0.50, regions of zero shear appear on the y/D = 1.0 surface at the lowest rotation rate. The characteristics and even the number of these regions change as Ro is varied. The flow in channels with blockage ratios of 0.75 is more complicated still.

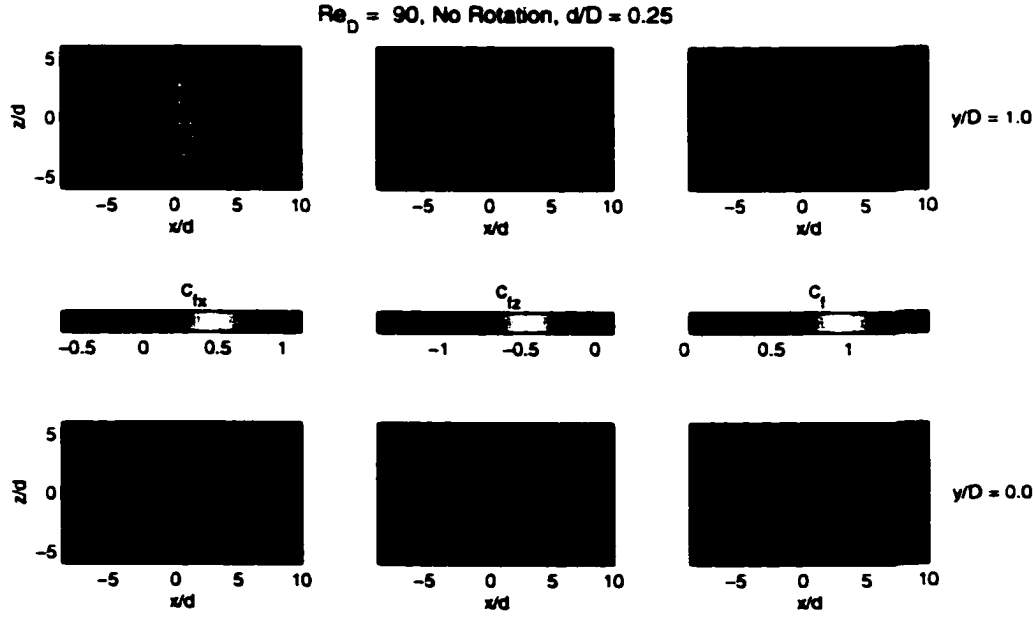

Figure 6.26: Friction coefficients on the y/D = 0 and y/D = 1 surface. $Re_D = 90$, No Rotation, d/D = 0.25

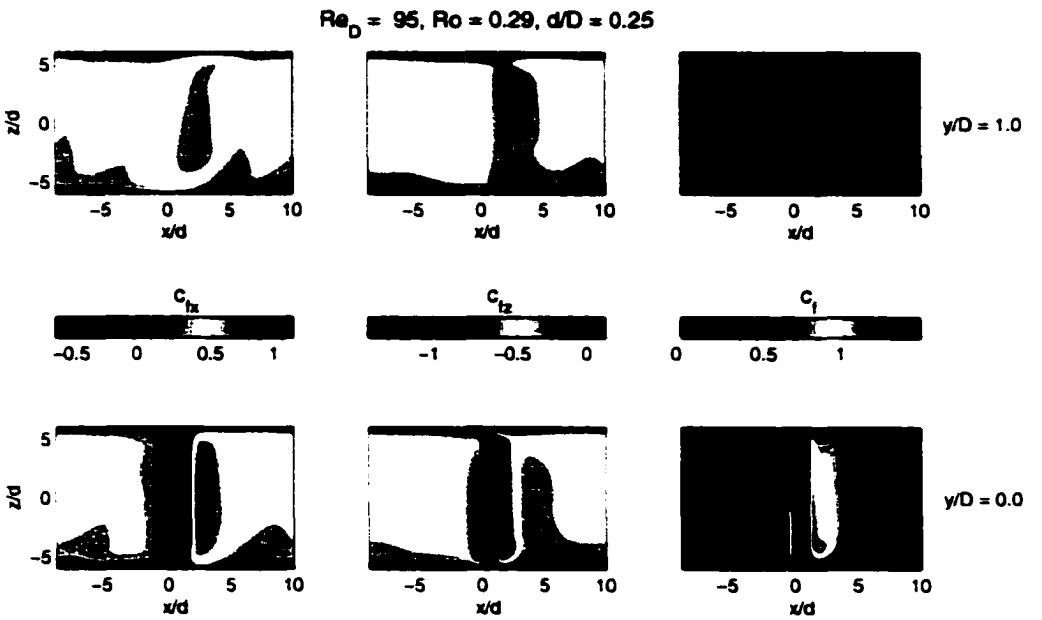

Figure 6.27: Friction coefficients on the y/D = 0 and y/D = 1 surface. Re_D = 95, Ro = 0.29. d/D = 0.25

Figure 6.29 presents contour slices of streamwise and spanwise velocity when d/D = 0.25. When there is no channel rotation, the only non-zero spanwise velocities are located close to the obstacle, and the streamwise velocity distributions are symmetric about the z = plane. As rotation is increased, strong spanwise velocities are generated which transport high momentum fluid above the obstacle towards the lagging sidewall. There are correspondingly large negative spanwise velocities along the y/D=0 surface just downstream of the obstacle. Inspection of the plane presented just downstream of the obstacle shows both that the maximum streamwise velocity is shifted towards the lagging wall and becomes significantly lower than in the case of no rotation. These characteristics are reminiscent of the flow in rotating channels presented in Chapter 4, but are significantly modified by the presence of obstacles in the flow. At Ro = 0.29 the flow has changed considerably, with two regions of positive spanwise velocity evident downstream of the obstacle near the y/D = 1 and y/D = 1 walls.

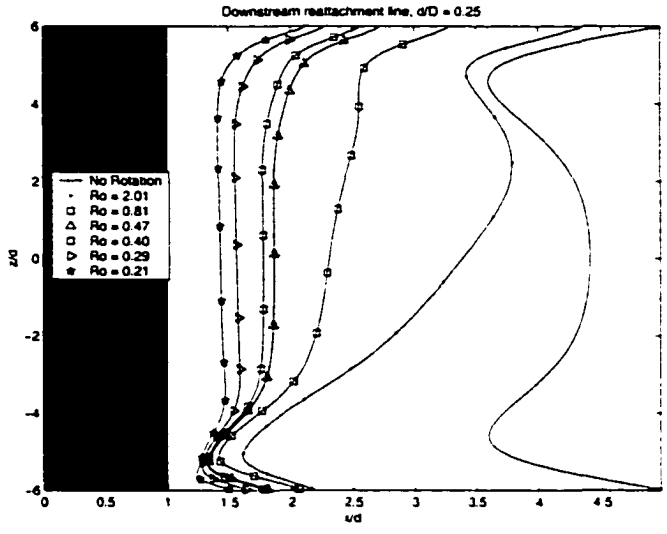

Figure 6.28: Position of the downstream reattachment line for various rates of rotation. d/D = 0.25.

Figure 6.30- 6.32 present similar plots in the case of d/D = 0.50 and d/D = 0.75. These flows are similar in character to the case of d/D = 0.25 only in the absence of rotation. The flow fields are complex, and vary greatly with Ro.

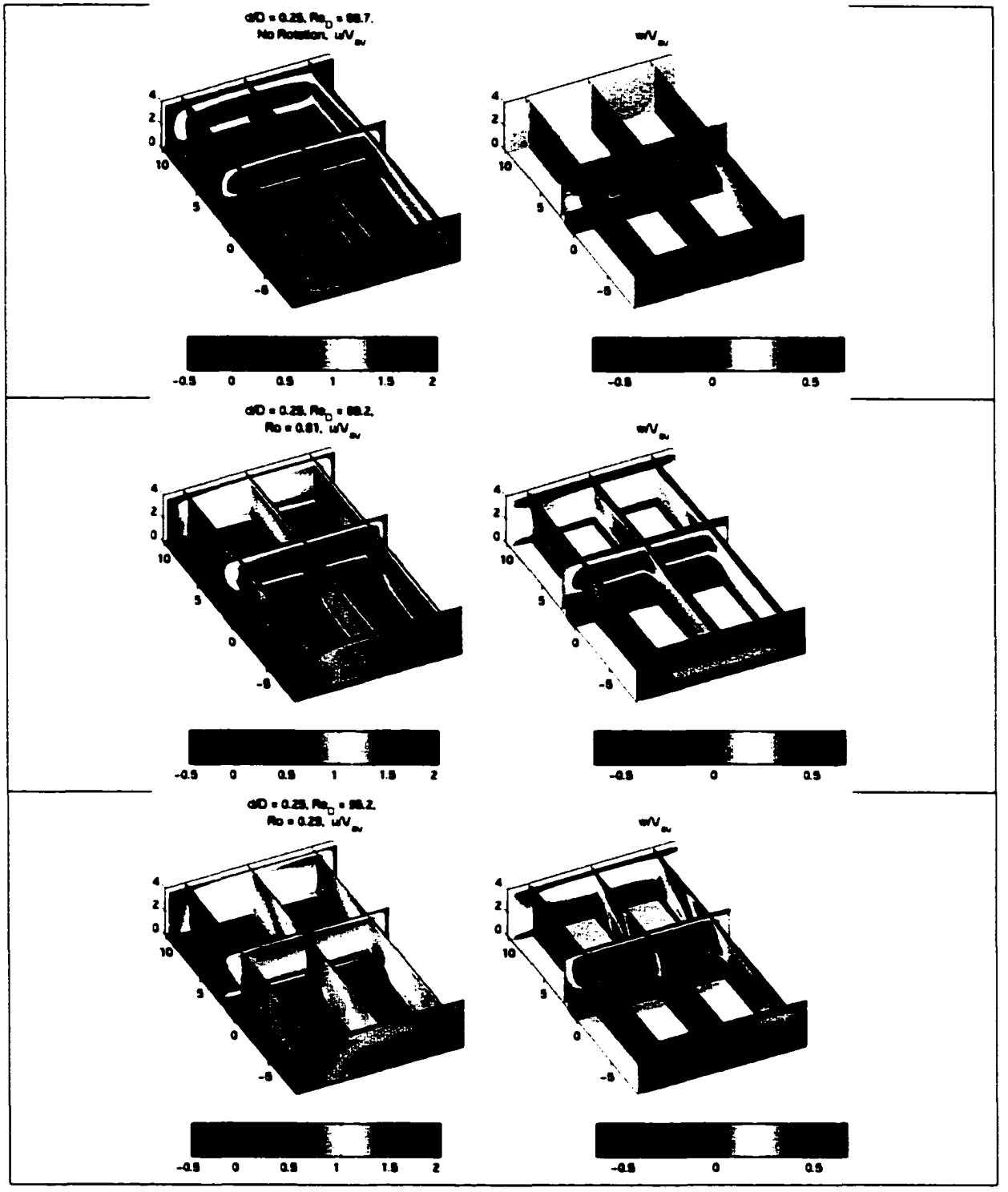

Figure 6.29: Contours of streamwise and spanwise velocity, d/D = 0.25. No Rotation (top), Ro = 0.81 (middle) and Ro = 0.29 (bottom).

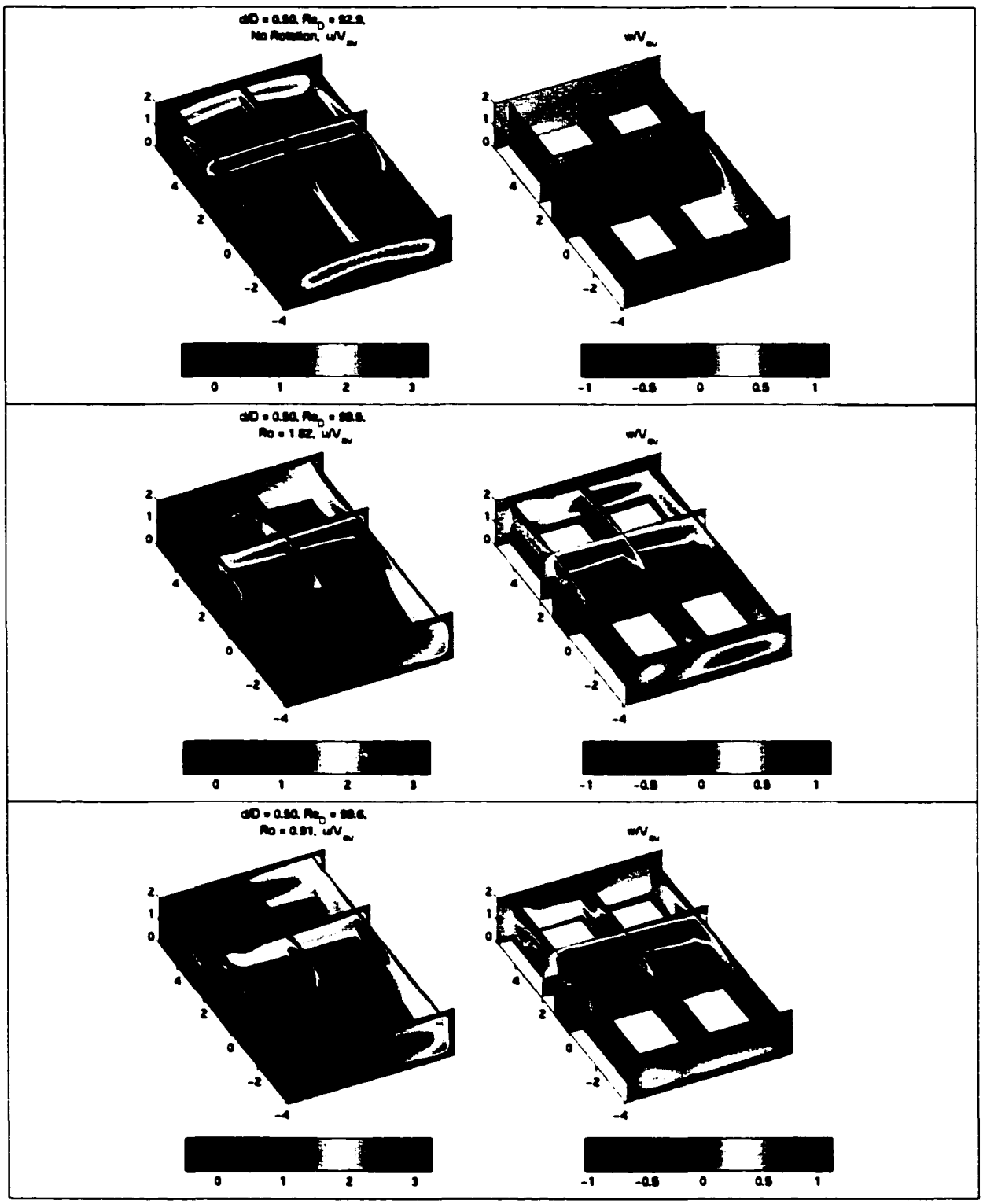

Figure 6.30: Contours of streamwise and spanwise velocity, d/D = 0.50. No Rotation (top), Ro = 1.82 (middle) and Ro = 0.!la91 (bottom).

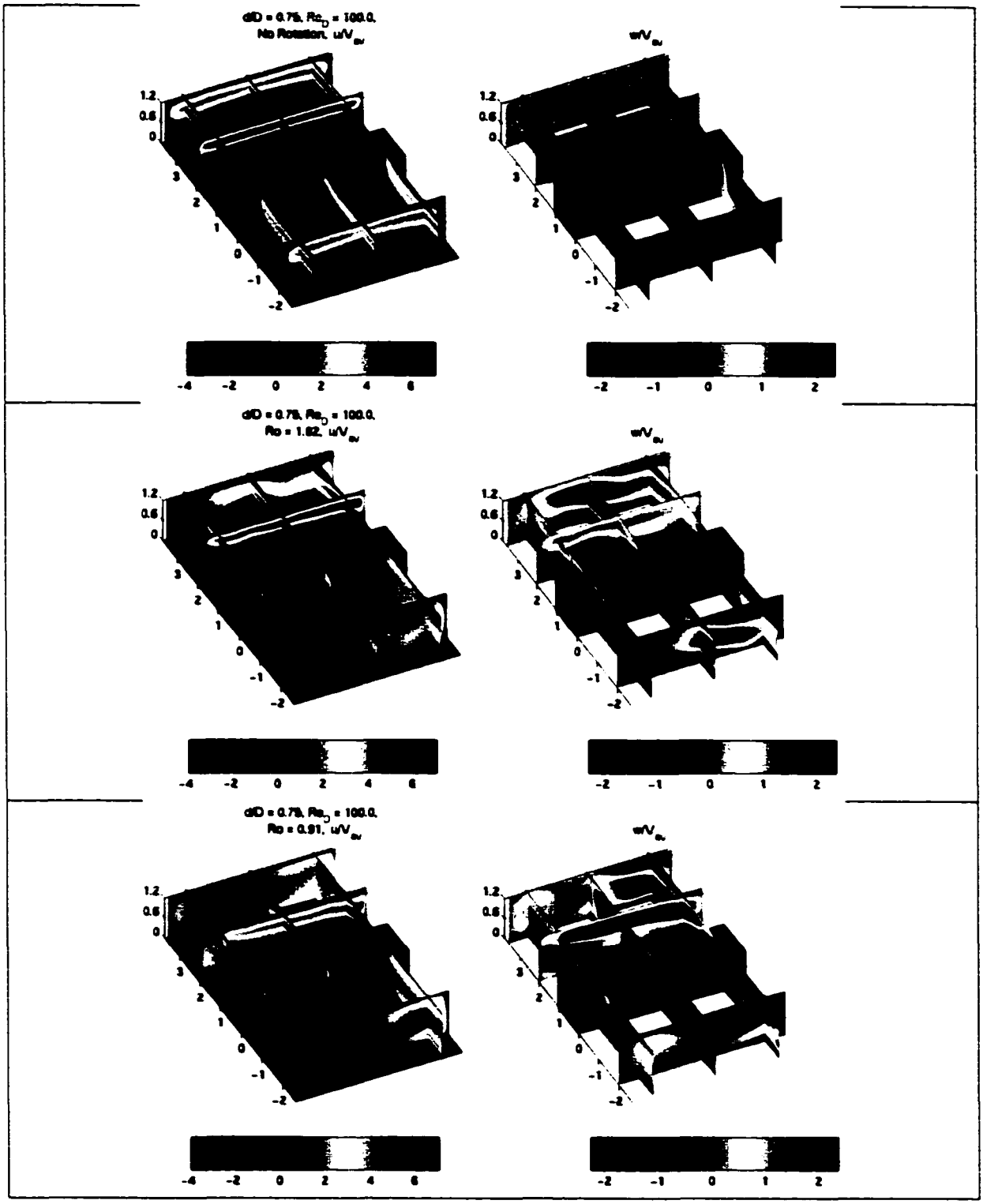

Figure 6.31: Contours of streamwise and spanwise velocity, d/D = 0.75. No Rotation (top), Ro = 1.82 (middle), Ro = 0.91 (bottom).

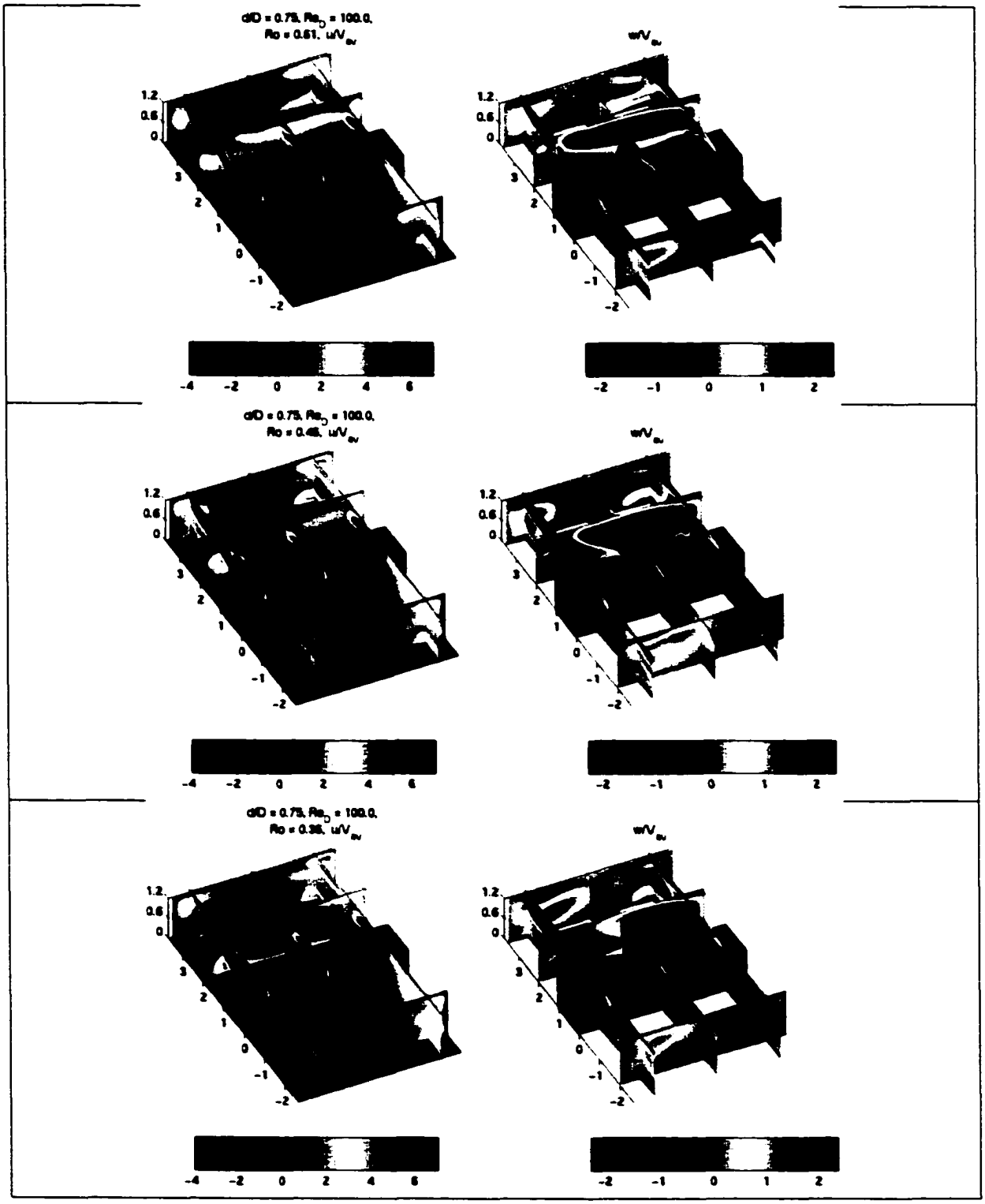

Figure 6.32: Contours of streamwise and spanwise velocity, d/D = 0.75. Ro = 0.61 (top), Ro = 0.46 (middle) and Ro = 0.36 (bottom).

6.8 Closure

Simulations were performed over a variety of periodic obstacle geometries relevant to membrane separation including surface mounted obstacles, alternating surface mounted obstacles and channel centred obstacles. These simulations were performed over arrays of 10 obstacles as well as for domains consisting of one obstacle with a streamwise periodic boundary condition to account for adjacent obstacles. The 10 obstacle results were compared with the periodic solutions and it was shown that at $Re_D = 100$ periodicity has little effect on the solution and the periodic solution develops at the first obstacle. In the case of $Re_D = 692$, the periodic solution takes approximately seven obstacles to develop and is markedly different than in the case of a single obstacle, with upstream and downstream recirculations merging such that reattachment does not occur.

The STM was used to predict membrane performance in the presence of various obstacle configurations in the absence of system rotation and it was found that

- In the case of non-rotating channels, the presence of flow obstacles improves membrane performance in all cases.
- The presence of flow obstacles results in local concentration maximums which exceed the corresponding concentration in the case of open channels.
- Channel centred obstacles are least performing while staggered obstacles are most performing.
- Channel centred obstacles result in the largest c_p (and hence shear) even though they are less performing.
- Recirculation zones are far more effective at mixing the flow than are accelerated flow regions.

- There is no general correlation between c_f and mass transfer performance.

In addition, it is very difficult to infer mass transfer characteristics from the hydrodynamics solutions. This point is perhaps most clearly made considering the case of staggered obstacles compared to surface mounted obstacles at $Re_D = 100$. The friction coefficients and flow characteristics are effectively the same, and yet the mass transfer performance of the two arrangements is clearly different.

A preliminary investigation into the effect of system rotation was also undertaken, indicating that rotation has a significant effect on the hydrodynamics. The resulting flow fields depend strongly on the blockage ratio and on Ro. With the introduction of rotation, friction coefficients are significantly higher, recirculation zones are greatly altered and the solutions are no longer symmetric. Mass transfer predictions will have to be carried out in the future to determine the effect of rotation on membrane performance.

Appendix A

CMS Operating Parameters

A.1 Fluid Properties

Much of the experimental and computational work has been carried out using aqueous NaCl solutions at concentrations of:10,000 ppm, 22,000 ppm, 35,000 ppm and 50,000 ppm. Basic fluid properties for these concentrations, at $25°C$, are given in Table A.1 [3].

Concentration $[ppm]$	Density $[kg/m^3]$	Dynamic Viscosity $[kgm/s] \times 10^4$	Kinematic Viscosity $[m^2/s] \times 10^7$	Osmotic Pressure [MPa]
0	997.19	8.973	8.998	[-]
10,000	1004.07	9.086	9.049	0.8529
22,000	1012.41	9.239	9.126	1.5679
35,000	1021.53	9.426	9.228	2.4652
50,000	1032.18	9.670	9.369	3.6594

Table A.1: Properties of NaCl Solutions at various concentrations and 25°C

Pressure $[MPa]$	Pressure $[psi]$	$\Omega[rad/s]$ (0 ppm)	$\Omega[rad/s]$ (10,000 ppm)	$\Omega[rad/s]$ (22,000 ppm)	$\Omega[rad/s]$ (35,000 ppm)
1.38	200	92.02	91.70	91.33	90.92
2.07	300	112.70	112.32	111.85	111.35
2.76	400	130.14	129.69	129.16	128.58
3.45	500	145.50	145.00	144.40	143.75
4.14	600	159.38	158.84	158.18	157.47
4.83	700	172.16	171.56	170.86	170.09
5.52	800	184.04	183.41	182.65	181.84

Table A.2: Rotational speed required to develop various transmembrane pressures in CMS plate and frame assemblies

A.2 CMS Operating Conditions

A.2.1 Plate and Frame System

The pressure differential across the membrane is called the transmembrane pressure (P_{TM}), and is the driving force for the separation processs. This pressure is almost constant over the entire membrane [65] and depends upon the rotation rate of the CMS device and the permeate release radius, r_p, according to

$$\Delta P_{TM} = \frac{1}{2}\rho\Omega^2 r_p^2. \tag{A.1}$$

The plate and frame experiments were carried out at either 2l/min, or 4l/min which, corresponding to cross flow velocities of 0.085 m/s and 0.17 m/s assuming nine open channels. The permeate release radius for this device was 0.5717m from the axis of rotation. Table A.2 shows the necessary rotational speed in order to develop various transmembrane pressures with this device.

Concentration [ppm]	Re (2 l/min / 4 l/min)
0	72.0 / 144.0
10,000	71.6 / 143.2
22,000	71.0 / 142.0
35,000	70.2 / 140.4

Table A.3: Reynolds numbers achieved in the plate and frame assemblies

Pressure [MPa]	Pressure [psi]	Ro (0 ppm)	Ro (10,000 ppm)	Ro (22,000 ppm)	Ro (35,000 ppm)
1.38	200	1.21 / 2.42	1.22 / 2.43	1.22 / 2.44	1.23 / 2.45
2.07	300	0.99 / 1.98	0.99 / 1.99	1.00 / 2.00	1.00 / 2.00
2.76	400	0.86 / 1.71	0.86 / 1.72	0.86 / 1.73	0.87 / 1.74
3.45	500	0.77 / 1.53	0.77 / 1.54	0.77 / 1.54	0.78 / 1.55
4.14	600	0.70 / 1.40	0.70 / 1.41	0.71 / 1.41	0.71 / 1.42
4.83	700	0.65 / 1.30	0.65 / 1.31	0.65 / 1.31	0.66 / 1.31
5.52	800	0.61 / 1.21	0.61 / 1.22	0.61 / 1.22	0.61 / 1.23

Table A.4: Rossby numbers at various operating conditions in CMS plate and frame assemblies. Rossby numbers are for feed flows of (2 l/min / 4 l/min) and assume nine open channels.

Pressure [MPa]	Pressure [psi]	Ek (0 ppm)	Ek (10,000 ppm)	Ek (22,000 ppm)	Ek (35,000 ppm)
1.38	200	0.0168	0.0170	0.0172	0.0175
2.07	300	0.0138	0.0139	0.0141	0.0143
2.76	400	0.0119	0.0120	0.0122	0.0124
3.45	500	0.0107	0.0107	0.0109	0.0111
4.14	600	0.0097	0.0098	0.0099	0.0101
4.83	700	0.0090	0.0090	0.0092	0.0093
5.52	800	0.0084	0.0085	0.0086	0.0087

Table A.5: Ekman numbers at various operating conditions in CMS plate and frame assemblies.

Pressure $[MPa]$	Pressure $[psi]$	Ω $[rad/s]$
2.76	400	180
3.45	500	201
4.14	600	220
4.83	700	238
5.52	800	254
6.21	900	270
6.89	1000	285

Table A.6: Rotational speed required to develop various transmembrane pressures in CMS spiral wound assemblies.

A.2.2 Commercial Spiral Wound Elements

Both the geometry of the membrane channels and the premeate release radius are different in the CMS apparatus designed for commercial spiral wound membrane elements. This apparatus is designed to use 2514 membrane modules which means that they have a nominal outer diameter of 2.5", and a length of 14". The permeate release radius is 0.41 m (16.25") from the axis of rotation, which means that the device must turn faster than the plate and frame assemby to generate the same transmembrane pressure. Table A.6 presents the required speeds to achieve various operating conditions, where the density has been assumed to be $1000 kg/m^3$ since the variations shown above are relatively small.

In order to quantify the fluid mechanical parameters, two different feed spacers, shown in figure A.1 will be considered: a ladder type spacer found in an Osmonics module and a diamond type spacer found in a FilmTec module.

The ladder spacer features nearly cylindrical primary elements running in the flow direction, with thinner cylindrical cross supports running in a perpendicular direction between them. These cross supports are flush with one edge of the primary

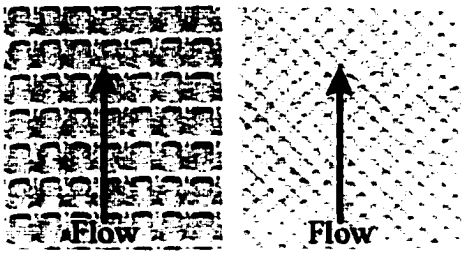

Figure A.1: Feed spacers removed from modules at UVic. Ladder type spacer on the left and diamond type spacer on the right.

Primary Elements	0.050"	1.27 mm
Cross Supports	0.030"	0.76 mm
Spacing between Primary Elements (inside dimensions	0.150"	3.81 mm
Spacing between Cross Supports (centre to centre	0.250"	6.35 mm

Table A.7: Dimensions of ladder type spacer

elements such that the spacer is planar on one side. Table A.7 presents the dimensions measured from the ladder spacer.

The diamond spacer features sets of identical elements running perpendicular to each other to form square cells oriented (in this case) at 45° to the flow direction. One set of these elements is laid on top of, and penetrates a certain distance into the other set such that neither face of the spacer is planar. Table A.8 presents the measured dimensions of the diamond spacer.

Overall Thickness	0.023"	0.58 mm
Element Thickness	0.015"	0.38 mm
Penetration Depth	0.007"	0.18 mm
Spacing between elements (centre to centre	0.110"	2.79 mm

Table A.8: Dimensions of diamond type spacer

Feed $[m^3/s]$	Feed $[lpm]$	Re	Ro (400 psi / 1000 psi)
6.67×10^{-5}	4	42.4	0.64 / 0.40
1.33×10^{-4}	8	42.4	0.64 / 0.40
2.50×10^{-4}	15	42.4	0.64 / 0.40
3.33×10^{-4}	20	42.4	0.64 / 0.40
3.83×10^{-4}	23	42.4	0.64 / 0.40

Table A.9: Reynolds numbers and Rossby numbers, based on spacer thickness, in the diamond spacer. Based on a 35,000 ppm feed. Rossby numbers are for speeds corresponding to 400 psi and 1000 psi respectively.

Feed $[m^3/s]$	Feed $[lpm]$	Re	Ro (400 psi / 1000 psi)
6.67×10^{-4}	4	92.1	0.29 / 0.19
1.33×10^{-4}	8	184.2	0.59 / 0.37
2.50×10^{-4}	15	345.3	1.10 / 0.69
3.33×10^{-4}	20	460.4	1.46 / 0.93
3.83×10^{-4}	23	529.5	1.68 / 1.06

Table A.10: Reynolds numbers and Rossby numbers, based on spacer thickness, in the ladder spacer. Based on a 35,000 ppm feed. Rossby numbers are for speeds corresponding to 400 psi and 1000 psi respectively.

	Plate & Frame	Diamond	Ladder
Re	70-144	42-244	92 - 530
Ro	0.61-2.45	0.64 - 2.31	0.19 - 1.68
Ek	0.0087 - 0.0175	0.01 - 0.015	0.002 - 0.003

Table A.11: Summary of operating conditions for various CMS devices.

Appendix B

Flux Equations for Flow Through Semi-Permeable Membranes

The flux equations for the transport of both solute and solvent can be derived using irreversible thermodynamics [4]. This approach states that the entropy increase due to reversible processes may be related to the sum of all fluxes and their driving forces, and that near equilibrium the forces and the fluxes are linearly related. In the membrane processes with which we are concerned, there are two driving forces, the chemical potential gradient of the solvent ($\Delta\mu_1$) and the solute ($\Delta\mu_2$), and two mass fluxes, the solvent flux (J_1) and the solute flux(J_2)

$$J_1 = -L_{11}\Delta\mu_1 - L_{12}\Delta\mu_2 \tag{B.1}$$

$$J_2 = -L_{21}\Delta\mu_1 - L_{22}\Delta\mu_2 \tag{B.2}$$

where L_{ij} are the coupling coefficients.

The chemical potential can be separated into a hydrodynamic pressure difference, ΔP, and a concentration gradient represented by the osmotic pressure difference, $\Delta\Pi$, where an ideal solution has been assumed in relating activities to concentrations. Following [4], equations (B.1) and (B.2) can be cast in terms of a total volume flux, j_v and a solute mass flux, J_s.

$$j_v = L_p(\Delta P - \sigma\Delta\Pi) \tag{B.3}$$

$$J_s = (1 - \sigma')\bar{c}j_v + \omega\Delta\Pi \tag{B.4}$$

where L_p is the hydraulic permeability of the membrane, ω is the solute permeability, $\bar{c}$ is the average concentration difference across the membrane, and σ and σ' are transport coefficients referred to as reflection coefficients. It is common at this point to invoke the principle of microscopic dynamic reversibility, or Onsager's principle [67], to equate σ and σ'.

In the literature, a perfectly rejecting membrane is said to have a reflection coefficient of 1, a non selective membrane is said to have a reflection coefficient of 0, and a selective membrane to have a reflection coefficient between 0 and 1. This term, in this context, relates only to the convective flux of solution, as it is apparent from equations (B.3) and (B.4) that with

$$\sigma = \sigma' = 1.0 \tag{B.5}$$

there is still a diffusive flux of solute which is proportional to the solute permeability. The rejection, R, is a true measure of the solute rejection, and is defined as

$$R = 1 - \frac{\rho_p \phi_p}{\rho_f \phi_f} \tag{B.6}$$

where $\rho\phi$ is the concentration, c, the subscript p refers to the permeate, and the subscript f refers to the feed. If we assume that the membrane is a perfect rejector with respect to convection, given by equation (B.5), then the flux equations reduce to

$$j_v = L_p(\Delta P - \Delta\Pi) \tag{B.7}$$

$$J_s = \omega\Delta\Pi \tag{B.8}$$

Since the osmotic pressure difference is representative of the concentration gradient across the membrane. Equation (B.8) may be rewritten as

$$J_s = \omega'\Delta c \tag{B.9}$$

and noting that the concentration of the permeate is

$$c_p = \frac{J_s}{j_v} \tag{B.10}$$

Equations (B.6) , (B.9) and (B.10) can be used to solve for the modified solute permeability

$$\omega' = \frac{j_v(1 - R)}{R} \tag{B.11}$$

giving a solute mass flux of

$$J_s = \frac{j_v(1-R)}{R}(c_f - c_p) \tag{B.12}$$

This means that if dynamic reversibility is assumed and if the membrane is a perfect rejector with respect to convection, the flux equations can be completely specified with only two experimentally determined constants, as was done in this paper. The hydraulic permeability, L_p can be determined from equation (B.7) by measuring the slope of the flux versus pressure curve for pure solvent since the $\Delta\Pi$ term goes to zero in the limit of pure solvent. The solute permeability can be set according to Equation (B.12) in order to achieve an experimentally observed rejection.

Appendix C

Rotating Obstacle Flow: Surface shear

C.1 d/D = 0.25

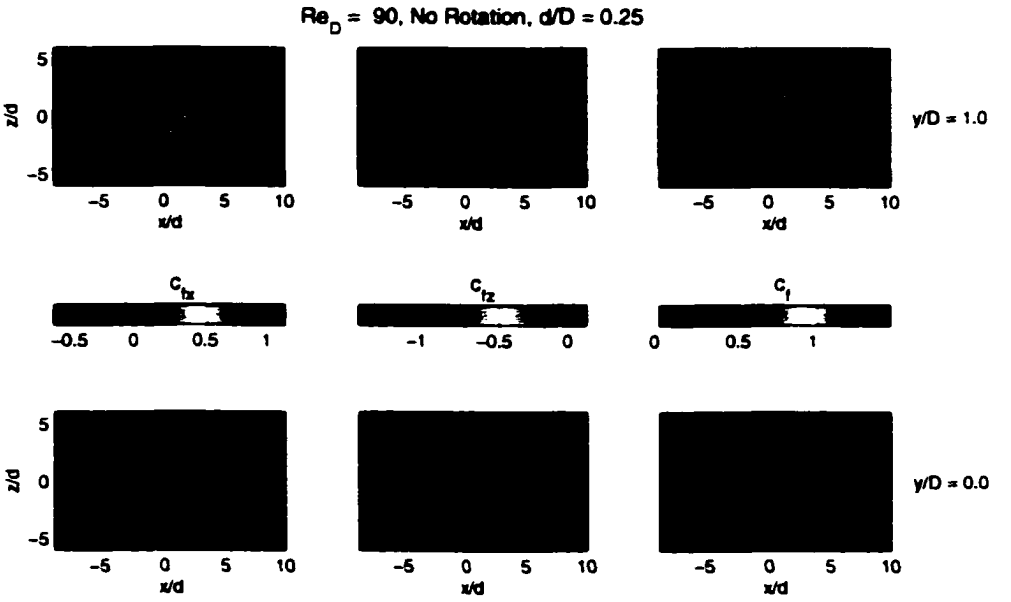

Figure C.1: Friction coefficients on the y/D = 0 and y/D = 1 surface. $Re_D = 90$, No Rotation, d/D = 0.25

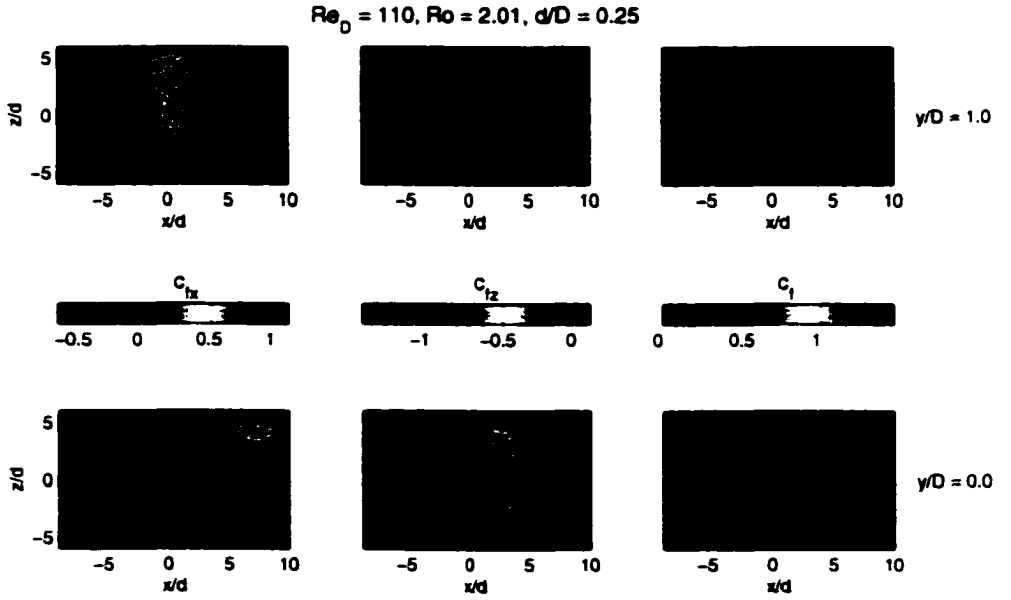

Figure C.2: Friction coefficients on the y/D = 0 and y/D = 1 surface. $Re_D = 110$, Ro = 2.01, d/D = 0.25

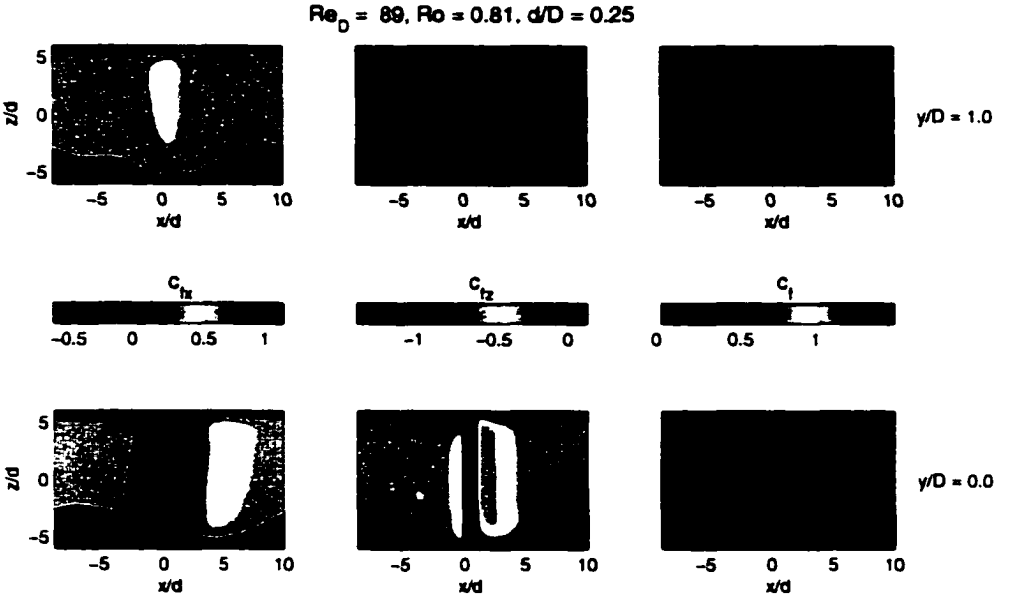

Figure C.3: Friction coefficients on the y/D = 0 and y/D = 1 surface. Re_D = 89, Ro = 0.81, d/D = 0.25

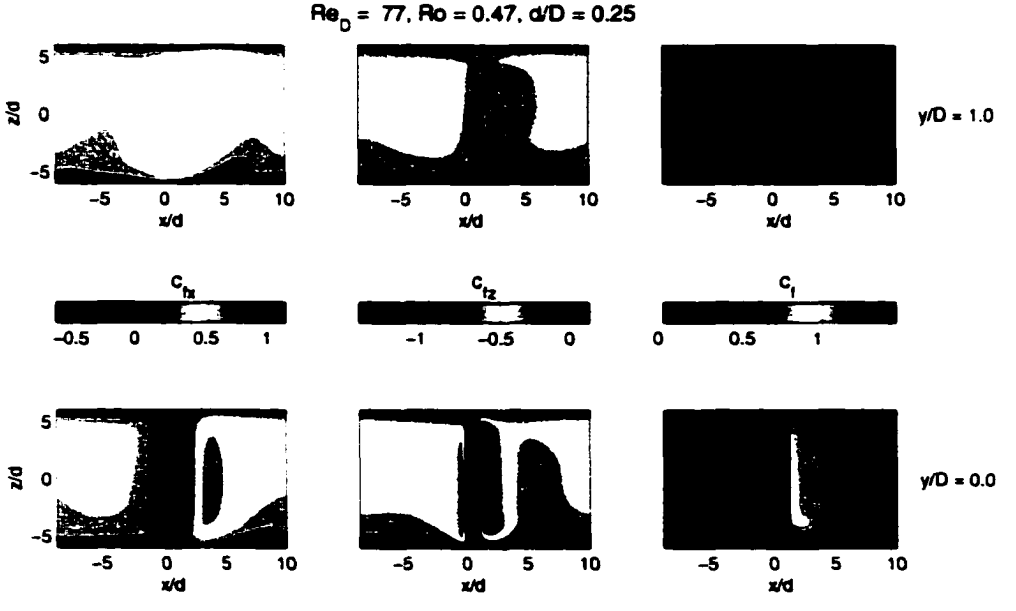

Figure C.4: Friction coefficients on the y/D = 0 and y/D = 1 surface. Re_D = 77, Ro = 0.47, d/D = 0.25

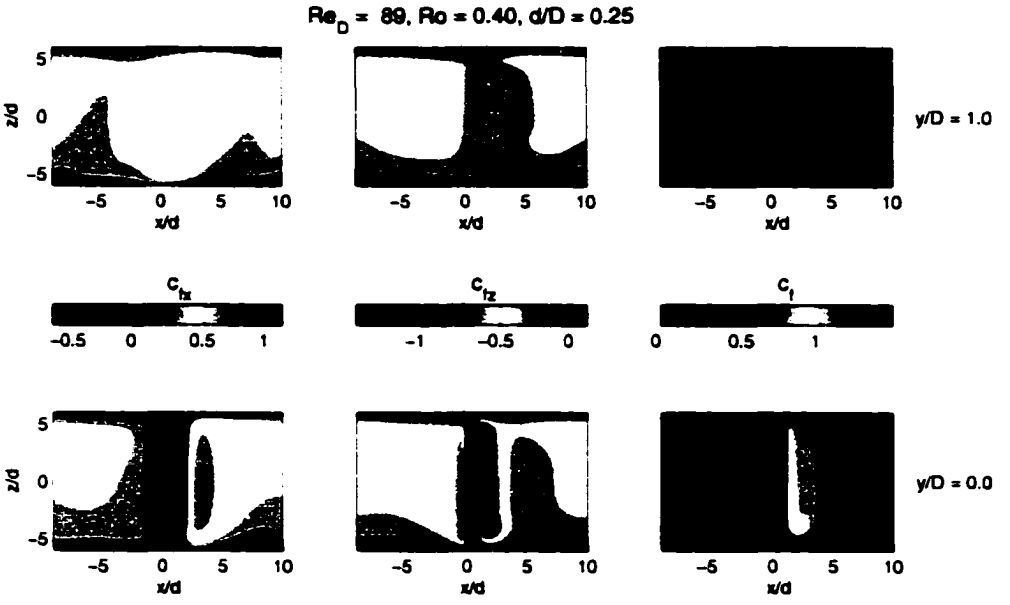

Figure C.5: Friction coefficients on the y/D = 0 and y/D = 1 surface. Re_D = 89, Ro = 0.40, d/D = 0.25

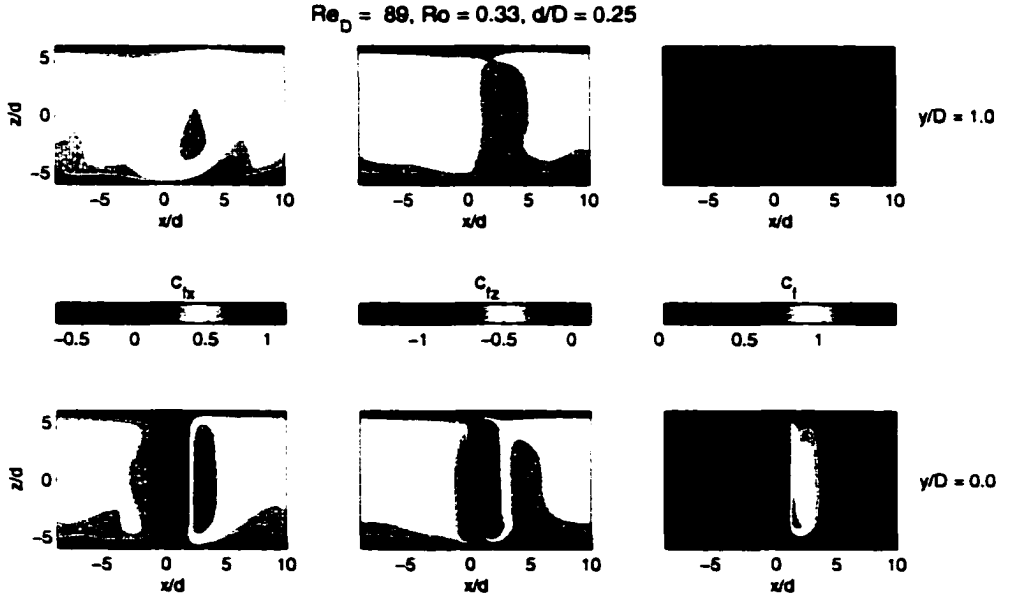

Figure C.6: Friction coefficients on the y/D = 0 and y/D = 1 surface. Re_D = 89, Ro = 0.33, d/D = 0.25

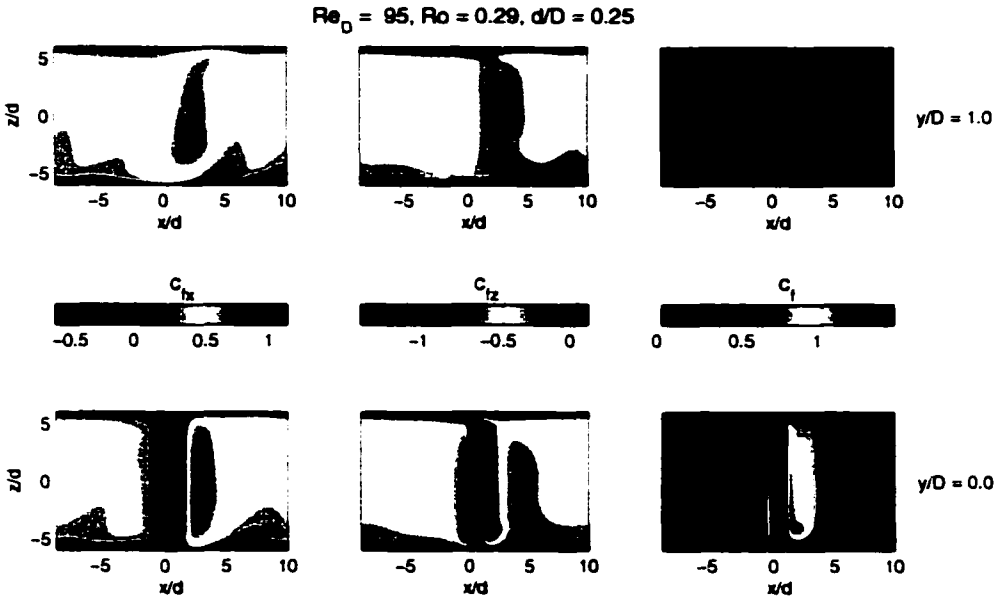

Figure C.7: Friction coefficients on the y/D = 0 and y/D = 1 surface. Re_D = 95, Ro = 0.29, d/D = 0.25

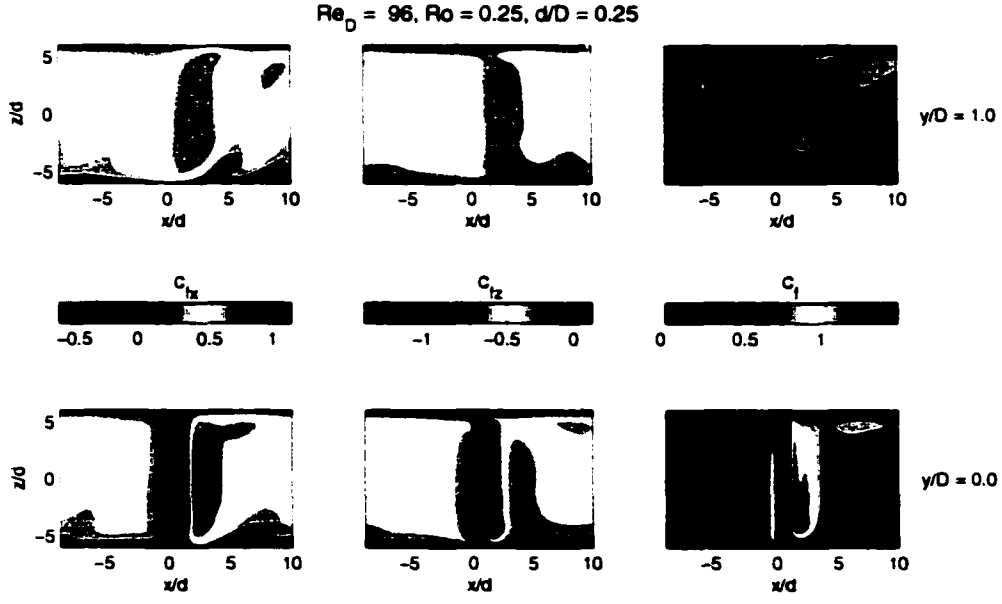

Figure C.8: Friction coefficients on the y/D = 0 and y/D = 1 surface. Re_D = 96, Ro = 0.25, d/D = 0.25

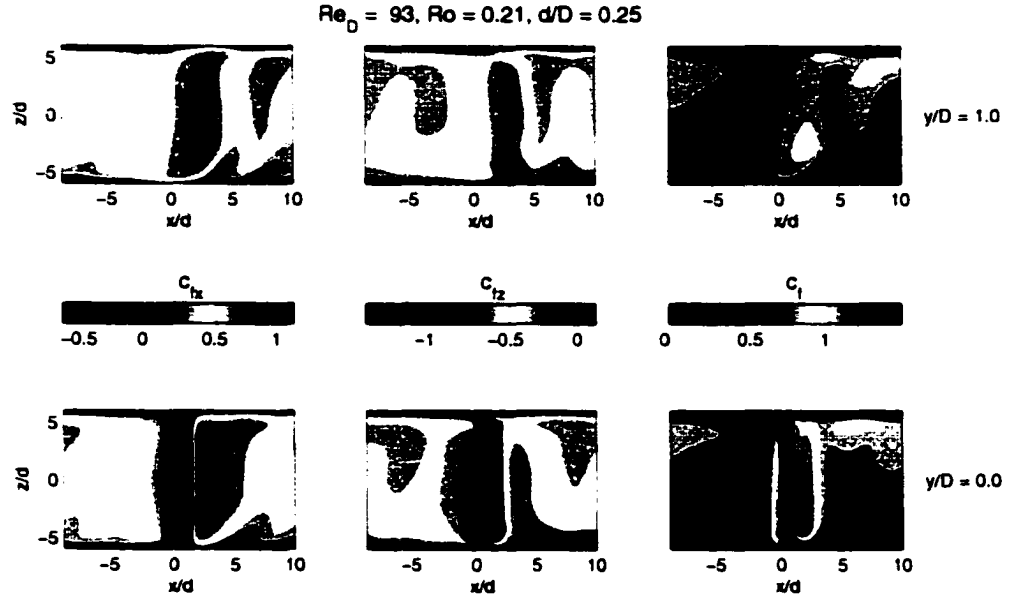

Figure C.9: Friction coefficients on the y/D = 0 and y/D = 1 surface. Re_D = 93, Ro = 0.21, d/D = 0.25

C.2 d/D = 0.50

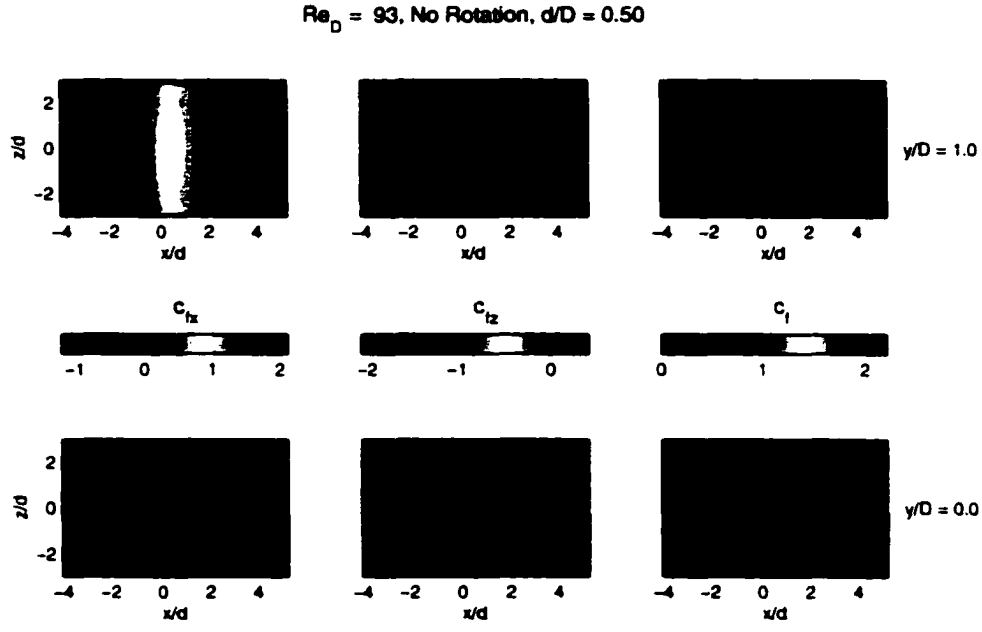

Figure C.10: Friction coefficients on the y/D = 0 and y/D = 1 surface. $Re_D = 93$. No Rotation. d/D = 0.50

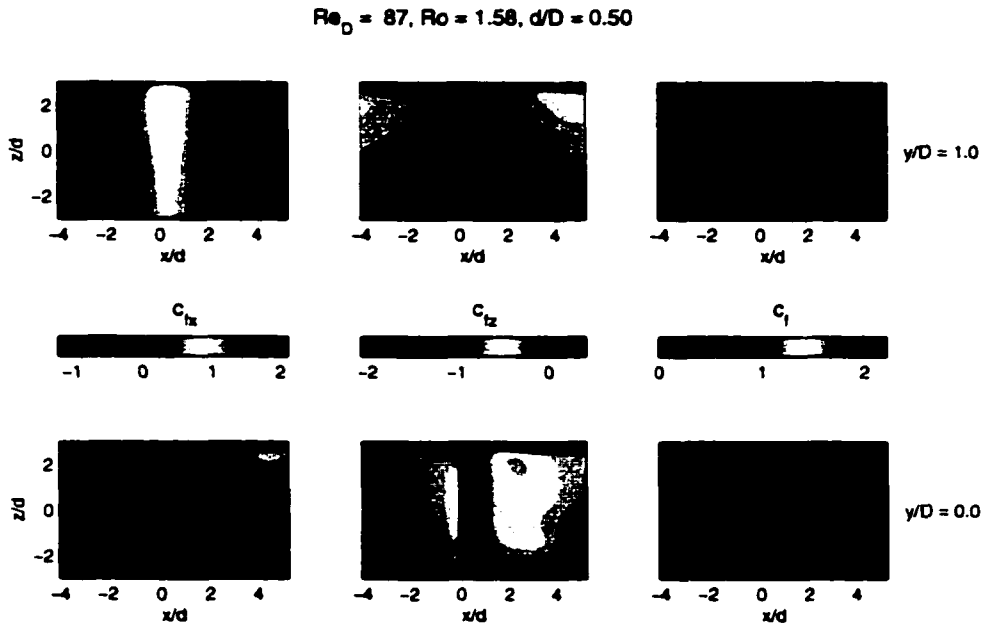

Figure C.11: Friction coefficients on the y/D = 0 and y/D = 1 surface. $Re_D = 87$, Ro = 1.58, d/D = 0.50

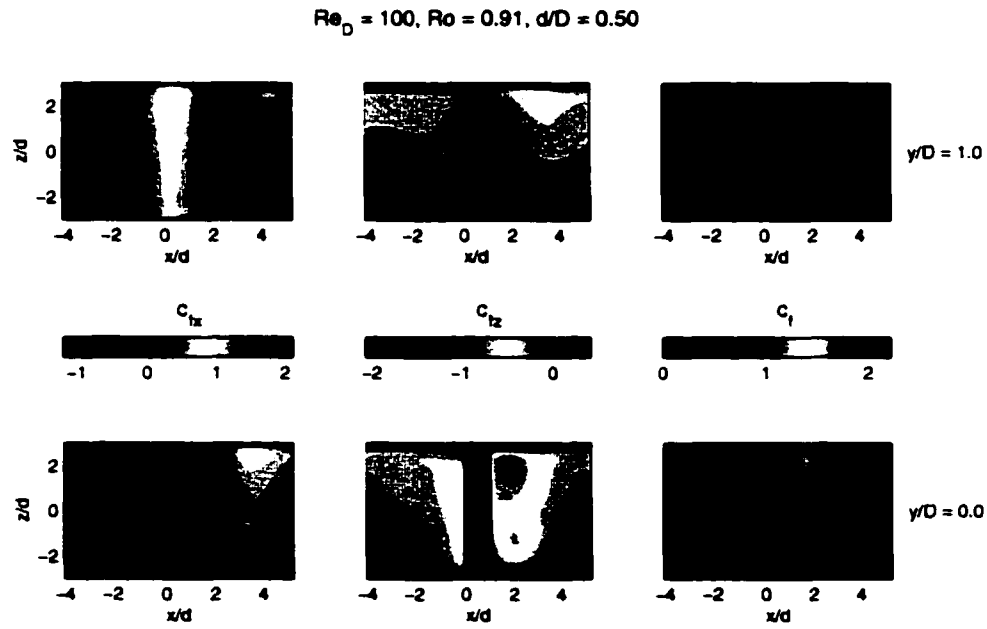

Figure C.12: Friction coefficients on the y/D = 0 and y/D = 1 surface. $Re_D = 100$, Ro = 0.91, d/D = 0.50

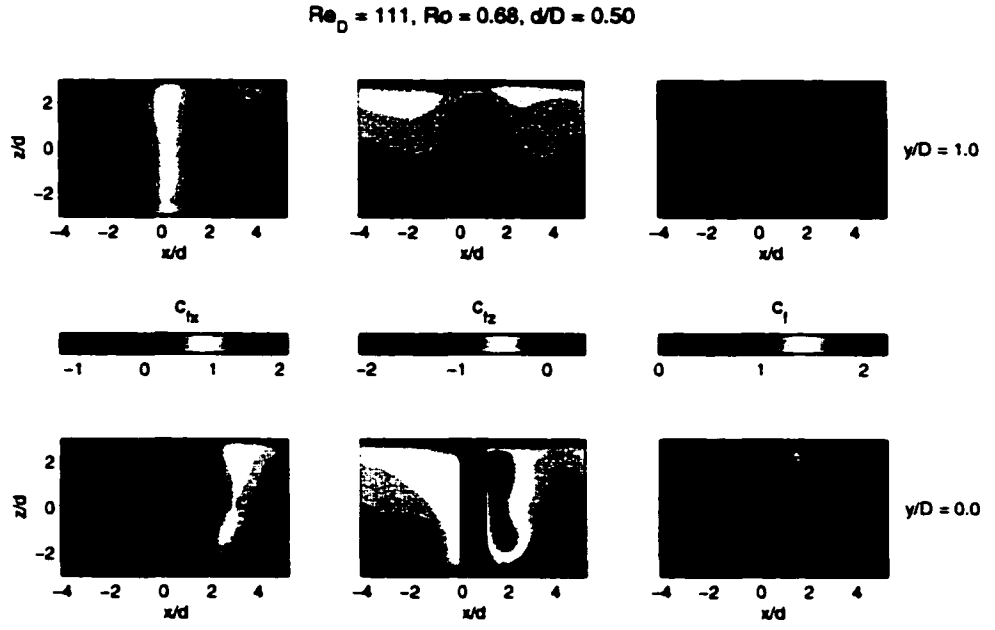

Figure C.13: Friction coefficients on the y/D = 0 and y/D = 1 surface. $Re_D = 111$, Ro = 0.68, d/D = 0.50

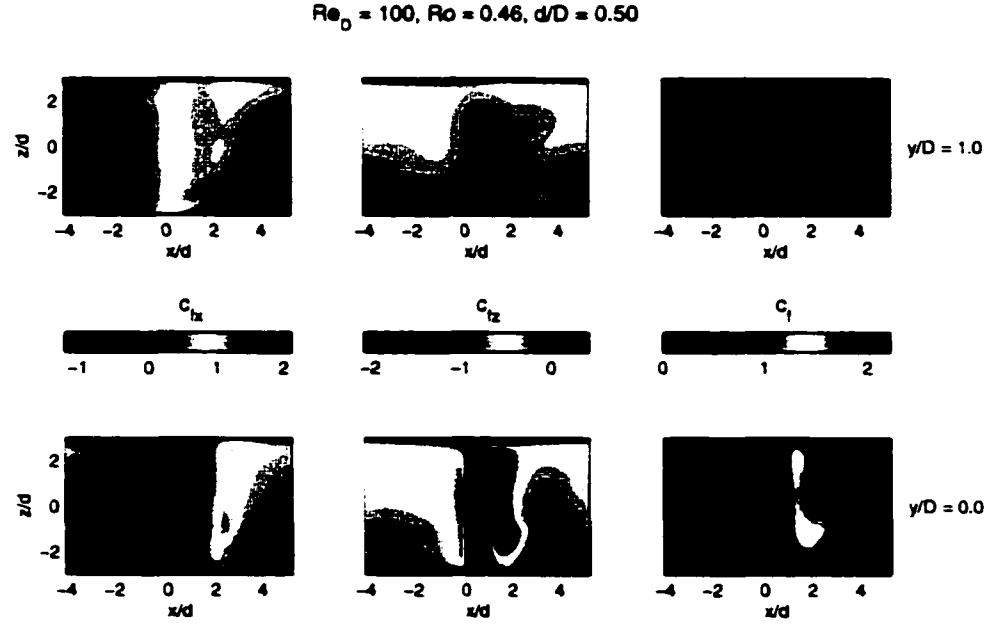

Figure C.14: Friction coefficients on the y/D = 0 and y/D = 1 surface. $Re_D = 100$, Ro = 0.46, d/D = 0.50

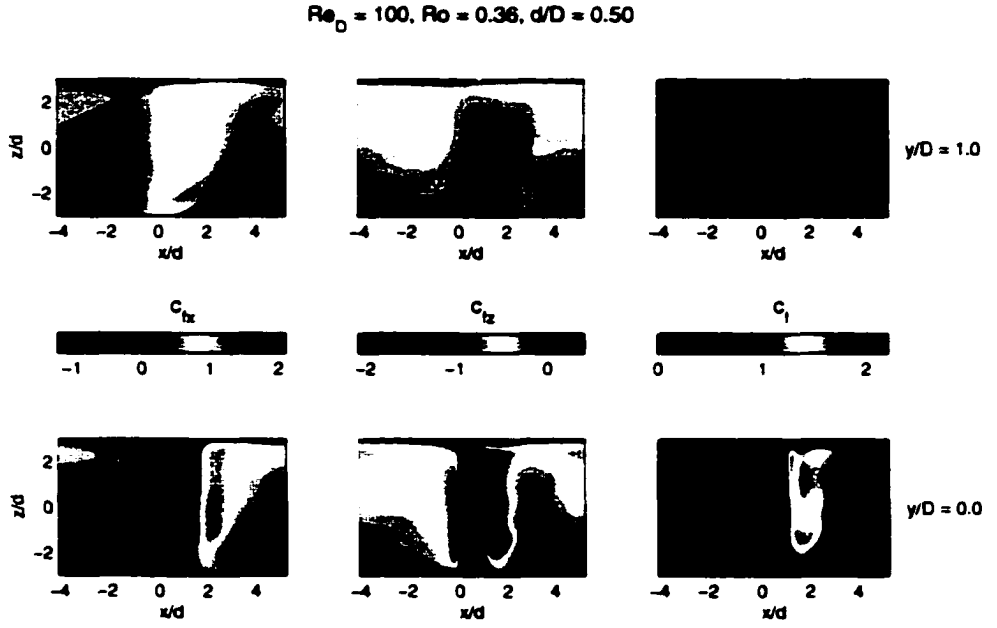

Figure C.15: Friction coefficients on the y/D = 0 and y/D = 1 surface. $Re_D = 100$, Ro = 0.36, d/D = 0.50

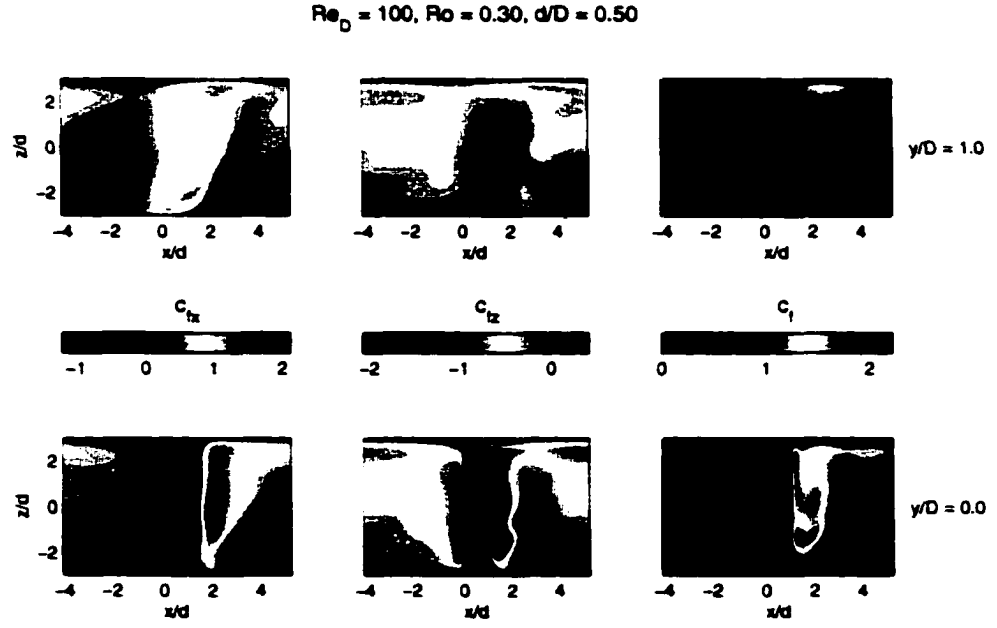

Figure C.16: Friction coefficients on the y/D = 0 and y/D = 1 surface. $Re_D = 100$, Ro = 0.30, d/D = 0.50

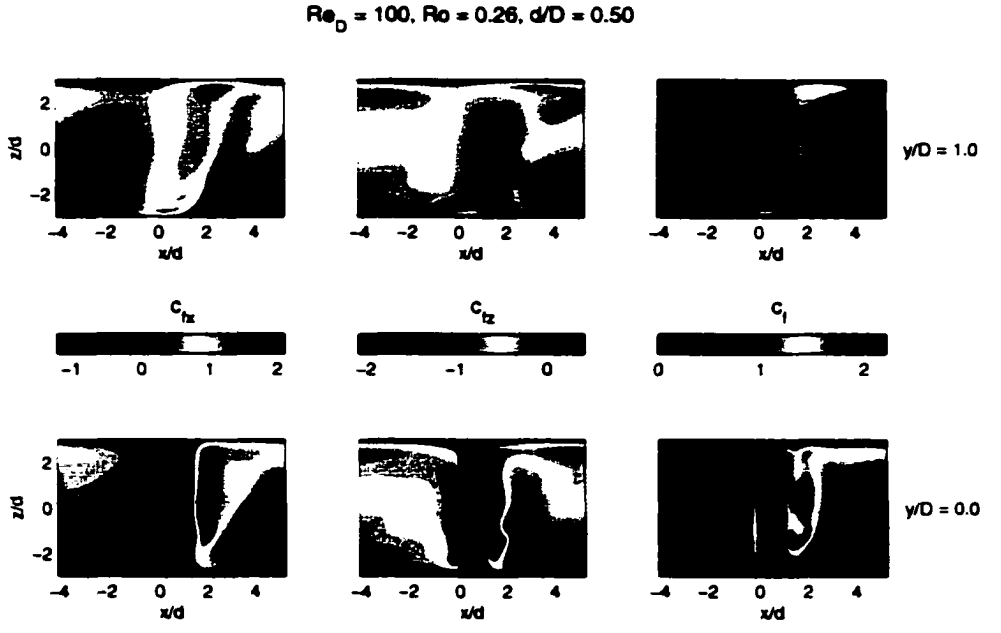

Figure C.17: Friction coefficients on the y/D = 0 and y/D = 1 surface. $Re_D = 100$, Ro = 0.26, d/D = 0.50

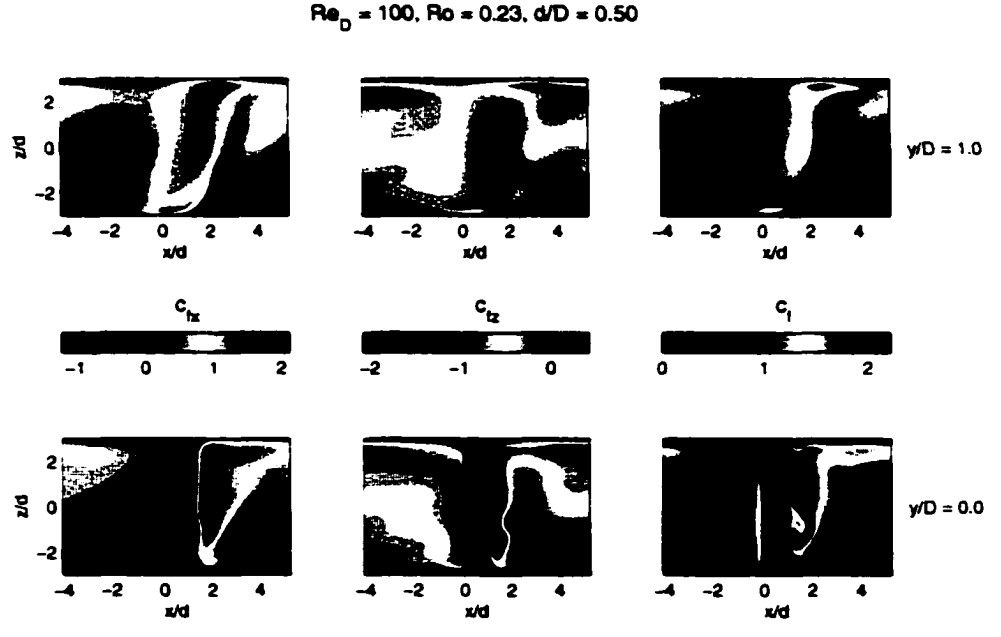

Figure C.18: Friction coefficients on the y/D = 0 and y/D = 1 surface. $Re_D = 100$, Ro = 0.23, d/D = 0.50

C.3 d/D = 0.75

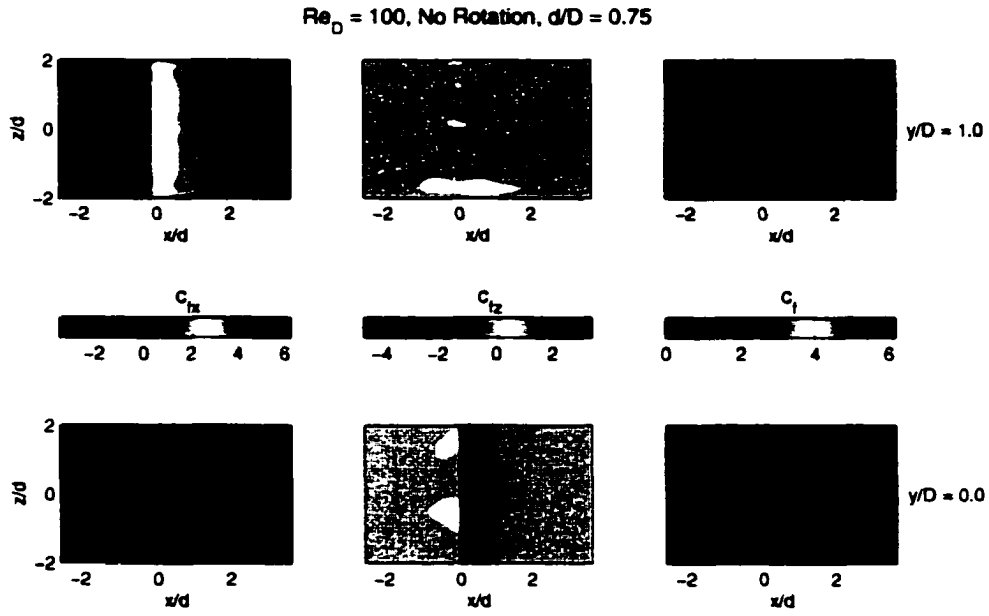

Figure C.19: Friction coefficients on the y/D = 0 and y/D = 1 surface. $Re_D = 100$, No Rotation, d/D = 0.75

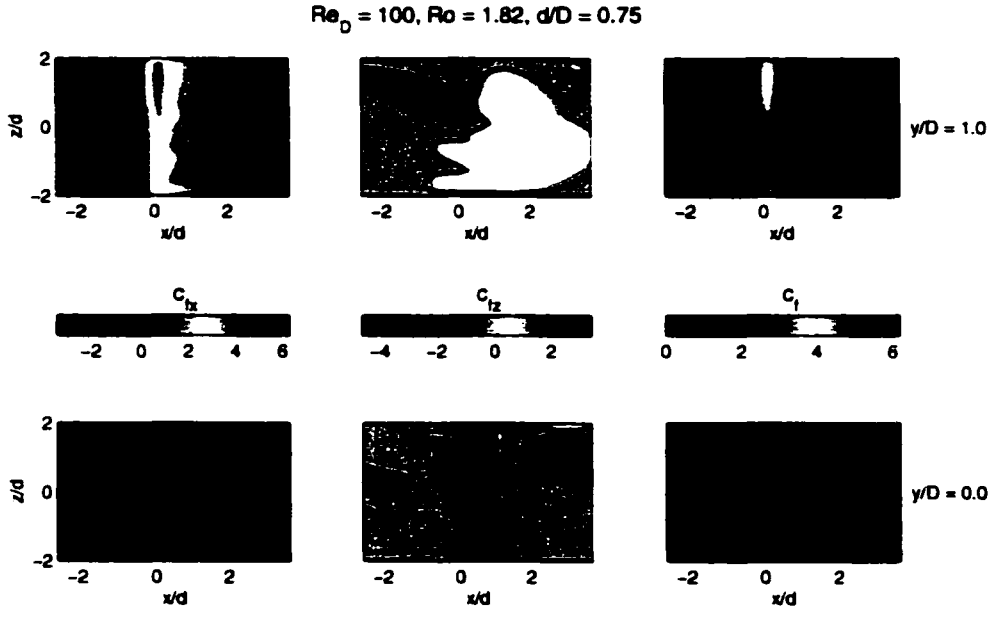

Figure C.20: Friction coefficients on the y/D = 0 and y/D = 1 surface. Re_D = 100, Ro = 1.82, d/D = 0.75

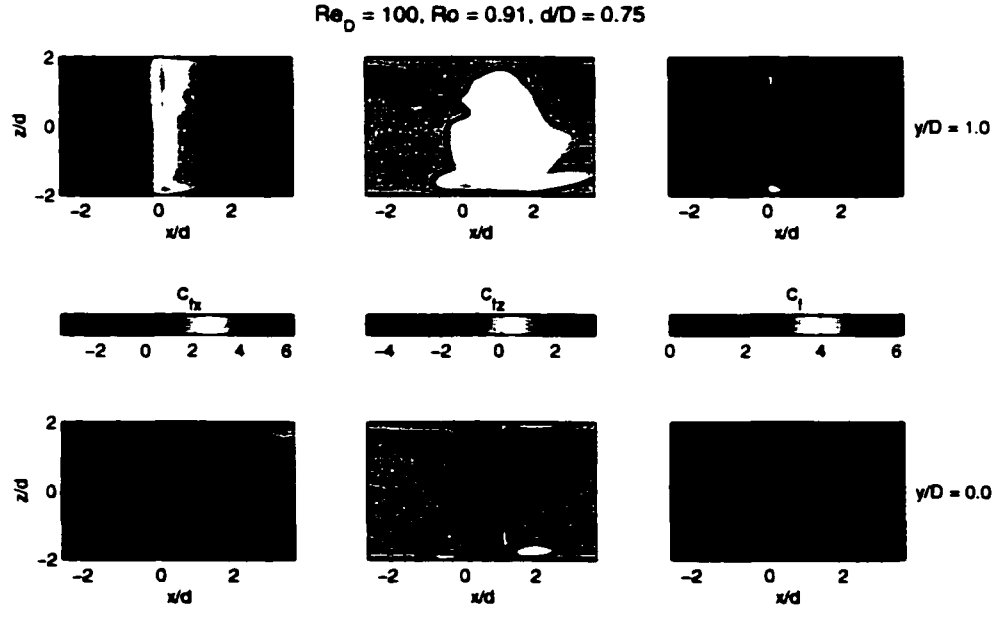

Figure C.21: Friction coefficients on the y/D = 0 and y/D = 1 surface. Re_D = 100, Ro = 0.91, d/D = 0.75

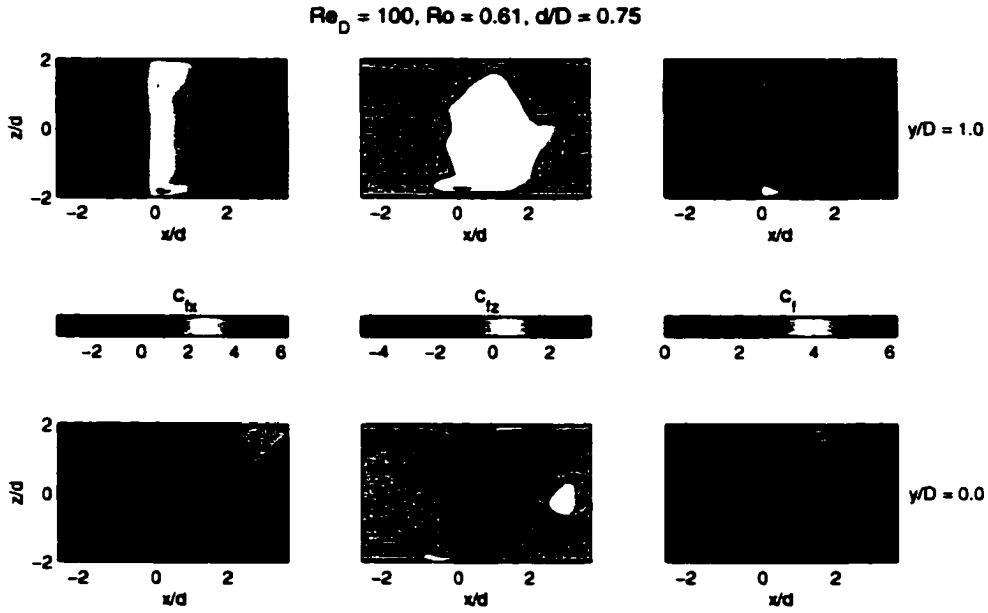

Figure C.22: Friction coefficients on the y/D = 0 and y/D = 1 surface. $Re_D = 100$, Ro = 0.61, d/D = 0.75

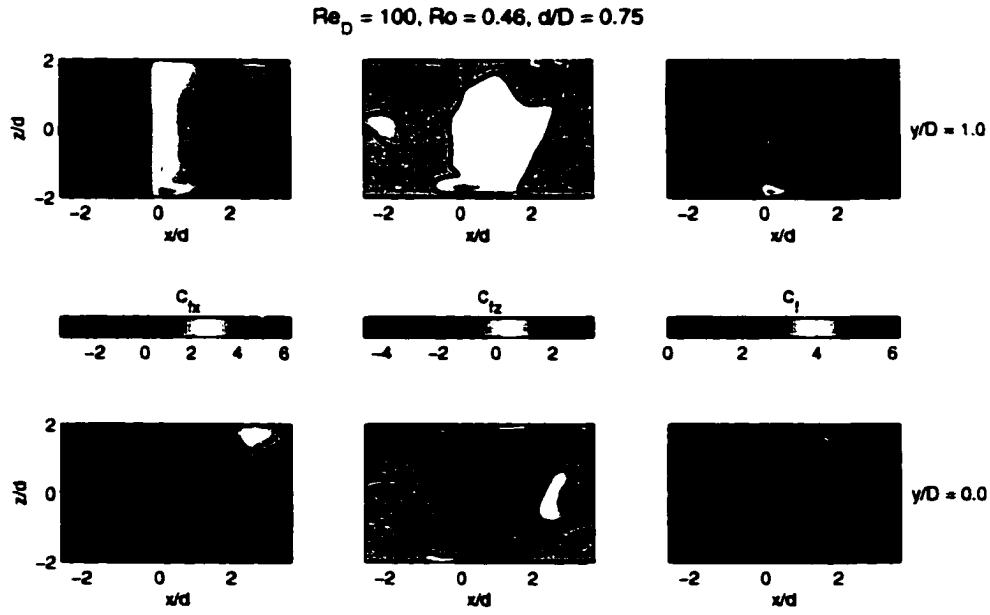

Figure C.23: Friction coefficients on the y/D = 0 and y/D = 1 surface. $Re_D = 100$, Ro = 0.46, d/D = 0.75

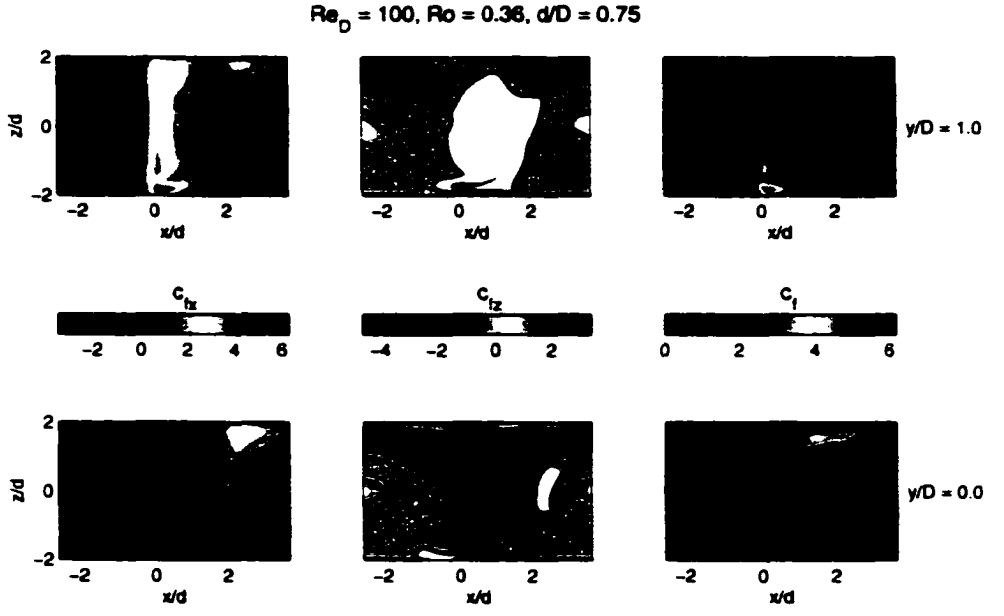

Figure C.24: Friction coefficients on the y/D = 0 and y/D = 1 surface. Re_D = 100, Ro = 0.36, d/D = 0.75

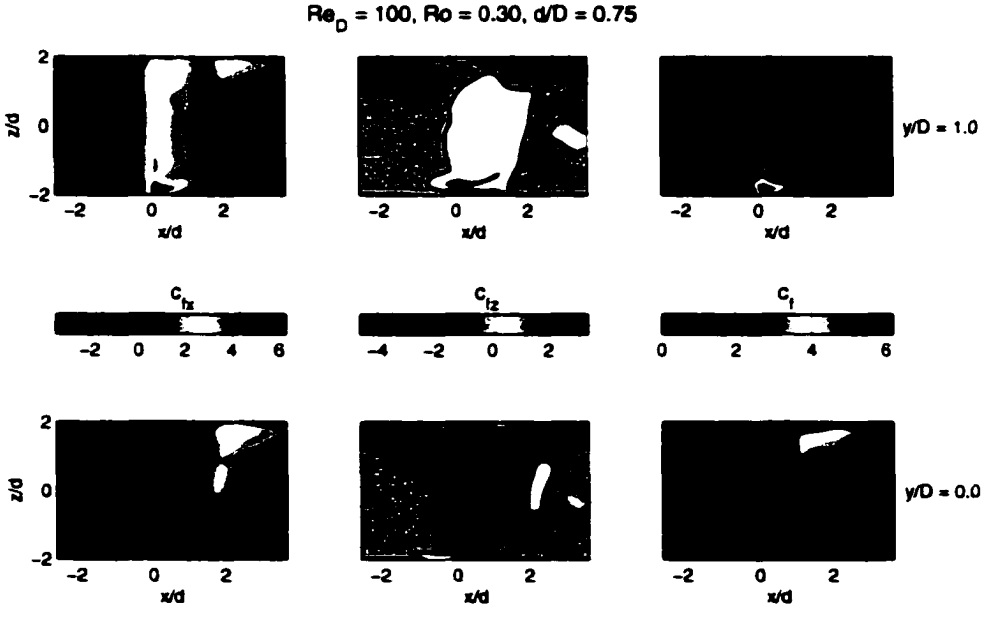

Figure C.25: Friction coefficients on the y/D = 0 and y/D = 1 surface. Re_D = 100, Ro = 0.30, d/D = 0.75

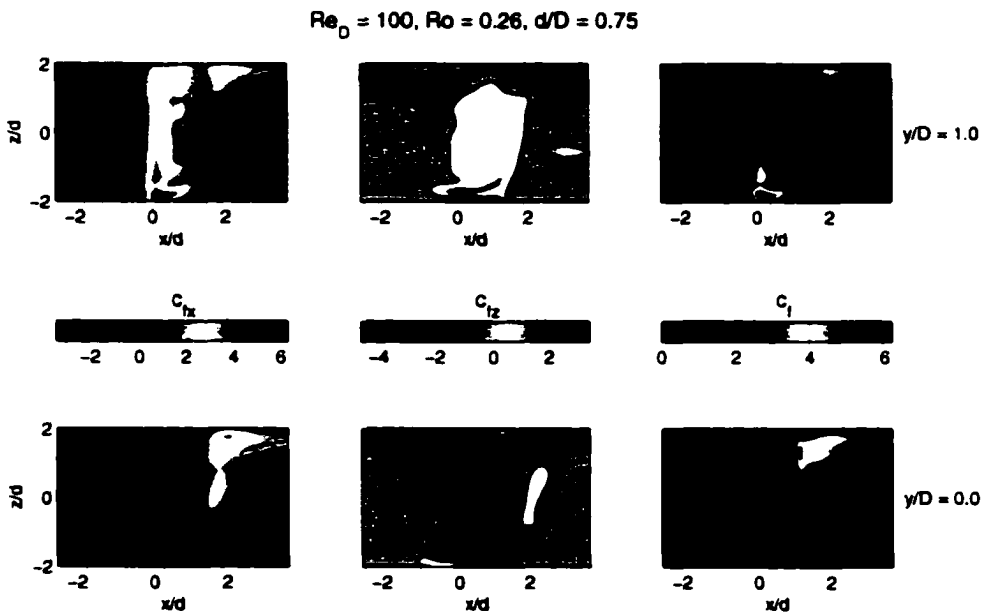

Figure C.26: Friction coefficients on the y/D = 0 and y/D = 1 surface. $Re_D = 100$, Ro = 0.26, d/D = 0.75

References

[1] Membrane news. *Membrane Quarterly*, 16(4):9, 2001.

[2] P.M. Wild, G.W. Vickers, and N. Djilali. The fundamental principles and design considerations for the implementation of centrifugal revese osmosis desalination. *J. Process Mech. Eng. (Proc.Inst.Mech.Eng E)*, 211:67–81, 1997.

[3] J.G. Pharoah. Computational modeling of centrifugal membrane and density separation. Master's thesis, University of Victoria, 1997.

[4] M. Mulder. *Basic Principles of Membrane Technology*. Kluwer Academic Publishers, 1996.

[5] Advanced Scientific Computing Ltd. *TASCflow3d V2.4 Theory Documentation*. ASC Ltd., 1995.

[6] AEA Technologies Ltd. *Cfx V4.1 User Guide*. AEA Technologies Ltd., 1995.

[7] A. Bergen, T.M. Fyles, D.S. Lycon, and G.W. Vickers. Flux enhancement in reverse osmosis using centrifugal membrane separation. *Journal of membrane Science*, 176:257–266, 2000.

[8] D. S. Lycon. *Flux Enhancement and Fouling Reduction in a Centrifugal Membrane Process*. Ph. D thesis, University of Victoria, 1999.

[9] A.S. Berman. Laminar flow in channels with porous walls. *J. Appl. Phys.*, 14(9), 1953.

[10] Y.C. Cheng and G.J. Hwang. Experimental studies of laminar flow and heat transfer in a one-porous-wall square duct with heat transfer. *Int. J. Heat & Mass Transfer*, 38(18):3475–3484, 1995.

[11] C.R. Bouchard, P.J. Carreau, T. Matsuura, and S. Sourirajan. Modeling of ultrafiltration: Prediction of concentration polarization effects. *Journal of Membrane Science*, 97:215–229, 1994.

[12] E. Pellerin, E. Michelitsch, K. Darcovich, S. Lin, and C.M. Tam. Turbulent transport in membrane modules by CFD simulation in two dimensions. *J. of Membrane Science*, 100:139–153, 1995.

[13] G. Belfort. Fluid mechanics in membrane filtration: Recent developments. *Journal of Membrane Science*, 40:123–147, 1989.

[14] H. Mallubhotla and G. Belfort. Flux enhancement during dean vortex microfiltration. 8. further diagnostics. *Journal of Membrane Science*, 125:75–91, 1997.

[15] G.B. Andeen. Effects of acceleration on reverse osmosis desalination. *Desalination*, 36:265–275, 1981.

[16] J.C. Eid and G.B. Andeen. Effects of acceleration on particulate fouling in reverse osmosis. *Desalination*, 47:191–199, 1983.

[17] S. Ilias and R. Govind. Potential applications of pulsed flow for minimizing concentration polarization in ultrafiltration. *Separation Science and Technology*, 25:1307–1324, 1990.

[18] C.D. Bertram H. Li and D.E. Wiley. Mechanisms by which pulsatile flow affects cross-flow filtration. *AIChE Journal*, 44(9):1950–1961, 1990.

[19] J.G. Pharoah, N. Djilali, and G.W. Vickers. Fluid mechanics and mass transport in centrifugal membrane separation. *Journal of Membrane Science*, 176:277–289, 2000.

[20] U. Schaflinger. Centrifugal separation of a mixture. *Fluid Dynamics Research*, 6:213–249, 1990.

[21] T.C Jen, A.S. Lavine, and G.J. Hwang. Simultaneously developing laminar convection in rotating isothermal square channels. *Int. J. Heat & Mass Transfer*, 35(1):239–254, 1992.

[22] S. Dutta, M.J. Andrews, and J.C. Han. Prediction of turbulent heat transfer in rotating smooth square ducts. *Int. J. Heat & Mass Transfer*, 39(12):2505–2514, 1996.

[23] Wei-Mon Yan. Effects of wall transpiration on mixed convection in a radial outward flow inside rotating ducts. *Int. J. Heat, Mass Transfer*, 38(13):2333–2342, 1995.

[24] K. Strewartson. On almost rigid rotations. *Journal of Fluid Mechanics*, 3:17–26, 1957.

[25] G.S Benton and D. Boyer. Flow through a rapidly rotating conduit of arbitrary cross-section. *Journal of Fluid Mechanics*, 26:69–79, 1966.

[26] V. Barcilon. Some inertial modifications of the linear viscous theory of steady rotating fluids. *Physics of Fluids*, 13(3):537–544, 1970.

[27] D.A. Bennetts and L.M. Hocking. Pressure-indiced flows at low rossby numbers. *Physics of Fluids*, 17(9):1671–1676, 1974.

[28] H.S. Kheshgi and L.E. Scriven. Viscous flow through a rotating square channel. *Physics of Fluids*, 29(10):2968–2978, 1985.

[29] J.E. Hart. Instability and secondary motion in a rotating channel flow. *Journal of Fluid Mechanics*, 45:341–353, 1971.

[30] D.E. Lezius and J.P. Johnston. Roll-cell instabilities in rotating laminar and turbulent channel flow. *Journal of Fluid Mechanics*, 77:153–175, 1976.

[31] C.G. Speziale. Numerical study of viscous flow in rotating rectangular ducts. *Journal of Fluid Mechanics*, 122:251–271, 1982.

[32] C.G. Speziale and S. Thangam. Numerical study of secondary flows and roll-cell instabilities in rotating channel flow. *Journal of Fluid Mechanics*, 130:377–395, 1983.

[33] S. Thangam and C. Speziale. Numerical study of thermal convection in rotating channel flow. *International Journal fo Numerical Methods in Fluids*, 5:133–154, 1985.

[34] K. Nandakumar, H. Raszillier, and F. Durst. Flow through rotating rectangular ducts. *Physics of Fluids A*, 3(5):770–781, 1990.

[35] A.V. Kuz'minskii and E.M. Smirnov. Experimental investigation of instabilities in flow through a long square channel rotating about a transverse axis. *Fluid Dynamics*, 31(2):235–239, 1996.

[36] H. Koyama, S. Masuda, I. Ariga, and I. Watanabe. Stabilizing and destabilizing effects of coriolis force on two-dimensional laminar and turbulent boundary layers. *Journal of Engineering for Power*, 101, 1979.

[37] L. Wang. Buoyancy-force-driven transitions in flow structures and their effects on heat transfer in a rotating curved channel. *International Journal of Heat and Mass Transfer*, 40(2):223–235, 1997.

[38] A.G. Fane J. Schwinge, D.E. Wiley and R. Guenther. Characterization of a zigzag spacer for ultrafiltration. *Journal of Membrane Science*, 172:19–31, 2000.

[39] S. Kakac, R. K. Shah, and W. Aung, editors. *Handbook of Single-Phase Convective Heat Transfer*. John Wiley and Sons, 1987.

[40] J.C. Han S. Dutta and C.P. Lee. Experimental heat transfer in a rotating triangular duct: effect of model orientation. *Journal of Heat Transfer*, 117:1058–1061, 1995.

[41] S. Dutta and J.C. Han. Local heat transfer in a rotating two-pass ribbed triangular duct with two model orientations. *International Journal of Heat and Mass Transfer*, 39(4):707–715, 1995.

[42] C.H. Hsu U. Lei. Flow through rotating straight pipes. *Physics of Fluids A*, 2(1):63–75, 1990.

[43] T.M. Liou, Y.Y. Wu, and Y. Chang. Ldv measurements of periodic fully developed main and secondary flows in a channel with rib-disturbed walls. *Journal of Fluids Engineering*, 115:109–114, 1993.

[44] T.M. Liou, W.B. Wang, and Y. Chang. Holographic interferometry study of spatially periodic heat transfer in a channel with ribs detached from one wall. *Journal of Heat Transfer*, 117:32–39, 1995.

[45] J.P. Tsia and J.J. Hwang. Measurements of heat transfer and fluid flow in a rectangular duct with alternate attached-detached rib-arrays. *International Journal of Heat and Mass Transfer*, 42:2071–2083, 1999.

[46] T.M. Liou, J.J. Hwang, and S.H. Chen. Simulation and measurement of enhanced turbulent heat transfer in a channel with periodic ribs on one principal wall. *International Journal of Heat and Mass Transfer*, 36:507–517, 1993.

[47] Y.T. Yang and S. Yang. Numerical study of turbulent flow in a two-dimensional channel with surface mounted obstacle. *International Journal of Heat and Mass Transfer*, 37:2985–2991, 1994.

[48] S.V. Patankar, C.H. Liu, and E.M. Sparrow. Fully developed flow and heat transfer in ducts having streamwise-periodic variations of cross-sectional area. *Journal of Heat Transfer*, 99:180–186, 1977.

[49] C.H. Amon, D. Majumdar, C.V. Herman, F. Mayinger, B.B. Mikic, and D.P Sekulic. Numerical and experimental studies of self-sustained oscillatory flows in comminucating channels. *International Journal of Heat and Mass Transfer*, 35(11):3115–3129, 1992.

[50] L.W. Zhang, S. Balachandar, D.K. Tafti, and F.M. Najjar. Heat transfer enhancement mechanisms in inline and staggered parallel-plate fin heat exchangers. *International Journal of Heat and Mass Transfer*, 40(10):2307–2325, 1997.

[51] L.W. Zhang, S. Balachandar, and D.K. Tafti. Effects of intrinsic three dimensionality on heat transfer and friction loss in a periodic array of parallel plates. *Numerical Heat Transfer, Part A*, 31:327–353, 1997.

[52] L.W. Zhang, D.K. Tafti, F.M. Najjar, and S. Balachandar. Computations of flow and heat transfer in parallel-plate fin heat exchangers on the cm-5: effects

of flow unsteadiness and three dimensionality. *International Journal of Heat and Mass Transfer*, 40(6):1325–1341, 1997.

[53] G. Belfort and G.A. Guter. An experimental study of electrodialysis hydrodynamics. *Desalination*, 10:221–262, 1972.

[54] A. Solan Y. Winograd and M. Toren. Mass transfer in narrow channels in the presence of turbulence promoters. *Desalination*, 13:171–186, 1973.

[55] J. Farkova. The pressure drop in membrane modules with spacers. *Journal of Membrane Science*, 64:103–111, 1991.

[56] C.C. Zimmerer and V. Kottke. Effects of spacer geometry on pressure drop, mass transfer, mixing behavior, and residence time distribution. *Desalination*, 104:129–134, 1996.

[57] G. Schock and A. Miquel. Mass transfer and pressure loss in spiral wound modules. *Desalination*, 64:339–352, 1987.

[58] C.J.D. Fell A.R. Da Costa, A.G. Fane and A.C.M. Franken. Optimal channel spacer design for ultrafiltration. *Journal of Membrane Science*, 62:275–291, 1991.

[59] A.G. Fane A.R. Da Costa and D.E. Wiley. Spacer characterization and pressure drop modelling in spacer-filled channels for ultrafiltration. *Journal of Membrane Science*, 87:79–98, 1994.

[60] S. K. Karode and A. Kumar. Flow visualization through spacer filled channels by computational fluid dynamics i. pressure drop and shear rate calculations for flat sheet geometry. *Journal of Membrane Science*, 193:69–84, 2001.

[61] D.E. Wiley Z. Cao and A.G. Fane. CFD simulations of net-type turbulence promoters in a narrow channel. *Journal of Membrane Science*, 185:157–176, 2001.

[62] D.A. Billeness, N. Djilali, and E. Zeidan. Low reynolds number flow over a square rib. *Transactions of the CSME*, 21(4):371–387, 1997.

[63] J.G. Pharoah and N. Djilali. Flow in a rotating rectangular channel. In *Proceedings of the Eighth Annual Conference of the CFD Society of Canada*, 2000.

[64] N. Al-Bastaki and A. Abbas. Use of fluid instabilities to enhance membrane performance: a review. *Desalination*, 136:252–262, 2001.

[65] P. M. Wild. *Development, Optimization and Implementation of the Design for a Centrifugal Reverse-Osmosis Desalination System*. Ph. D thesis, University of Victoria, 1994.

[66] D. Veyret P. Moulin and F. Charbit. Dean vortices: comparison of numerical simulation of shear stress and improvement of mass transfer in membrane processes at low permeation fluxes. *Journal of Membrane Science*, 183:149–162, 2001.

[67] L. Onsager. Reciprocal relations in irreversible processes I. *Physical Review*, 37:405–426, 1931.